

## ABSTRACT

Title of Document: FORCE FED MICROCHANNEL HIGH HEAT  
FLUX COOLING UTILIZING  
MICROGROOVED SURFACES

Edvin Cetegen, Doctor of Philosophy, 2010

Directed By: Michael Ohadi, Professor  
Department of Mechanical Engineering

Among other applications, the increase in power density of advanced electronic components has created a need for high heat flux cooling. Future processors have been anticipated to exceed the current barrier of  $1000 \text{ W/cm}^2$ , while the working temperature of such systems is expected to remain more or less the same. Currently, the well known cooling technologies have shown little promise of meeting these demands.

This dissertation investigated an innovative cooling technology, referred to as force-fed heat transfer. Force-fed microchannel heat sinks (FFMHS) utilize certain enhanced microgrooved surfaces and advanced flow distribution manifolds, which create a system of short microchannels running in parallel. For a single-phase FFMHS, a numerical model was incorporated in a multi-objective optimization algorithm, and the optimum parameters that generate the maximum heat transfer

coefficients with minimum pumping power were identified. Similar multi-objective optimization procedures were applied to Traditional Microchannel Heat Sinks (TMHS) and Jet Impingement Heat Sinks (JIHS). The comparison study at optimum designs indicates that for a  $1 \times 1 \text{ cm}^2$  base heat sink area, heat transfer coefficients of FFMHS can be 72% higher than TMHS and 306% higher than JIHS at same pumping power. For two-phase FFMHS, three different heat sink designs incorporating microgrooved surfaces with microchannel widths between  $21 \text{ }\mu\text{m}$  and  $60 \text{ }\mu\text{m}$  were tested experimentally using R-245fa, a dielectric fluid. It was demonstrated that FFMHS can cool higher heat fluxes with lower pumping power values when compared to conventional methods.

The flow and heat transfer characteristics in two-phase mode were evaluated using a visualization test setup. It was found that at low hydraulic diameter and low mass flux, the dominant heat transfer mechanism is dynamic rapid bubble expansion leading to an elongated bubble flow regime. For high heat-flux, as well as combination of high heat flux and high hydraulic diameters, the flow regimes resemble the flow characteristics observed in conventional tubes.

The present research is the first of its kind to develop a better understanding of single-phase and phase-change heat transfer in FFMHS through flow visualization, numerical and experimental modeling of the phenomena, and multi-objective optimization of the heat sink.

FORCE FED MICROCHANNEL HIGH HEAT FLUX COOLING UTILIZING  
MICROGROOVED SURFACES

By

Edvin Cetegen

Dissertation submitted to the Faculty of the Graduate School of the  
University of Maryland, College Park, in partial fulfillment  
of the requirements for the degree of  
Doctor of Philosophy  
2010

Advisory Committee:  
Professor Michael Ohadi, Chair/Advisor  
Professor Avram Bar-Cohen  
Professor Marino di Marzo  
Professor Jungho Kim  
Professor Gary Pertmer  
Research Professor Serguei Dessiatoun

© Copyright by  
Edvin Cetegen  
2010

# Dedication

*To my wife, Basak, my son, Alp, and to my parents for their endless encouragement  
and support that helped me complete this work*

## **Acknowledgments**

First and foremost I would like to express my deepest appreciation to Dr. Serguei Dessiatoun for his guidance, encouragement, help and support. What I learned from him, I will always carry with me throughout the rest of my life.

I am grateful to my advisor, Dr. Michael Ohadi not only for his dedication, intellectual guidance and support but also for teaching me how to push further my limits and capabilities.

I also wish to thank to Dr. Avram Bar-Cohen for his help and technical guidance. His invaluable experience, comments and feedback helped me to see the light at end of the tunnel.

I would like to take this opportunity to thank Dr. Amir Shooshtari for his help and support throughout the course of this research project. I am also grateful for my friends at Smart and Small Thermal Systems Laboratory for providing a stimulating, constructive and peaceful working environment. It was a pleasure to work beside Dr. Parisa Foughi, Dr. Sourav Chowdhury, Dr. Ebrahim Al-Hajri, Dr. Mohammed Al Shehhi, Mr. Tim McMillin, Mr. Thomas Baummer, Ms. Elnaz Kermani and Mr. Ratnesh Tiwari.

Finally, the acknowledgements would not be complete without thanks to the Office of Naval Research and the Center for Environmental Energy Engineering, Advanced Heat Exchangers Consortium who provided the financial support and made this research possible.

# Table of Contents

List Of Tables .....	VII
List Of Figures .....	VIII
List Of Acronyms .....	XIII
Nomenclature .....	XIV
CHAPTER 1: INTRODUCTION .....	1
1.1. Motivation of the Study .....	1
1.2. Research Objectives .....	5
1.3. Dissertation Organization .....	6
CHAPTER 2: WORKING PRINCIPLES AND THEORETICAL BACKGROUND .....	8
2.1. Force Fed Microchannel Heat Sinks (FFMHS) .....	8
2.2. The Microgrooved Surfaces .....	11
2.3. FFMHS for Single-Phase Heat Transfer .....	13
2.3.1. Heat Transfer and Pumping Power in Short Channels .....	14
2.3.2. Heat Transfer and Pressure Drop for Thermally and Hydrodynamically Developing Flow .....	18
2.3.3. Heat Transfer and Pressure Drop in Turning Bends .....	20
2.3.4. Literature Survey on Single-Phase FFMHS .....	22
2.4. FFMHS for Two Phase Heat Transfer .....	31
2.4.1. Flow Boiling in Conventional Channels .....	33
2.4.2. Flow Boiling in Microchannels .....	35
2.4.3. Effect of Channel Hydraulic Diameter on Inception of Nucleate Boiling .....	42
2.4.4. Critical Heat Flux in Microchannels .....	44
2.4.5. Literature Survey on Two-Phase Heat Transfer in Microchannels .....	46
2.4.6. Literature Survey on High Heat Flux Cooling Using Dielectric Working Fluids .....	50
2.1. Summary .....	54
CHAPTER 3: SINGLE-PHASE NUMERICAL STUDY .....	55
3.1. Computational Domain .....	55
3.2. Single-Phase Modeling with Computational Fluid Dynamics .....	58
3.3. Numerical Simulation of a Sample FFMHS .....	61
3.3.1. Grid Generation and Numerical Mesh .....	61
3.3.2. Boundary Conditions and Output Parameters .....	62
3.3.3. Grid Independency Test .....	65
3.3.4. Numerical Results .....	66
3.4. Parametric Numerical Study .....	78
3.4.1. Practical Geometrical Range of Microgrooved Surfaces Fabricated by Micro Deformation Technology .....	80
3.4.2. Effect of Fin Thickness and Fin Height .....	80
3.4.3. Effect of Microchannel Width .....	85
3.4.4. Effect of Inlet and Outlet Feed Channel Widths .....	87
3.4.5. Effect of Microchannel Length .....	89
3.4.6. Effects of Microgrooved Surface Base Thickness and Manifold Height .....	91

3.5. Conclusions.....	91
<b>CHAPTER 4: MULTI-OBJECTIVE OPTIMIZATION OF SINGLE-PHASE FFMHS</b>	<b>93</b>
4.1. Heat Sink Design and Optimization .....	93
4.2. Parametric CFD Simulation Interface.....	95
4.3. Approximation Assisted Optimization .....	98
4.3.1. Design of Experiment.....	99
4.3.2. Metamodeling.....	100
4.3.3. Metamodeling Validation.....	102
4.3.4. Multi-Objective Optimization .....	103
4.4. Selection of Optimization Parameters .....	104
4.5. Single-Phase Optimization Results of FFMHS .....	107
4.5.1. Analysis of Optimum FFMHS Geometry .....	110
4.6. Single-Phase Cooling Technology Comparison Study.....	116
4.6.1. Single-Phase Optimization of TMHS.....	116
4.6.2. Single-Phase Optimization of JIHS.....	118
4.6.3. Performance Comparison of FFMHS, TMHS and JIHS.....	122
4.7. Conclusions.....	127
<b>CHAPTER 5: EXPERIMENTAL TEST SETUP</b> .....	<b>130</b>
5.1. Experimental Test Setup .....	130
5.2. Test Chamber .....	133
5.2.1. Flow Distribution Header .....	137
5.2.2. The Heater Assembly .....	139
5.3. Working Fluid Selection .....	141
5.4. Calculation of Heat Losses .....	144
5.4.1. Heat Loss Evaluation and Calculation for a Sample Case .....	151
5.5. Uncertainty Propagation Calculations .....	153
5.6. Summary .....	154
<b>CHAPTER 6: EXPERIMENTAL RESULTS ON FFMHS THERMAL</b>	<b>155</b>
<b>PERFORMANCE</b> .....	<b>155</b>
6.1. Experimental Procedure.....	155
6.2. Data Reduction.....	158
6.3. Single Phase Heat Transfer and Pressure Drop .....	163
6.4. Two-Phase Heat Transfer and Pressure Drop.....	168
6.4.1. Surface #17.....	172
6.4.2. Surface #12.....	178
6.4.3. Surface #C .....	182
6.5. Comparison of Experimental Data with Convective Saturated Boiling	
Correlations.....	185
6.5.1. Chen correlation .....	190
6.5.2. Kandlikar correlation.....	191
6.5.3. Tran correlation .....	193
6.5.4. Lazarek and Black correlation.....	193
6.5.5. Warriar correlation .....	194
6.5.6. Results .....	194
6.6. Critical Heat Flux Results.....	199

6.7. Performance Comparison of FFMHS with Other High Heat Flux Cooling Technologies .....	203
6.8. Conclusions.....	205
CHAPTER 7: VISUALIZATION STUDY .....	208
7.1. Introduction to Visualization Study.....	208
7.2. Visualization Test Section .....	211
7.3. Heat Loss Calculations and Data Reduction.....	217
7.4. Visualization Results for Gap of 225 $\mu\text{m}$ and $G=200 \text{ kg/m}^2\text{s}$ .....	221
7.5. Visualization Results for Gap of 70 $\mu\text{m}$ and $G=240 \text{ kg/m}^2\text{s}$ .....	230
7.6. Visualization Results for Gap of 70 $\mu\text{m}$ and $G=780 \text{ kg/m}^2\text{s}$ .....	236
7.7. Conclusions.....	240
CHAPTER 8: CONCLUSIONS AND FUTURE WORK RECOMMENDATIONS .....	251
8.1. Conclusions Summary .....	251
8.2. Future Work Recommendations .....	254
CHAPTER 9: APPENDICES .....	259
9.1. Appendix A.....	259
9.1.1. Test chamber assembly .....	260
9.1.2. Test Chamber Flow Distribution Header .....	261
9.1.3. Test Chamber Top Flange .....	262
9.1.4. Test Chamber Bottom Flange.....	263
9.1.5. Test Chamber Heater Assembly.....	264
9.1.6. Test Chamber Microgrooved Surface .....	265
9.1.7. Visualization Test Section Assembly.....	266
9.1.8. Visualization Test Section Base .....	267
9.1.9. Visualization Test Section Heat Conductor .....	268
9.1.10. Visualization Test Section Teflon Layer 2.....	269
9.1.11. Visualization Test Section Teflon Layer 1 .....	270
9.2. Appendix B .....	271
9.3. Appendix C .....	274
9.3.1. TMHS Model Used in Optimization.....	274
9.3.2. TMHS Optimization Results.....	279
9.3.3. JIHS Optimum Results.....	282
9.4. Appendix D.....	284
REFERENCES .....	286

# List of Tables

Table 2-1. Dimensions of tested microgrooved surface and feed channels (all dimensions in microns).....	13
Table 2-2. Summary of related work on single phase FFMHS's .....	29
Table 2-3. Publication list of recent work performed for boiling in microchannels...	48
Table 2-4. Summary of technologies used for high heat flux cooling.....	53
Table 3-1. The boundary conditions applied to computational domain .....	63
Table 3-2. Results of grid independency test.....	66
Table 3-3. Numerical simulation results for reference cases .....	68
Table 4-1. The curve fit coefficients for Equations (4-7),(4-8) and (4-9) .....	125
Table 5-1. List of system components used in the experimental test setup.....	131
Table 5-2. Properties of common refrigerants at 30°C saturated liquid phase .....	144
Table 6-1. Experimental test conditions for FFMHS utilizing microgrooved Surface #12.....	170
Table 6-2. Experimental test conditions for FFMHS utilizing microgrooved Surface #17.....	170
Table 6-3. Experimental test conditions for FFMHS utilizing microgrooved Surface #C.....	171
Table 7-1. Summary of parameters used for visualization tests .....	221
Table 9-1. Optimum results obtained for the 1 x 1 cm <sup>2</sup> TMHS.....	279
Table 9-2. Optimum results obtained for the 2 x 2 cm <sup>2</sup> TMHS.....	280
Table 9-3. Optimum results obtained for JIHS.....	282

# List of Figures

Figure 2-1. Schematic flow representation of a typical FFMHS .....	9
Figure 2-2. (a) Picture of a typical microgrooved surface profile fabricated with MDT, (b) Profile of three microgrooved surfaces selected for present study	13
Figure 2-3. Schematic of flow in (a) single long channel and (b) multiple short channels.....	15
Figure 2-4. Flow and heat transfer regimes in a uniformly heated horizontal circular tube (adopted from (Ghiaasiaan, 2008)) .....	33
Figure 2-5. Major flow regimes for flows in microchannels observed by (Cornwell & Kew, 1992).....	36
Figure 2-6. Flow boiling regimes proposed by (Kandlikar, 2003) .....	39
Figure 2-7. Rapid bubble growth in 200 micron square microchannels observed by (Steinke & Kandlikar, 2003)-Each image is 8 milliseconds apart.....	40
Figure 2-8. Diagram illustrating a liquid slug, an elongated bubble and a vapor slug of model developed by (Thome et al., 2004) .....	41
Figure 2-9. Cyclic variation in heat transfer coefficient with time (adopted from (Thome et al., 2004)) .....	42
Figure 3-1. Numerical computational domain .....	56
Figure 3-2. (a) Front view and (b) perspective view for grid generated for $H_{ch}=480 \mu\text{m}$ , $w_{ch}/2=36 \mu\text{m}$ , $t_{fin}/2 = 24 \mu\text{m}$ , $L=800 \mu\text{m}$ , $w_l/2=200 \mu\text{m}$ , $w_v/2=200 \mu\text{m}$ , $L_{man}=2 \text{ mm}$ , $H_{base} = 400 \mu\text{m}$ .....	63
Figure 3-3. (a) Variation of effective heat transfer coefficient with Reynolds number, (b) Variation of pumping power with Reynolds number.....	67
Figure 3-4. Velocity vectors and velocity magnitude distribution at $z=0$ for (a) Case #1 at $h=50,000 \text{ W/m}^2\text{K}$ , (b) Case #2 at $h=150,000 \text{ W/m}^2\text{K}$ , (c) Case #3 at $h=250,000 \text{ W/m}^2\text{K}$ .....	69
Figure 3-5. Static pressure distribution at $z=0$ for (a) Case #1 at $h=50,000 \text{ W/m}^2\text{K}$ , (b) Case #2 at $h=150,000 \text{ W/m}^2\text{K}$ , (c) Case #3 at $h=250,000 \text{ W/m}^2\text{K}$ .....	69
Figure 3-6. Velocity vectors created by secondary flows at several cross sections in the computational domain for Case #3 at $h=250,000 \text{ W/m}^2\text{K}$ and $De=61$ .....	73
Figure 3-7. Pathlines at $z=0$ plane for (a) Case #1 at $h=50,000 \text{ W/m}^2\text{K}$ and $De=2$ , (b) Case #2 at $h=150,000 \text{ W/m}^2\text{K}$ and $De=16$ , (c) Case #3 at $h=250,000 \text{ W/m}^2\text{K}$ and $De=61$ .....	74
Figure 3-8. Working fluid temperature distribution at $z=0$ for (a) Case #1 at $h=50,000 \text{ W/m}^2\text{K}$ , (b) Case #2 at $h=150,000 \text{ W/m}^2\text{K}$ , (c) Case #3 at $h=250,000 \text{ W/m}^2\text{K}$ .....	75
Figure 3-9. Fin feat flux distribution for (a) Case #1 at $h=50,000 \text{ W/m}^2\text{K}$ , (b) Case #2 at $h=150,000 \text{ W/m}^2\text{K}$ , (c) Case #3 at $h=250,000 \text{ W/m}^2\text{K}$ .....	75
Figure 3-10. Temperature contours of fin surface, microchannel bottom wall and base material for (a) Case #1 at $h=50,000 \text{ W/m}^2\text{K}$ , (b) Case #2 at $h=150,000 \text{ W/m}^2\text{K}$ , (c) Case #3 at $h=250,000 \text{ W/m}^2\text{K}$ .....	77

Figure 3-11. Effect of fin and microchannel height ( $H_{ch}$ ) on pumping power at heat transfer coefficients of 50,000 W/m <sup>2</sup> K, 150,000 W/m <sup>2</sup> K and 250,000 W/m <sup>2</sup> K .....	82
Figure 3-12. Schematic of flow and a typical streamline for (a) high channel height (b) low channel height FFMHS configuration.....	83
Figure 3-13. Effect of fin thickness ( $t_{fm}$ ) on pumping power at heat transfer coefficients of 50,000 W/m <sup>2</sup> K, 150,000 W/m <sup>2</sup> K and 250,000 W/m <sup>2</sup> K .....	83
Figure 3-14. Effect of microchannel width ( $w_{ch}$ ) on pumping power at heat transfer coefficients of 50,000 W/m <sup>2</sup> K, 150,000 W/m <sup>2</sup> K and 250,000 W/m <sup>2</sup> K .....	86
Figure 3-15. Effect of inlet feed channel width ( $w_i$ ) on pumping power at heat transfer coefficients of 50,000 W/m <sup>2</sup> K, 150,000 W/m <sup>2</sup> K and 250,000 W/m <sup>2</sup> K .....	88
Figure 3-16. Effect of outlet feed channel width ( $w_o$ ) on pumping power at heat transfer coefficients of 50,000 W/m <sup>2</sup> K, 150,000 W/m <sup>2</sup> K and 250,000 W/m <sup>2</sup> K .....	88
Figure 3-17. Effect of microchannel length ( $L_{ch}$ ) on pumping power at heat transfer coefficients of 50,000 W/m <sup>2</sup> K, 150,000 W/m <sup>2</sup> K and 250,000 W/m <sup>2</sup> K .....	90
Figure 4-1. Flow diagram for Parametric CFD Simulation Interface.....	97
Figure 4-2. Example of Kriging (adopted from (Wikipedia®, 2009)) .....	102
Figure 4-3. Distribution of objective functions for sampling points obtained for FFMHS optimization study.....	108
Figure 4-4. Distribution of objective functions for sampling and validation points obtained for FFMHS optimization study .....	109
Figure 4-5. Distribution of objective functions for sampling and optimal points obtained for FFMHS optimization study .....	109
Figure 4-6. Variation of Reynolds and Dean numbers with pumping power .....	114
Figure 4-7. Variation of microchannel height with pumping power .....	114
Figure 4-8. Variation of microchannel width and fin thickness with pumping power .....	114
Figure 4-9. Variation of inlet and outlet feed channel widths with pumping power .	114
Figure 4-10. Variation of fin density with pumping power .....	115
Figure 4-11. Variation of manifold number per cm with pumping power .....	115
Figure 4-12. Variation of surface temperature uniformity with pumping power .....	115
Figure 4-13. Variation of channel velocity with pumping power.....	115
Figure 4-14. TMHS model used in optimization study .....	117
Figure 4-15. Optimum Pareto solutions of TMHS at 1 x 1 cm <sup>2</sup> and 2 x 2 cm <sup>2</sup> base areas .....	118
Figure 4-16. Jet impingement heat sink (JIHS) developed by (Meyer et al., 2005).	119
Figure 4-17. (a) Schematic of flow in a typical JIHS, (b) Computational domain...	120
Figure 4-18. Sampling, optimum and validation point distribution for optimization process of JIHS .....	122
Figure 4-19. Optimum Pareto solution for three cooling technologies for 1 x 1 cm <sup>2</sup> base area heat sink .....	124
Figure 4-20. Optimum Pareto solution for three cooling technologies for 2 x 2 cm <sup>2</sup> base area heat sink .....	124
Figure 4-21. Optimum heat transfer coefficients for three cooling technologies at constant pumping power (a) 1 x 1 cm <sup>2</sup> heat sink, (b) 2 x 2 cm <sup>2</sup> heat sink....	126

Figure 4-22. Optimum pumping power values for three cooling technologies at constant heat transfer coefficient (a) 1 x 1 cm <sup>2</sup> heat sink, (b) 2 x 2 cm <sup>2</sup> heat sink .....	126
Figure 5-1. Experimental test setup used for single-phase and two-phase thermal performance tests .....	132
Figure 5-2. Flow diagram of experimental test setup .....	133
Figure 5-3. Picture of the experimental test chamber .....	135
Figure 5-4. Schematic of the experimental test chamber.....	136
Figure 5-5. (a) 3D view of flow distribution header, (b) picture of the actual flow distribution header .....	137
Figure 5-6. (a) Flow distribution in the header, (b) Position of thermocouples .....	138
Figure 5-7. The heater assembly (a) exploded schematic view, (b) actual picture and schematic of assembled view .....	141
Figure 5-8. Thermocouple locations on the back of the microgrooved surface .....	141
Figure 5-9. Resistance analogy for heat transfer in heater assembly.....	145
Figure 5-10. Temperature distribution on the bottom part of the heater assembly for a thin-film resistor temperature of 320 K and 300K fluid temperature .....	147
Figure 5-11. Thermal resistance network between microgrooved surface base and ambient fluid .....	147
Figure 5-12. Thermal resistance network between the microgrooved surface base and the fluid in the microchannel and manifold channel.....	149
Figure 5-13. Experimentally measured R <sub>mm</sub> values.....	151
Figure 5-14. Percentage of parasitic heat loss distribution and boiling curve for FFMHS using microgrooved Surface #17 at G=1000 kg/m <sup>2</sup> s constant mass flux .....	152
Figure 6-1. Schematic of microgrooved surface and manifold configuration .....	159
Figure 6-2. Single-phase results of experimental and numerical heat transfer coefficients .....	165
Figure 6-3. Single-phase results of experimental and numerical pressure drop values .....	165
Figure 6-4. Velocity and static pressure distribution in the center plane for (a) Surface #12, G=200 kg/m <sup>2</sup> s, (b) Surface #17, G=200 kg/m <sup>2</sup> s, (c) Surface #C, G=200 kg/m <sup>2</sup> s, (a) Surface #12, G=1000 kg/m <sup>2</sup> s, (a) Surface #17, G=1000 kg/m <sup>2</sup> s, (a) Surface #C, G=1000 kg/m <sup>2</sup> s, .....	167
Figure 6-5 Boiling curves for FFMHS Surface #17 for (a) 200 < G < 600 kg/m <sup>2</sup> s and (b) 700 < G < 1400 kg/m <sup>2</sup> s .....	173
Figure 6-6. (a) Heat transfer coefficient based on base area versus base heat flux and (b) heat transfer coefficient based on wetted area versus outlet quality for FFMHS Surface #17 .....	176
Figure 6-7. Pressure drop values versus outlet quality for FFMHS Surface #17 .....	177
Figure 6-8. Boiling curves for FFMHS Surface #12 .....	179
Figure 6-9. Heat transfer coefficient based on base area versus base heat flux and (b) heat transfer coefficient based on wetted area versus outlet quality for FFMHS Surface #12 .....	180
Figure 6-10. Pressure drop values versus outlet quality for FFMHS Surface #12 ...	181
Figure 6-11. Boiling curves for FFMHS Surface #C.....	183

Figure 6-12. Heat transfer coefficient based on base area versus base heat flux and (b) heat transfer coefficient based on wetted area versus outlet quality for FFMHS Surface #C.....	184
Figure 6-13. Pressure drop values versus outlet quality for FFMHS Surface #C ....	185
Figure 6-14. Flow schematic in (a) an FFMHS (b) a straight microchannel.....	188
Figure 6-15. Heat transfer coefficient comparison for single-phase convective heat transfer for selected microgrooved surfaces .....	190
Figure 6-16. Comparison of saturated convective boiling heat transfer correlations with experimental data of FFMHS Surface #12, (a) $G=300 \text{ kg/m}^2\text{s}$ and $Re=100$ , (a) $G = 1200 \text{ kg/m}^2\text{s}$ and $Re=400$ .....	196
Figure 6-17. Comparison of saturated convective boiling heat transfer correlations with experimental data of FFMHS Surface #17, (a) $G=300 \text{ kg/m}^2\text{s}$ and $Re=70$ , (a) $G = 1400 \text{ kg/m}^2\text{s}$ and $Re=320$ .....	198
Figure 6-18. Comparison of saturated convective boiling heat transfer correlations with experimental data of FFMHS Surface #C, (a) $G=400 \text{ kg/m}^2\text{s}$ and $Re=50$ , (a) $G = 1000 \text{ kg/m}^2\text{s}$ and $Re=130$ .....	198
Figure 6-19. Critical heat flux based on wet channel area versus channel mass flux data obtained for Surface #17 .....	200
Figure 6-20. Variation of surface temperature and inlet fluid temperature with time at critical heat flux condition for Surface #17, $G=300 \text{ kg/m}^2\text{s}$ and $q''_{\text{wall}} = 72.1 \text{ W/cm}^2$ , $\Delta T_{\text{subcool}} = 2.6 \text{ }^\circ\text{C}$ .....	202
Figure 6-21. Variation of surface temperature and inlet fluid temperature with time at critical heat flux condition for Surface #17, $G=1400 \text{ kg/m}^2\text{s}$ and $q''_{\text{wall}} = 154.9 \text{ W/cm}^2$ , $\Delta T_{\text{subcool}} = 8.5 \text{ }^\circ\text{C}$ .....	203
Figure 6-22. Thermal performance comparison of different high heat flux cooling technologies .....	204
Figure 7-1. Schematic of visualization test section (a) front isometric view (b) back isometric view.....	212
Figure 7-2. Exploded view of visualization test section components.....	214
Figure 7-3. Picture of the visualization test section.....	215
Figure 7-4. Test surface and area of interest for the visualization study.....	216
Figure 7-5. (a) Heat conduction paths in the test set section, (b) Location of thermocouples.....	218
Figure 7-6. Calculated total heat losses for the test surface with a gap of $70 \text{ }\mu\text{m}$ ....	219
Figure 7-7. Calculated total heat losses for the test surface with a gap of $225 \text{ }\mu\text{m}$ ..	220
Figure 7-8. Single-phase velocity vectors and static pressure distribution in test section for $225 \text{ }\mu\text{m}$ gap and $G=200 \text{ kg/m}^2\text{s}$ mass flux.....	222
Figure 7-9. Two-phase flow regimes for gap of $225 \text{ }\mu\text{m}$ and mass flux of $G=200 \text{ kg/m}^2\text{s}$ at (a) $q''_{\text{wall}} = 3.1 \text{ W/cm}^2$ , (b) $q''_{\text{wall}} = 4.6 \text{ W/cm}^2$ , (c) $q''_{\text{wall}} = 9.3 \text{ W/cm}^2$ .....	224
Figure 7-10. Two-phase flow regimes for gap of $225 \text{ }\mu\text{m}$ and mass flux of $G=200 \text{ kg/m}^2\text{s}$ at (a) $q''_{\text{wall}} = 15.5 \text{ W/cm}^2$ , (b) $q''_{\text{wall}} = 23.8 \text{ W/cm}^2$ (c) $q''_{\text{wall}} = 32.8 \text{ W/cm}^2$ .....	226
Figure 7-11. Two-phase flow regimes for gap of $225 \text{ }\mu\text{m}$ and mass flux of $G=200 \text{ kg/m}^2\text{s}$ at (a) $q''_{\text{wall}} = 46.2 \text{ W/cm}^2$ (b) $q''_{\text{wall}} = 88.9 \text{ W/cm}^2$ .....	227

Figure 7-12. Two-phase flow instability observed for gap of 225 $\mu\text{m}$ , $G=200 \text{ kg/m}^2\text{s}$ , $q''_{\text{wall}}= 103.1 \text{ W/cm}^2$ .....	229
Figure 7-13. Single-phase velocity vectors and static pressure distribution in test section for 70 $\mu\text{m}$ gap and $G=240 \text{ kg/m}^2\text{s}$ mass flux .....	231
Figure 7-14. Two-phase flow regimes for gap of 70 $\mu\text{m}$ and mass flux of $G=240 \text{ kg/m}^2\text{s}$ at (a) $q''_{\text{wall}}= 9.8 \text{ W/cm}^2$ (b) $q''_{\text{wall}}= 13.4 \text{ W/cm}^2$ (c) $q''_{\text{wall}}= 15.1 \text{ W/cm}^2$ (d) $q''_{\text{wall}}= 18.2 \text{ W/cm}^2$ .....	234
Figure 7-15. Two-phase flow instability observed for gap of 70 $\mu\text{m}$ , $G=240 \text{ kg/m}^2\text{s}$ , $q''_{\text{wall}}= 40.9 \text{ W/cm}^2$ .....	235
Figure 7-16 Single-phase velocity vectors and static pressure distribution in test section for 70 $\mu\text{m}$ gap and $G=780 \text{ kg/m}^2\text{s}$ mass flux .....	236
Figure 7-17. Two-phase flow regimes for gap of 70 $\mu\text{m}$ and mass flux of $G=780 \text{ kg/m}^2\text{s}$ at (a) $q''_{\text{wall}}= 17.7 \text{ W/cm}^2$ (b) $q''_{\text{wall}}= 24.1 \text{ W/cm}^2$ (c) $q''_{\text{wall}}= 31.8 \text{ W/cm}^2$ (d) $q''_{\text{wall}}= 46.7 \text{ W/cm}^2$ .....	239
Figure 7-18. Two-phase flow regimes for gap of 70 $\mu\text{m}$ and mass flux of $G=780 \text{ kg/m}^2\text{s}$ at (a) $q''_{\text{wall}}= 61.9 \text{ W/cm}^2$ (b) $q''_{\text{wall}}= 81.4 \text{ W/cm}^2$ (c) $q''_{\text{wall}}= 92.0 \text{ W/cm}^2$ .....	240
Figure 7-19. Variation of experimental heat transfer coefficients with stability criteria for Surface #12.....	246
Figure 7-20. Variation of experimental heat transfer coefficients with stability criteria for Surface #17.....	246
Figure 7-21. Variation of experimental heat transfer coefficients with stability criteria for Surface #C .....	247
Figure 7-22. Schematic of flow model in the inlet region for (a) Half FFMHS unit cell (a) Flow between parallel plates with constant wall heat flux.....	247
Figure 7-23. Local heat transfer coefficients versus non dimensional entrance length for (a) Surface #C, (b) Surface #12.....	248
Figure 7-24. Onset of Nucleate Boiling (ONB) and wall and liquid superheats calculated for (a) Surface #C, (b) Surface #12 .....	250
Figure 8-1. Low profile FFMHS with zigzag manifold design .....	258
Figure 9-1. Boundary conditions and computational domain.....	271
Figure 9-2. The meshed geometry used in numerical model.....	272
Figure 9-3. Total thermal resistance versus mass flow rate for the bottom part of the heater assembly.....	273
Figure 9-4. Mathematical model of TMHS .....	274

## List of Acronyms

1D	One Dimensional
2D	Two Dimensional
3D	Three Dimensional
AAO	Approximation Assisted Optimization
CFC	Chlorofluorocarbon
CFD	Computational Fluid Dynamics
CHF	Critical Heat Flux
DOE	Design of Experiment
EDM	Electron Discharge Machining
EES	Engineering Equation Solver
FFMHS	Force Fed Microchannel Heat Sink
FPI	Fins Per Inch
GA	Genetic Algorithm
HCF	Hydrofluorocarbons
HVAC	Heating Ventilation and Air Conditioning
JHHS	Jet Impingement Heat Sink
MDT	Micro Deformation Technology
MED	Maximum Entropy Design
MOGA	Multi Objective Genetic Algorithm
ONB	Onset of Nucleate Boiling
OTEC	Ocean Thermal Energy Conversion
PCFDSI	Parametric CFD Simulation Interface
PTFE	Polytetrafluoroethylene
RMSE	Root Mean Square Error
RRMSE	Relative RMSE
MSFCVT	Multi-response Space Filling Cross Validation Tradeoff
TMHS	Traditional Microchannel Heat Sink

## Nomenclature

$A$	Heat transfer area, $m^2$
$Br$	Brinkman number: $Br = \mu V^2 / k (T_s - T)$
$c_p$	Specific heat at constant pressure, J/kgK
$D$	Diameter, m
$f$	Friction loss coefficient
$g$	Gravitational acceleration, $m/s^2$
$G$	Mass flux (mass velocity), $kg/m^2s$ ; Geometrical parameter, mm
$h$	Heat transfer coefficient, $W/m^2K$ ; Enthalpy, J/kg
$\bar{h}$	Average heat transfer coefficient, $W/m^2K$
$H$	Height, mm
$I$	Current, Amp
$K$	Local pressure loss coefficient
$k$	Thermal conductivity, $W/mK$
$L$	Length, mm
$\dot{m}$	Mass flow rate, kg/s
$n$	Number of channels/tubes
$N$	Number of computational cells
$Nu$	Nusselt number: $Nu = hD_h / k$
$\overline{Nu}$	Average Nusselt number
$P$	Pressure, Pa; Power, W; Perimeter, m
$\bar{P}$	Average pressure
$Pr$	Prandtl number: $Pr = \nu / \alpha$
$q$	Heat transfer rate, W
$q''$	Heat flux, $W/cm^2$
$R$	Curvature radius, mm; Thermal resistance, K/W
$Re$	Reynolds number: $Re = \rho V D / \mu$
$S$	Source term
$t$	Thickness, mm
$T$	Temperature, K; Constant temperature
$\bar{T}$	Average temperature
$\nu$	Specific volume, $m^3/kg$
$V$	Fluid velocity, m/s; Voltage, V
$\dot{V}$	Volumetric flow rate, $m^3/s$
$w$	Width, mm
$We$	Webber number: $We = \rho V^2 D / \sigma$

## Greek symbols:

$\alpha$	Thermal diffusivity, m <sup>2</sup> /s
$\gamma$	Aspect ratio
$\Delta$	Difference
$\delta$	Film thickness
$\rho$	Density, kg/m <sup>3</sup>
$\eta$	Fin efficiency
$\chi$	Relative rate of change of geometrical parameters
$\Gamma$	Mass flow rate per unit depth, kg/sm
$\nu$	Kinematic viscosity, m <sup>2</sup> /s
$\tau$	Shear stress vector, Pa
$\sigma$	Surface tension, N/m; Area expansion ratio
$\psi$	Relative rate of change of pumping power
$\mu$	Viscosity, Pa-s

## Subscripts:

<i>AlNi</i>	Aluminum nitride
<i>app</i>	Apparent
<i>base</i>	Base
<i>c</i>	Contraction; Curvature; Conductive
<i>h</i>	Channel
<i>e</i>	Expansion
<i>f</i>	Film
<i>fd</i>	Fully developed
<i>film</i>	Film
<i>fin</i>	Fin
<i>h</i>	Hydraulic diameter; hydrodinamically; heated
<i>hab</i>	Bottom part of heater assembly
<i>heater</i>	Heater
<i>i</i>	Inlet; index
<i>inf</i>	Ambient
<i>l</i>	Liquid
<i>lam</i>	Laminar
<i>lv</i>	Liquid-vapor
<i>m</i>	Mean (average)
<i>max</i>	Maximum
<i>mg</i>	Microgrooved surface to fluid
<i>min</i>	Minimum
<i>mm</i>	Microgrooved surface to manifold
<i>o</i>	Outlet
<i>pump</i>	Pumping
<i>ref</i>	Reference
<i>s</i>	Heated surface

<i>sat</i>	Saturation
<i>solder</i>	Solder
<i>t</i>	Thermally; Thermocouple; Total
<i>v</i>	Vapor
<i>wall</i>	Heat transfer wet area
<i>x</i>	Local

# CHAPTER 1: INTRODUCTION

## 1.1. Motivation of the Study

Active thermal management is required in many applications such as power electronics, plasma facing components, high heat load optical components, laser diode arrays, X-ray medical devices, and power electronics in hybrid vehicles. In general, the exposed area that needs to be cooled for these systems is limited, and the amount of heat that needs to be removed is extremely high, thus requiring cooling of high heat fluxes. More importantly, the performance of many of these systems is often directly related to their cooling capacity and heat transfer efficiency. While high heat flux cooling is essential, to create an efficient cooling system there are usually also other system requirements, such as low thermal resistance, surface temperature uniformity, low pumping power, compact design, suitability for large area cooling and compatibility for use with dielectric fluids.

For example, the power electronics capacity and functionality has grown significantly during the past decade. Currently, most of the advanced electronic components already generate heat fluxes exceeding  $100 \text{ W/cm}^2$ , while some future microprocessors and power-electronic components, such as high power laser and electronic radar systems, have been projected to generate heat fluxes over  $1000 \text{ W/cm}^2$  (Mudawar, 2001), (Kandlikar, 2005), (Kandlikar & Bapat, 2007). The increase in power density of the components has also created a need for advanced cooling technologies to achieve high heat dissipation rates in order to keep the electronic system at desired working temperatures. At this point, traditional and well

known cooling methods such as conduction and natural/forced air convection will prove insufficient for such high heat fluxes leaving the possibility open for the introduction of new competitive technologies.

Depending on whether single-phase or phase-change cooling is selected, the two options generally accepted as the most effective active cooling methods for next-generation high heat-flux systems are; single phase liquid cooling and two phase convective boiling, respectively. Single-phase cooling systems are currently used to cool power electronics usually by directly forcing liquid water over the heat transfer surface of a heat sink. These cooling systems can yield very high heat transfer coefficients when combined with microchannels. However, this technique requires high pumping power to sustain the very large pressure drops associated with driving the single-phase flow through the typical micro-channels with small hydraulic diameters. But one particular design advantage of single-phase systems is that the heat transfer and fluid flow physical mechanisms are relatively well understood and well established, and a large variety of numerical simulation CFD tools can be used to simulate flow in complex geometries.

Two-phase cooling systems are generally more accepted as the ultimate solution to meet demanding cooling requirements of future power electronics in terms of heat transfer efficiency, compactness, and weight and energy consumption. For the same heat sink geometry and flow conditions, the transfer coefficients generated during phase change can be expected to be several times higher than those for convective liquid cooling. Two-phase systems benefit from the large latent heat capacity of the working fluid, which is much higher than the sensible heat of a single

phase cooling system. But although they are superior to single-phase systems in several aspects, two-phase systems also present certain challenges, including the complexity of two-phase flow regimes and heat transfer phenomena. The complexity is even more pronounced when phase-change occurs in small hydraulic diameter channels such as microchannels. Also, the two-phase flow instabilities and the difficulty of mathematical modeling are other issues that need to be considered when designing two-phase flow systems.

Several cooling systems for both single-phase and two-phase active cooling have been proposed for cooling high heat fluxes. The current leading options are systems such as microchannel, jet impingement and spray cooling systems. A detailed overview of these technologies, along with a discussion of their fundamental physics, can be found in reviews of (Bar-Cohen, Arik, & Ohadi, 2006), (Agostini, Fabbri et al., 2007), (Kandlikar & Bapat, 2007) and for spray cooling alone, (J. H. Kim, 2007). In general, jet impingement and spray cooling techniques use high-pressure liquid jets and shattered liquid droplets aimed directly at the electronic device being cooled or at a heat spreader in contact with the electronic device. Spray cooling systems can provide good isothermal surface temperature and can remove high heat fluxes, but due to small nozzle diameters and the high pressure required to produce small droplets, spray nozzles are more prone to clogging, inconsistent spray characteristics and erosion, while also representing high pressure drops. The heat transfer performance of Jet Impingement Heat Sinks (JIHS) mostly depends on the jet velocity, which can be highly non-uniform over the cooled surface, so using a heat spreader may be necessary to improve the temperature uniformity. This in turn results

in additional thermal resistance to the heat sink. Traditional Microchannel Heat Sinks (TMHS) are constructed using microchannels running in parallel connected by an inlet and outlet manifold. This technology has demonstrated the ability to generate high heat transfer coefficients. However, the issues of high pressure drops, and two-phase flow instabilities accompanied by flow maldistribution, suppress the cooling limits and applicability ranges of microchannel heat sinks.

All the current active thermal management systems, whether working in single-phase or two-phase mode, have their own applicability advantages and challenges, and none of these systems have been accepted yet as the universal cooling technology. Therefore, the field is open for the introduction of new cooling systems that can remove heat fluxes exceeding  $1000 \text{ W/cm}^2$  with higher heat transfer coefficients and reasonable pumping power requirements. To meet all of these requirements, innovative technologies and concepts have been proposed in several publications. Single phase Force Fed Microchannel Heat Sink (FFMHS) concept (also known as the manifold microchannel heat sink) was first introduced by (Harpole & Eninger, 1991), and later studies reported that FFMHS can achieve heat transfer coefficients of 30% (Y. I. Kim, Chun, Kim, Pak, & Baek, 1998) to 50% (Ryu, Choi, & Kim, 2003) higher than TMHS at same pumping power. However, due to flow and geometrical complexities, FFMHS have received less attention, and the optimum geometry and flow conditions have not been studied in detail yet. Moreover, all available published data is based on microgrooved surfaces created on silicon substrates, while similar enhanced surfaces created from metal substrates such as copper have several advantages. For two-phase heat transfer, the fundamentals of

FFMHS have not been investigated, but a few experimental results performed at the University of Maryland's, Smart and Small Thermal Systems Laboratory through the earlier phases of current study showed that force-fed cooling has the ability to cool heat fluxes up to  $925 \text{ W/cm}^2$  with heat transfer coefficient of  $130,000 \text{ W/m}^2\text{K}$  using the non aqueous refrigerant HFE 7100. These results demonstrated that FFMHS is a promising candidate for applications that require high heat-flux cooling with high efficiency. The present work therefore represents a focus on exploring and pushing the technological boundaries of FFMHS working in both single-phase and two-phase heat transfer modes.

## **1.2. Research Objectives**

The main research objectives and contributions of this dissertation are as follows:

- To develop a better understanding of single-phase and phase-change heat transfer in FFMHS through experimental and numerical modeling of the phenomena, multi-objective optimization of the heat sink and its comparison with widely known cooling technologies, and flow visualization studies that all contributed to advance the basic understanding of the complex physics involved in a force-fed micro channel heat sinks.
- To formulate metamodels that can predict single-phase heat transfer coefficients and pumping power for FFMHS at given geometrical and flow conditions, and to validate the metamodel prediction capability and demonstrate its efficiency.

- To optimize the single-phase FFMHS using a multi-objective optimization algorithm by selecting the most important and relevant geometrical parameters as optimization variables and objective functions.
- To compare the single-phase thermal performance of FFMHS with the performance of other well-known high heat-flux cooling systems such as TMHS and JIHS to better quantify major advantages and limitation of the force-fed micro channel cooling technique
- To apply the force-fed cooling principle to two-phase cooling and to identify the parameters that most significantly affect the heat transfer performance.
- To determine the two-phase flow regimes and to understand the heat transfer and critical heat flux (CHF) mechanisms that control two-phase FFMHS.

### **1.3. Dissertation Organization**

Chapter 2 explains the working principles of FFMHS in both single-phase and two-phase heat transfer modes. Fluid flow and heat transfer fundamentals are covered, including the relevant literature survey. Chapter 3 discusses the single-phase numerical modeling strategy for FFMHS and the effects of several geometrical and flow parameters on heat transfer coefficients and pressure drops. In Chapter 4, the FFMHS is optimized by the Approximation Assisted Optimization technique, and then the thermal performance at optimum conditions is compared to TMHS and JIHS. The experimental test setup, test section and the test procedure are explained in detail in Chapter 5, and the single-phase and two-phase results are presented and analyzed in Chapter 6. In order to visualize the flow patterns in a unit FFMHS cell, a visualization test section was fabricated. The design procedure of the test section and

the resulting visualization results are presented in Chapter 7. The dissertation concludes with Chapter 8, where the conclusions are summarized, followed by the recommended future work.

## **CHAPTER 2: WORKING PRINCIPLES AND THEORETICAL BACKGROUND**

This chapter begins with an introduction to the working concepts of Force Fed Microchannel Heat Sinks (FFMHS). The design and geometrical properties of the microgrooved surfaces that provide the heat transfer area enhancement of FFMHS, are described next. The chapter concludes with review of fundamental aspects of fluid flow and heat transfer mechanisms that appear to govern thermal performance of FFMHS. Both single-phase and two-phase heat transfer modes are analyzed, and relevant literature survey is presented.

### **2.1. Force Fed Microchannel Heat Sinks (FFMHS)**

An FFMHS is a combination of a microgrooved surface and a system of manifolds. The flow schematic of a typical FFMHS is shown in Figure 2-1. The flat side of the microgrooved surface is attached to the heat source, while the fins and microchannels on the other side are in contact with the working fluid. On the top of the microchannels is a series of manifolds, usually aligned perpendicularly to the fins and microchannels. The manifolds do not contribute to heat transfer, significantly and their role is mainly to distribute the fluid and to provide structural integrity of FFMHS. Each gap between two neighboring manifolds forms a feed channel, which is used to direct the fluid in (inlet feed channel) or out (outlet feed channel) of the microchannels. This gap can have similar or different dimensions for inlet and outlet feed channels, depending on the desired design configuration. From a design stand

point, compared with microchannels, the feed channels have much greater hydraulic diameters and lower flow velocities. The manifolds and the microgrooved surface are usually attached to each other by use of compressive force that seals the tip of the fins to the bottom of the manifolds.

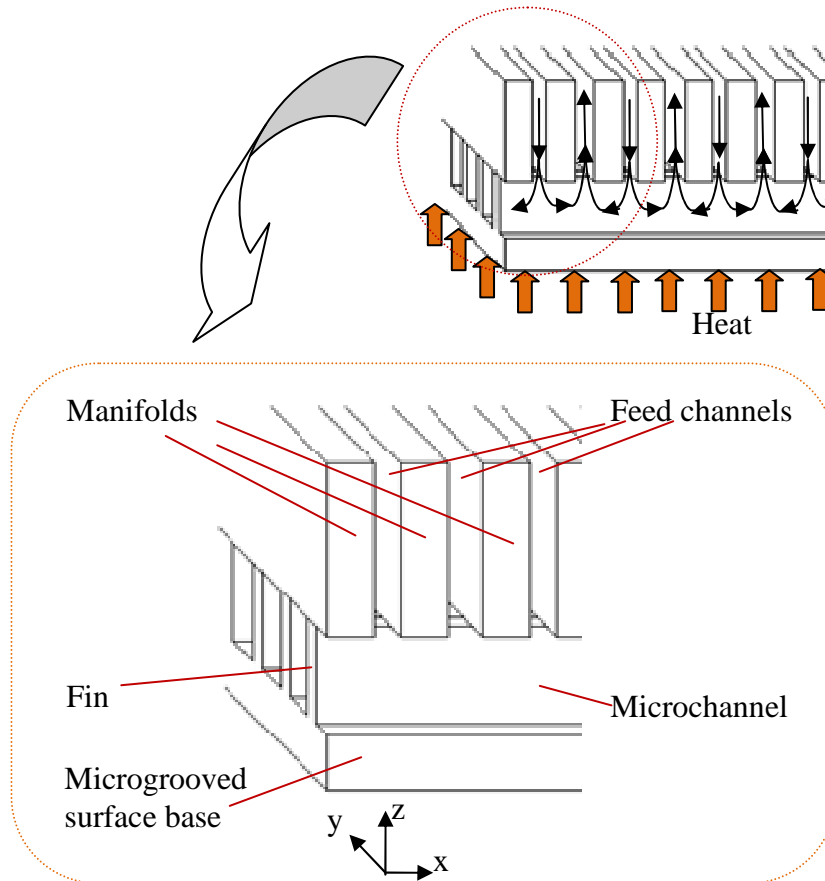


**Figure 2-1. Schematic flow representation of a typical FFMHS**

Generally, all the inlet feed channels are connected to a larger common volume, such as a reservoir, which supplies the fluid and pressure needed to drive the flow. Thus, being fed from the same pressure source, each inlet feed channel will deliver same amount of fluid. The flow in the feed channels can be considered as flow between two parallel plates due to the usually high aspect ratio of feed channels.

After entering and flowing along the feed channel, the fluid will encounter the microchannels and fins of the microgrooved surface. Here the fluid will be forced to enter the microchannel from the top, perpendicularly to the microchannel direction. This entrance will create a flow area reduction and in turn will increase the flow velocity and decrease the static pressure at the entrance region of the microchannel. After entering the microchannel area, the flow will start to develop until it flows down to the bottom of the channel, eventually creating an impingement zone. After the stagnation point, the fluid splits in two streams, each stream turning  $90^\circ$  and flowing in the opposite direction in the microchannel. The fluid continues to flow a short distance in the microchannel, where the flow and heat transfer occurs similar to that in a typical TMHS. This distance of the straight microchannel is defined by the thickness of the manifolds. At the end of the straight microchannel, the fluid will make a second  $90^\circ$  turn, joining with the counter stream and leaving the area through the corresponding outlet feed channel. The exit from the microchannel to the outlet feed channel creates a pressure increase and velocity reduction due to an increase in flow area. This flow configuration is repetitive and results in the formation of arrays of short microchannels working in parallel.

The key geometrical arrangements and flow distributions that make FFMHS an effective heat transfer cooling system are listed as follows:

- The system pressure drop is decreased significantly due to the short flow length of a turning path in the microchannels. The system, in fact, is a network of short microchannels working in parallel, and therefore the total system pressure drop is the pressure drop of a single microchannel flow turn.

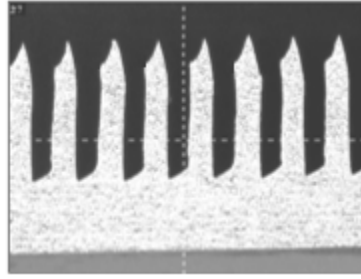
- FFMHS is suitable for cooling of large areas and can be easily expandable in the x-y directions (Figure 2-1). By increasing the flow rate proportional to the base area expansion rate, the system pressure drop and effective heat transfer coefficient remain constant.
- FFMHS benefits from multiple inlet entrance effects. The area in the microchannel flow inlet region is very effective and can yield very high heat transfer coefficients. This effect is the result of thermally developing flow in this region, which is associated with very thin boundary layers and low thermal resistance values. Having multiple inlet regions enhances the overall heat transfer coefficient of the heat sink.
- Generally, chips that need to be cooled are spaced close together on the substrate, and there is limited space in the x-y direction for including additional equipment such as flow distributing manifolds. In this case, it could be more convenient to include additional parts in the z-direction, which makes FFMHS design favorable.

## **2.2. The Microgrooved Surfaces**

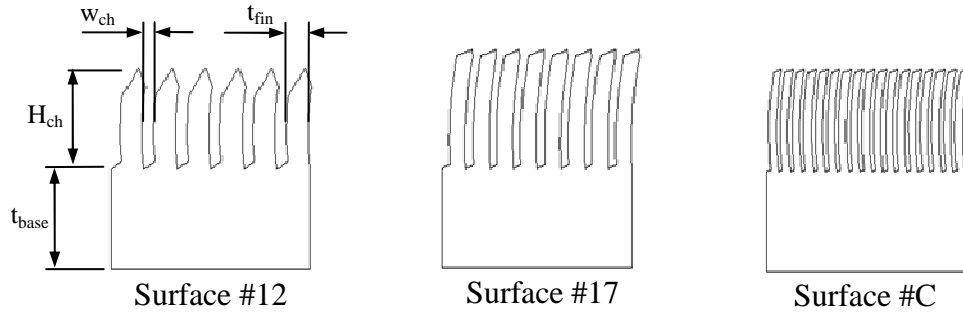
As shown in Figure 2-1, the FFMHS design requires enhanced surfaces with alternating fins and channels, also known as microgrooved surfaces. Depending on the substrate material and geometric features, several fabrication methods are currently used for this purpose. For example, the silicon microfabrication technique can create very fine surfaces with microchannels having hydraulic diameters in the order of microns. Micromachining is another process that can create microchannels using methods such as Electron Discharge Machining (EDM) or micro-milling. These

methods are the most suitable for metal substrates. The microgrooved surfaces selected and used in this study were fabricated using Micro Deformation Technology (MDT). This relatively new fabrication method allows fabrication of enhanced surfaces with very high aspect ratios from a wide range of metals. MDT was initially developed to produce enhanced heat transfer tubes and was later adopted for flat surfaces. The fabrication principle of MDT is based on a continuous process of skiving and bending material on the top of a metal substrate. The major advantage of MDT is that it can be cost effective when adapted for mass production. Detailed information on MDT can be found in (Thors & Zoubkov, 2009).

A cross section of a typical microgrooved surface fabricated using MDT is shown in Figure 2-2 (a). The fin geometry created by MDT is usually slightly different from the fin structure of a traditional microgrooved surface fabricated usually by silicon microfabrication technique. Based on the cutting tool geometry used during fabrication, MDT microgrooved surfaces have an unconventionally sharp fin-tip and a slightly bent fin geometry. For the present work, three types of microgrooved surfaces with different geometries have been selected and fabricated by MDT. All three samples were fabricated from copper, and the experimental test procedure is described in detail in Chapter 5. The cross-sectional profile of selected samples is shown in Figure 2-2, while dimensions are given in Table 2-1.



(a)



(b)

**Figure 2-2. (a) Picture of a typical microgrooved surface profile fabricated with MDT, (b) Profile of three microgrooved surfaces selected for present study**

**Table 2-1. Dimensions of tested microgrooved surface and feed channels (all dimensions in microns)**

Sample Name	Fin Density [FPI]	Fin Pitch [ $\mu\text{m}$ ]	Channel Height – $H_{\text{ch}}$ [ $\mu\text{m}$ ]	Channel Width – $w_{\text{ch}}$ [ $\mu\text{m}$ ]	Fin Thickness – $t_{\text{fin}}$ [ $\mu\text{m}$ ]	Channel Aspect Ratio
Surface #12	143	178	406	60	118	6.8
Surface #17	200	127	483	42	85	11.5
Surface #C	409	62	415	22	40	18.7

### 2.3. FFMHS for Single-Phase Heat Transfer

It is expected that the flow pattern and geometrical configuration of a typical FFMHS have the potential to enhance single-phase thermal performance compared to

other conventional high heat flux cooling technologies. But first, the basic mechanisms and flow regimes behind the possible heat transfer enhancement need to be demonstrated. The following sections address these issues.

### **2.3.1. Heat Transfer and Pumping Power in Short Channels**

A simple analysis can demonstrate the thermal performance advantages of FFMHS in comparison to traditional microchannel single-phase flow. To simplify the analysis, consider the two flow configurations shown in Figure 2-3 (a) and (b). The first case, Case 1, shown in Figure 2-3 (a), depicts flow in a single long tube with hydraulic diameter of  $D_h$ , tube length  $L$ , mass flow rate  $\dot{m}$ , constant surface temperature  $T_s$  and inlet temperature of  $T_i$ . This case is analogous to a single channel in a traditional microchannel heat sink with a highly conductive microgrooved surface base material. The second case, Case 2, shown in Figure 2-3 (b), represents the same tube divided into  $n$  equal length, short tube segments. This case is analogous to FFMHS flow configuration formed for a single microchannel. The mass flow rate running in each tube is divided equally, resulting in a mass flow rate of  $\dot{m}/n$  in each single short tube. All other parameters, such as hydraulic diameter and inlet, outlet and surface temperatures, were kept constant. At this stage, to further simplify the problem, the ratio of channel length to hydraulic diameter  $L/D_h$  for both cases was assumed to be high; therefore, entrance effects were neglected and flow was assumed to be fully developed. The flow in microchannels is generally in laminar flow regime; therefore, Reynolds number was assumed to be always below  $Re < 2300$ . Also, the major pressure losses were assumed to be dominantly higher, and inlet and outlet

minor losses were neglected. Heat was applied to the surface at constant temperature  $T_s$ .

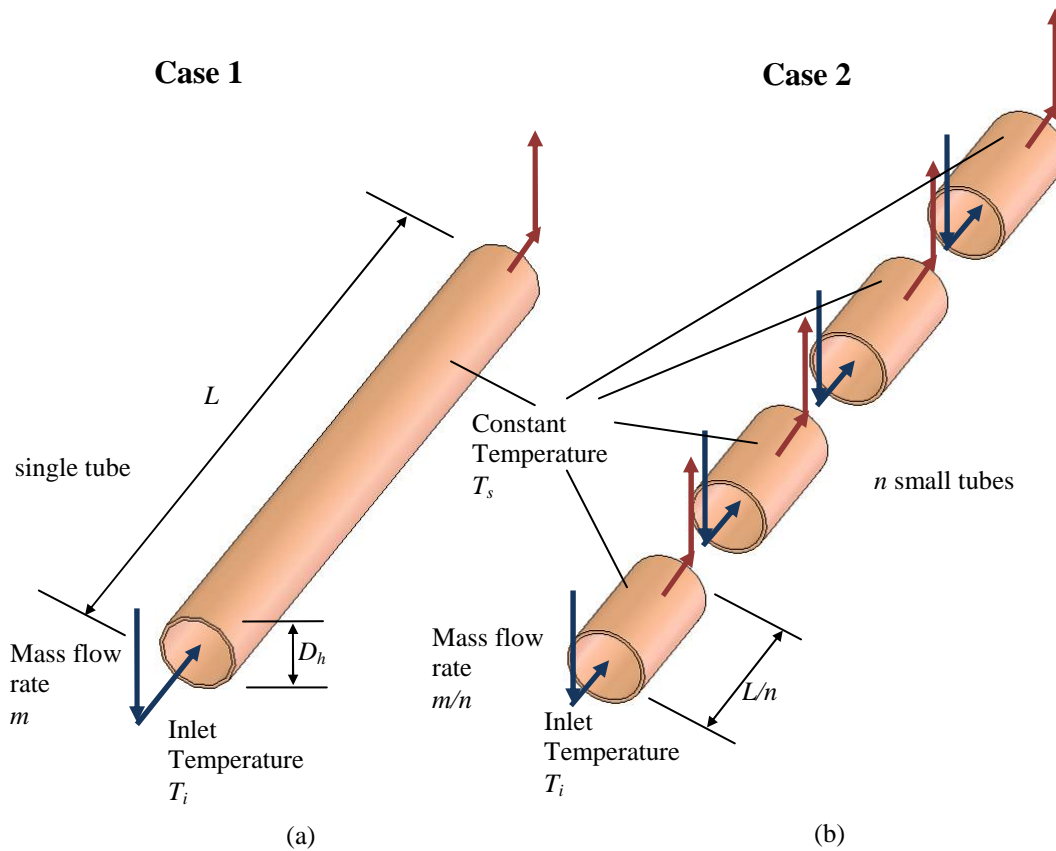


**Figure 2-3. Schematic of flow in (a) single long channel and (b) multiple short channels**

Usually the most important performance parameters considered in a heat sink design are overall heat transfer coefficient and pumping power. While the overall heat transfer coefficient is desired to be as high as possible to increase heat transfer efficiency, the pumping power values need to be minimized. Since these parameters conflict, a reasonable comparison can be made by keeping one parameter constant and performing the comparison based on the other one. Here, the overall heat transfer coefficients for Case 1 and Case 2 will be kept constant and the pumping power will be evaluated.

It can be shown that with constant surface temperature assumption, the outlet fluid temperature  $T_{o,1}$  for Case 1 can be calculated from (Incropera & DeWitt, 2002) as:

$$\frac{T_s - T_{o,1}}{T_s - T_i} = \exp\left(-\frac{\pi D_k L \bar{h}}{\dot{m} c_p}\right) \quad (2-1)$$

where  $\bar{h}$  is the average heat transfer coefficient. For the current case this value is constant along the tube and is equal to:

$$\bar{h} = h_z = Nu_T \frac{k}{D_h} = 3.66 \frac{k}{D_h} \quad (2-2)$$

Here  $Nu_T = 3.66$  is the Nusselt number defined for fully developed flow in a tube (Incropera & DeWitt, 2002), and  $k$  denotes the thermal conductivity of the working fluid. The heat transfer to the fluid is then calculated based on logarithmic mean temperature difference:

$$q_{Case1} = \bar{h} (\pi D_h L) \frac{(T_s - T_{o,1}) - (T_s - T_i)}{\ln \frac{T_s - T_{o,1}}{T_s - T_i}} \quad (2-3)$$

Similarly, for each short tube defined in Case 2 the outlet fluid temperature  $T_{o,2}$  can be calculated as:

$$\frac{T_s - T_{o,2}}{T_s - T_i} = \exp\left(-\frac{\pi D_k L / N \bar{h}}{\dot{m} / N c_p}\right) = \exp\left(-\frac{\pi D_k L \bar{h}}{\dot{m} c_p}\right) \quad (2-4)$$

The right-hand side of Equations (2-1) and (2-4) are identical which concludes that for two cases the outlet temperatures are equal. The total heat transfer in Case 2 is then evaluated by substituting  $T_{o,1} = T_{o,2}$  and summing the heat transfer surface as:

$$q_{Case2} = \sum_{i=1}^n \bar{h} \left( \pi D_h L / n \right) \frac{(T_s - T_{o,2}) - (T_s - T_i)}{\ln \frac{T_s - T_{o,2}}{T_s - T_i}} = \bar{h} (\pi D_h L) \frac{(T_s - T_{o,1}) - (T_s - T_i)}{\ln \frac{T_s - T_{o,1}}{T_s - T_i}} \quad (2-5)$$

Equations (2-3) and (2-5) are equal, which demonstrates that the heat transferred from both the single-tube configuration of Case 1 and multiples tubes with the same hydraulic diameter and heat transfer area of Case 2 is the same. A common practice for identifying single-phase heat transfer performance for heat sinks is to calculate effective heat transfer coefficient. This parameter is defined as the ratio of heated surface heat flux and temperature difference between inlet and heated surface temperature. Since inlet temperature is constant and equal for both cases, the effective heat transfer coefficient will be the same as well.

The isentropic pumping power for a control volume is the product of volumetric flow rate and pressure drop:

$$P_{pump} = \Delta P \cdot \frac{\dot{m}}{\rho} \quad (2-6)$$

The major pressure losses for laminar flow in a tube can be calculated as:

$$\Delta P = f \frac{L}{D_h} \rho \frac{V^2}{2} \quad (2-7)$$

where  $V = \dot{m} / \rho \pi D_h^2$  is the mean fluid velocity in the tube and the pressure loss coefficient for fully developed laminar flow is defined as:

$$f = \frac{64}{\text{Re}} = \frac{64\mu}{\rho V D_h} \quad (2-8)$$

Substituting Equations (2-7) and (2-8) into Equation (2-6), the total pumping power required for Case 1 and Case 2 can be calculated as:

$$P_{pump,1} = \left( \frac{128}{\pi} \frac{1}{D_k^4} \frac{\mu}{\rho^2} \right) L \dot{m}^2 \quad (2-9)$$

$$P_{pump,2} = \sum_{i=1}^n \left( \frac{128}{\pi} \frac{1}{D_k^4} \frac{\mu}{\rho^2} \right) L/n \left( \dot{m}/n \right)^2 \quad (2-10)$$

Based on these two equations the pumping power reduction can be calculated as:

$$\frac{P_{pump,2}}{P_{pump,1}} = \frac{1}{n^2} \quad (2-11)$$

Equation (2-11) demonstrates that for the same overall heat transfer coefficient, the split-flow configuration with multiple inlet and outlets has the potential to decrease the pumping power proportional to the square of number of divisions. However, it should be noted that tube hydraulic diameter and total tube length was assumed to be the same for both cases, and no optimization study was performed. More realistic performance comparison would be to compare pumping powers for two cases at optimum channel dimensions and at the same heat transfer.

### 2.3.2. Heat Transfer and Pressure Drop for Thermally and Hydrodynamically Developing Flow

For the analysis performed in the previous section, it was assumed that the flow is fully developed along the whole tube. This assumption is not valid when the tube length over the tube hydraulic diameter ratio ( $L/D_h$ ) becomes small. In this case, the heat transfer and momentum transfer occur mostly in the entrance region, where the hydrodynamic and thermal boundary layers are developing. Therefore, the heat transfer coefficient and friction factor in the entrance region depend on distance from entrance, Reynolds number and fluid physical properties and are not constant

anymore. This may have a significant impact on thermal performance of FFMHS where the heat transfer occurs mostly in the entrance region and the flow is hydrodynamically and thermally developing.

Assuming uniform velocity profile at the inlet, the hydrodynamic entry length  $L_{fd,h}$  for laminar flow in a tube is obtained from the following relation given by (Langhaar, 1942):

$$\left( \frac{L_{fd,h}}{D} \right)_{lam} \approx 0.05 \text{ Re} \quad (2-12)$$

The friction factors in the hydrodynamically developing region are higher than those defined for fully developing flow. Both the skin friction and additional momentum rate change due to change in the velocity profile are added together to define apparent friction coefficient. For circular tubes, (Shah & London, 1978) proposed the following correlation:

$$f_{app} \text{ Re} = 3.44 (x^+)^{-0.5} + \frac{1.25 + (f \text{ Re})_{fd} - 3.44 (x^+)^{-0.5}}{1 + 2.12 \cdot 10^{-4} (x^+)^{-0.2}} \quad (2-13)$$

where  $(f \text{ Re})_{fd} = 64$  is defined for fully developed flow and  $x^+$  is the non-dimensional channel length defined as:

$$x^+ = \frac{L}{\text{Re} D} \quad (2-14)$$

For thermally developing laminar flows, (Kays & Crawford, 1980) proposed the following equation to calculate the thermal entry length  $L_{fd,t}$ :

$$\left( \frac{L_{fd,t}}{D} \right)_{lam} \approx 0.05 \text{ Re Pr} \quad (2-15)$$

For combined hydrodynamically developing region and thermal entry region for laminar flow in a circular tube, the average Nusselt number is given by (Sieder & Tate, 1936):

$$\overline{Nu} = 1.86 \left( \frac{Re Pr}{L/D} \right)^{1/3} \left( \frac{\mu}{\mu_s} \right)^{0.14} \quad (2-16)$$

Equations (2-13) and (2-16) demonstrate that in the entry region both heat transfer coefficients and pressure drop increase compared to fully developed flow. This result may have an important impact on thermal performance of FFMHS, where the length of channels is usually comparable to hydraulic diameters. When considering pumping power and heat transfer coefficients as the most important heat sink design parameters, both hydrodynamic and thermal entry effects need to be considered. At this point, a multi-objective optimization procedure can be useful in revealing the flow and geometrical conditions that maximize the heat transfer and minimize the pressure losses at the entry region.

### **2.3.3. Heat Transfer and Pressure Drop in Turning Bends**

In FFMHS, the fluid enters and exits the microgrooved surface from the top, perpendicular to the microchannel axis. This configuration creates a 180° flow turn which may have significantly different flow and heat transfer characteristics from straight channel flow. As the fluid makes the turn, centrifugal forces affect the flow field. The magnitude of the centrifugal forces that act on a fluid particle are proportional to  $V^2/R$  where  $V$  is velocity and  $R$  is the curvature radius. For laminar flow in a tube or rectangular channel, due to no slip boundary conditions, the axial velocities in the vicinity of the channel walls are much smaller than those in the

center of the channel. This difference in axial velocity results in centrifugal forces acting with different magnitude on each fluid particle. A significant difference in centrifugal forces in turn can induce secondary flows. For flow in a helical circular tube, (Ujhidy, Nemeth, & Szepvolgyi, 2003) described the flow pattern as a double vortex that appears on the cross section of the tube and is superimposed on the axial velocity profile. Dean (Dean, 1927) was first to analyze the formation of secondary flows and concluded that the friction loss for laminar flow in a curved pipe is a function of a dimensionless parameter called the Dean number:

$$De = Re \sqrt{\frac{D}{2R}} \quad (2-17)$$

where  $Re$  is the Reynolds number and  $D$  is tube diameter. Equation (2-17) shows that the Dean number represents the ratio of inertia and centrifugal forces to the viscous forces. The Dean number can also be interpreted as the measure of magnitude of secondary flows.

The vortices created by secondary flows can enhance the heat transfer by disturbing the thermal boundary layer and by replacing the hotter fluid close to the heated wall with colder fluid in the fluid core. This mixing mechanism has been reported for flow in helical tubes by (Xin & Ebadian, 1997) who proposed the following correlation to calculate the average Nusselt number:

$$\overline{Nu} = (2.153 + 0.318De^{0.643})Pr^{0.177} \quad (2-18)$$

The equation was validated for the parametrical range of  $20 < De < 2000$ ,  $0.7 < Pr < 175$  and  $0.0267 < D/R < 0.0884$ . Single phase heat transfer enhancement by introducing secondary flows has been investigated extensively and several other

authors also proposed heat transfer correlations based on their own experimental data (Yanase, Mondal, & Kaga, 2005), (Rosaguti, Fletcher, & Haynes, 2007), (Ligrani, Choi, Schallert, & Skogerboe, 1996) and (Joye, 1994).

(Ju, Huang, Xu, Duan, & Yu, 2001) investigated pressure losses in helical pipes with small bending radii. For laminar flow they suggested the following correlation to evaluate the friction loss coefficient.

$$\frac{f_c}{f} = \begin{cases} 1 & , De < 11.6, Re < 2300 \\ 1 + 0.015 Re^{0.75} \left( \frac{D}{2R} \right)^{0.4} & , De > 11.6, Re < 2300 \end{cases} \quad (2-19)$$

where  $f$  is the friction coefficient in the straight tube and  $f_c$  is the friction coefficient in the helical tube.

Equations (2-18) and (2-19) demonstrate that the secondary flows created by centrifugal forces may have a significant effect on heat transfer and pressure loss in a channel where the flow makes turns. Again, these two objectives conflict, since the heat transfer needs to be maximized while the pressure losses are desired to be low. The phenomena become even more complex for flow in an FFMHS where the velocities in the channel tend to change continuously due to the flow area change during the bends. In this case, the most practical design solution would be to perform a multi-objective optimization utilizing numerical simulation tools to simulate the flow and heat transfer in FFMHS.

#### **2.3.4. Literature Survey on Single-Phase FFMHS**

Although single phase flow and heat transfer in TMHS have been studied extensively after the initial work of (Tuckerman & Pease, 1981), FFMHSs have

received less attention. Below is the summary of literature published on single-phase FFMHS.

The earliest study that introduced and investigated the heat transfer and fluid flow in an FFMHS is (Harpole & Eninger, 1991). They considered microchannels and manifolds etched from silicon and an optional diamond face sheet attached between the heat sink and heat source for heat spreading and enhancing the surface temperature uniformity. By neglecting the entrance effects and convective heat transfer by assuming a low Reynolds number flow and constant Nusselt number, they formulated the flow and heat transfer using a 2D model. Based on this model, they performed a parametrical analysis of the microchannel geometry and flow by varying one parameter and keeping the other parameters constant. They concluded that when water is used as a coolant, heat fluxes on the order of  $1000 \text{ W/cm}^2$  can be cooled effectively with pressure drop values on the order of 1 bar. They also noted that although the pressure losses at the inlet and outlet to the microchannels were not considered in the model, they can be significant and need to be included in a more detailed design.

(Copeland, 1995a) analyzed flow and heat transfer in an FFMHS by assuming 1D flow and building a simple model based on the hydrodynamically and thermally developing flow correlations in straight tubes. The heat sink material was assumed to be poorly conductive, and a uniform heat flux was applied to the base. Using the mathematical model, parametrical analyses were performed to investigate the variation of thermal resistance with flow and geometrical parameters. The analysis strategy was to investigate thermal resistance by varying two parameters at a time

while keeping other parameters constant. The results show that increasing the manifold number per unit length of heat sink can decrease thermal resistance, and for a given manifold number and pumping power there exists an optimum channel width and fin thickness.

(Copeland, 1995b) and (Copeland, Behnia, & Nakayama, 1997) numerically analyzed the heat transfer and pressure drop in an FFMHS for 32 different cases with different geometries and inlet flow conditions. Fluent was used as the numerical solver, and the computational domain was simplified by neglecting the conjugate heat transfer in the solid part of the microgrooved surface. Therefore, only the fluid flow was modeled, and constant heat flux or constant temperature boundary condition was applied to all heat transfer surfaces (microchannel base and fin surfaces). Their model also neglected both the pressure losses created due to flow contraction and expansion at the inlet and outlet to the microchannels and the heat transfer from the tip of the fins. Based on the numerical results, two different heat transfer characteristics were observed and reported. The first heat transfer mode occurred at low channel velocities of 0.1 m/s. In these cases, the local heat transfer coefficients peaked at the inlet region and then gradually decreased to the end of the microchannel. The second mode of heat transfer was reported at high flow velocities of 1 m/s. Here the local heat transfer coefficient was non-uniformly distributed along the channel walls, with the maximum close to the inlet region and two other local maxima at the channel bottom below the inlet and close to the outlet at the end of microchannel. Although not reported in their study, these different heat transfer characteristics are the result of flow impingement and secondary flow-induced vortices, which can create local maximum heat transfer

coefficient regions. The study also compared the numerical results with 1D straight channel models, and it was found that such a simplified model failed to predict the pressure drop and thermal resistance values obtained by numerical simulations.

(Y. I. Kim et al., 1998) experimentally investigated the thermal performance of FFMHSs for air-cooling. Several experimental tests were performed for nine different copper microgrooved surfaces and two manifold systems with different geometrical dimensions. As a general trend for all cases, it was found that thermal resistance is a strong function of flow rate and that thermal resistance decreases linearly with increasing pumping power on a log-log plot. Among the investigated geometrical parameters, microchannel width and manifold inlet and outlet feed channel widths were found to affect the thermal resistance the most. Interestingly, they also reported that for two heat sinks with identical microgrooved surfaces but different manifold designs, increasing manifold number per unit heat sink length increased thermal resistance at the same pumping power. This result conflicts with the work of (Copeland, 1995a), where it was shown that increasing the manifold number had a beneficial effect on decreasing thermal resistance. The geometrical design case that delivered the lowest thermal resistance was compared with a traditional microchannel heat sink, and it was found that FFMHS design can work with 35% less thermal resistance at the same pumping power.

(Ng & Poh, 1999) used Ansys/Flotran to analyze thermal performance of FFMHSs numerically for 16 cases with different geometrical dimensions and flow conditions. The numerical model was validated by the numerical results of (Copeland, 1995b). They also formulated a 1D analytical model based on straight

channel pressure drop and heat transfer correlations. The numerical model was compared with the analytical model for thermal resistance at similar geometrical and flow parametric input conditions. The comparison showed that the 1D analytical model can predict the thermal resistance values at an acceptable range only at very low Reynolds numbers ( $Re < 50$ ). At higher Reynolds numbers the analytical model largely under-predicted (up to 400%) the thermal resistance values. Overall, it was concluded that simple 1D analytical models based on straight channel flow cannot predict the thermal performance of an FFMHS accurately.

(Ryu et al., 2003) analyzed the heat transfer and flow in an FFMHS by solving numerically the 3D Navier Stokes equations. Using a finite volume approach, their numerical model considers both the convective heat transfer in the channel and the heat transfer through fins and base material. The base material selected was silicon, and water was used as the working fluid. By keeping the pumping power and manifold number constant and varying other parameters, they optimized the geometry using a steepest-descent technique to minimize the thermal resistance. They compared their results with traditional microchannel heat sinks and reported that the thermal resistance can be reduced by more than a half, while the temperature uniformity on the heated wall can be improved by tenfold.

(Jankowski, Everhart, Morgan, Geil, & McCluskey, 2007) explored experimentally the possibility of reducing the thermal resistance of power electronics used in hybrid vehicles by integrating two different cooling systems that involve microchannels. The first approach consisted of integrating an FFMHS to cool chips directly on a silicon substrate. The second approach used a TMHS with

microchannels created in an aluminum nitride substrate. The thermal resistance values for both systems were measured at pressure drops of 17 kPa and 35 kPa. The results show that the thermal resistance values for both systems were comparable at 17 kPa and for 35kPa FFMHS thermal resistance was lower by only about 12% compared with the THMS design. The authors explained this low difference by addressing the non-optimized geometries of FFMHS and suggested that the heat transfer geometry needs to be optimized for future potential improvement.

(Xia, Liu, Qi, & Xu, 2008) investigated experimentally the effect of two different surfactants on pressure drop in a single channel manifold microchannel with the final goal of increasing the system drag reduction. They used Sodium Dodecyl Sulphate and Alkyl Polyglycoside aqueous solutions as working fluids. They found that the measured drag reduction values are not significant for laminar flow regime, but that the pressure drop reduction can be more effective in transition flow at high temperatures. The transition from laminar flow to transitional flow occurred at a critical Reynolds number around 800.

(Haller, Woias, & Kockmann, 2009) investigated experimentally and numerically the pressure loss and heat transfer in bending and branching microchannels such as L-bends and T-joints for rectangular channels with a 90° turning angle. This geometrical configuration is similar to a unit cell of a FFMHS without the second turning bend at the end of the microchannel. Using water, they tested silicon-based channel flow for Reynolds numbers ranging from 10 to 3000. Based on both numerical and experimental results, they reported that flow turning can enhance the heat transfer when fluid was redirected in the 90° bend. This effect was

the result of flow vortices induced by secondary flows created by centrifugal forces. They also reported that the creation of such vortices also increased the pressure drop of the system due to higher viscous dissipation losses. The heat transfer efficiency and pressure drop characteristic were found to be always conflicting, with higher heat transfer performance always requiring higher pumping power. They also unsuccessfully attempted to model the pressure loss of the laminar flow in microchannel bends with vortices. They conceded that the main challenge of building such a model is the different flow characteristics observed at different flow conditions and channel geometries. For example, the creation of no vortices, one pair or two pairs of vortices was strongly dependent on Reynolds number, shape and aspect ratios of the channel.

A summary of this literature survey is given in Table 2-2. Two major conclusions can be drawn. First, FFMHS has the potential to achieve higher thermal performance values than TMHS. However, such a comparison needs a more systematic approach. One substantive method would be to compare the thermal performance of FFMHS with other conventional cooling technologies at optimum design and working conditions. Second, all the parametric studies and optimization techniques used in previous studies are based on single objective optimization methods. In order to obtain the real optimum designs, a multi-objective optimization technique is necessary. Here, the thermal performance can be optimized based on the most important objective functions, which in this case are heat transfer coefficient and pumping power. The objective should be to maximize the heat transfer coefficients while minimizing the pumping power.

**Table 2-2. Summary of related work on single phase FFMHS's**

<b>Authors</b>	<b>Type of Work</b>	<b>Microgrooved Surface Material (TSM) and Working Fluid (WF)</b>	<b>Microchannel Hydraulic Diameter [micron]</b>	<b>Reynolds Number and Flow Regime</b>	<b>Parametrical study or Optimization Performed</b>	<b>Conclusion</b>
<b>(Harpole &amp; Eninger, 1991)</b>	2D Analytical Model	TSM: Silicon WF: Water	15-66	15 – 400 (laminar flow)	Yes	FFMHS has the possibility to be used effectively for effectively cooling high fluxes
<b>(Copeland, 1995a)</b>	1D Analytical Model	TSM: Low conductive material WF: Water	8-64	(laminar flow)	Yes	There exists optimum points for microgrooved surface and manifold dimensions
<b>(Copeland et al., 1997)</b>	3D Numerical Simulation using Fluent	TSM: Silicon WF: Water	113-226	18 – 485 (laminar flow)	Yes	1D models based on straight channel flow cannot predict thermal performance of FFMHS
<b>(Y. I. Kim et al., 1998)</b>	Experimental	TSM: Copper WF: Air	700-2000	(laminar flow)	Yes	FFMHS's can perform 30% better comparing with TMHS thermal performance
<b>(Ng &amp; Poh, 1999)</b>	3D Numerical Simulation using Ansys/Flotran	TSM: Silicon WF: Water	113-226	10-800 (laminar flow)	Yes	1D models based on straight channel flow can under predict thermal performance of FFMHS by 400%
<b>(Ryu et al., 2003)</b>	3D numerical model	TSM: Silicon WF: Water	10-60	1-100 (laminar flow)	Yes	Comparing with TMHS thermal performance, FFMHS can perform 50% better with ten times better surface temperature uniformity

<b>(Jankowski et al., 2007)</b>	Experimental	TSM: Silicon and AlN WF: Water	40-760	(laminar flow)	No	FFMHS needs to be optimized to achieve comparable better performance
<b>(Xia et al., 2008)</b>	Experimental	TSM: Silicon WF: Aqueous surfactant solution	200	100-3500 (laminar and transitional flow)	No	Surfactants can decrease pressure drop at high temperatures and Reynolds numbers
<b>(Haller et al., 2009)</b>	Experimental and 3D numerical model	TSM: Silicon WF: Water	300-1200	10-3000 (laminar and transitional flow)	No	Creation of secondary flows at high Re numbers can enhance heat transfer

## 2.4. FFMHS for Two Phase Heat Transfer

In the two-phase cooling mode, the inlet to the FFMHS is liquid in single phase, usually with few degrees of subcooling. The working fluid then enters the microchannel, where it starts to receive heat from the microchannel walls, and boiling is initiated when enough superheat is achieved. The vapor-liquid mixture exits the microchannel from the outlet into the outlet feed channel, where it is directed out of the heat sink area. The expected flow and heat transfer characteristics of two-phase heat transfer in FFMHS can be summarized as follows:

- Similar to single-phase heat transfer mode, the fluid manifolding technique used in FFMHS forms a series of short microchannels working in parallel with microchannels having small  $L/D_h$  ratios. The low  $L/D_h$  ratio has several impacts on system performance. First, system pressure drop, which is also equal to the pressure drop between inlet and outlet of microchannels and proportional to  $L/D_h$  ratio, can be significantly reduced for a given hydraulic diameter, heat flux and outlet quality. Second, small pressure drop in the microchannels decreases the saturation temperature variation along the microchannel, thereby providing a more uniform surface temperature distribution.
- The FFMHS configuration allows the use of microchannels with very small hydraulic diameters with less pressure drop penalty. This scaling down of hydraulic diameter in turn, has the potential to enhance the heat transfer performance due to increase in local heat transfer coefficients.

- For a constant diameter and mass flux, the critical heat flux increases as the channel length decreases, therefore, it can accommodate more heat flux. For example, (Bergles, Lienhard, Kendall, & Griffith, 2003) concluded that the most beneficial two-phase flow configuration is a system with short microchannels working in parallel. For the same heat input conditions, this solution was found to require much less pumping power compared with two-phase TMHS systems.
- The feed channels for two-phase FFMHS are generally designed to be small for inlet feed channels and larger at outlet feed channels. This geometrical design can contribute to system performance by helping the vapor in the microchannel to be easily directed into the outlet feed channel. However, such design implementation requires fundamental knowledge about the flow regimes and flow characteristics of FFMHS.

The flow and heat transfer in FFMHS are expected to be complex phenomena that include the flow and heat transfer mechanisms observed in two-phase microchannel flow, at turning bends under centrifugal acceleration, and at the entrance region. The combination of these phenomena makes the physics even more challenging to understand. Nevertheless, a fundamental understanding needs preliminary knowledge of boiling phenomena in conventional channels and microchannels. The following sections give the theory behind the flow and heat transfer regimes observed in these channels. This knowledge, in combination with experimental results obtained in this study, will be used to explain the flow regimes and dominant heat transfer mechanisms in two-phase FFMHS.

### 2.4.1. Flow Boiling in Conventional Channels

Flow boiling occurs when a fluid flows in a heated channel and when it starts to change flow regimes as the quality is increased. The flow and heat transfer phenomena are very complex due to the coupling of hydrodynamics and multiphase heat transfer processes. Figure 2-4 shows the two-phase flow and heat transfer regimes and the trend of local heat transfer coefficient along the axis of a uniformly heated horizontal conventional tube. At the inlet to the tube, the liquid is subcooled, and there is not enough superheat to initiate the nucleation: therefore, the flow regime is single-phase liquid, and the heat transfer regime is forced convection. After the initiation of boiling, the observed flow regimes are bubbly flow, plug/slug flow, annular flow, mist flow and single-phase vapor flow.

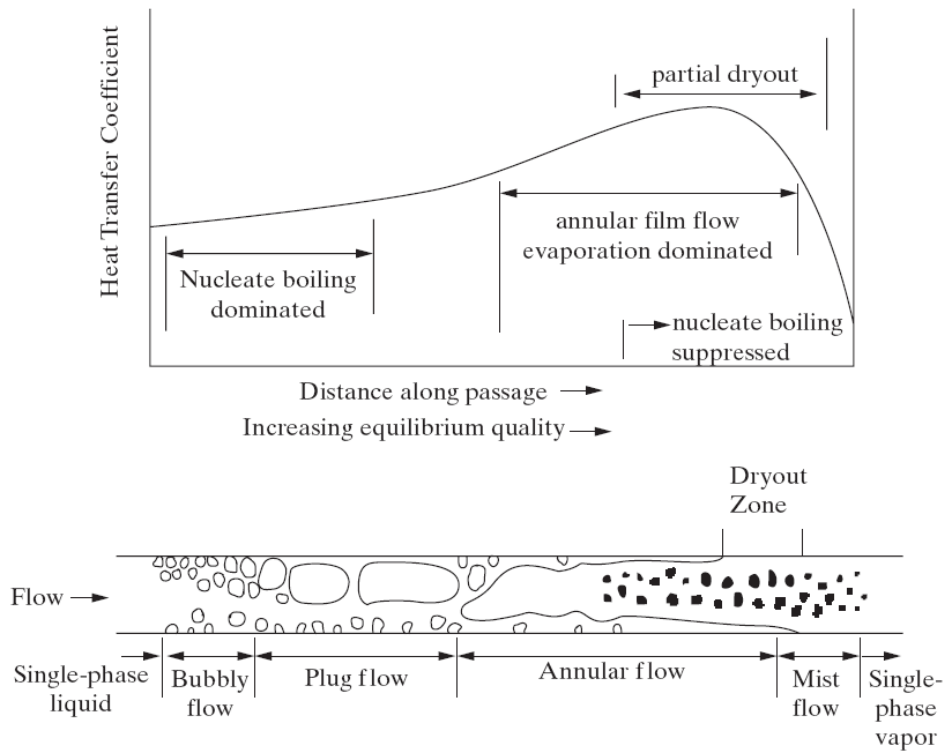


**Figure 2-4. Flow and heat transfer regimes in a uniformly heated horizontal circular tube (adopted from (Ghiaasiaan, 2008))**

Nucleate boiling is the dominant heat transfer mechanism in bubble flow and slug flow regimes. In annular flow, the convective evaporation process becomes the dominant heat transfer mechanism. In this flow regime, the heat transfer occurs in the thin film that covers the heated walls. The heat transfer coefficients are the highest in this region due to the low thermal resistance in the thin film, and the low superheat suppresses nucleation. The termination of the annular flow regime is usually represented by dryout, where the thin film is completely or partially depleted due to evaporation. Since Figure 2-4 depicts the flow in a horizontal conventional tube, gravity can be important, as it creates stratification between the liquid and vapor. This effect, however, is generally negligible in microscale tubes where surface tension forces are much higher than gravitational forces. After annular flow, depending on inlet conditions and tube geometry, small droplets of liquid separated from the surface can be present in the form of mist flow. Further downstream, these droplets will be eventually completely evaporated, and single-phase vapor flow regime prevails. The heat transfer coefficients after the film dryout can be several orders of magnitude lower than those in the nucleate boiling and convective boiling flow regimes. The heated wall temperatures have a large increase at dryout conditions, and the effect is similar to the critical heat flux observed in pool boiling.

In saturated flow boiling, both nucleate and convective boiling contribute to heat transfer. The dominant heat transfer mechanism and the transitions are dependent on heat flux, mass flux and local equilibrium vapor quality. At low qualities, the dominant heat transfer mechanism is nucleate boiling. Here the heat transfer coefficients are a strong function of heat flux and are generally insensitive to mass

flux and local qualities. As the vapor quality increases, the convective boiling that is represented by annular flow starts to become dominant. The nucleation is suppressed, and the heat transfer occurs due to evaporation in the thin liquid film. The transition between these heat transfer mechanisms is generally smooth, and the contribution to heat transfer of both mechanisms can be comparable. Most successful heat transfer correlations such as Chen correlation (J. C. Chen, 1966), take into account both of these heat transfer mechanisms.

#### **2.4.2. Flow Boiling in Microchannels**

The basic heat flow and transfer mechanisms in microchannels and their similarities with conventional channels is a matter of debate, and a universal understanding is not been established yet. It has been argued, however, that the basic mechanism of nucleation in small hydraulic diameter channels is similar to conventional channels, as long as small nucleation crevices exist on the heat transfer surface (Kendall, Griffith, Bergles, & Lienhard, 2001), (Zhang, Wang, Goodson, & Kenny, 2005). Also, the characteristic diameter of these crevices needs to be smaller than the hydraulic diameter of the microchannel in order for the assumption to be valid. Here, the vapor and gases trapped in the crevices initiate the bubble nucleation when sufficient superheat is achieved. Using the analogy from conventional channel flow, it can be expected that the departed small bubbles later mix with the bulk fluid, forming larger intermittent slug-flow regimes and eventually ending with the annular flow regime. However, the bubble confinement effect resulting from the small hydraulic diameter can affect the two-phase flow regimes. These phenomena are important when the bubbles diameter becomes comparable to the channel hydraulic

diameter. According to (Cornwell & Kew, 1992), the confinement effects need to be considered when the confinement number  $N_{conf}$  satisfies:

$$N_{conf} = \frac{\sqrt{\sigma / g \Delta \rho}}{D_h} > 0.5 \quad (2-20)$$

where is defined as the dimensionless confinement number  $N_{conf}$ ,  $\sigma$  as the surface tension,  $\Delta\rho$  as the density difference between liquid and vapor phases, and  $D_h$  as the hydraulic diameter. The confinement number was derived by correlations developed for pool boiling and represents the ratio of bubble departure diameter to the channel hydraulic diameter. For a confined two-phase flow, based on their observations, they also proposed a microchannel flow regime based on three distinctive flow regimes as shown in Figure 2-5.

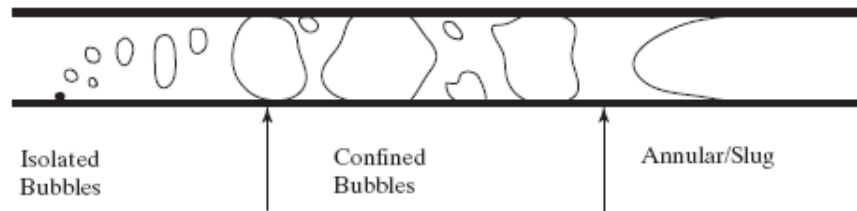


**Figure 2-5. Major flow regimes for flows in microchannels observed by (Cornwell & Kew, 1992)**

The isolated bubble flow has small vapor bubbles mixed in the liquid phase flowing in the microchannel. Here, the characteristic diameter of the bubbles is smaller than the microchannel width and this flow regime is similar to the bubbly flow regime in conventional channels. The diameters of the bubbles can be very small, as (Kandlikar, 2002) reported presence of bubble diameters as small as 10-20 microns. The confined bubble flow consists of large bubbles that are created by the growth or coalescence of small bubbles and are confined with the microchannel walls. A thin liquid film

separates the bubble and the walls, and this flow regime is similar to the plug flow in flow boiling in conventional channels. The confined bubble flow regime ends when the confined bubbles grow significantly in the axial direction by destroying the liquid slugs/columns separating them and leading to an annular-like flow regime. Therefore, the third and last major flow regime is annular slug flow, which represents all flow patterns that occur after the termination of confined bubble regime. As seen, the proposed flow regime is similar to flow regime shown in Figure 2-4 for conventional channels. The major difference is the confinement effect, which results in only three major flow regimes and which can possibly shift the rate of transition between flow regimes eventually switching to annular flow at much lower vapor qualities.

It should be noted, however that the confinement number  $N_{conf}$  is based on geometrical considerations only. It does not include the effects of heat flux and liquid and wall superheat. (Kandlikar, 2003) argued that the effect of gravity in microchannel flows is negligible and that the use confinement number needs to be reevaluated. He suggested that the new criteria should be defined considering relevant forces in microchannel flow. Based on force balance applied to a bubble, (Kandlikar, 2004)suggested using the following non-dimensional group:

$$K_1 = \left( \frac{q''}{Gh_{lv}} \right)^2 \frac{\rho_l}{\rho_v} \quad (2-21)$$

The  $K_1$  number represents the ratio of evaporative momentum force to the inertia forces of incoming liquid. For large values, it indicates that the evaporative momentum forces dominate the inertia forces, and this may result in vapor pushing back the liquid, creating backflows. The reversed flows in microchannels have been

reported by many authors including (Steinke & Kandlikar, 2003), (Peles, Yarin, & Hestroni, 2001) and (Kandlikar & Balasubramanian, 2003). While the  $K_1$  number is useful in determining the dominant forces in microchannel boiling, it assumes that the vapor mass flux transferred to the bubble is equal to the idealized mass flux calculated based on wall heat flux as  $q''/h_{lv}$  and is not dependent on hydraulic diameter. However, hydraulic diameter in fact can be very important in determining the liquid superheat that contributes to vapor generation.

Based on experimental observations, (Kandlikar, 2003) defined the heat transfer mechanism in microchannels based on the elongated bubble (also known as expanding bubble, and sometimes explosive bubble) model shown in Figure 2-6. Similarly to flow regime observed by (Cornwell & Kew, 1992), the heterogeneous nucleation starts from the wall crevices. However, the growth rate of the bubble is much higher, and the rapidly bubble growth process continues even after the bubble departs. This short period may not allow the bubble to interact with other bubbles and create slug/plug flow, but instead it is rapidly confined by channel walls. After the confinement period, the bubble experiences a fast expansion in the axial direction as shown in the picture.

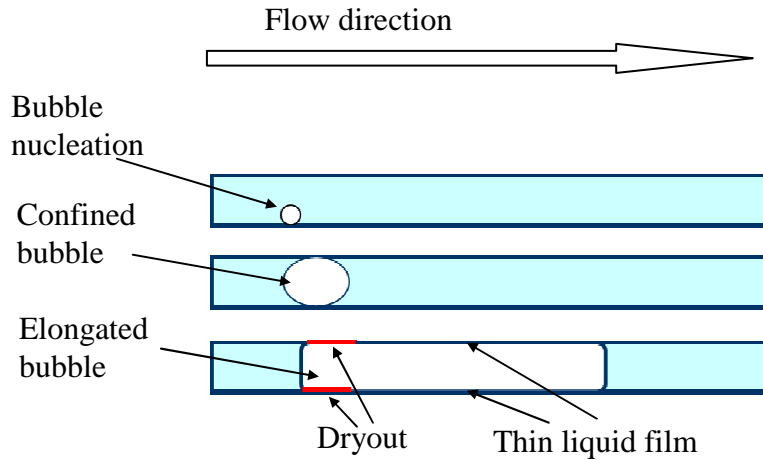


**Figure 2-6. Flow boiling regimes proposed by (Kandlikar, 2003)**

There are two important issues that need to be addressed here. First, the source of rapid bubble expansion is explained by Kandlikar, as the liquid and wall superheat build before nucleation. The high local heat transfer coefficients at small hydraulic diameters decrease the thermal boundary layer and can suppress nucleation. Utilizing microchannels with smooth walls and without nucleation cavities will also further suppress nucleation. When the conditions to nucleate the bubble are satisfied, the liquid around the bubble is largely superheated. Therefore, the energy stored in the liquid superheat is released into the bubble in the form of evaporation, and the large amount of vapor generation forces the rapid bubble growth. If the evaporative forces are much higher than the forces associated with liquid inertia, then the elongated bubble grows both upstream and downstream. For example, a set of images taken at 8 milliseconds apart observed by (Steinke & Kandlikar, 2003) is shown in Figure 2-7. The bubble is heated from the walls and starts to grow rapidly downstream, while the upstream also experiences the force created by evaporative momentum. Therefore the upstream liquid front is pushed back closer to the inlet,

where it is more or less stationary until the vapor in the channel exits from the outlet and the next cycle with liquid front moving downstream is released again.

Second, the process has a transient nature and is repeated for each cycle. During the elongated bubble regime, as the bubble front advances, a thin liquid film is created on the heated surface by the receding liquid vapor interface. As the bubbles become larger, the thin film will provide a very highly efficient heat transfer zone. This thin film will eventually start to dry if the bubbles become too large, and localized dryouts will induce reduction in heat transfer.

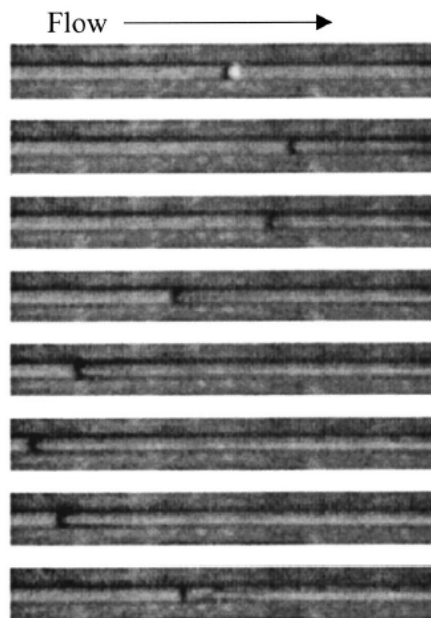


**Figure 2-7. Rapid bubble growth in 200 micron square microchannels observed by (Steinke & Kandlikar, 2003)-Each image is 8 milliseconds apart**

(Thome, Dupont, & Jacobi, 2004) developed a three-zone model to investigate the evaporation process of elongated bubbles in microchannels. The schematic of their heat transfer model is shown in Figure 2-8 and includes the heat transfer from three major zones: the liquid slug, the elongated bubble with thin liquid film on

heated surface and the dry zone with vapor in contact with walls. Due to the transient nature of the process, a time-averaged approach was adopted in calculating the heat transfer coefficients.

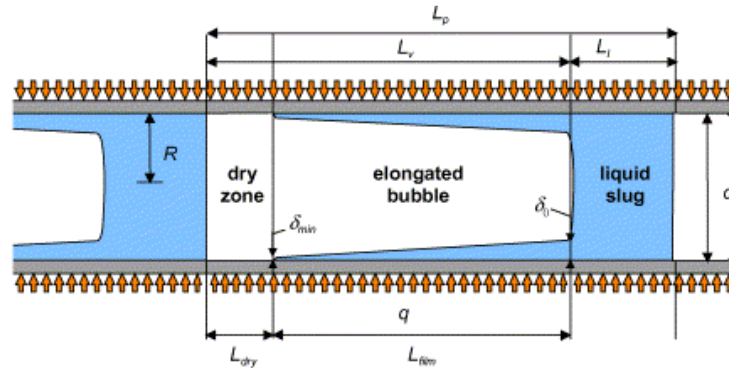


**Figure 2-8. Diagram illustrating a liquid slug, an elongated bubble and a vapor slug of model developed by (Thome et al., 2004)**

The calculated heat transfer coefficients for the three heat transfer zones at two cyclic variations are shown in Figure 2-9. As expected, the minimum heat transfer is observed at the dry zone where the thermal resistance between vapor and surface is very high. The heat transfer coefficients in the liquid zone are slightly higher than the vapor zone. In the elongated bubble zone, however, the heat transfer coefficients can achieve very high values, on the several orders of magnitude higher than the liquid and dry zones. However, as the resistance of the thin film is dictated by conduction, the heat transfer values change significantly as film thickness changes. It is also interesting to note that the ratio of the area occupied by each region may have a direct relation with averaged heat transfer values. When the dry and liquid slug regions are large compared to the elongated bubble region, the high heat transfer associate with thin-film evaporation becomes less effective when averaged over the whole heat transfer surface. Based on this model, (Thome et al., 2004) concluded that

the dominant heat transfer mechanism in microchannels is thin-film evaporation under the elongated bubble, and not nucleate or convective boiling alone.

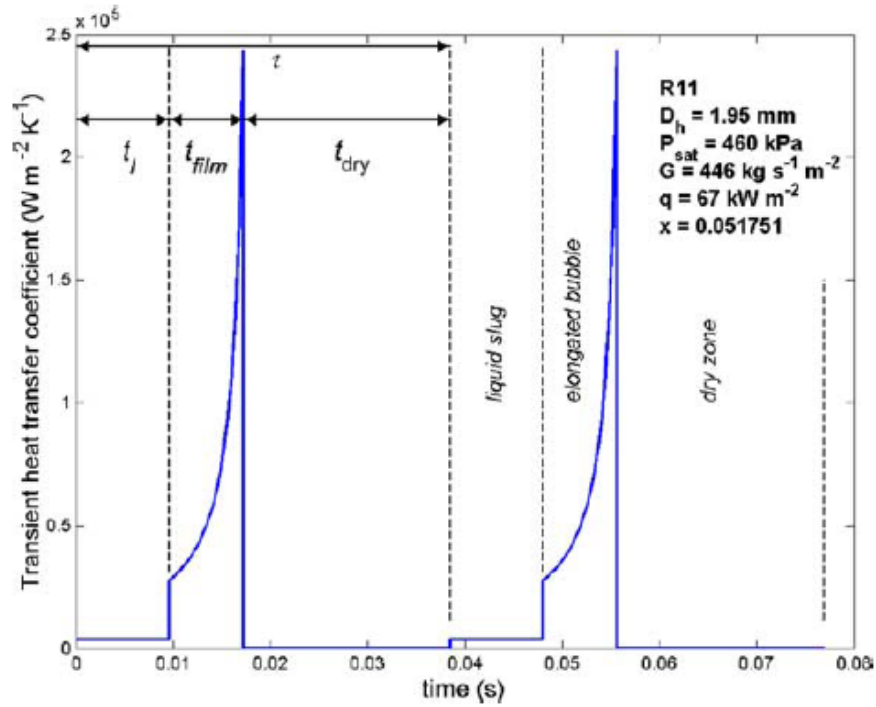


Figure 2-9. Cyclic variation in heat transfer coefficient with time (adopted from (Thome et al., 2004))

### 2.4.3. Effect of Channel Hydraulic Diameter on Inception of Nucleate

#### Boiling

The effect of channel hydraulic diameter on initiation of nucleate boiling needs to be evaluated. This effect is particularly important in the development of the elongated bubble flow regime mentioned in the previous section. The suppression and delay of nucleate boiling can increase wall and liquid superheat that can result in the rapid bubble expansion phenomena.

Let us assume that flow in the channel shown in Figure 2-4 at constant heat flux boundary condition. The flow at inlet is subcooled and as the fluid flows

downstream, both the wall and liquid temperatures increase. The onset of nucleate boiling will occur at a specific flow condition in crevices present on the heated tube wall that fall in a certain range of sizes. Assuming that the heated surface contains nucleation crevices of all sizes, (Hsu & Graham, 1961) proposed the following equation to calculate the minimum amount of wall superheat required to initiate nucleation:

$$\Delta T_{sat,ONB} = \frac{4\sigma T_{sat} v_{lv} h_x}{k h_{lv}} \left[ 1 + \sqrt{1 + \frac{k h_{lv} \Delta T_{sub}}{2\sigma T_{sat} v_{lv} h_x}} \right] \quad (2-22)$$

where  $T_{sat}$  is saturation temperature in units of [K],  $\sigma$  is surface tension,  $v_{lv}$  is liquid-vapor specific volume,  $k$  is fluid thermal conductivity,  $h_{lv}$  is evaporation enthalpy, and  $h_x$  is local heat transfer coefficient. The equation can be further simplified by assuming saturated inlet flow conditions by introducing  $\Delta T_{sub} = 0$  and by using the definition of the Nusselt number of  $Nu_x = h_x D_h / k$ . The new form can be cast as:

$$\Delta T_{sat,ONB} = \frac{8\sigma T_{sat} v_{lv} Nu_x}{D_h h_{lv}} \quad (2-23)$$

One important observation in Equation (2-23) is the relation between the local Nusselt number, hydraulic diameter and wall superheat. Single-phase flow regime in microchannels and FFMHS is generally laminar. For long channels, where the entrance effects can be negligible, the Nusselt number is constant, and wall superheat is reversely proportional to hydraulic diameter. This in turn highlights that for smaller microchannel hydraulic diameter dimensions, higher wall superheat values are needed to initiate nucleation, and the expanding bubble flow regime is more likely to occur at smaller channel geometries. On the other hand, in FFMHS, the entrance effects can

be significant due to small values of channel length to hydraulic diameter ratios ( $L/D_h$ ) which can result in large developing regions. Heat transfer coefficients in this thermally developing region are much higher than the fully developed flow and such difference can affect the initiation of nucleation by further increasing the required wall superheat given in Equation (2-23). In this case, (Kandlikar, Garimella, Colin, Li, & King, 2004) suggested using entry region correlations to calculate the local Nusselt number. For thermally developing laminar flow between two parallel plates and for constant heat flux boundary condition, (Shah & London, 1978) proposed the following correlation:

$$Nu_x = \begin{cases} 1.49(x^*)^{-1/3} & , x^* \leq 0.0002 \\ 1.49(x^*)^{-1/3} + 0.4 & , 0.0002 < x^* \leq 0.001 \\ 8.235 + 8.68(10^3 x^*)^{-0.506} e^{-164x^*} & , x^* > 0.001 \end{cases} \quad (2-24)$$

where  $x^* = L / \text{Re Pr } D_h$  is non-dimensional length. By substituting Equation (2-24) into Equation (2-23), one can calculate the minimum wall superheat required to initiate nucleation close to the inlet region of FFMHS at a given hydraulic diameter.

#### 2.4.4. Critical Heat Flux in Microchannels

One of the most important parameters that limit the system performance is the critical heat flux (CHF). CHF is the upper limit of safe operation of two-phase heat sinks, since the heat transfer coefficients of the post-CHF zone are extremely low. In most cases, the CHF represents the system burnout condition due to the large jump in surface temperature. The CHF process is very complex due to the strong coupling of flow and heat transfer phenomena in two-phase flow. For example, CHF mechanisms

are quite sensitive to flow regimes, orientation (when gravity is important) and flow path. Therefore, it is expected that the CHF mechanism for FFMHS will be different from that of straight microchannels where the flow is not affected by turning flow and impingement effects. Nevertheless, the correlations developed for CHF in straight microchannels can indicate some important aspects about the relevant, important parameters.

(Bowers & Mudawar, 1994) developed a correlation to predict CHF in minichannels. The correlation, given as Equation (2-25) was validated based on experimental data obtained for square channels with a hydraulic diameter of 2 mm and using R-113 as the working fluid.

$$q_{CHF}'' = 0.16Gh_v We^{-0.19} \left( \frac{L}{D_h} \right)^{-0.54} \quad (2-25)$$

where  $G$  is mass flux,  $h_v$  is evaporation enthalpy and  $We$  is the Webber number based on liquid properties.

(Qu & Mudawar, 2004) followed a similar procedure and proposed their correlation based on experimental data obtained for rectangular microchannels with hydraulic diameters ranging from 0.78 mm to 3.63 mm. The working fluids used in their experiments were R-113 and water. The resulting CHF correlation was proposed as follows:

$$q_{CHF}'' = 33.43Gh_v We^{-0.21} \left( \frac{L}{D_h} \right)^{-0.36} \left( \frac{\rho_v}{\rho_l} \right)^{1.1} \quad (2-26)$$

where  $\left( \frac{\rho_v}{\rho_l} \right)$  is the ratio of vapor and liquid densities.

Equations (2-25) and (2-26) both show that CHF is reversely proportional to length to hydraulic diameter parameter  $L/D_h$ . This, in fact, suggests that FFMHS has the potential to increase CHF by decreasing this parameter alone. In a typical FFMHS design, the length of channel and hydraulic diameter are comparable in size.

#### **2.4.5. Literature Survey on Two-Phase Heat Transfer in Microchannels**

The numerical modeling of two-phase flow is still in rudimentary stages and has been applied mostly for very simple geometries such as straight tubes and channels. Most of the related published literature consists of experimental work. A review of the recent literature on flow boiling in microchannels is given in Table 2-3. The reviewed publications contain recent studies performed with both HFC fluids and water. As shown in the table, the minimum hydraulic diameter investigated is the microchannels with 162-microns hydraulic diameters investigated by (P. S. Lee & Garimella, 2008). This value is almost eight times higher than the microchannel width of Surface #C, and three times higher than the microchannel width of Surface #12 (Table 2-1). It is also important to note that the maximum aspect ratio investigated in the publications listed in Table 2-3 is 5, much less than the aspect ratios of microgrooved surfaces investigated in this study (up to 18.7 for Surface #C). Another parameter of importance is the  $L/D_h$  ratio, which is the ratio of microchannel length to hydraulic diameter, whose importance was discussed in the previous section. As shown in the table, this value is over  $L/D_h > 40$  for almost all studies except for the work done by (Bertsch, Groll, & Garimella, 2008), in which they investigated channels with  $L/D_h = 8.74$ . The microgrooved surface and manifold combination used in the current study correspond to a range of  $6.3 < L/D_h < 18.4$ . From this literature

review it can be concluded that none of the available studies represents the flow and geometrical conditions in FFMHS. Additionally, the flow turning in FFMHS can also have a significant impact that may result in deviation from straight microchannel data. To understand all these factors, an experimental study needs to be performed.

**Table 2-3. Publication list of recent work performed for boiling in microchannels**

Author(s)	Year	Fluid	Channel Depth [ $\mu\text{m}$ ]	Channel Aspect ratio	L [mm]	L/D <sub>h</sub>	$\Delta P$ [kPa]	D <sub>h</sub> [ $\mu\text{m}$ ]	Channel number, geometry	T <sub>sat</sub> [°C]	G [kg/m <sup>2</sup> s]	q'' [W/cm <sup>2</sup> ]	x	Visualization
<b>(Yan &amp; Lin, 1998)</b>	1998	R134a	-	-	100	50	5	2000	28 circular	5–31	50–200	0.5–2.0 wetted area	0.05–0.85 local	No
<b>(Lin, Kew, &amp; Cornwell, 2001)</b>	2001	R141b	-	-	NA	NA	220	1000	1 circular	39–56	300–2000	1–115 wetted area	0–1 local	No
<b>(H. J. Lee &amp; Lee, 2001)</b>	2001	R113	400–200	0.02–0.1	300	384–82	30	780–3630	1 rectangular	...	50–200	0.3–1.5 wetted area	0.15–0.75 overall	No
<b>(Steinke &amp; Kandlikar, 2004)</b>	2004	Water	214	0.93	57.15	272	200	210	6 rectangular	100	157–1782	Up to 93 base area	<0.0–>1.0 local	Yes
<b>(J. Lee &amp; Mudawar, 2005a, 2005b)</b>	2005	R134a	713	3	25.3	72	over 20	350	53 rectangular	-18 to +25	127–654	31.6–93.8 base area	0.2–0.9 local	No
<b>(P. S. Lee, Garimella, &amp; Liu, 2005)</b>	2005	Water	884–2910	5	25.4	79–28	NA	318–903	10 rectangular	100	1000–2400	4.5 base area	Overall	No
<b>(Lie &amp; Lin, 2005)</b>	2005	R134a	-	-	730	365–183	NA	2000–4000	1 annular	10, 15	200–300	0–5 wetted area	...	Yes
<b>(Saitoh, Daiguji, &amp; Hihara, 2005)</b>	2005	R134a	-	-	1620–3240	552–3240	480 at G=300 kg/m <sup>2</sup> s	510, 1120, 3101	1 circular	5, 15	150–450	0.5–3.9 wetted area	0.2–1 local	Yes
<b>(T. L. Chen &amp; Garimella, 2006)</b>	2006	FC-77	389	1	12.7	33	3.5	390	24 rectangular	97	160–275	5–70 base area	<0–0.7 overall	Yes

<b>(Lie &amp; Lin, 2006)</b>	2006	R134a	-	-	730	365-183	NA	2000-4000	1 annular	10-15	200-300	0-5.5 wetted area	Subcooled overall	Yes
<b>(Yen, Shoji, Takemura, Suzuki, &amp; Kasagi, 2006)</b>	2006	R123	214	1	100	467	NA	200-214	1 rectangular and circular	...	100-800	0-5 wetted area	0-0.8 overall	Yes
<b>(Yun, Heo, &amp; Kim, 2006)</b>	2006	R410A	1200	0.67-0.76	NA	NA	over 40kPa/m	1360-1440	7-8 rectangular	0, 5, 10	200-400	1.0-2.0 wetted area	0-0.85 overall	No
<b>(D. Liu &amp; Garimella, 2007)</b>	2007	Water	636 - 1063	2.31-2.61	25.4	66-32	1.2 at G=324 kg/m <sup>2</sup> s	384-796	25 rectangular	100	221-1283	Up to 129 base area	0-0.2 local	No
<b>(Schneider, Kosar, &amp; Peles, 2007)</b>	2007	R123	264	1.32	10	44	NA	227	5 rectangular	38-80	622-1368	0-213 base area	Overall	Yes
<b>(P. S. Lee &amp; Garimella, 2008)</b>	2007	Water	4	4-0.4	12.7	78-22.3	40	162-570	25 rectangular	100	368-738	10 - 340 base area	0-0.19 Overall	No
<b>(Agostini, Thome et al., 2007a)</b>	2007	R236fa	68	3	20	60	105	335	67 rectangular	25	280-1500	3.6-221.7 base area	0.2-0.75 Local	No
<b>(Agostini, Thome et al., 2007b)</b>	2007	R245fa	68	3	20	60	125	335	67 rectangular	23.7	281-1501	3.6-190 base area	0-0.78 Local	No
<b>(Kuo &amp; Peles, 2007)</b>	2007	Water	253	1.26	10	44.8	NA	223	5 rectangular	100	83-303	0-643 base area	0-0.40 Local	yes
<b>(Harirchian &amp; Garimella, 2008)</b>	2008	FC-77	400	0.06-4	12.7	79-16.97	25 at G=700 kg/m <sup>2</sup> s	160-748	2-60 rectangular	100	240-1600	0-65 base area	0-1	No
<b>(Bertsch et al., 2008)</b>	2008	R-134a	1900	2.5	9.53	8.74	0.3	1090	17 rectangular	8.9-21	20-81	0-20 wetted area	0-0.9	No

## 2.4.6. Literature Survey on High Heat Flux Cooling Using Dielectric

### Working Fluids

Since this work focuses on high heat flux cooling, the current position and level of technology advancement need to be determined. The objective of the following literature surveys was to define the technologies that proved to cool high heat fluxes using dielectric fluids. The resulting thermal performance of the technologies values will be used in later chapters to compare them to those of FFMHS.

(Agostini, Fabbri et al., 2007) presented a comprehensive review of high heat flux cooling technologies for literature published between 2003 and 2006. The highest heat flux achievable for TMHS was  $q''=93.8 \text{ W/cm}^2$  using FC-72, reported by (J. Lee & Mudawar, 2005a, 2005b), and for jet impingement cooling was  $q''=161 \text{ W/cm}^2$  using FC-72, from the work of (Fabbri et al., 2006). However, as will be seen in next paragraphs, the technological advancement in high heat flux cooling during the years since 2006 have generated more advanced technologies and higher heat flux values.

(Agostini, Thome, Fabbri, & Michel, 2008) investigated boiling of refrigerant R-236fa in TMHS composed of 134 parallel channel of 67 microns wide, 680 microns high and 2 cm long. The maximum heat flux at the base of the heat sink was  $255 \text{ w/cm}^2$ , corresponding to a pressure drop of 90 kPa and wall superheat of 25 °C. To the best of this author's knowledge, this value represents the highest heat flux achieved by a TMHS using a dielectric fluid and working in two phase heat transfer mode. Using an extrapolation technique on their experimental data, they argued that

the microchannel heat sink has the potential to keep the chip temperature 13°C lower than water liquid cooling at same pumping power. For these analyses they assumed a base heat flux of 350 W/cm<sup>2</sup>.

(Kosar & Peles, 2007) performed two-phase experimental tests to analyze the thermal performance of a silicon heat sink with hydrofoil pin fins. The fins were 243 microns deep and equally spaced at 150 microns apart. The authors selected R-123 as working fluid and the maximum critical heat flux of 312 W/cm<sup>2</sup> was achieved at 2349 kg/m<sup>2</sup>s mass flux. The corresponding pressure drop was measured as 300 kPa. Finally, they concluded that the CHF mechanism is triggered by dryout and that CHF increases with increase in mass velocity and decreases with increase in vapor quality.

(Visaria & Mudawar, 2008) studied the effect of subcooling on critical heat flux for spray-cooling systems. They utilized three different full-cone spray nozzles to spray FC-77, and a 1x1 cm<sup>2</sup> heated copper surface was selected as test heated surface. They reported that enhancement of CHF at low subcooling values was mild but that at higher subcooling values it was significantly higher. Using a highly subcooled spray, they could achieve a maximum critical heat flux of 349 W/cm<sup>2</sup> with a corresponding pressure drop of 174 kPa. They concluded that besides an increase in subcooling, CHF can also be increased by increasing volumetric flow rate and/or decreasing droplet diameter.

(Sung & Mudawar, 2009) explored subcooled boiling and CHF in a novel heat sink designed by the authors and named “hybrid microchannel and jet impingement cooling module.” They used a copper microgrooved surface with a base footprint area of 2x1 cm<sup>2</sup> as the heat transfer surface. The fluid was HFE-7100 and was forced into

each microchannel from the top, using 14 small equally spaced orifices, each 0.39 mm in diameter. The highest critical heat flux achieved was  $1127 \text{ W/cm}^2$ , which corresponds to a jet velocity of 6.5 m/s, pressure drop of 172 kPa and subcooling of  $143 \text{ }^\circ\text{C}$ . The authors argued that this is the highest ever heat flux achieved for a dielectric coolant at near atmospheric pressure.

A summary of cooling technologies and the important parameters used in these studies is listed in Table 2-4. These values will be used as a basis for comparison with the performance of two-phase FFMHS in the next chapters.

**Table 2-4. Summary of technologies used for high heat flux cooling**

Authors	Cooling Technology	Heat Sink Base Area [cm <sup>2</sup> ]	Fluid	Pressure Drop [kPa]	Subcooling [°C]	Pumping Power / Cooling Capacity (x 10 <sup>3</sup> )	$\Delta T_{\text{sat}}$ [°C]	Maximum Achievable Heat Flux [W/cm <sup>2</sup> ]
<b>(Agostini et al., 2008)</b>	Microchannel	2x1	R236fa	90	10	1.97	27.0	<b>250</b>
<b>(Kosar &amp; Peles, 2007)</b>	Hydrofoil based micro pin fin	1x0.18	R-123	300	76 <sup>(1)</sup>	1.3	27.5 <sup>(1)</sup>	<b>312</b>
<b>(Visaria &amp; Mudawar, 2008)</b>	Spray Cooling	1x1	F-77	174	70	11.9	32.4	<b>349</b>
<b>(Sung &amp; Mudawar, 2009)</b>	Hybrid Microchannel and Jet Impingement	2x1	HFE-7100	172	114.3 <sup>(2)</sup>	4.5	104.6 <sup>(2)</sup>	<b>1127</b>

(1)-Calculated for  $P_{\text{out}}=500$  kPa, and assuming a room temperature of  $T_{\text{amb}}=25$  °C

(2)-Calculated by assuming the outlet pressure to be  $P_{\text{out}}=P_{\text{atm}}=101$  kPa

## **2.1. Summary**

In this chapter working principles of FFMHS in single-phase and two-phase heat transfer modes are defined and the possible benefits of using such systems are highlighted. The fabrication methodology, advantages and manufacturing limitation of microgrooved surfaces adopted for this study are reviewed. The important fundamentals of flow and heat transfer mechanisms expected to dominate heat transfer in FFMHS are covered and relevant equations are given. The literature on single-phase FFMHS, two-phase saturated boiling in microchannels and high heat flux cooling systems are reviewed and important conclusions are tabulated.

## **CHAPTER 3: SINGLE-PHASE NUMERICAL STUDY**

The objective of this chapter is to analyze single phase Force Fed Microchannel Heat Sink (FFMHS) heat transfer and fluid flow and to determine the geometrical and flow parameters that affect the thermal performance. For this purpose a numerical model is introduced and the numerical simulation methodology is discussed in detail. Applying the numerical model, a typical FFMHS geometry is analyzed and important flow parameters are discussed. Finally, a parametric analysis is performed by changing several geometrical and flow variables and calculating the rate of change on heat transfer and pumping power. This study will create a base understanding that will help to determine the optimization variables discussed in Chapter 4.

### **3.1. Computational Domain**

Numerical modeling of a real scale complete heat sink show in Figure 2-1 using CFD tools is neither feasible nor practical and presents real challenges in terms of computational time. A practical solution for this problem is to define a computational domain consisting of a much smaller but repetitive part of the real-scale heat sink. For this study, the selected computational domain is shown in detail in Figure 3-1. Due to the repetitive nature of the computational domain over the entire heat sink on the Y-Z and X-Y planes, symmetry boundary conditions can be used at the boundary surfaces located at these planes. The model is a combination of the microgrooved surface modeled as solid material and the fluid that flows through the

feed channels and the microchannels. Because the microgrooved surface is symmetrical, it is modeled as the base and half of a fin, the microchannel consists of half of a channel, and similarly the inlet and outlet feed channels are considered only half of the channel width size.

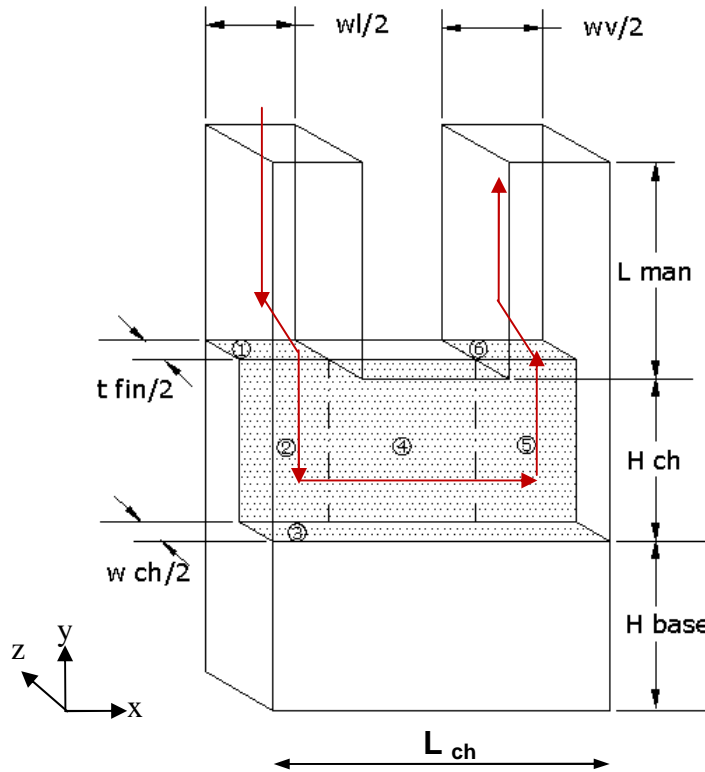


**Figure 3-1. Numerical computational domain**

Selection of the computational domain shown in Figure 3-1 includes several assumptions:

- The flow rate in each feed channel is steady and equal. For an FFMHS the inlet feed channels have identical geometries and they are fed from the same pressure source. The outlet feed channels are formed by the gap between two neighboring manifolds, and therefore the pressure loss for each unit cell is constant. The only exception is the feed channels at the edges (the first

and last feed channels), where there is no counter-manifold to create symmetry.

- The fins and channels of the microgrooved surfaces are usually not straight and may have a slightly bent geometry, as shown in Figure 2-2 (a)-(b), and the fins may end with an unconventional sharp fin tip. The geometry of the surface is a function of the process and tools used for manufacturing. Here the microgrooved surface geometry was simplified by assuming straight fin geometry with flat fin tips.
- The heat flux applied from the bottom of the microgrooved surface is constant. A non-uniform heat flux distribution is not possible, since any variation in X and Z directions will violate the symmetry conditions.
- The thermal properties (thermal conductivity) of the metal substrate are isotropic. Similarly, the symmetry boundary condition can only be applied for solids with isotropic thermal properties in the X and Z directions.
- The heat transfer through the manifolds is neglected and the manifolds are adiabatic. There are two means of possible heat transfer in the manifolds. The first mechanism is the heat transfer through the incoming and outgoing fluid streams in the neighboring inlet and outlet feed channels. Here a temperature gradient forms due to the temperature difference in the fluid streams, where fluid leaving the heat sink is hotter than inlet steam due to the energy gained during heat transfer on the microgrooved surface. The heat transfer caused by this temperature gradient was neglected by assuming the manifolds to be made of poor conductive material such as low conductivity plastic. The

second possible heat transfer mechanism is the thermal conduction through the tip of the fins to the manifold. In many practical applications, the manifolds are not bonded to the microgrooved surface, but rather kept in place by compressive forces. This configuration allows the microgrooved surfaces to be cleaned by easily disassembling the heat sinks in case of fouling and microchannel clogging. As shown in Figure 2-2 (a)-(b), the fin tips usually have a sharp edge, which creates a line of contact when compressed with the manifold top face, therefore creating a relatively high thermal contact resistance. To further simplify the problem and eliminate uncertainties associated with linear thermal contact resistance, an adiabatic manifold was assumed for the numerical simulations.

There are six distinctive heat transfer areas between the fluid and solid walls, and each was numbered as shown in Figure 3-1. The first zone is the fin tip under the inlet feed channel; the second zone is the side fin area under the inlet feed channel; the third zone is the base area; the fourth zone is the straight microchannel zone; the fifth zone is the side fin area under the outlet manifold; and the sixth zone is defined as the fin tip area under the outlet feed channel. The heat transfer characteristics of each of these zones will be analyzed in the next sections.

### **3.2. Single-Phase Modeling with Computational Fluid Dynamics**

Due to the complex three-dimensional geometry of the computational domain, an exact analytical solution for flow field and heat transfer cannot be obtained; therefore, a numerical approach needs to be considered. Modeling techniques

incorporating computational fluid dynamics (CFD) are based on numerically solving the flow field for a given geometry and given boundary conditions. The solver selected for this work is Fluent® 6.3.26, which is a CFD package well known for its capability to solve fluid flow and heat transfer problems. Fluent® uses the finite volume discretization method with implicit or explicit formulation to solve the Navier-Stokes equation. For flows involving heat transfer an additional equation of energy balance is solved. Additional detailed information about the finite volume method and solution procedure can be found in (Fluent-Inc, 2008), (LeVegue, 2002) and (Versteeg & Malalasekera, 2007). The continuity equation is shown in general form in Equation (3-1) :

$$\frac{\partial \rho}{\partial t} + \nabla \cdot (\rho \vec{V}) = S_m \quad (3-1)$$

For steady-state incompressible flow with no mass source term, the conservation equation can be further simplified by eliminating the first terms on the left-hand side and right-hand side, respectively. The conservation of momentum in a non-accelerating reference frame is given in Equation (3-2) where the stress tensor  $\bar{\tau}$  is given by Equation (3-3). The terms on the left-hand side represent the momentum change rate and convective momentum transfer rate, while the right-hand side represents pressure forces, diffusive momentum transfer rate, gravitational forces and external body forces, respectively. For incompressible and steady-state flow with zero body force, the first and last terms of Equation (3-2) will be neglected. For all numerical simulations performed in this study laminar flow regime was considered.

$$\frac{\partial}{\partial t} (\rho \vec{V}) + \nabla \cdot (\rho \vec{V} \vec{V}) = -\nabla p + \nabla \cdot (\bar{\tau}) + \rho \mathbf{g} + \vec{F} \quad (3-2)$$

$$\bar{\tau} = \mu \left[ (\nabla \vec{V} + \nabla \vec{V}^T) - \frac{2}{3} \nabla \cdot \vec{V} \vec{I} \right] \quad (3-3)$$

The general form of energy equation is given in Equation (3-4). The left-hand side represents the temporal energy change and convective energy transfer. The first three terms on the right hand-side represent energy transfer due to conduction, species diffusion, and viscous dissipation, respectively.  $S_h$  includes the heat of chemical reaction, and any other defined volumetric heat sources.

$$\frac{\partial}{\partial t} (\rho E) + \nabla \cdot [\vec{V} (\rho E + p)] = \nabla \cdot \left[ k_{eff} \nabla T - \sum_j h_j \vec{J}_j + (\bar{\tau}_{eff} \cdot \vec{V}) \right] + S_k \quad (3-4)$$

The energy equation does not include the viscous dissipation effect, which is turned off by default in Fluent. The viscous dissipation can be important at high Brinkman numbers ( $Br > 1$ ); the Brinkman number is defined as the ratio of viscous heating rate to the heat transferred through walls. The heat flux considered in the numerical simulations was fairly high, 1000 W/cm<sup>2</sup> base heat flux for all cases. Therefore, for the calculated numerical cases  $Br \ll 1$  was always satisfied and the viscous dissipation term was not calculated. However, based on authors experience from preliminary numerical simulations, special attention should be given in cases with low to moderate heat fluxes on the order of ~10 W/cm<sup>2</sup>, where viscous heating effect can be significant at small hydraulic diameters and high velocity flows.

All fluid physical properties were calculated at 101 kPa pressure and 20 °C using Engineering Equation Solver (E-Chart-Inc, 2009), and solid material properties were evaluated at the same temperature using property tables given in (Incropera & DeWitt, 2002).

### 3.3. Numerical Simulation of a Sample FFMHS

A basic understanding of heat transfer and flow in FFMHS is needed before performing any design, optimization or modeling. Therefore, as the first step, a typical FFMHS was numerically simulated and analyzed. The purpose of these numerical simulations was to create an understanding of the working principle and to serve as the initial design concept that would later be used in the optimization process. The selected sample FFMHS configuration consisted of a microgrooved surface with channel height of  $H_{ch}=480 \mu\text{m}$ , fin thickness of  $t_{fin} = 48 \mu\text{m}$ , microchannel width of  $w_{ch} = 72 \mu\text{m}$ , base thickness of  $H_{base} = 400 \mu\text{m}$  and manifold system with inlet feed channel width of  $w_i = 400 \mu\text{m}$ , outlet feed channel width of  $w_v = 400 \mu\text{m}$  and total channel length of  $L_{man}=2 \text{ mm}$ . These values were based on previous numerical and experimental experience: the microgrooved surface dimensions are close to those of Surface #17 given in Table 2-1, and the manifold and feed channel dimensions were based on the manifold designed for experimental tests, with equal inlet and outlet width of feed channels. The microgrooved surface material and working fluid were copper and water, respectively.

#### 3.3.1. Grid Generation and Numerical Mesh

Selection of the proper mesh for the computational domain is important due to the tradeoff between computational time and model accuracy. A mesh generated with fine grid spacing will have higher accuracy but will require higher computational time. Selection of an optimum mesh was even more important in the current

optimization procedure, in which several hundreds of numerical solutions were to be solved for different geometries and flow conditions.

The first step in meshing process is the selection of mesh type which can be either structured or unstructured. The unstructured grids can be applied to almost any geometry but require more information to be stored furthermore, controlling the local grid resolution is difficult, and such grids are not suitable for automated grid generation. Therefore, as a general numerical strategy, structured grids are preferred when they are applicable. The computational domain shown in Figure 3-1 has a “straight” geometry which does not include any round corners or bended angled edges. The geometry can be formed by combining different rectangular volumes, and therefore a structural grid can be successfully applied. The mesh generation was performed by Gambit®, which is a software package available in the Fluent® 6.3.26 package. The meshed computational domain consists of 68,850 structured hexahedral cells and is shown in Figure 3-2 (a) and (b), front view and isometric views, respectively.

### **3.3.2. Boundary Conditions and Output Parameters**

A complete list of applied boundary conditions is given in Table 3-1, based on the coordinate system shown in Figure 3-1. Boundaries not included in the table were selected as adiabatic wall as default. The specified inlet mass flow rate boundary condition uses flow rate as input and calculates the static pressure based on the flow field. Therefore, the inlet static pressure is not known as *a priori* until the convergence is obtained. Similarly, the outlet boundary condition is specified as static pressure and the total pressure is calculated after convergence is obtained.

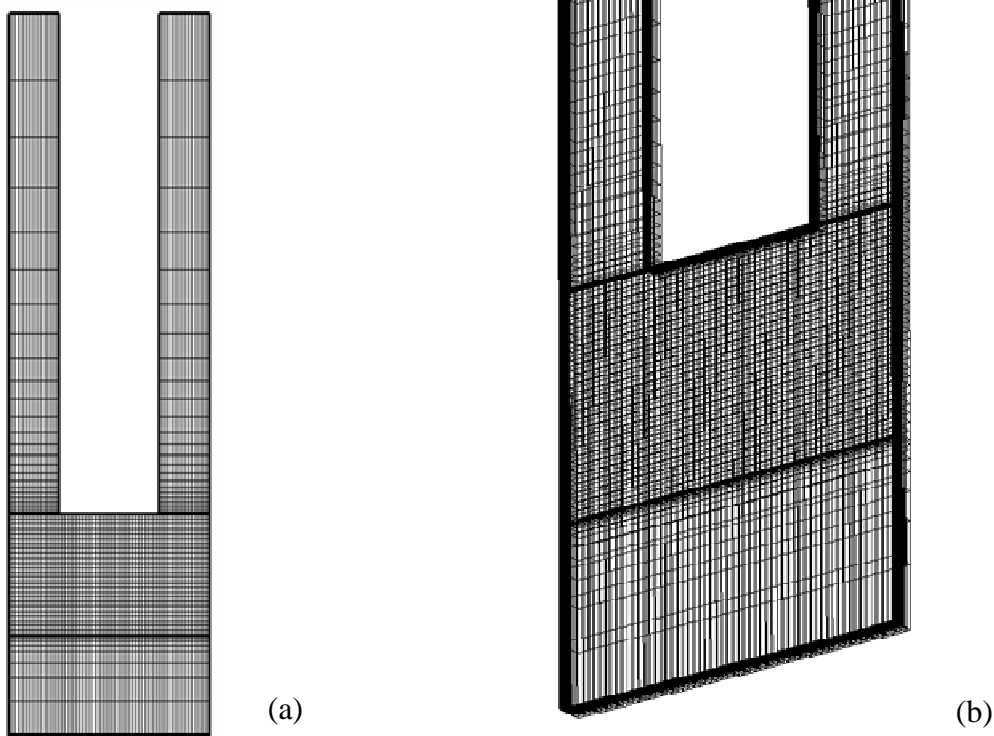


Figure 3-2. (a) Front view and (b) perspective view for grid generated for  $H_{ch}=480 \mu\text{m}$ ,  $w_{ch}/2=36 \mu\text{m}$ ,  $t_{fin}/2 = 24 \mu\text{m}$ ,  $L=800 \mu\text{m}$ ,  $w_l/2=200 \mu\text{m}$ ,  $w_v/2=200 \mu\text{m}$ ,  $L_{man}=2 \text{ mm}$ ,  $H_{base} = 400 \mu\text{m}$

Table 3-1. The boundary conditions applied to computational domain

Location of applied boundary condition	Boundary Condition
$x = 0$	Symmetry
$x=L$	Symmetry
$z=0$	Symmetry
$z=t_{fin}/2+w_{ch}/2$	Symmetry
$y=0$	Uniform Heat Flux of $q''=1 \text{ kW/cm}^2$
$y=H_{base} + H_{ch} + L_{man}$	Specified inlet mass flow rate
$0 < x < w_l/2$	
$0 < z < t_{fin}/2+w_{ch}/2$	
$y=H_{base} + H_{ch} + L_{man}$	Pressure outlet (zero outlet static pressure)
$(L-w_v/2) < x < L$	
$0 < z < t_{fin}/2+w_{ch}/2$	

The analyses were based on two output functions, the heat transfer coefficient and pumping power. Once the numerical convergence was achieved, these functions were evaluated based on post-processing data obtained from the flow field. The effective heat transfer coefficient was defined for the temperature difference between average surface temperature and inlet fluid temperature:

$$h = \frac{q''}{\bar{T}_{surf} - \bar{T}_{in}} \quad (3-5)$$

where the temperature values were area averaged over the surface as:

$$\bar{T} = \frac{1}{A} \int T \cdot dA \quad (3-6)$$

The pumping power was calculated for the unit base area. Pumping power is defined as the product of total pressure difference between inlet and outlet boundaries and volumetric flow rate passing through unit base area heat sink:

$$P''_{pump} = \frac{\dot{m}(\bar{P}_o - \bar{P}_i)}{\rho \left[ L \left( \frac{t_{ch}}{2} + \frac{w_{ck}}{2} \right) \right]} \quad (3-7)$$

where the pressure values were area averaged as well at inlet and outlet:

$$\bar{P} = \frac{1}{A} \int P \cdot dA \quad (3-8)$$

The pumping power definition in Equation (3-7) is practical for the extrapolation of pumping power for heat sinks with different base areas. In this case, for constant microchannel mass flux and microgrooved surface geometry, the pressure difference for the heat sink will remain the same while the flow rate will increase linearly with increasing the heat sink base area.

Since heat transfer and pumping power are functions of flow rate, information regarding the flow conditions needs to be defined. This was performed by introducing the Reynolds number based on flow in the straight channel part of the microchannel (Zone 4 in Figure 3-1) defined as:

$$\text{Re} = \frac{V_{ch} D_h}{\nu} \quad (3-9)$$

where

$$V_{ch} = \frac{\dot{m}}{\rho H_{ch} w_{ch}} \quad (3-10)$$

$$D_h = \frac{4H_{ch} w_{ch}}{2(H_{ch} + w_{ch})} \quad (3-11)$$

Here  $\dot{m}$  is the total mass flow rate,  $V_{ch}$  is the average velocity and  $D_h$  is the hydraulic diameter, all defined for the flow in the straight part of the microchannel. All other geometrical dimensions are shown in Figure 3-1.

### 3.3.3. Grid Independency Test

A grid independency study was performed for the sample geometry shown in Figure 3-2. One general practice of testing the grid independency is doubling the number of computational cells and comparing the change in the specified computational parameters. Five different grid generations, each consisting of 35840, 48576, 68850, 98604 and 137280 number of cells were selected as test cases in this study. The heat transfer coefficient and pumping power per unit heat sink area were used as parameters for checking the grid independency, and the results are given in Table 3-2. The results indicate that selecting Case C with 68,850 cells, is reasonably

accurate for the current study. When the number of cells was increased by almost two times, which corresponds to Case E, the variation in heat transfer coefficient and pumping power were calculated to be 0.29 % and 0.47 %, respectively. It is also important to note from now, that these values are about one order of magnitude lower than the accuracy of the metamodel, which will be discussed in the optimization chapter.

**Table 3-2. Results of grid independency test**

	Units	Case A	Case B	Case C	Case D	Case E
<b>cell no</b>		35840	48576	<b>68850</b>	98604	137280
$\bar{T}_i$	[K]	300.0000	300.0000	<b>300.0000</b>	300.0000	300.0000
$\bar{T}_o$	[K]	300.7966	300.7983	<b>300.7997</b>	300.8011	300.8020
$h$	[W/m <sup>2</sup> K]	251067	250532	<b>250094</b>	249656	249376
$\bar{P}_i$	[Pa]	18608.88	18541.91	<b>18415.42</b>	18358.97	18331.88
$\bar{P}_o$	[Pa]	2409.41	2404.68	<b>2398.93</b>	2397.13	2388.92
$P''_{pump}$	[W/m <sup>2</sup> ]	7981.687	7950.105	<b>7888.828</b>	7861.094	7851.508

For all calculated cases the convergence factor for continuity, three momentum equations, and energy equations were set as 1e-5, 1e-5 and 1e-11. The computational run time for Case C was about 25 minutes on a PC with an Intel Pentium D 3.4 Ghz processor and 2 GB of memory.

### 3.3.4. Numerical Results

The first set of numerical simulations evaluated the heat transfer coefficients and pumping power for different flow rates. The numerical simulations cover the heat transfer coefficients ranging from 50,000 W/m<sup>2</sup>K to 250,000 W/m<sup>2</sup>K. The resulting variations of effective heat transfer coefficient and pumping power with Reynolds

number are given in Figure 3-3 (a) and (b) plotted on log-log charts. For these plots, the results indicate an almost linear variation for both heat transfer coefficients and pumping power values with increased flow rate. Having a slope different than one, the linear trend on a log-log plot indicates a power-law dependence. For fully developed laminar flow in a channel with constant cross section area, the pumping power is proportional to the square of the channel velocity or Reynolds number, indicating a power-law trend with power coefficient of two. On the other hand, the pumping power curve obtained in Figure 3-3 (b) has a power-law coefficient of  $\approx 2.4$ . This in turn may suggest a strong influence of developing flow, secondary flows or other recirculation zones not present in straight channel flow.

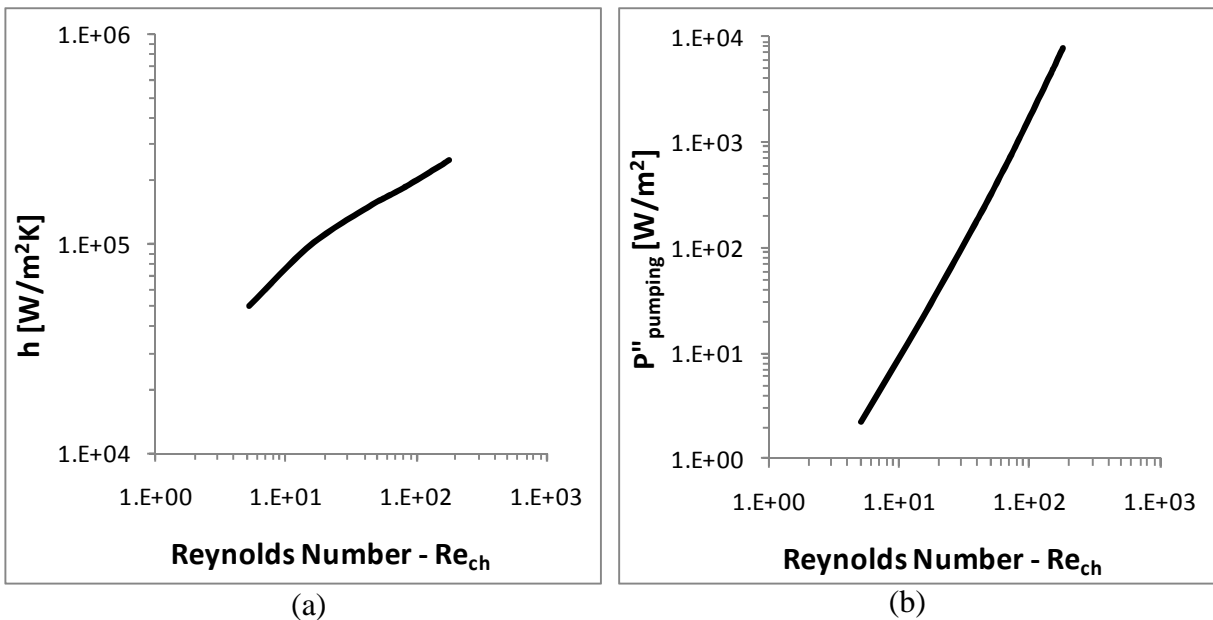


**Figure 3-3. (a) Variation of effective heat transfer coefficient with Reynolds number, (b) Variation of pumping power with Reynolds number**

To analyze the possible effects of these parameters, three different specific cases resulting in heat transfer coefficients of 50,000 W/m<sup>2</sup>K, 150,000 W/m<sup>2</sup>K and 250,000 W/m<sup>2</sup>K were selected as case studies. The three cases represent the low,

medium and high heat transfer coefficient designs. For each case, the mass flow rate was adjusted to give the targeted  $h$  value. The resulting numerical values of heat transfer coefficient and pumping power for these cases are given in Table 3-3.

**Table 3-3. Numerical simulation results for reference cases**

	Unit	Case #1	Case #2	Case #3
Re	[-]	5	43	177
$h$	[W/m <sup>2</sup> K]	50022	150035	250094
$P_{pump}''$	[W/m <sup>2</sup> ]	2.2	227.3	7888.8

The velocity vectors and velocity magnitude distribution on the mid-symmetry plane of  $z=0$  are shown in Figure 3-4 (a),(b) and (c) for three case studies at  $h=50,000$  W/m<sup>2</sup>K,  $150,000$  W/m<sup>2</sup>K and  $250,000$  W/m<sup>2</sup>K, respectively. The flow trend observed in three cases is explained as follows. The fluid enters the system through the inlet feed channel located on the left, it becomes fully developed and then reaches the microgrooved surface, where it contracts as it is forced into the microchannel. The area contraction creates a local decrease in static pressure and a local maximum in velocity magnitude. Due to entrance effects, the flow is hydrodynamically and thermally developing, starting with the inlet into the microchannel. The flow then turns 90° to the right as it undergoes an area expansion due to higher flow area of microchannel comparing to inlet flow area. The velocity magnitude distribution in this straight part of the microchannel is stratified in the  $y$  direction and with little variation in  $x$  direction. The fluid exits the microchannel by making a second 90° turn and expanding into the outlet feed channel on the right. A second velocity maximum is present right before the exit from the microchannel due to the flow area contraction-expansion effect.

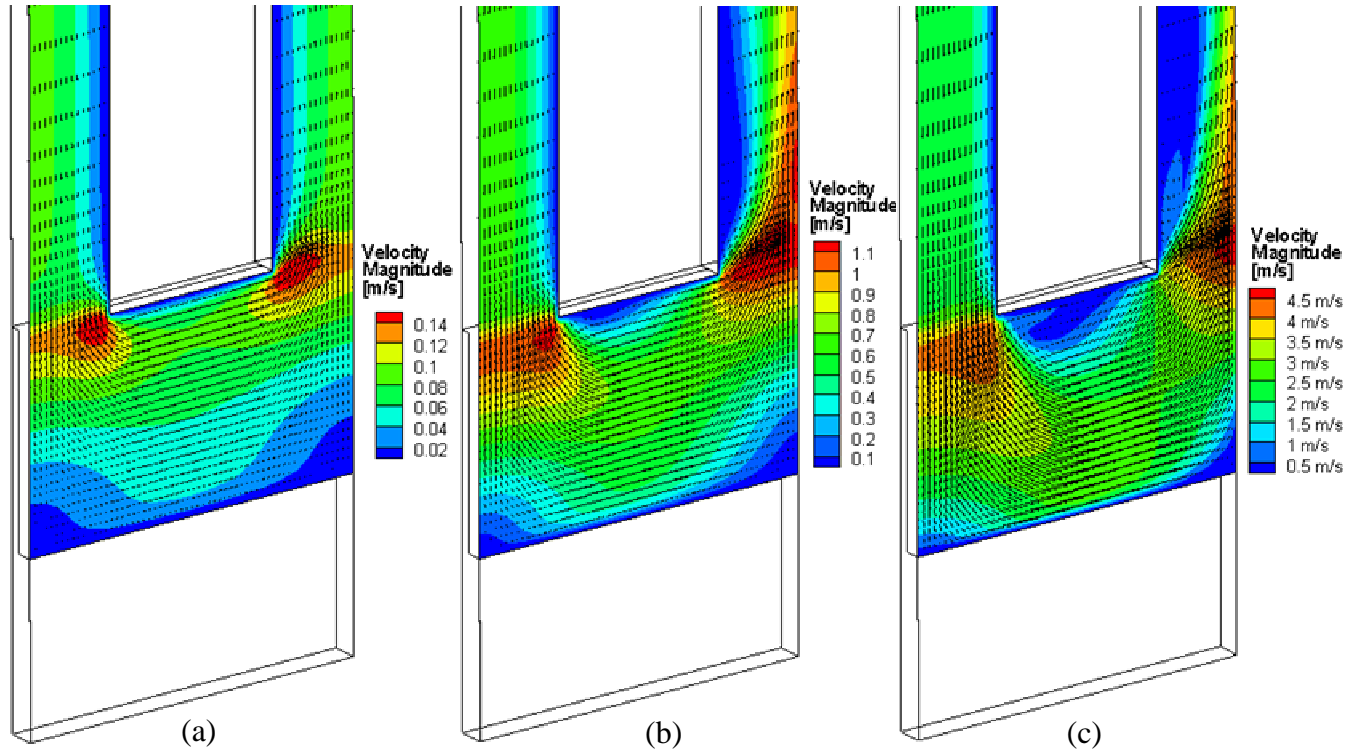


**Figure 3-4. Velocity vectors and velocity magnitude distribution at  $z=0$  for (a) Case #1 at  $h=50,000 \text{ W/m}^2\text{K}$ , (b) Case #2 at  $h=150,000 \text{ W/m}^2\text{K}$ , (c) Case #3 at  $h=250,000 \text{ W/m}^2\text{K}$**

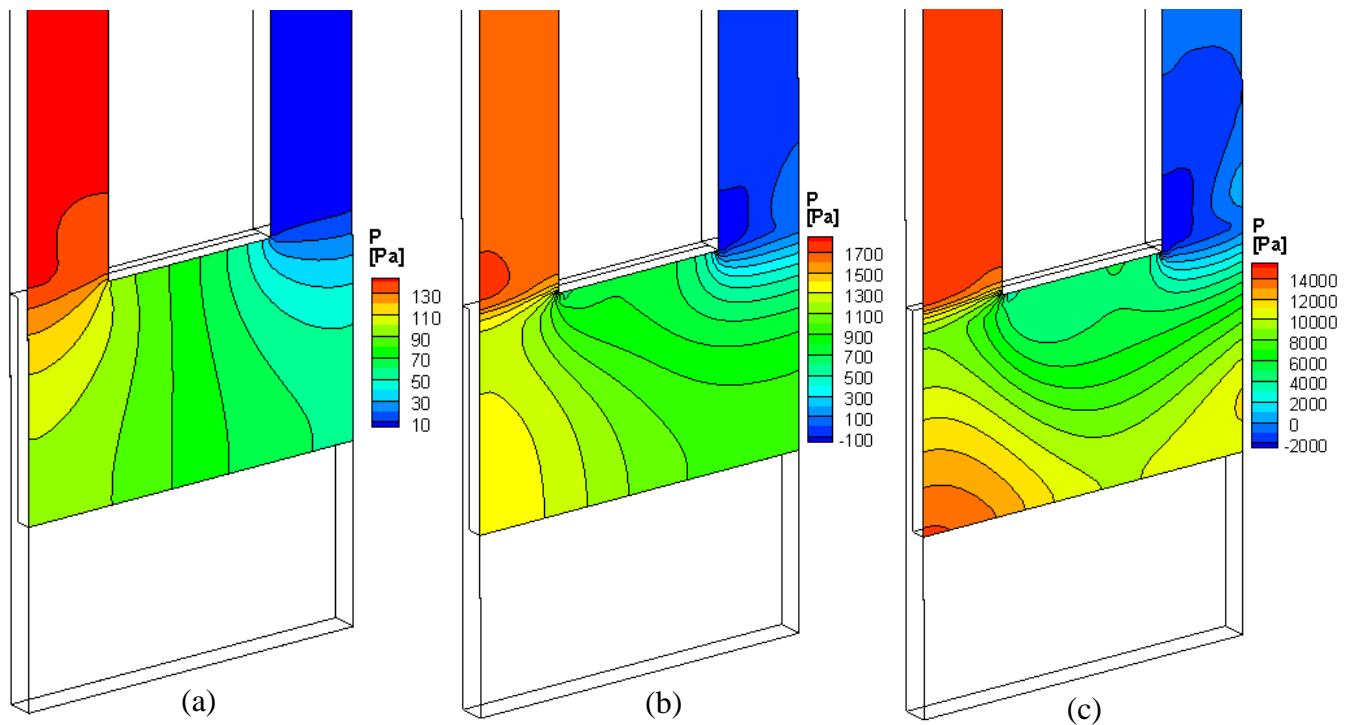


**Figure 3-5. Static pressure distribution at  $z=0$  for (a) Case #1 at  $h=50,000 \text{ W/m}^2\text{K}$ , (b) Case #2 at  $h=150,000 \text{ W/m}^2\text{K}$ , (c) Case #3 at  $h=250,000 \text{ W/m}^2\text{K}$**

While the results of the three cases shown in Figure 3-4 have several common flow characteristics as discussed above, they are different in terms of the physical mechanisms that characterize the flow. For example, at low Re number flows (Figure 3-4 (a)), the inertial forces of the fluid entering the microchannel are comparable to the viscous forces in the microchannel. Therefore the inertial forces of the incoming fluid are insufficient to push the fluid to the bottom of the microchannel and to create an impingement zone. Instead, due to the significant effect of viscous forces, the fluid follows the path with the least friction losses, which creates a bypass zone right under the manifold between the inlet and outlet feed channels. The bypass zone in turn creates stratification in velocity distribution in the y direction with high velocities accumulated on the top and with low velocity flow close to the bottom of the microchannel. The flow maldistribution is even more pronounced in the bottom microchannel regions under the inlet and outlet manifolds with creation of “dead zones” with velocities below 0.02 m/s. This effect can be also explained by studying the static pressure distribution along the microchannel, as given in Figure 3-5 (a) for low Re number flows. The static pressure distribution is uniform, and starting from microchannel inlet, it decreases gradually along the microchannel length until it reaches the outlet zone. Due to fluid bypass effect present the top region, the fluid is not impinging the channel bottom and no pressure increase is observed in this region.

Increasing the Reynolds number by increasing the flow rate (Figure 3-4 (b) and (c)), leads to a different flow trend. First of all, the inertial force of the fluid entering the microchannel is high enough to push the liquid to the bottom of the microchannel and create an impingement zone. The fluid will first decelerate as it

approaches this stagnation zone, will turn the  $90^\circ$  bend and then start to accelerate again as it moves towards the straight part of the microchannel. The static pressure in the impingement zone will increase due to momentum exchange of this turning fluid (Figure 3-5 (b) and (c)). Second, the high inlet velocities and sharp corners of the manifold lead to flow separation that creates a recirculation zone under the manifold. The recirculation zone grows by increasing the Reynolds number. Interestingly, the velocity stratification for this case is opposite the low Reynolds number case. There is a high velocity core close to the bottom of the microchannel and low velocity recirculation zone at the top of the microchannel. A second recirculation zone is present at the bottom of the microchannel zone, under the outlet feed channel. In this region the flow is turning towards the outlet of the microchannel and does not flow deep into the corner of the channel, which has much higher flow resistance. The third recirculation zone appears right after the outlet from microchannel, in the outlet feed channel. Similarly, the velocity distribution tends to be stratified, with the high velocity core close to the center of the outlet feed channel. This separation is the result of the high outlet velocities at the sharp manifold corner.

Besides the flow conditions discussed above, the flow velocity can affect the flow field by creating secondary flows. Due to the bulk flow rotation, a centrifugal force acting from the center of rotation to the channel bottom becomes present and the fluid at the side walls is pressed in the opposite direction. This, in turn, forces the fluid to produce vortex pairs that can fill the channel cross-section. The magnitude of the centrifugal force depends on the flow velocity and radius of curvature of the bend and is a function of Dean number. According to (Kockmann, Engler, & Haller, 2005),

for flows with Dean number  $De < 10$  the centrifugal force effect is negligible and the flow regime is similar to the straight channel flow. At higher Dean flows of  $10 < De < 100$  the centrifugal forces create a single vortex pair, while for flows with  $De > 100$  a secondary vortex pair may be present, dependent on channel geometry. The development of secondary flows changes both heat transfer and flow characteristics. The vortices create continuous fluid mixing by moving the “cold” fluid at the center to the side-walls of the microchannel, therefore enhancing the convective heat transfer. This process disturbs and decreases the thickness of the thermal boundary layer that started to develop at the inlet to the microchannel. On the pressure drop side, however, the flow energy associated with vortices will eventually dissipate into heat, and the pumping power required to drive the fluid in a curved pipe will be always higher compared with straight-tube and channel geometries at the same flow rate. These conflicting objectives of heat transfer efficiency and pumping power need to be considered for a clear evaluation of the possible benefits of secondary flows.

Velocity vectors at several cross sections in the computational domain for Case #3 are shown in Figure 3-6. As the fluid starts to turn at both the first and second bends, vortex pairs are created in the microchannel as the fluid in the center is pushed down and forces the liquid close to the walls to move in the opposite direction. Due to symmetry conditions, only one half of the channel, and therefore only one vortex is shown in the figure. The pathlines and transition between flow regimes at different Reynolds number flows are shown in Figure 3-7 (a),(b) and (c). The corresponding Dean numbers were calculated as  $De = 2$ ,  $De = 15$  and  $De = 61$ ,

respectively. For Case #1, the low Reynolds number leads to low Dean numbers, and therefore the centrifugal forces are negligible, and the secondary flows are not present. The pathlines are uniform and almost symmetric, with no disturbance in the flow. As the Reynolds number is increased in Case #2 and later in Case #3 by achieving  $De > 10$ , the centrifugal forces start to become important. The vortices formed during flow turning disturb the flow, and the pathlines show a less uniform pattern. As seen in Figure 3-7 (c), due to secondary flows and the mixing effect, the pathlines can cross over each other on the plane of view.

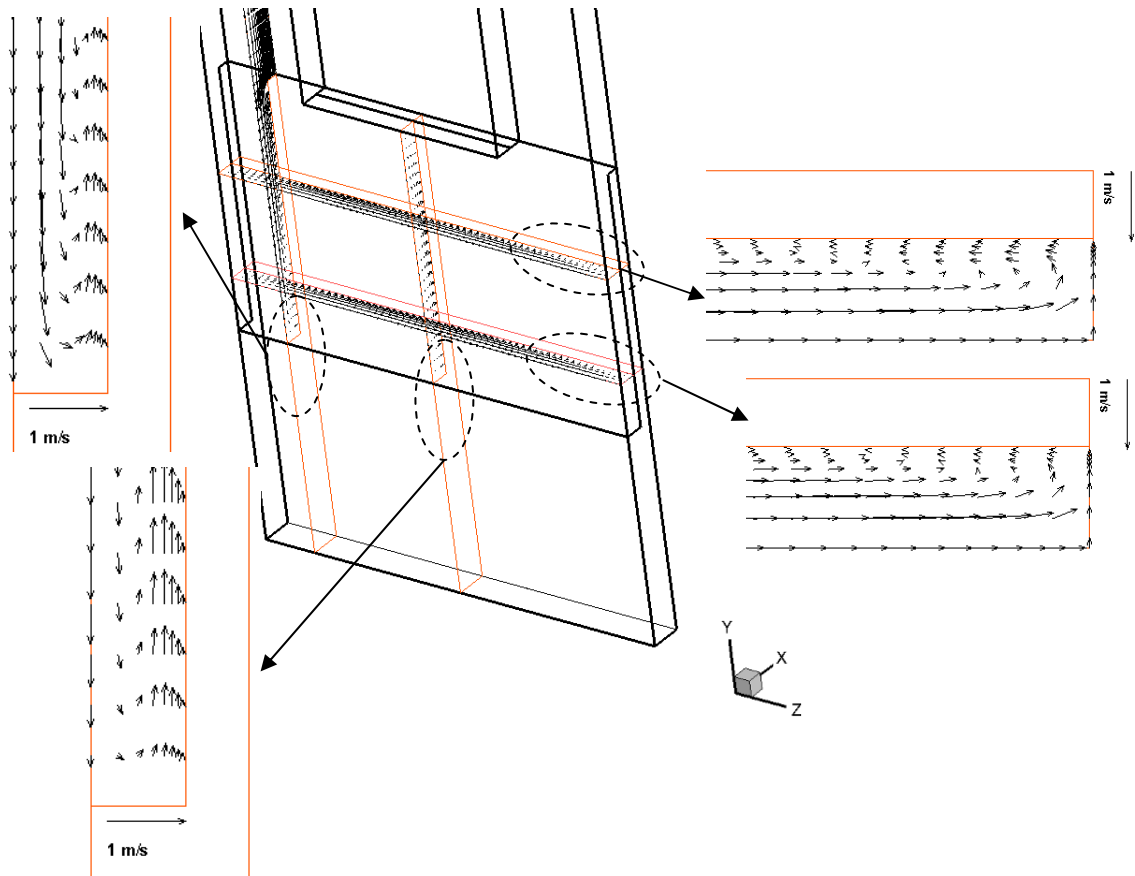


**Figure 3-6. Velocity vectors created by secondary flows at several cross sections in the computational domain for Case #3 at  $h=250,000 \text{ W/m}^2\text{K}$  and  $De=61$**

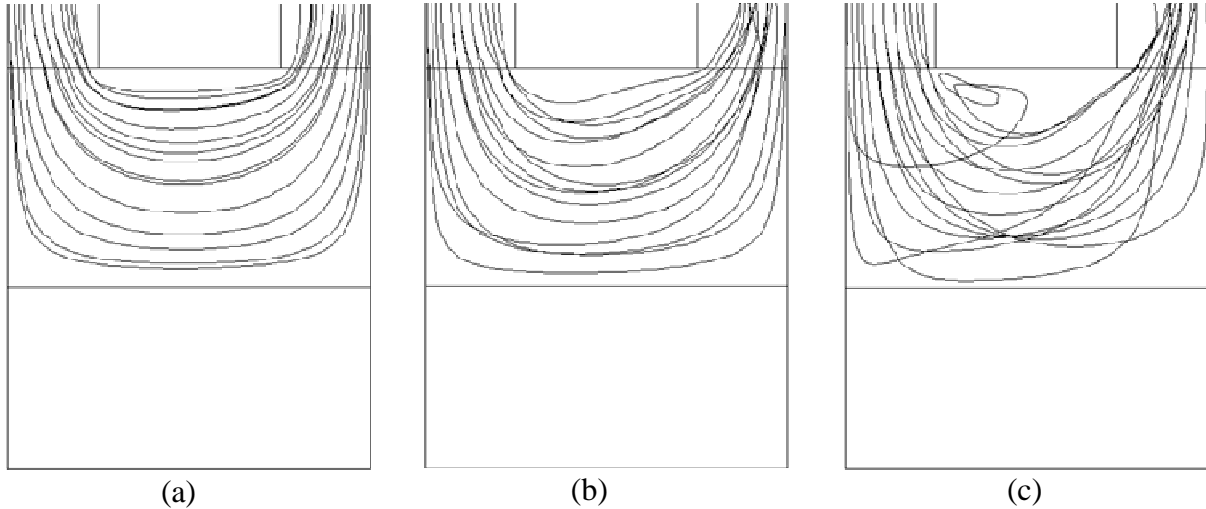


**Figure 3-7. Pathlines at  $z=0$  plane for (a) Case #1 at  $h=50,000 \text{ W/m}^2\text{K}$  and  $De=2$ , (b) Case #2 at  $h=150,000 \text{ W/m}^2\text{K}$  and  $De=16$ , (c) Case #3 at  $h=250,000 \text{ W/m}^2\text{K}$  and  $De=61$**

The fluid temperature distribution at the symmetry plane of  $z=0$  is shown in Figure 3-8 (a), (b) and (c) for Case #1, Case #2 and Case #3 respectively. Two different trends become important as the flow Reynolds number goes from low to high. First, the temperature rise of the fluid is significant at low flow rates. This is expected, since the mass flux is lower and fluid can be heated much more before exiting the microchannel. Second, the velocity stratification shown in Figure 3-4 also creates temperature stratification. The low velocity zones close to the bottom of the microchannel at low Reynolds number flows and “dead zones” in the high Reynolds number cases create high temperature zones. Similarly, the relatively low velocities allow the liquid to be heated for longer times therefore a temperature difference is observed in these regions.

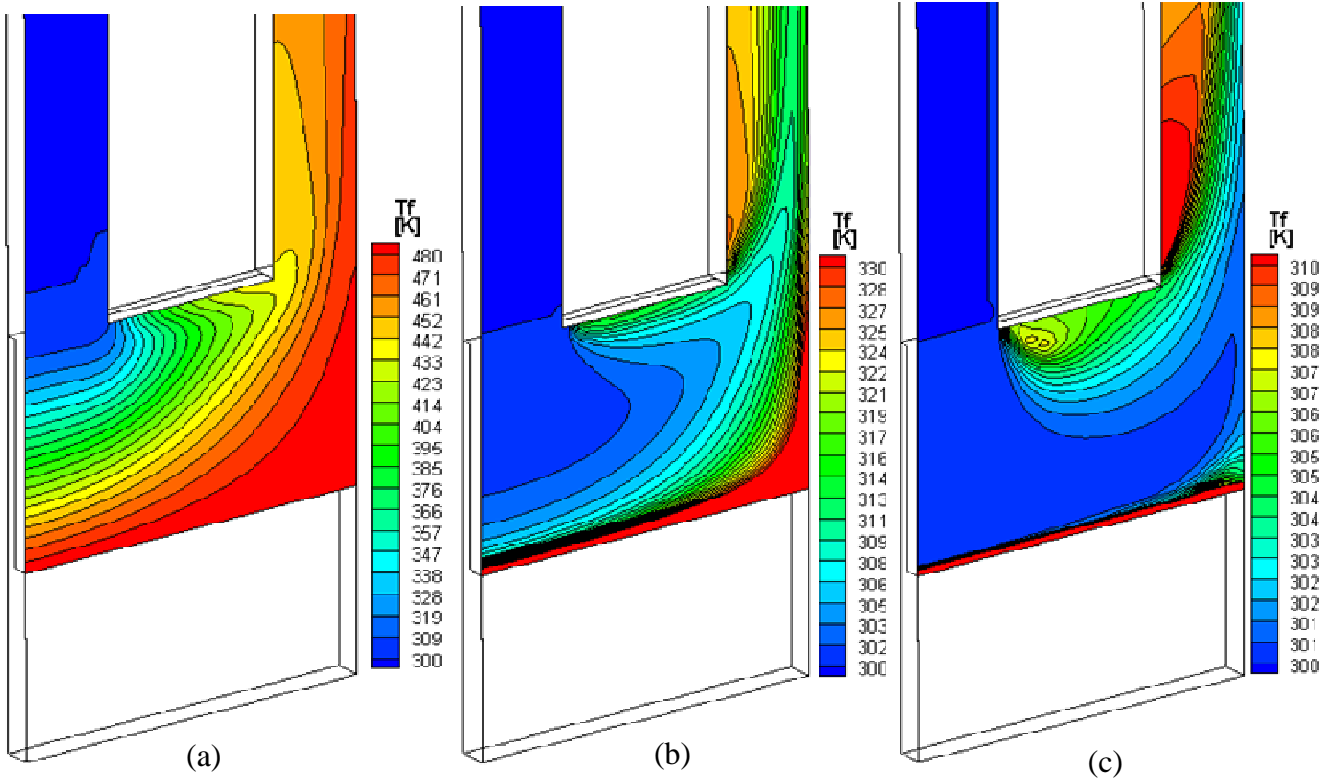


**Figure 3-8. Working fluid temperature distribution at  $z=0$  for (a) Case #1 at  $h=50,000 \text{ W/m}^2\text{K}$ , (b) Case #2 at  $h=150,000 \text{ W/m}^2\text{K}$ , (c) Case #3 at  $h=250,000 \text{ W/m}^2\text{K}$**

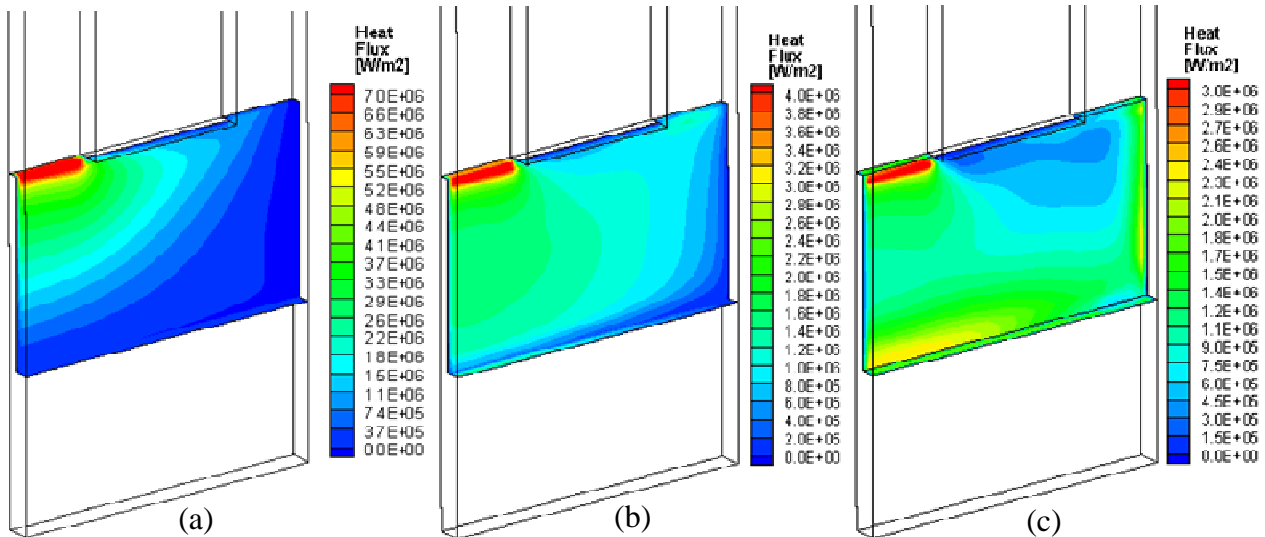


**Figure 3-9. Fin heat flux distribution for (a) Case #1 at  $h=50,000 \text{ W/m}^2\text{K}$ , (b) Case #2 at  $h=150,000 \text{ W/m}^2\text{K}$ , (c) Case #3 at  $h=250,000 \text{ W/m}^2\text{K}$**

The heat flux distribution on the fin and microchannel base for the three cases is shown in Figure 3-9 (a),(b) and (c). Although the mass flux has a significant effect on heat flux distribution on the fin surface, the maximum heat flux always occurs at the inlet region to the microchannel. This global maximum is the result of the large temperature difference between the fluid and surface and the significant entrance region effects where thermal boundary layer is relatively thin and heat transfer resistance is low.

At low Reynolds number flows (Figure 3-9 (a)) the heat sink efficiency decreases due to increase in non effective areas which do not contribute to heat transfer. The temperature difference between bulk liquid and surface is low in these regions. The heat transfer characteristic changes significantly with higher Reynolds number flows (Figure 3-9 (c)). First, the heat flux becomes more uniformly distributed along the fin surface with the heat flux gradient decreasing slightly along the microchannel length. However, local minimums are present at the heat transfer surfaces under the recirculation zones. The fluid trapped in the recirculation zones has high bulk temperatures, thereby decreasing the convective heat transfer efficiency. Second, the secondary local maxima starts to appear close to the impingement zones under the inlet and outlet feed channels. Similar local high heat transfer zones were reported by (Copeland, 1995b), (Copeland et al., 1997) and (Ng & Poh, 1999). Close to the impingement zones, the local fluid acceleration and vortices created during the flow turning have the effect of reducing the thermal boundary layer thickness and enhance heat transfer. These local high heat transfer zones are a strong function of Reynolds and Dean numbers.

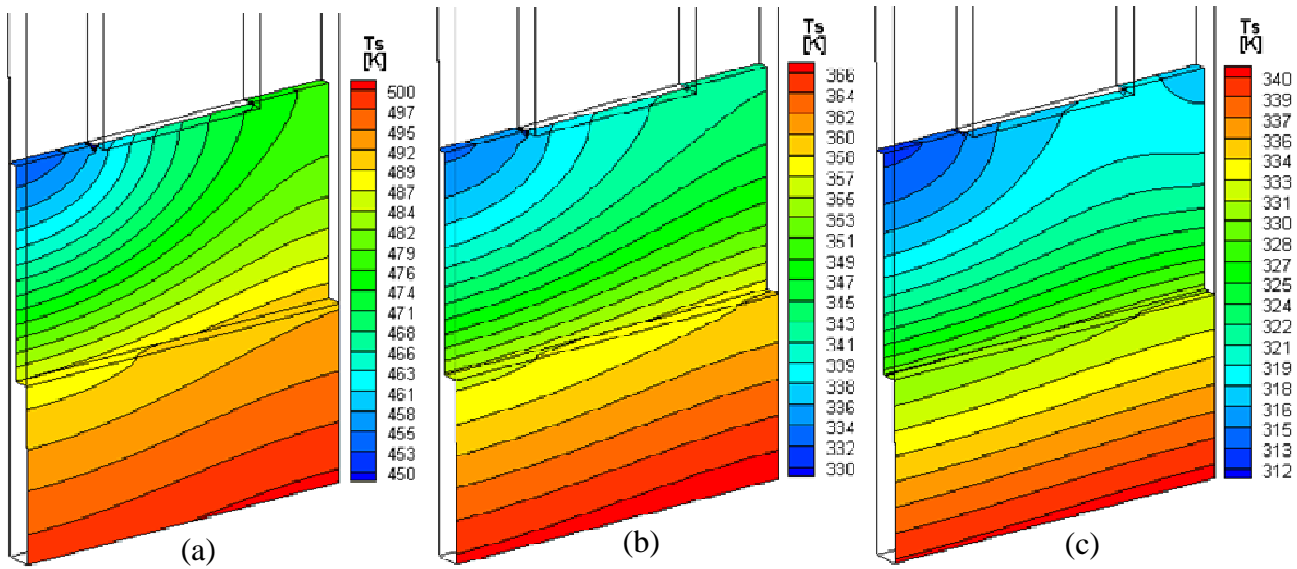


**Figure 3-10. Temperature contours of fin surface, microchannel bottom wall and base material for (a) Case #1 at  $h=50,000 \text{ W/m}^2\text{K}$ , (b) Case #2 at  $h=150,000 \text{ W/m}^2\text{K}$ , (c) Case #3 at  $h=250,000 \text{ W/m}^2\text{K}$**

Finally, the surface temperature distributions on the fin surface, microchannel base and middle of base material are shown in Figure 3-10 (a),(b) and (c) for the selected three reference cases. The minimum fin temperature occurs close to the tip of the fin region, where the fluid enters the microchannel. Due to high heat transfer coefficients and relatively large temperature differences between the surface and fluid, the local fin temperature can decrease significantly. At low Reynolds number flows all the heat that is transferred to the fluid is localized at the inlet region with heat flowing from all directions, perpendicular to the isotherms shown in Figure 3-10 (a). Increasing the flow rate to higher Reynolds numbers (Figure 3-10 (a) and (b)) increases the heat transfer efficiency and significantly decreases the heat sink temperatures. On the other hand, the temperature isotherms become more horizontal, indicating a more uniform heat flow from the bottom of the base material to the fin heat transfer surface.

### 3.4. Parametric Numerical Study

In the previous section several numerical simulations were performed for a single geometry with various inlet flow conditions. The numerical simulation results indicated that flow regimes and thermal performance of FFMHS are a strong function of flow parameters or Reynolds number. In order to investigate the geometrical effects, a similar parametric study was initiated. The goal of this study was to identify the effects of each geometrical parameter on heat transfer and pumping power. The parametric analyses were performed by selecting and varying one of the geometrical parameters of interest while keeping other parameters constant. Each new design variation was simulated three times to yield heat transfer coefficients of 50,000 W/m<sup>2</sup>K, 150,000 W/m<sup>2</sup>K and 250,000 W/m<sup>2</sup>K, respectively. This was accomplished by adjusting the flow inlet conditions until the desired heat transfer coefficient was obtained. The effect of selected geometrical parameter was then analyzed by calculating the pumping power rate of change compared with a selected benchmark reference case. The reference cases are the selected case studies shown in Table 3-3. The resulting pumping power values were compared with reference cases at similar heat transfer coefficient values. The geometrical variation of each parameter was calculated by evaluating:

$$\chi_i = \frac{G_i}{G_{i,ref}} \quad (3-12)$$

where  $G_i$  represents the dimension of geometrical parameter  $i$  being studied (microchannel height, microchannel width, manifold dimensions, microchannel length and base thickness), and  $G_{i,ref}$  is the reference value for the same parameter

taken from Table 3-3. The  $\chi_i$  value represents the relative change of the investigated parameters to the reference case. The relative change in pumping power was normalized similarly by dividing the resulting pumping power of the investigated parameter  $P''_{pump}$  by the pumping power of the reference case at the same heat transfer coefficient,  $P''_{pump,ref}$ , taken from Table 3-3:

$$\psi_{pp} = \frac{P''_{pump}}{P''_{pump,ref}} \quad (3-13)$$

The advantage of using a  $\chi_i$  versus a  $\psi_{pp}$  graph is the ease of showing the relative change in pumping power in terms of relative change in geometry at fixed heat transfer coefficients. For example, a  $\psi_{pp}$  value greater than one indicates an increase in pumping power compared with the benchmark reference case.

The geometry variation was based on the practical fabrication range of microgrooved surfaces and manifolds. While increasing the ratio of the microgrooved enhanced heat transfer surface area to the base area by increasing the fin height or fin aspect ratio is highly desirable, fabrication limitations restrict the geometrical design ranges. These limitations also play an important role in defining the optimization parameters' lower and upper bounds and prevent heat transfer geometries that might be theoretically superior heat transfer surfaces but that are practically impossible to fabricate. Therefore, the lower and upper bounds of the geometrical parameters of microgrooved surfaces were defined before performing any parametrical study.

### 3.4.1. Practical Geometrical Range of Microgrooved Surfaces Fabricated by Micro Deformation Technology

The copper microgrooved surfaces are fabricated by Micro Deformation Technology (MDT) and are designed to improve heat transfer by creating parallel microfins that enhance heat transfer area. Currently, MDT is under continuous development, but according to Wolverine Inc., which has patented this technology, the current practical limitations that can be applied for cost effective surfaces are as follows:

$$0.2 \text{ mm} \leq H_{ch} \leq 5.0 \text{ mm} \quad (3-14)$$

$$\frac{H_{ch}}{t_{fin}} \leq 10 \quad (3-15)$$

$$0.2 \leq \frac{w_{ch}}{t_{fin}} \leq 1.5 \quad (3-16)$$

The inequality shown in Equation (3-14) defines the practical minimum and maximum bounds for fin and microchannel height  $H_{ch}$ ; Equation (3-15) represents the maximum fin aspect ratio  $H_{ch}/t_{fin}$ ; and Equation (3-16) defines the limits for channel width to fin thickness ratio  $w_{ch}/t_{fin}$ .

### 3.4.2. Effect of Fin Thickness and Fin Height

The effect of fin thickness  $t_{fin}$  and channel height  $H_{ch}$  on pressure drop is shown in Figure 3-11 and Figure 3-13, respectively. For each constant  $h$  value taken into consideration, the cases of  $\chi_{tfin} = 1$  and  $\chi_{Hch} = 1$  represent the reference cases and the corresponding fin aspect ratio at these values is  $H_{ch}/t_{fin} = 10$ . It should be noted

that this value is actually equal to the practical limitation dimension defined by Equation (3-15). The parametric study was performed by increasing fin thickness or decreasing channel height which resulted in FFMHS designs utilizing microgrooved surfaces with fin aspect ratios lower than 10. As noted before, numerical results for these cases were obtained by variation of flow rate until desired heat transfer coefficient of 50,000 W/m<sup>2</sup>K, 150,000 W/m<sup>2</sup>K or 250,000 W/m<sup>2</sup>K was achieved.

Two important results can be drawn from Figure 3-11. First, the pumping power variations are relatively small when the channel height is decreased up to 20% but increase drastically at small channel heights where the height is reduced up to 60%. The change in channel height affects active heat transfer area, microchannel cross-section flow area and the length of a typical streamline passing through the microchannel. Decreasing the fin height will decrease the heat transfer area and microchannel cross-section flow area; therefore, it will require higher flow rates to increase the convective heat transfer and keep the desired heat transfer coefficient constant. The high flow rate and smaller flow area in turn will rise the pumping power significantly at small  $\chi_{Hch}$  values. The second important result that can be obtained from Figure 3-11 is the decreasing trend of pumping power with decreasing channel height for constant heat transfer coefficient curve of 250,000 W/m<sup>2</sup>K between  $0.6 \leq \chi_{Hch} \leq 0.8$ . In this region the pumping power can be lowered by about 15% by decreasing the channel height. This effect can be explained by the flow schematic shown in Figure 3-12. For a high channel height case, a typical streamline passing through the middle of the channel is longer than the streamline passing through a microgrooved surface with shorter channel height; therefore, the flow

resistance decreases. On the other hand, convective heat transfer in the region close to the inlet into the microchannels is very high due to the thin thermal boundary layer of thermally developing flow. At high Reynolds numbers the local heat transfer coefficient in the region close to the tip of the fin is very high, and the fin efficiency in this region drops significantly. Decreasing the channel height will decrease the heat transfer area but in turn will increase fin efficiency by decreasing the fin height and therefore the fin thermal resistance as well. In summary, by decreasing channel height and thus shortening of the flow path and increasing fin efficiency, it is possible to enhance the heat sink performance by lowering the pumping power at heat transfer coefficients of 250,000 W/m<sup>2</sup>K. However, this trend is observed only at high heat transfer coefficients where the flow rate is relatively high and the decrease in pumping power is not more than 20%.

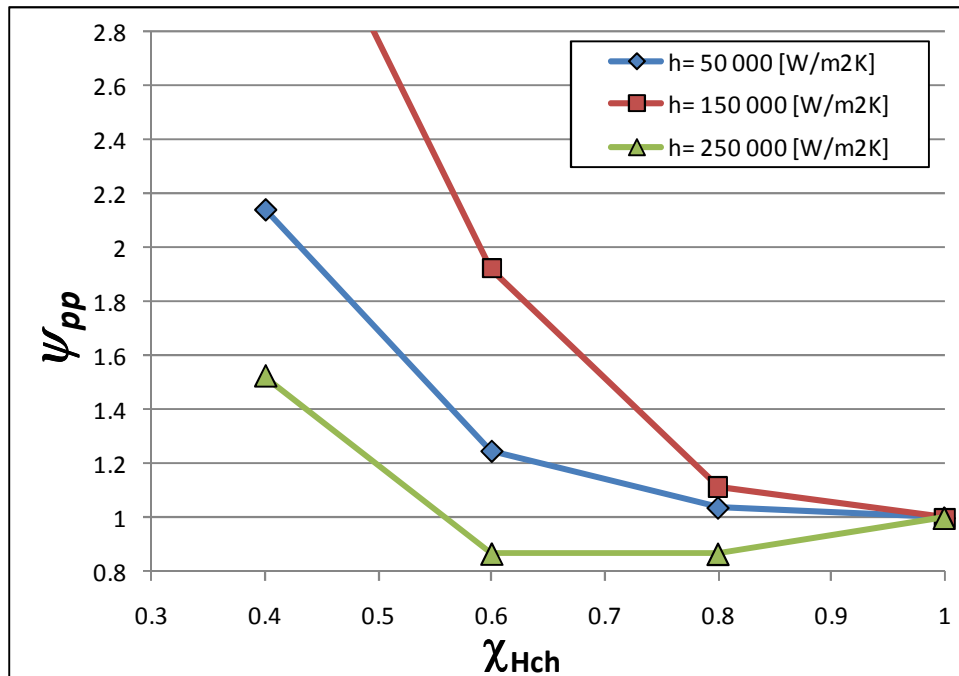


**Figure 3-11. Effect of fin and microchannel height ( $H_{ch}$ ) on pumping power at heat transfer coefficients of 50,000 W/m<sup>2</sup>K, 150,000 W/m<sup>2</sup>K and 250,000 W/m<sup>2</sup>K**

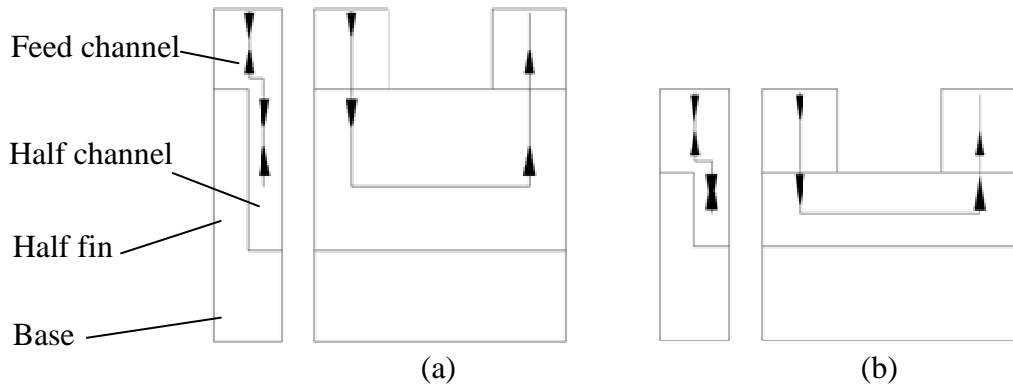


**Figure 3-12. Schematic of flow and a typical streamline for (a) high channel height (b) low channel height FFMHS configuration**

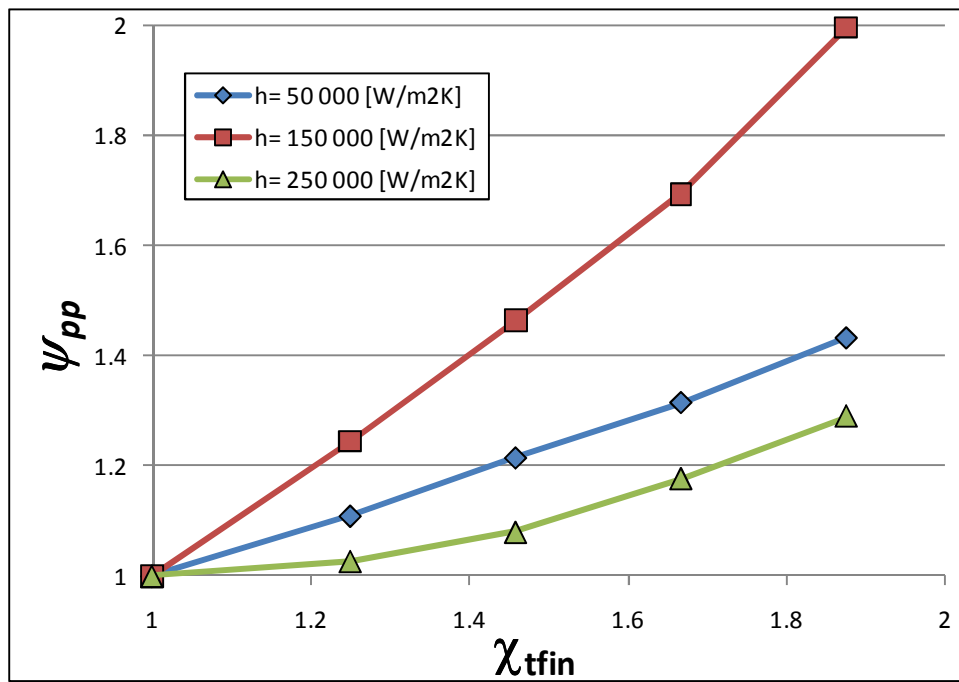


**Figure 3-13. Effect of fin thickness ( $t_{fin}$ ) on pumping power at heat transfer coefficients of 50,000 W/m<sup>2</sup>K, 150,000 W/m<sup>2</sup>K and 250,000 W/m<sup>2</sup>K**

The effect of fin thickness on pumping power is shown in Figure 3-13. Increasing the fin thickness will decrease the fin aspect ratio, will increase the fin efficiency and will decrease the flow area per unit base heat sink area. Therefore, a larger amount of fluid needs to pass through the microchannels to remove more heat

and to keep heat transfer constant at selected constant values. The resulting effect is a monotonic and almost linear increase in pumping power with increased fin thickness. An interesting observation seen in both Figure 3-11 and Figure 3-13 is that the pumping power increase for the intermediate heat transfer coefficient of 150,000 W/m<sup>2</sup>K is significantly higher than the values for 50,000 W/m<sup>2</sup>K and 250,000 W/m<sup>2</sup>K at the same  $\chi_i$  values. This trend results from the beneficiary effects of increase in mass flux by decreasing the fluid temperature close to the outlet region of the microchannel. For example, consider the fluid temperature variations calculated at fixed heat transfer coefficients shown in Figure 3-8 (a),(b) and (c). Here, going to higher heat transfer coefficients an increase in mass flow rates was required. For high mass fluxes (Figure 3-8 (c)) the fluid temperature that exits the microchannel is very close to the inlet temperature, therefore a moderate increase in mass flux will have a negligible impact on fluid temperature distribution. On the other hand, at low mass fluxes (Figure 3-8 (a)), there is a significant fluid temperature variation in the microchannel and a moderate increase in mass flux will have a significant impact on total heat transfer. The increase in fluid velocity will create higher temperature differences at microchannel outlet region and will decrease the less efficient heat transfer areas close to the microchannel bottom. When the channel height decreases or fin thickness increases, to balance the increase in heat dissipation and to keep the heat transfer coefficients at desired constant values, the mass flux in the microchannel needs to increase. This increase in mass flux in turn, will enhance the heat transfer efficiency much more significantly at low  $h$  values, when compared to high  $h$  values. This additional benefit in heat transfer will require less pumping power increase at

$h=50,000 \text{ W/m}^2\text{K}$ , resulting in  $\chi_i$  values ending in intermediate region between curves of  $h=150,000 \text{ W/m}^2\text{K}$  and  $h=250,000 \text{ W/m}^2\text{K}$ .

### **3.4.3. Effect of Microchannel Width**

Varying the microchannel width while keeping other parameters constant has a significant effect on both heat transfer coefficient and pumping power. In fact, heat transfer coefficients and pumping power values conflict when the microchannel width is changed. A heat sink design with smaller microchannels can benefit from the increase of local heat transfer coefficients as it scales down. However the consequent decreases in the ratio of flow-area per unit heat-sink base area and the smaller hydraulic diameters are the parameters that decrease the heat sink performance. The variation of pumping power rate with microchannel width is shown in Figure 3-14. Here, the trend of pumping power rate curves is significantly dependent on the heat transfer coefficient.

At low heat transfer coefficients ( $50,000 \text{ W/m}^2\text{K}$ ), a decrease in channel width has a continuously increasing trend on pumping power rate. Here the flow rate is relatively low and the fluid temperature will rise rapidly along the channel. Most of the heat will be transferred in a small region close to the microchannel entrance, while the end part will not contribute much due to the relatively low temperature difference, similar to Figure 3-8 (a) and Figure 3-9 (a). Therefore, decreasing the microchannel width and hydraulic diameter will increase the local heat transfer coefficients, but will have little or negligible effect on overall heat transfer coefficient due to the small temperature differences between liquid and heated wall. On the other

hand, the increase in pumping power due to the decrease in hydraulic diameter will have a more dominant effect and will further increase the pumping power.

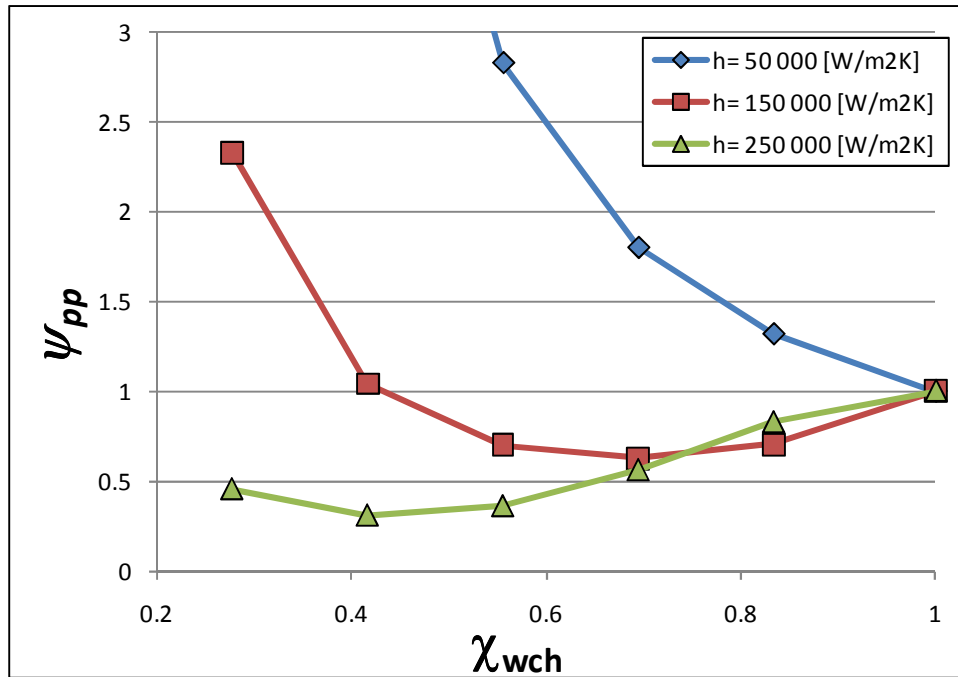


**Figure 3-14. Effect of microchannel width ( $w_{ch}$ ) on pumping power at heat transfer coefficients of 50,000 W/m<sup>2</sup>K, 150,000 W/m<sup>2</sup>K and 250,000 W/m<sup>2</sup>K**

The opposite effect is dominant for high heat transfer coefficients. For a constant heat transfer coefficient of 250,000 W/m<sup>2</sup>K decreasing the channel width has a significant positive effect on pumping power, continuously decreasing it up to 60%. The local increase in heat transfer is much more effective here, where the flow rate is high and the rise in fluid temperature along the microchannel is less. Therefore, much less fluid needs to flow through the microchannels to compensate for the pressure increase due to hydraulic diameter and the lower flow area per unit base area. It is clear, however, that at a given heat transfer level, a further reduction in channel width

will create very small gaps and flow areas, and pumping power will eventually rapidly increase.

#### **3.4.4. Effect of Inlet and Outlet Feed Channel Widths**

The variations of the rate of pumping power per unit area with changes to inlet and outlet feed channel widths are given in Figure 3-15 and Figure 3-16, respectively. Changes in feed channel widths have a significant impact on both pumping power and heat transfer. As the inlet feed channel width decreases, the reduced inlet flow area will decrease inlet hydraulic diameter and therefore the inlet flow resistance will increase. On the other hand, the reduction in feed channel will reduce the base area of the unit cell and therefore the total heat input will decrease, requiring less heat to be cooled. This in turn will decrease the fluid temperature increase along the microchannel, and the end parts of the heat sink will work more efficiently due to the increased temperature difference between the microgrooved surface and working fluid. Another benefit of decreasing feed channel width may be the decrease in flow length which will decrease the characteristic flow length, and flow resistance. Interestingly, increasing the inlet and outlet feed channel widths at low to intermediate heat transfer coefficients of  $50,000 \text{ W/m}^2\text{K}$  and  $150,000 \text{ W/m}^2\text{K}$  have little effect on pumping power, while decreasing the width at the same values creates a sudden increase in pumping power rate. Further reductions in the feed channel width will eventually create a rapid increase in pumping power rate due to the excessive pressure drop caused by the inlet area restriction.

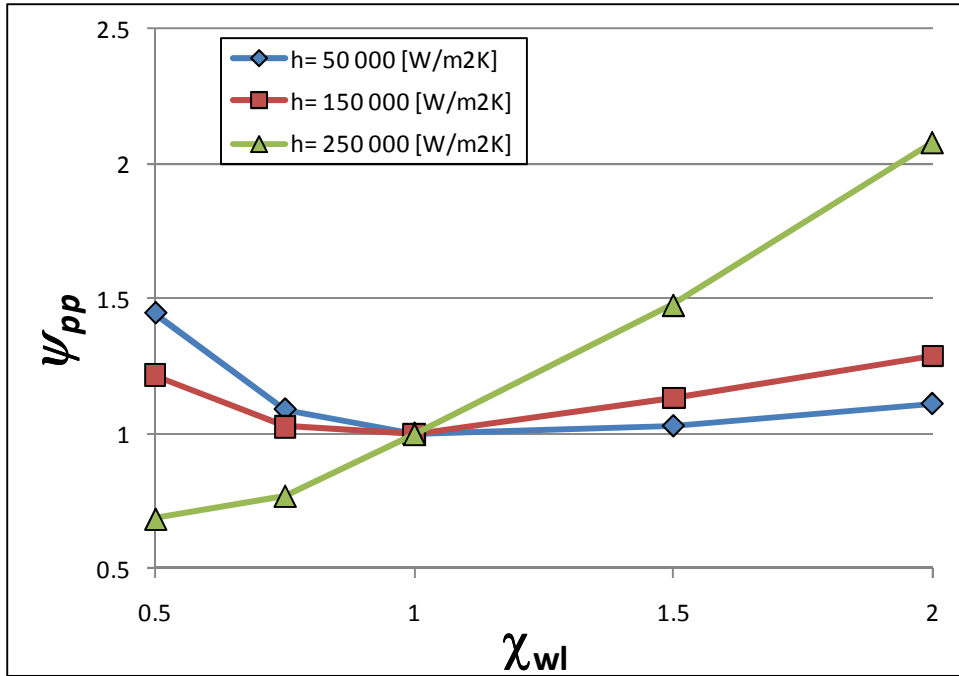


**Figure 3-15.** Effect of inlet feed channel width ( $w_l$ ) on pumping power at heat transfer coefficients of 50,000 W/m<sup>2</sup>K, 150,000 W/m<sup>2</sup>K and 250,000 W/m<sup>2</sup>K

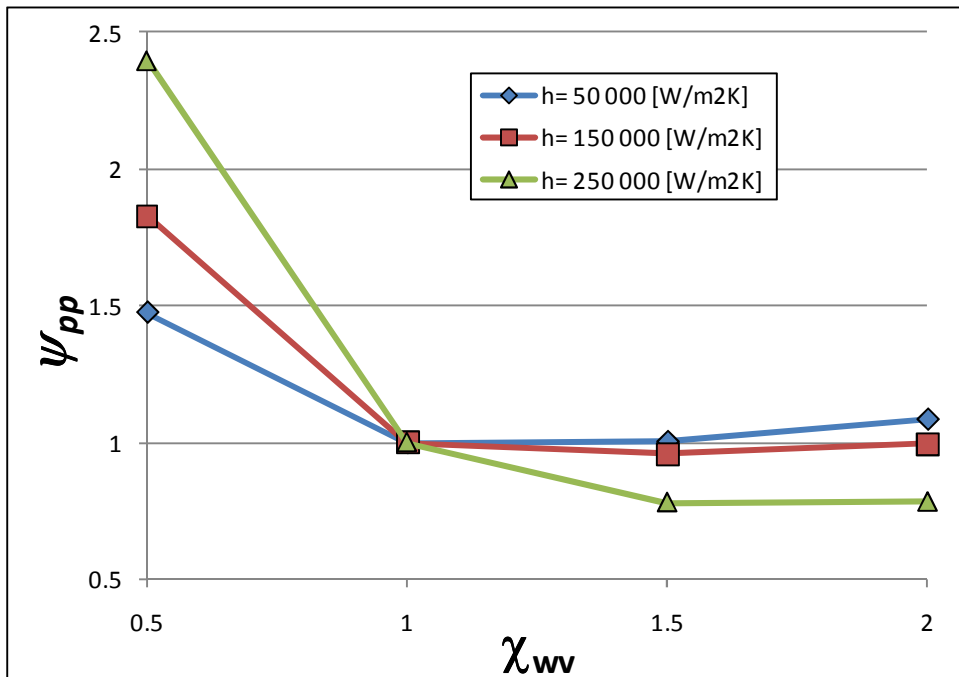


**Figure 3-16.** Effect of outlet feed channel width ( $w_v$ ) on pumping power at heat transfer coefficients of 50,000 W/m<sup>2</sup>K, 150,000 W/m<sup>2</sup>K and 250,000 W/m<sup>2</sup>K

At a high heat transfer coefficient of  $250,000 \text{ W/m}^2\text{K}$  the pumping power shows a different trend with respect to variations in the inlet and outlet feed channels. Here, decreasing the inlet feed channel width has the beneficial effect of decreasing the pumping power significantly, while decreasing the outlet feed channel width produces a continuous rising trend in the pumping power curve. Again, the reduction in fin efficiency at the inlet regions has a negative effect on heat sink performance, and therefore the heat sink reduces this effect by decreasing the fin tip area under the inlet feed channel and increasing the heat transfer area close to the end of the channels under the outlet feed channel, where the fin efficiency is significantly higher.

### **3.4.5. Effect of Microchannel Length**

In the study of microchannel length effect, the dimension of inlet and outlet feed channels were kept constant and only the manifold length was varied. The case of  $\chi_{Lch} = 1$  corresponds to a manifold thickness of  $t_{man} = 0.4 \text{ mm}$ . In general, short manifolds are desired for typical FFMHS designs as suggested by (Copeland, 1995a), (Ryu et al., 2003) and (Copeland et al., 1997). Decreasing the manifold thickness will improve the heat sink performance by decreasing the flow length and therefore the flow resistance. Similarly, the base area will decrease, and less cooling will be required to cool the heat generated in a single FFMHS unit cell. Also shortening the channel will increase the effectiveness range of the inlet regions associated with high local heat transfer coefficients.

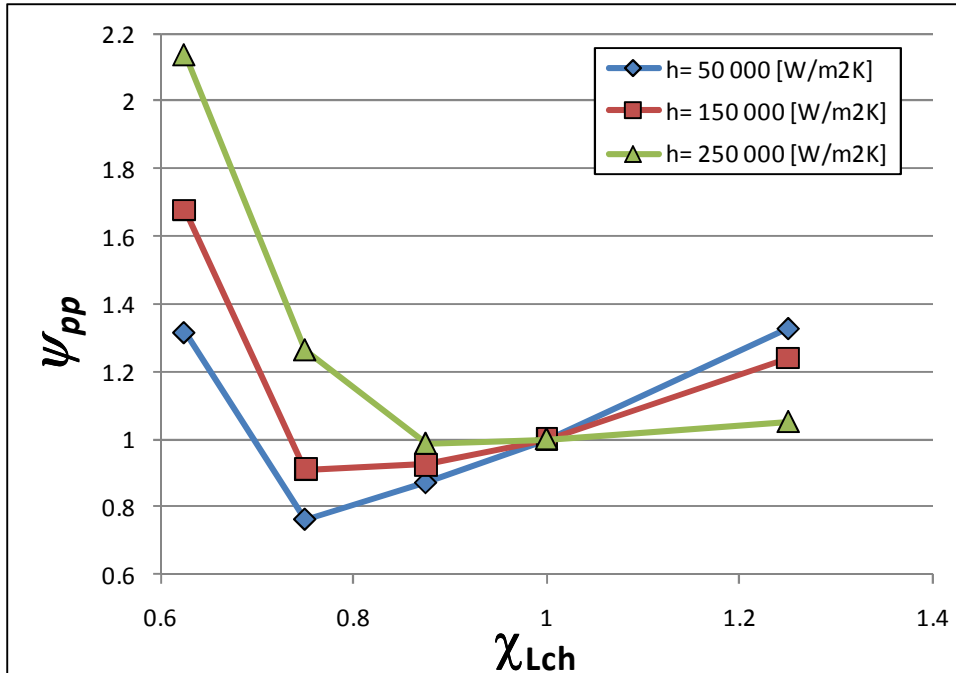


**Figure 3-17. Effect of microchannel length ( $L_{ch}$ ) on pumping power at heat transfer coefficients of 50,000 W/m<sup>2</sup>K, 150,000 W/m<sup>2</sup>K and 250,000 W/m<sup>2</sup>K**

Here, there are two factors that limit the performance improvement resulting from the decrease of the manifold thickness. First, as the channel becomes shorter, the flow resistance of flow passing the channel through different pathlines will be significantly different. More specifically, the length of a pathline located close to the top of the microgrooved surface will be much shorter compared with a pathline passing all the way down to the bottom of the microchannel. The resulting difference will facilitate creation of a bypass of fluid in the regions close to the top of the microgrooved surface and the feed channels, and it will require an increase in flow rate to increase the fluid inertia enough to be pushed to the bottom of the channel. The bypass effect is clearly shown in Figure 3-17, where decreasing the microchannel length more than 25% forces the heat sink to go to higher flow rates to achieve desirable heat transfer coefficients, therefore increasing the pumping power. The

second limitation is related to the fabrication and manufacturing of manifolds. Since the coupling of microgrooved surfaces and the manifold system was designed to be implemented using compression forces, the manifolds should be structurally sound and also easy to manufacture. Fabricating micron size manifolds is thus not always practical.

### **3.4.6. Effects of Microgrooved Surface Base Thickness and Manifold**

#### **Height**

One particularly interesting parameter is the height/thickness of the microgrooved surface base ( $H_{base}$  shown in Figure 3-1). The base thickness does not affect the pressure drop and does not conflict with heat transfer coefficient. In fact, it contributes to additional thermal resistance to heat transfer from the bottom of the microgrooved surface to the fins and it is generally desired to design it to be as thin as possible, especially for high heat flux cooling applications. A possible increase in base thickness is usually considered only in applications where the surface temperature uniformity is important and adding extra material will increase the heat spreading through the base. The surface temperature uniformity was not selected as a parameter in this study, but resulting temperature variations will be reported in next chapter.

## **3.5. Conclusions**

A sample FFMHS geometry was first investigated numerically at different inlet flow conditions. It was found that the flow Reynolds numbers have a significant effect on both flow regimes and heat transfer characteristics. At low Reynolds

number flows, the fluid stratifies uniformly by creating a bypass zone between the inlet and outlet feed channels at the top of the microchannel. This effect in turn creates inefficient dead zones with low fluid circulation and low heat transfer. Increasing the Reynolds number reverses the velocity stratification, with the higher fluid core close to the bottom of the microchannel and with fluid recirculation zones close to the top part. The increase in fluid velocity also initiates secondary flows manifested in the forms of vortex pairs in the microchannel cross section. The vortices and flow impingement in turn reduce the convective thermal resistance and create local heat transfer maximums.

The effects of geometrical parameters on pumping power were analyzed for three different heat transfer coefficient values of 50,000 W/m<sup>2</sup>K, 150,000 W/m<sup>2</sup>K and 250,000 W/m<sup>2</sup>K. It was found that each geometrical parameter can affect the thermal performance in both positive and negative ways. Usually the change in geometrical parameters has conflicting effects on heat transfer and pressure drop, and an optimum point may exist at a specific flow condition. Here, the main difficulty in calculating optimal flow and geometrical conditions is due to the large number of parameters that affect the FFMHS performance. Therefore, the results of this study will be used in next chapter as a basis for selecting key optimization parameters and their lower and upper bounds.

## **CHAPTER 4: MULTI-OBJECTIVE OPTIMIZATION OF SINGLE-PHASE FFMHS**

This chapter discusses the optimization procedure for Force Fed Microchannel Heat Sinks (FFMHS). The chapter starts with an introduction to heat sink optimization and a description of the metamodeling and optimization algorithm and its implementation with a numerical Computational Fluid Dynamics (CFD) solver. Then the optimization procedure is applied for three different cooling technologies; Force Fed Microchannel Heat Sink (FFMHS), Traditional Microchannel Heat Sink (TMHS) and Jet Impingement Heat Sink (JIHS) for comparison purposes. A detailed analysis of the FFMHS metamodeling results and the effect of its variables on thermal performance is performed. The chapter concludes with a comparison between the investigated cooling technologies at their optimum designs.

### **4.1. Heat Sink Design and Optimization**

The design of heat sinks is a complicated process because the final thermal and hydraulic performance is dependent on many parameters such as geometrical dimensions, coolant fluid properties, flow conditions and heat sink material properties. Geometrical parameters can be channel dimensions through which the coolant fluid passes, extended surface dimensions such as rectangular fin thickness or pin fin diameter, and height or base-plate thickness. The coolant and material parameters depend on physical properties such as thermal conductivity, density, specific heat and fluid viscosity, and the flow condition that is generally specified as

the total fluid mass flux that passes through the heat sink. All those parameters are coupled, affecting performances of the heat sink and thus should be considered in the optimization.

TMHS for high heat flux cooling applications using liquid cooling have been investigated extensively since their early introduction by (Tuckerman & Pease, 1981). Several authors performed optimization studies by numerically and analytically modeling TMHS's with the objective of minimizing the overall thermal resistance (Khan, Culham, & Yovanovich, 2009), (Kandlikar & Upadhye, 2005), (D.-K. Kim, 2007), (S. J. Kim, 2004), (Dong Liu & Garimella, 2005), (Phillips, 1987), (Shao, Sun, & Wang, 2007). The analytically developed models have the advantage of eliminating the relatively time-consuming computational time and providing a functional form that can be easily implemented in any programming language. Along with simplifying assumptions, this method was successfully used in predicting heat transfer performance of TMHS's, and it was demonstrated by (Dong Liu & Garimella, 2005) that analytical models offer sufficiently accurate predictions for practical designs, while being straightforward to use. On the other hand, the CFD based numerical models have the advantage of being applicable to more complex geometries and being able to simulate advanced physical phenomena such as conjugate heat transfer between fluid and solid surfaces, temperature and pressure dependent properties, and turbulence modeling as well as transient flow modeling. The CFD based models are particularly useful in modeling, designing and predicting heat sink performances where traditional heat transfer and pressure drop correlations cannot be applied, such as complex unconventional geometries.

The complex geometry and flow field encountered in FFMHS's make it challenging to generate any analytical based models, and to date no such models have been published. At this point, CFD-based methods are more accurate and straightforward techniques to investigating FFMHS performance. Therefore, adopting a similar approach to that described in previous chapter, Fluent® was selected as the numerical solver for the optimization purposes. However, a direct implementation of CFD tools with any optimization algorithm can be prohibitively time expensive and not practical. As a practical solution at this point, Approximation Assisted Optimization (AAO) technique proved to be a successful candidate. AAO combines the advantages of CFD modeling with time efficient metamodeling methods.

## **4.2. Parametric CFD Simulation Interface**

Although AAO methods were developed to minimize the computational time, the number of CFD simulation evaluations that need to be performed is still large, mostly in the order of 100 runs. Manual mesh generation and numerical simulation for each case is not practical and may require continuous user interaction. This problem was eliminated by automating the process with the help of Parametric CFD Simulation Interface (PCFDSI). The code of PCDSI was written in Matlab and serves as a function that accepts optimization variables as inputs and generates the desired objective functions, temperature distribution, velocity field and wall heat flux distribution.

The flow diagram of PCFDSI is shown in detail in Figure 4-1. The function accepts one set of variables as input. These variables, combined with constant parameters defined in the function, set the problem. In other words, the geometrical

dimensions, flow input conditions, material properties, grid distribution, boundary conditions and CFD solution procedure are set for the given input conditions. Based on these set values, the PCFDSI function creates Fluent® and Gambit® script files, also known as journal files. The journal file created for Gambit® contains commands for building the computational geometry, meshing the domain and setting up boundary conditions. The Fluent journal file incorporates command syntax that is used for mesh import, grid checking, scaling, initializing the energy model, applying the inlet and outlet boundary condition values, controlling and initializing the post-processing of the results, and saving the case and data files.

The next process is initialization of Gambit® with the journal file created, which in turn generates the mesh file of the computational domain. After the end of this process, Fluent® is initiated and run with the input of the journal file and mesh file. The numerical solution procedure is performed at this stage, which mainly determines the period of a PCFDSI function evaluation. After the numerical convergence is achieved, post-processing is performed by generating the desired data such as velocity, temperature and pressure values at specified locations in the computational domain. Post-processing was also used to validate the numerical convergence in case of reaching maximum iteration number. (O. A. A. Abdelaziz, 2009) suggested tracking static pressure difference for a given number of last iterations and evaluating the solution by comparing standard deviations of this value.

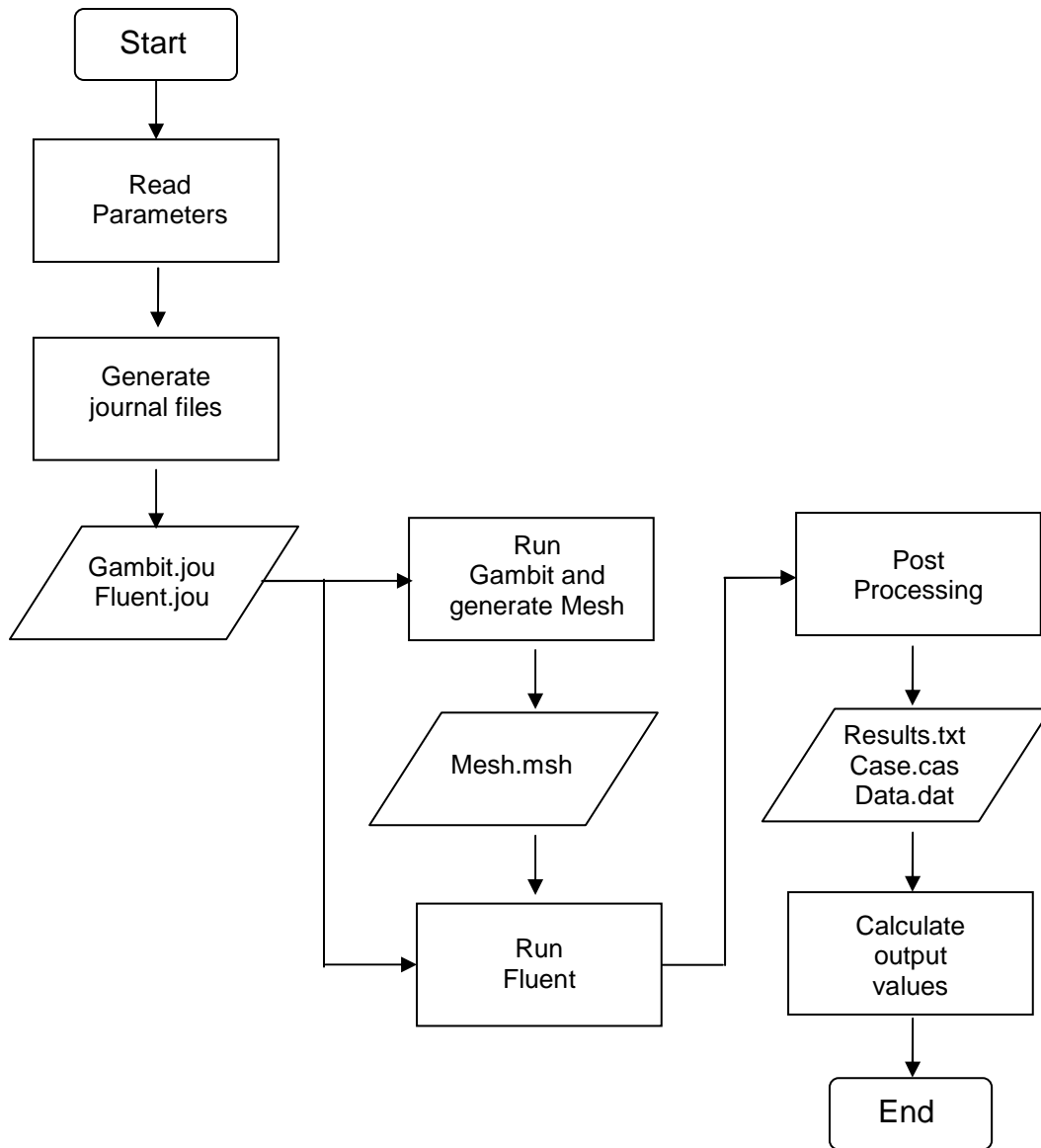


**Figure 4-1. Flow diagram for Parametric CFD Simulation Interface**

In this study, the total pressure differences between the inlet and outlet boundaries and average base temperatures for the last recorded 100 iterations were recorded. In the case reaching the total iteration number, the standard deviations for these values were calculated and evaluated. The case was accepted if standard deviation values were less than 0.5%. Finally, the post-processing data were evaluated to generate the desired outputs, which were the objective functions used for

optimization, effective heat transfer coefficient and pumping power per unit base area.

### **4.3. Approximation Assisted Optimization**

Approximation is the process that uses metamodels (also known as surrogate models) to decrease the computational load and numerical evaluation time of CFD solvers. The reason approximation methods are particularly useful in optimization using CFD simulations is related to their ability to decrease the number of evaluations of design points required to achieve the optimum designs by utilizing metamodels. The metamodels are functions or subroutines that mimic the response of the simulation model based on simulated sampling data. They are cheap in terms of computational time, and a large selection of available metamodels is available for this purpose.

There are two types of responses in the approximation methods, the real response and the predicted response. The real response is the true value resulted from an experiment or CFD numerical simulation, while the predicted response is the response of the metamodel. The real responses are obtained in the Design of Experiment (DOE) stage, where the design space is sampled and the results in turn are used in metamodels to generate the predicted results. The obtained metamodel is then validated for goodness assessment and finally used in optimization.

The steps involved in AAO are individually discussed below. For DOE data sampling process the Space Filling Cross Validation Tradeoff method developed by (Aute, Abdelaziz, Azarm, & Radermacher, 2008) and (O. Abdelaziz, Aute, & Radermacher, 2009) was used. Kriging was used for metamodeling and Multi

Objective Genetic Algorithm (MOGA) was applied for optimization of the metamodel.

#### **4.3.1. Design of Experiment**

The sampling process is performed in the DOE stage and can be based on several strategies. (O. A. A. Abdelaziz, 2009) summarized and reviewed the DOE methods used in literature. There are three different methods of sampling: classical methods, space filling methods and adaptive methods. Classical methods are based on sampling the majority of the points from boundaries while leaving few sampling points in the center of the design space. Space filling methods tend to fill out the design space more uniformly based on a specific algorithm. Adaptive methods select the new samples by processing and modeling the available previously selected samples and by understanding the behavior of the model. While classical models and space filling methods offer a time-effective method of sampling, they do not capture the important changes and trends, and the metamodels based on these methods are usually less accurate. Adaptive methods on the other hand, can distribute the sampling more efficiently by increasing the sampling at regions with high gradients and large variations while coarsening the samples at regions where less variation is observed.

In this study, a Matlab computer code developed at University of Maryland by a joint effort of Professor Shappour Azarm and Professor Reinhard Radermacher's research groups was implemented for DOE sampling (Aute et al., 2008), (O. Abdelaziz et al., 2009). The algorithm and computer code uses a two-step combined process of the space filling and adaptive method for sampling. In the first step, the

design space is sampled using a space filling method, namely Maximum Entropy Design (MED). The MED principle is based on generating a natural probability distribution in the design space where the entropy is a measure of the amount of information contained in the distribution of a sampling dataset (Shewry & Wynn, 1987), (Johnson, Jones, & Fowler, 2008). Since MED is based on a probability distribution, it does not require any previous sampling knowledge. The second step of the DOE sampling consists of an adaptive methodology. The sampling technique called Multi-response Space Filling Cross Validation Tradeoff (MSFCVT) selects new samples based on the tradeoff between cross validation error and the space validation error. Here, a multi-objective optimization is applied to generate the tradeoff between space filling and cross validation. A more detailed explanation of the MED, MSFCVT methods and the DOE sampling algorithm can be found in (O. A. A. Abdelaziz, 2009).

#### **4.3.2. Metamodeling**

Metamodeling is defined as the process of predicting unobserved points based on previously observed points. In different disciplines metamodels may have different names: response surface, compact model or emulator. (Van Beers, 2005). Classical metamodeling techniques use approximation methods based on least square fitting after the DOE stage. This approach was found to be not practical because it requires the fitting function type to be known as a priori. The solution for obtaining the right function type requires an iterative process and is time-consuming. At this point, stochastic techniques have the advantage of not having a functional form, which makes them more appropriate to be used in a design space with a large number of

parameters and samples. Among these stochastic techniques, Kriging has been successfully used in metamodeling of different engineering optimization designs (Sacks, Welch, Mitchell, & Wynn, 1989), (Park, Oh, & Lim, 2006), (O. A. A. Abdelaziz, 2009).

Kriging metamodeling is very suitable with nonlinear problems and show a high degree of flexibility. Kriging method approximates the non-observed points by using spatial correlation information of known points. The formulation consists of a combination of linear regression and departure estimation (Park et al., 2006):

$$y(x) = f(x) + z(x) \quad (4-1)$$

where  $x$  is the design variable,  $y(x)$  represents the unknown function of interest,  $f(x)$  is the known linear regression function, and  $z(x)$  is the departure represented by a stochastic function with mean zero and variance and nonzero covariance. The selection of the regression function and the stochastic correlation is generally dependent on the problem of interest, and the appropriate functions can be selected by investigating their fitness to the metamodel. The DACE® Toolbox for Matlab® developed by (Lophaven, Nielsen, & Søndergaard, 2002) provides Kriging metamodeling by incorporating a series of optional linear regression functions and stochastic correlations. This toolbox was used in this work due to its programming flexibility and robust performance. The variance associated by Kriging can be useful in predicting the space filling criteria. For example, large spacing between neighboring points will create large variance and therefore a large uncertainty in response.

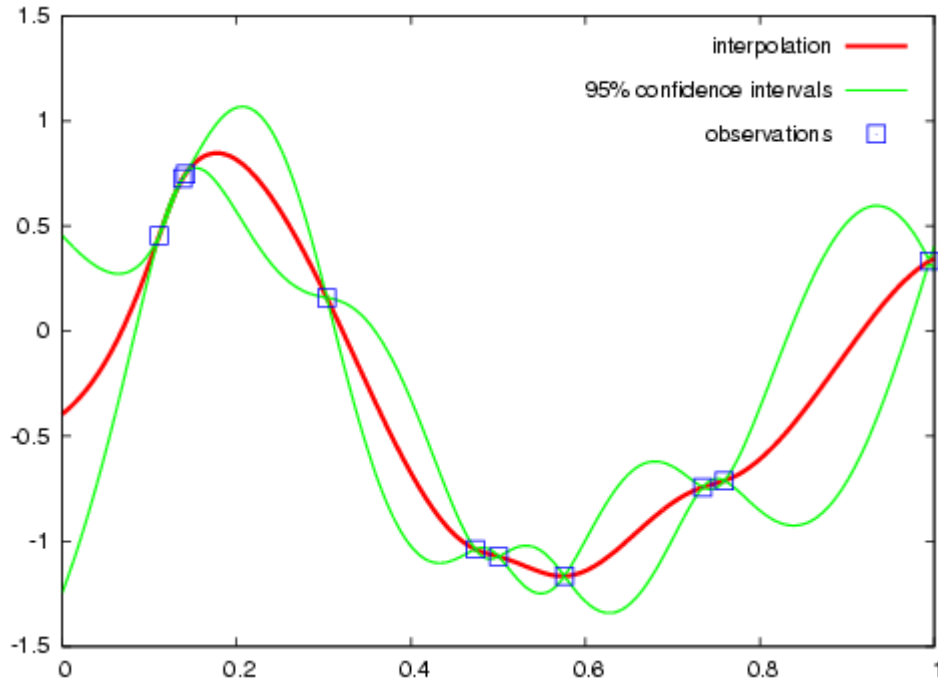


**Figure 4-2. Example of Kriging (adopted from (Wikipedia®, 2009))**

A simple Kriging example based on one parameter is shown in Figure 4-2. Kriging interpolation shown by red line was applied for several observed points, shown in blue squares. The 95% confidence interval shown between the green lines becomes smaller in regions where spacing of observed data is small and increases between points with large spacing.

### 4.3.3. Metamodeling Validation

There is a tradeoff between the sampling number and the accuracy of the metamodel. A metamodel with a large number of samples will predict the desired points with less average error, but it will be time expensive in the DOE stage. The desired metamodel accuracy can be achieved by testing the metamodel for randomly selected points in the design space and by estimating the error. In case where the errors are high, the DOE step needs to be run for additional sampling. A few

iterations of trial and error may need to be run until the errors drop below a desired value. The Relative Root Mean Squared Error (RRMSE) and Relative Maximum Absolute Error (RMAE) are calculated as:

$$RRMSE = \sqrt{\frac{1}{n} \sum_{i=1}^n e_i^2} \quad (4-2)$$

$$RMAE = \max(|e_i|) \quad (4-3)$$

where

$$e_i = \frac{y(x_i) - \hat{y}(x_i)}{y(x_i)} \quad (4-4)$$

#### 4.3.4. Multi-Objective Optimization

Multi-objective optimization is the process of minimizing or maximizing several objective functions simultaneously with several equality and/or inequality constraints. At this point, the Multi Objective Genetic Algorithm (MOGA) offers several attractive features and has been applied successfully to several engineering optimization problems (Xie, Sunden, & Wang, 2008), (Hilbert, Janiga, Baron, & Thévenin, 2006), (Peng & Ling, 2007), (O. A. A. Abdelaziz, 2009). The main advantage of MOGA is that it always searches for the global minimum, and unlike gradient search techniques, it is less prone to get stuck at local minimum points. It is also very successful in solving combined continuous and discrete mixed problems.

MOGA is a model of the machine learning process, which mimics nature's evolutionary process. The model creates a population of points in the design space and characterizes every point by encoding it with a series of several genes. Then the algorithm manipulates the decision-making genes using operators such as mutation

and crossover to generate new design populations with the hope of getting better genes that are closer to the global minimum. The process is iteratively continued for every step (evolution). More detailed information about MOGA can be found in (Goldberg, 1989) and (Mitchell, 1998).

#### **4.4. Selection of Optimization Parameters**

The selection of the right parameters for optimization needs to be clarified before continuing, since this procedure has several implications on the overall optimization process. There is a tradeoff between the number of parameters and computational time. In fact, the real challenge of an FFMHS optimization is the dependence of thermal performance on the large number of geometrical parameters, each affecting the heat transfer and pressure drop. The geometry of the computational domain shown in Figure 3-1 consists of eight possible geometrical parameters: microchannel width  $w_{ch}$ , microchannel and fin height  $H_{ch}$ , fin thickness  $t_{fin}$ , base material thickness  $H_{base}$ , inlet feed channel width  $w_l$ , outlet feed channel width  $w_v$ , microchannel length  $L$  and feed channel/manifold length  $L_{man}$ . These parameters together with one flow parameter add up to a total of nine optimization variables. A model that includes many variables is more realistic. On the other hand, the large number of parameters can also inconveniently increase computational time and make the optimization process not practical. A more feasible solution for this problem is to select only the parameters that affect the objective functions the most, and setting the parameter number based on computational resources. The total of nine optimization variables is very high for the scope of this work, and therefore comparative analysis

needed to be done to identify the important ones. In terms of parameters numbers, the practical number was selected based on previous reported experience. For example, (O. A. A. Abdelaziz, 2009) performed multi-objective AAO for a heat exchanger model consisting of six variables and two objective functions. The model was numerically solved on a multi-cluster super computer. Therefore it was realistic to select five optimization parameters for an optimization done using a single PC with a dual core processor.

The most important parameters selected for this study were based on the parametric numerical study performed in the previous chapter and considering the fabrication limitations of microgrooved surfaces and manifold systems. The selected five optimization parameters were: channel height  $H_{ch}$ , channel width to fin thickness ratio  $w_{ch}/t_{fin}$ , inlet feed channel width  $w_l$ , outlet feed channel width  $w_v$  and Reynolds number. The fin aspect ratio  $H_{ch}/t_{fin}$  was maximized by selecting a value of 10 as indicated by Equation (3-15). Although decreasing the fin aspect ratio may have a positive impact on FFMHS performance at high heat transfer coefficients, as shown in Figure 3-11, the effect is small and not present for low to medium heat transfer coefficients. The manifold thickness was selected constant at  $t_{man} = 0.4$  mm. This value corresponds to  $\chi_{Lch} = 1$  in Figure 3-17 where the pumping power has a decreasing trend for all three cases. A smaller manifold thickness has the potential to improve the heat sink performance, but fabrication of channels with such small features is not practical. Finally, the base thickness of the microgrooved surface  $H_{base}$  should be as small as possible to minimize the thermal resistance. Therefore the

minimum applicable and practical base thickness of  $H_{base} = 0.4$  mm was selected.

Based on these analyses the optimization process was formulized as follows:

maximize  $h$

minimize  $P''_{pump}$

subject to:

$$0.2 < H_{ch} < 1.0 \text{ [mm]}$$

$$0.2 < w_{ch} / t_{fin} < 1.5$$

$$0.1 < w_l / 2 < 0.4 \text{ [mm]}$$

$$0.1 < w_v / 2 < 0.4 \text{ [mm]}$$

$$10 < Re < 400$$

$$H_{ch} / t_{fin} = 10$$

$$t_{man} = 0.4 \text{ [mm]}$$

$$H_{base} = 0.4 \text{ [mm]}$$

The Reynolds number was selected to be lower than the critical Reynolds number of 2300 for internal flows to avoid using turbulence models. It should be noted that by definition from Equations (3-9)-(3-11) the Reynolds number is defined for the straight microchannel flow, while the velocities close to the inlet and outlet region of the microchannel can be higher, depending on geometrical heat sink configuration. Therefore selecting a Reynolds number much smaller than the critical

value will also ensure that laminar flow is present in these regions. All other computational procedures were performed similarly to those discussed in Section 3.3.

#### **4.5. Single-Phase Optimization Results of FFMHS**

The sampling distribution of the objective functions in the design space is shown in Figure 4-3. The first objective function of pumping power per unit heat sink base area is shown on the x-axis, while the second objective function of effective heat transfer coefficient is shown on the y-axis of the graph. Each point represents a single FFMHS design in the design space, based on the selected input variables. A total of 520 sample points was calculated, for which 200 points were selected based on MED and the remaining 320 points were selected based on adaptive DOE algorithms. The total computational run-time was about 125 hours on a PC with an Intel Pentium D 3.4 Ghz processor and 2GB of memory. As mentioned before, the sampling process is automated and does not require any user interaction; therefore, the time required for this stage is solely dependent on computational capabilities.

The metamodeling was performed based on Kriging technique. Since the metamodel is a regression method, it needs to be validated before being used in MOGA. The basic idea in metamodel validation is to randomly select several points in the design space and then to check the metamodel prediction goodness of selected points. For this purpose 100 design points were selected randomly and the error estimation was performed as discussed in Section 4.3.3. The distribution of objective functions for random points in the design space is shown in Figure 4-4. For effective heat transfer coefficients, the metamodel was able to predict the selected random points with a RRMSE of 1.93 and RMAE of 3.47. For pumping power, the

metamodeling yielded RRMSE and RMAE values of 4.43 and 13.33, respectively. In general, it was observed that prediction of pumping power values always resulted in higher error values comparing to prediction of effective heat transfer coefficients. This characteristic is the result of pressure drop being more strongly dependent on hydraulic diameter and showing a large variation in the design space. On the other hand, the heat transfer coefficients are relatively less dependent on flow rate and hydraulic diameter, and so the variation is much less.

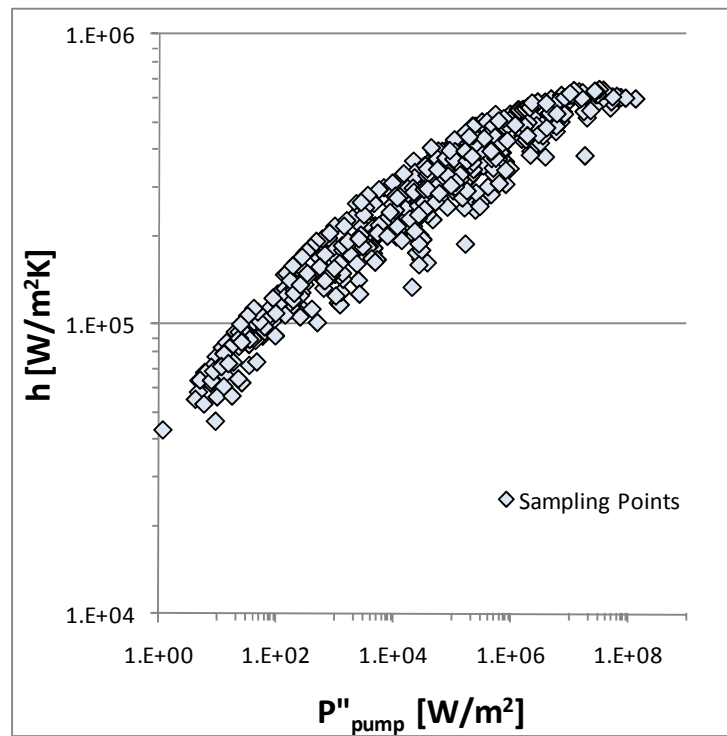


**Figure 4-3. Distribution of objective functions for sampling points obtained for FFMHS optimization study**

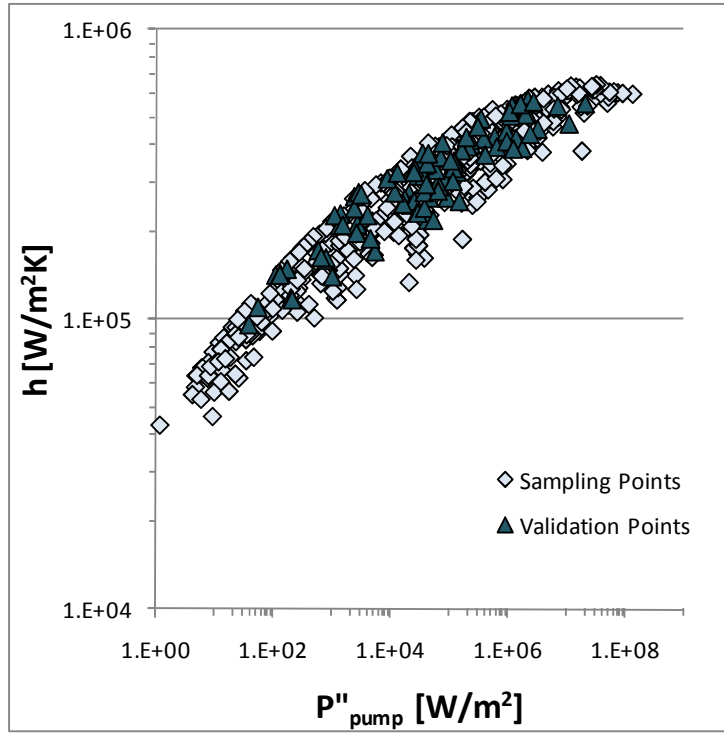


Figure 4-4. Distribution of objective functions for sampling and validation points obtained for FFMHS optimization study

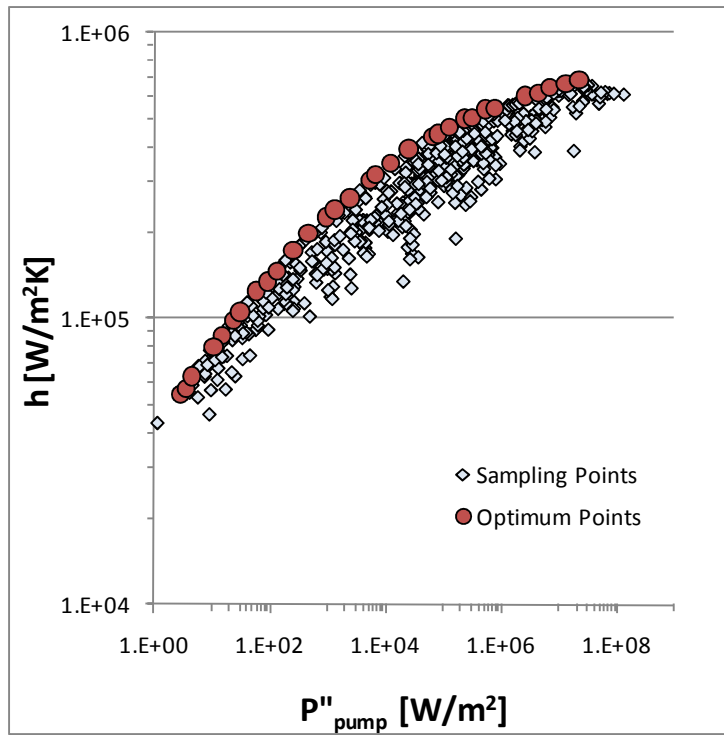


Figure 4-5. Distribution of objective functions for sampling and optimal points obtained for FFMHS optimization study

The last step in the optimization procedure is applying MOGA to the metamodel. The resulting optimum points are shown in Figure 4-5. It is important to note that since the optimization process is multi objective, the resulting optimum solution is a curve and not a single design point. The solution curve is sometimes called as the Pareto frontier and represents the set of solution design points that can yield the maximum heat transfer at any given pumping power value. As shown in the figure plotted on a log-log scale, the Pareto curve shows a linear trend from low to medium pumping power levels, while it starts to bend at higher pumping powers. The resulting geometrical variations at optimum points will be discussed in the next section.

The optimum design points can be also verified by calculating the actual objective functions using Fluent and comparing them with the metamodel optimum results. The RRMSE and RMAE values for heat transfer coefficients were calculated as 1.63 and 4.36 and for pumping power as 4.36 and 9.54, respectively.

#### **4.5.1. Analysis of Optimum FFMHS Geometry**

The variation of optimal geometrical and flow parameters with pumping power is shown in Figure 4-6 to Figure 4-13. The general trend of optimum solutions can be summarized as follows. For low heat transfer coefficients and pumping powers the optimum geometry is achieved with high fin height (Figure 4-7), high channel width (Figure 4-8), high inlet/outlet feed channels (Figure 4-9) and with low Reynolds number (Figure 4-6). Thus, to minimize pumping power, the channel flow area and hydraulic diameter should be enlarged and the flow velocity decreased. The relatively low flow velocities and high turn radii in the microchannel leads to Dean

numbers below 10 (Figure 4-6), which suggests that secondary flows are not present. Because of rapid fluid temperature rise along the microchannel, for low Reynolds number flows most of the heat is transferred at the very short inlet region where the fluid is at inlet temperature and the boundary layer is thin, and the end part of the microchannel contributes much less to heat transfer. Therefore, the largest surface temperature nonuniformity, defined as the difference between maximum and minimum temperatures, is expected at low Reynolds number flows, as shown in Figure 4-12. But even for the worst case, due to the high conductivity of copper and short length of the microchannels, a large amount of heat can be conducted in the longitudinal direction, creating a heat spreading. The maximum base surface temperature nonuniformity can be kept below 2.5 °C.

On the other hand, when searching for optimum designs that can yield higher heat transfer coefficients, the trend is reversed. All geometrical parameters (fin height, microchannel width, inlet/outlet width channels) tend to decrease when both Reynolds number and Dean number are increased exponentially. The increase in local heat transfer coefficient is achieved by decreasing the microchannel width, and therefore the hydraulic diameter. This will lead to an increase in the microchannel surface area/volume ratio which will require higher flow velocities in order to prevent the rapid fluid temperature increase along the microchannel. To decrease the system pressure drop and to increase the heat sink flow area, the fin thickness is reduced, together with fin height, keeping a constant fin aspect ratio of 10. The inlet/outlet feed channel widths in turn will decrease to accommodate the change in fin height. This net effect is the formation of FFMHS designs incorporating microgrooved surfaces

with high fin density (Figure 4-10) and a high number of manifolds (Figure 4-11). Increasing the flow velocity and scaling down the geometry has a positive impact on surface uniformity, as shown in Figure 4-12. The increase in heat transfer efficiency and shorter microchannel length significantly decreases the temperature gradients, creating a more uniform surface temperature distribution.

Interestingly, the Dean numbers evaluated for the optimum points show that the secondary flows are effective only at very high flow velocities with all Dean numbers remaining below  $De = 50$ . This may suggest that although secondary flows have a positive effect on enhancing the heat transfer, the resulting excess pressure drop effect is counter-balancing the performance. Therefore, the heat transfer enhancement for optimum designs is achieved mainly by scaling down the hydraulic diameter and increasing the local heat transfer coefficient rather than increasing the microchannel width to benefit from secondary flow vortices.

Another important piece of information resulting from the optimization procedure is the effect of microgrooved surface fabrication limitation on the thermal performance. This can be clearly seen in Figure 4-7, where microchannel height values ( $H_{ch}$ ) are plotted versus pumping power. The  $H_{ch}$  values have monotonic decreasing trend until they reach the minimum value of 0.2 mm set by Equation (3-14). Further increasing the flow rates will force the microchannel height values to remain almost constant for the rest of the points. The microchannel width and fin thickness follow a similar trend, as shown in Figure 4-8. Both parameters look equal for most of the calculated range except at very low and very high pumping power

values. When fin thickness parameter hits the minimum value of 0.02 mm it starts a constant trend, allowing the microchannel width parameter to decrease further.

The variation of inlet and outlet feed channel widths are given in Figure 4-9. As seen, both parameters have a monotonic decreasing trend, but they are not equal, with outlet feed channel width being slightly higher than inlet feed channel width. At the inlet to the microchannel, the fin tip temperature is usually much lower than the rest of the heat sink, similar to the case shown in Figure 3-10. Therefore the local fin efficiency may drop substantially, favoring the optimization tool to go to lower inlet feed channel widths.

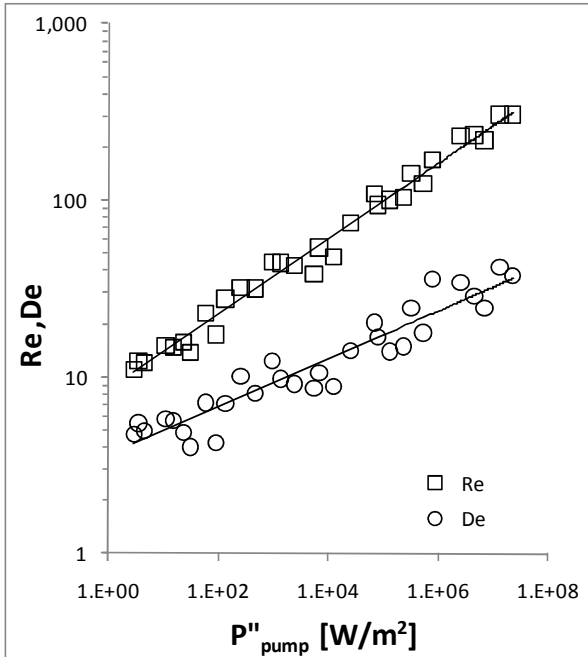


**Figure 4-6. Variation of Reynolds and Dean numbers with pumping power**

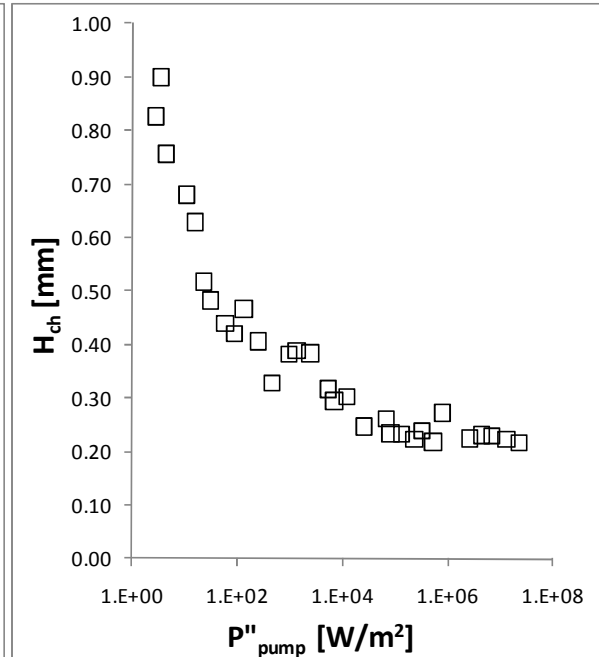


**Figure 4-7. Variation of microchannel height with pumping power**

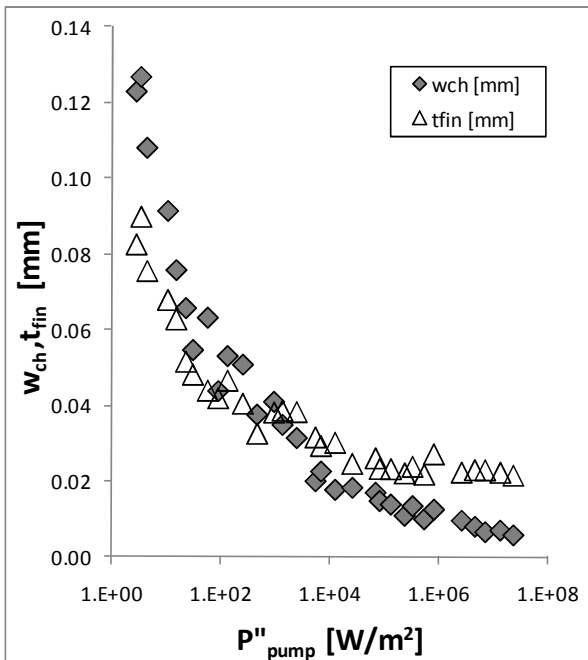


**Figure 4-8. Variation of microchannel width and fin thickness with pumping power**

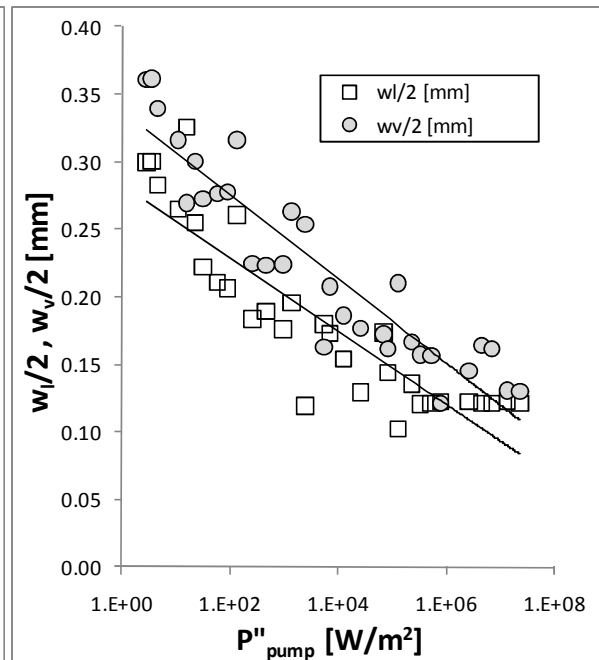


**Figure 4-9. Variation of inlet and outlet feed channel widths with pumping power**

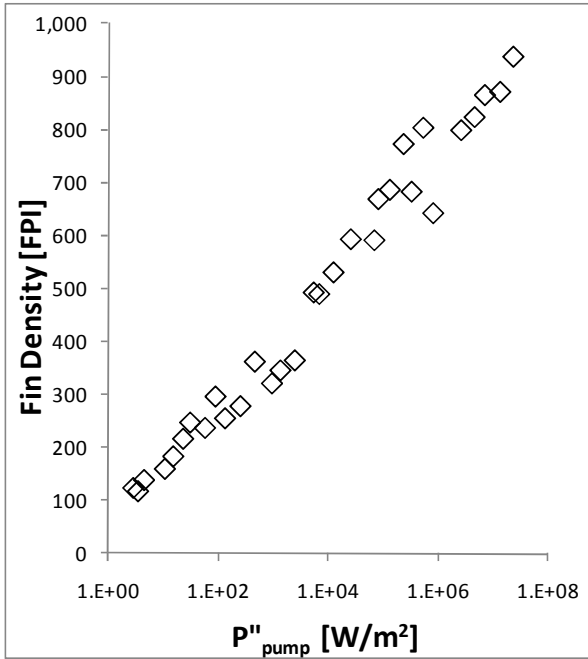


**Figure 4-10. Variation of fin density with pumping power**

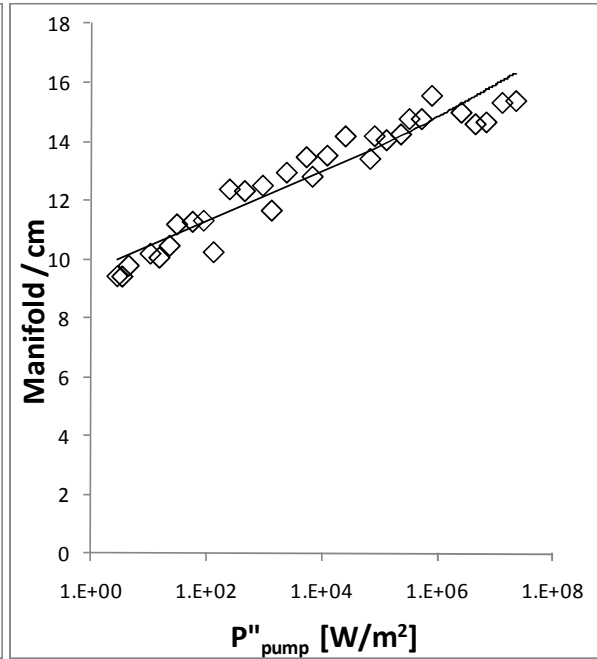


**Figure 4-11. Variation of manifold number per cm with pumping power**

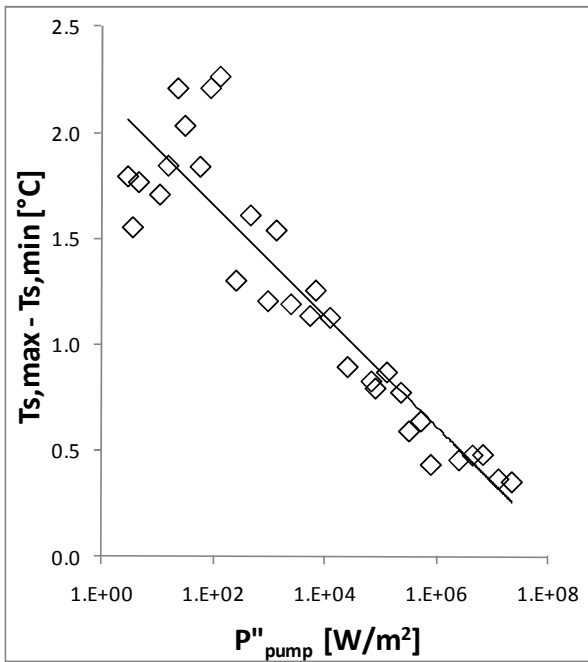


**Figure 4-12. Variation of surface temperature uniformity with pumping power**

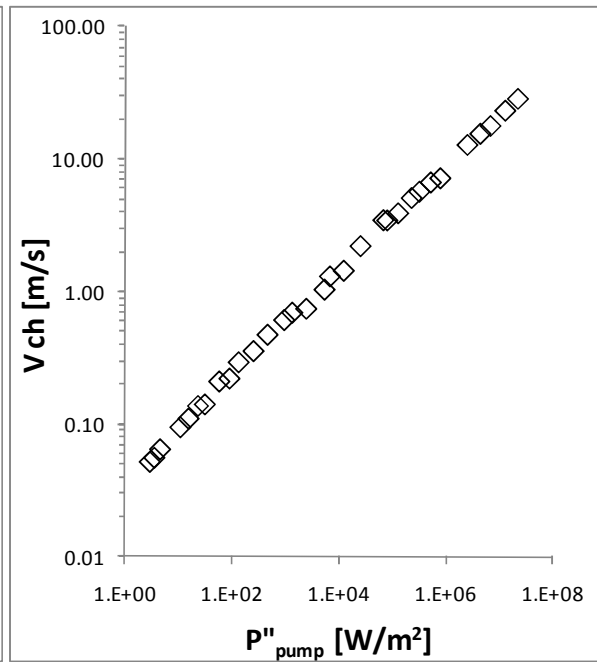


**Figure 4-13. Variation of channel velocity with pumping power**

## 4.6. Single-Phase Cooling Technology Comparison Study

To quantitatively compare several advanced cooling technologies, a similar MOGA technique was applied to a typical TMHS and a JIHS. The goal of this study was to compare the performance of all three cooling technologies based on their optimum designs at maximum heat transfer coefficient and minimum pumping power. The three cooling technologies were compared on two different areas of  $1 \times 1 \text{ cm}^2$  and  $2 \times 2 \text{ cm}^2$ . The modeling and optimization procedure of TMHS and JIHS is described in next sections.

### 4.6.1. Single-Phase Optimization of TMHS

TMHS was modeled using a simplified 1-D flow and heat transfer model. The schematic representation of the model is shown in Figure 4-14. The mathematical model simplifies the optimization process by eliminating the AAO and metamodeling process, therefore decreasing substantially the computational time. The pressure drop and heat transfer were modeled based on correlations developed for hydraulically and thermally developing laminar flow in rectangular microchannels. A description of the TMHS model and the calculation procedure is given in detail in Appendix C. The optimization problem was set as:

maximize  $h$

minimize  $P_{pump}$

subject to:

$$0.2 < H_{ch} < 5.0 \text{ [mm]}$$

$$0.2 < w_{ch} / t_{fin} < 1.5$$

$$5 < H_{ch} / t_{fin} < 10$$

$$10 < Re < 2300$$

with:

$$H_{base} = 0.4 \text{ [mm]}$$

It is important to note that, for constant fluid velocity in the microchannel, the pressure drop and heat transfer coefficient values of a TMHS change with the heat sink dimension. As heat sinks increase in size, the pressure drop will increase while heat transfer coefficients will decrease due to an increase in fluid bulk temperature along the microchannel. Therefore, optimum pumping power and heat transfer coefficient values need to be recalculated each time the heat sink is resized.

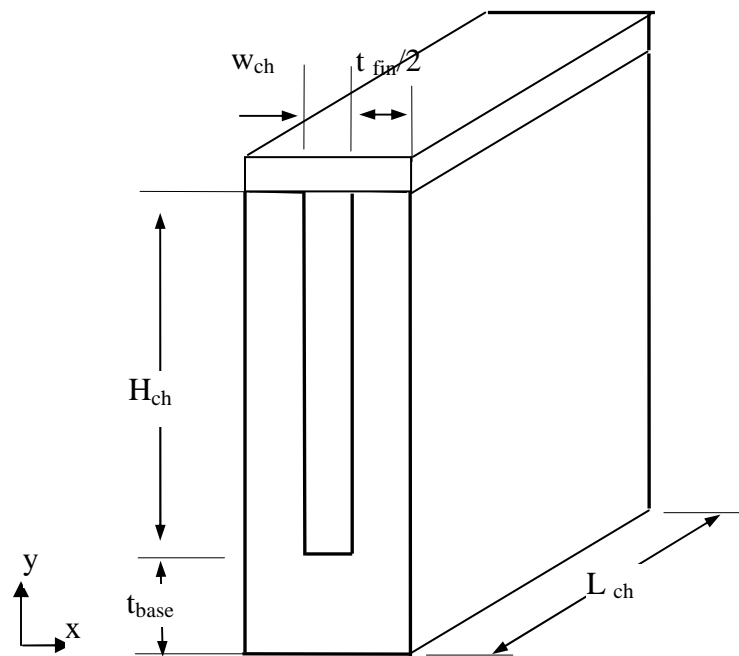


**Figure 4-14. TMHS model used in optimization study**

Constant temperature was used as the boundary condition at the bottom wall and copper and water were selected as the base material and working fluid. Similarly,

MOGA was used to optimize the TMHS. The optimum Pareto solutions for TMHS at 1x1 cm<sup>2</sup> and 2x2 cm<sup>2</sup> base areas are shown in Figure 4-15, while the optimum variables are numerically listed in Table 9-1 and Table 9-2 in Section 9.3.2 of Appendix C.

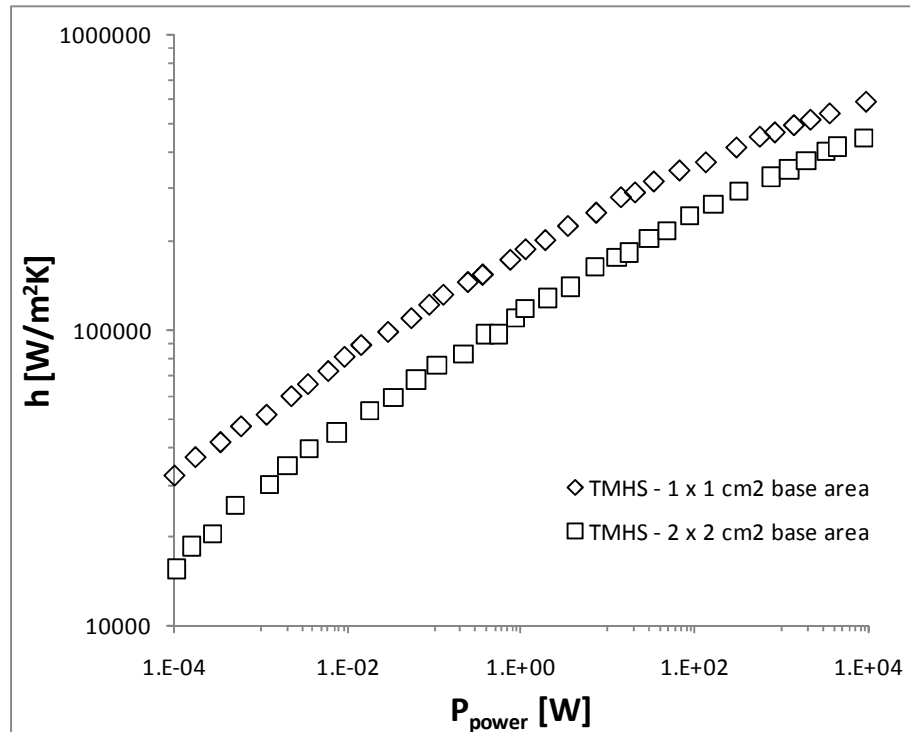


**Figure 4-15. Optimum Pareto solutions of TMHS at 1 x 1 cm<sup>2</sup> and 2 x 2 cm<sup>2</sup> base areas**

#### 4.6.2. Single-Phase Optimization of JIHS

Jet impingement is known to be an effective cooling technology, as it substantially decreases the thermal resistance at stagnation zone and has low pressure drop; therefore, it has been extensively investigated (Agostini, Fabbri et al., 2007). The jets can be single or multiple and working in parallel, mostly depending on the size of the cooling area. Recently (Meyer, Mudawar, Boyack, & Hale, 2005)

proposed a heat sink design based on an array of rectangular jets that can lower the pressure drop and maintain desirable surface uniformity. The working schematic and the array jet slots used in their study is shown in Figure 4-16. The fluid enters the heat sink through feed channels that are formed by a parallel manifolding system. The feed channels lead the fluid into the jet orifices where the velocity is increased and the jet is formed. After the jet impinges on the target surface, it is split into two streams, each stream passing a short distance before combining with the neighboring stream and leaving the heated area through gaps opened between manifolds. This configuration is similar to a typical FFMHS without the microgrooved surface. Due to geometrical simplicity and relevance to the nature of this study, this heat sink configuration was also selected as the typical JIHS for optimization and comparison study performed in next sections.

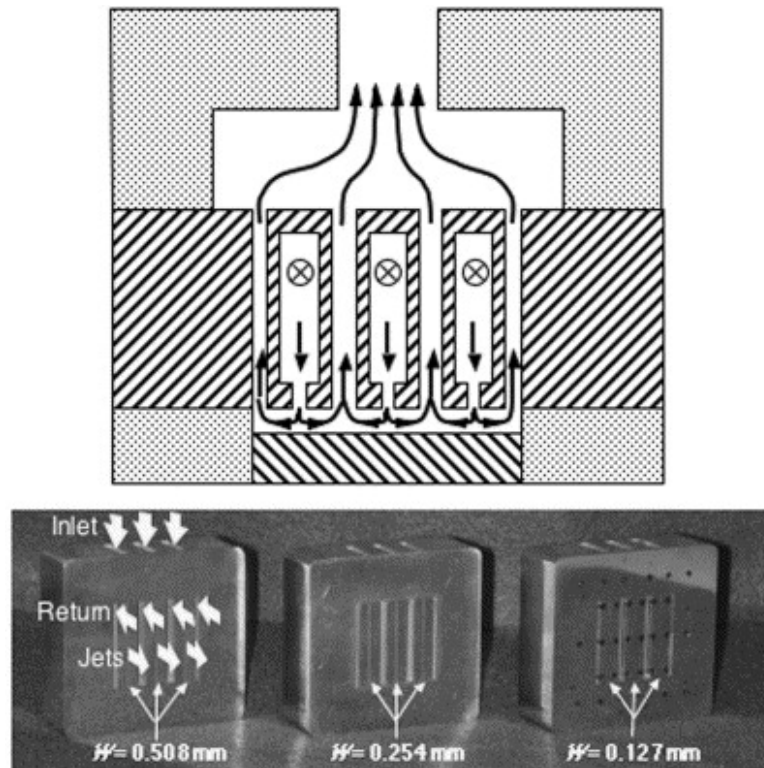


**Figure 4-16. Jet impingement heat sink (JIHS) developed by (Meyer et al., 2005)**

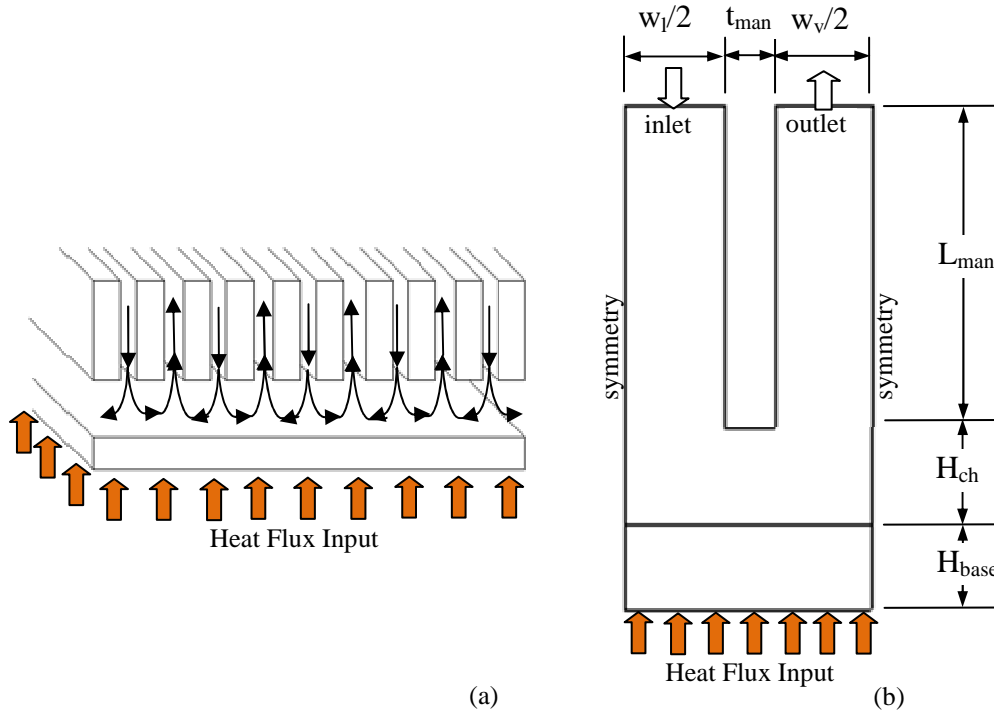


**Figure 4-17. (a) Schematic of flow in a typical JIHS, (b) Computational domain**

The JIHS can be further simplified by assuming the flow schematic shown in Figure 4-17 (a). The feed channels are assumed to be long, and the heat sink can be modeled based on a 2D approach with boundary conditions shown in Figure 4-17 (b).

The optimization problem was set as follows:

maximize  $h$

minimize  $P_{pump}''$

subject to:

$$0.05 < H_{ch} < 0.2 \text{ [mm]}$$

$$0.025 < w_l / 2 < 0.2 \text{ [mm]}$$

$$0.1 < t_{man} < 0.5 \text{ [mm]}$$

$$0.025 < w_v / 2 < 0.2 \text{ [mm]}$$

$$1 < \text{Re}_{pp} < 1000$$

$$H_{base} = 0.4 \text{ [mm]}$$

where the Reynolds number was defined for flow between base and manifold, similar to flow between two parallel plates:

$$\text{Re}_{pp} = \frac{\rho V_{pp} (2H_{ch})}{\mu} \quad (4-5)$$

$$V_{pp} = \frac{\dot{m}'}{\rho H_{ch}} \quad (4-6)$$

Because the geometry is 2D, the mass flow rate  $\dot{m}'$  in the computational domain is defined for unit width and has the units of [kg/ms]. The AAO optimization procedure performed for FFMHS was repeated here to optimize JIHS. The simplified 2D geometry allowed the selection of many more sampling points than the 3D computational domain of FFMHS. A total of 720 sampling points was selected in the design space and 100 random points were used to validate the metamodel. The resulting metamodel was able to predict the validation points with an RRMSE and RMAE of 2.7 and 8.3 for heat transfer coefficients and 6.2 and 18.7 for pumping power values. MOGA was applied to the metamodel, and the resulting optimum Pareto is shown in Figure 4-18, while the numerical optimum results are listed in Table 9-3 in Section 9.3.3 of Appendix C. The RRMSE and RMAE obtained for Pareto front were calculated as 2.16 and 8.2, respectively, for heat transfer coefficients and 5.6 and 9.7, respectively, for pumping power values.

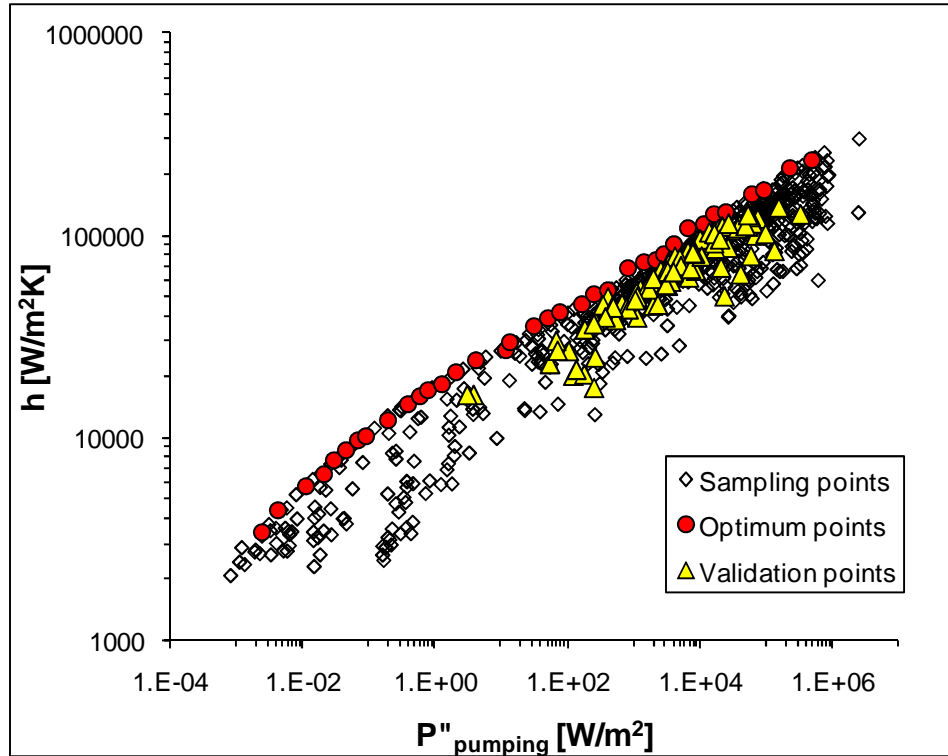


**Figure 4-18. Sampling, optimum and validation point distribution for optimization process of JIHS**

Similarly to FFMHS, the pressure drop and heat transfer coefficient of JIHS are not functions of base cooling area when the flow velocity is constant. The only term that will affect the pumping power is the flow rate, which is proportional to the cooling area. Therefore for a JIHS, only a single case needs to be optimized, and optimum geometries for different base areas can be easily calculated.

#### **4.6.3. Performance Comparison of FFMHS, TMHS and JIHS**

The results of the optimization study performed for FFMHS, TMHS and JIHS can be used to compare these cooling technologies at optimum designs. In order to obtain the effect of base heat sink area, two different cases of  $1 \times 1 \text{ cm}^2$  and  $2 \times 2 \text{ cm}^2$  base areas were considered for comparison. For each given base heat sink area the

Pareto solutions for three cooling technology can be plotted on a single graph. For  $1 \times 1 \text{ cm}^2$  and  $2 \times 2 \text{ cm}^2$  base area heat sinks, the comparison plots are shown in Figure 4-19 and Figure 4-20, respectively, for pumping power variations between  $1 \times 10^{-3}$  and  $1 \times 10^3 \text{ W}$ . For the given range, the heat transfer coefficients show a monotonic and exponential like increase with increased pumping power. The Pareto fronts for each cooling technology look similar but shifted away and do not cross each other. For both  $1 \times 1 \text{ cm}^2$  and  $2 \times 2 \text{ cm}^2$  base area cases, the FFMHS show a better performance with higher heat transfer coefficients at all pumping power values. In terms of performance, FFMHS is followed by TMHS and JIHS. When going to larger cooling areas, from  $1 \times 1 \text{ cm}^2$  and  $2 \times 2 \text{ cm}^2$ , the heat transfer coefficients tend to decrease for all cooling technologies. This is expected, since the flow rates are decreasing to meet the specified pumping power values. However, the decreasing trend for TMHS is more significant compared with FFMHS and JIHS. Again, the performance drop for TMHS with the increase in flow length comes from increases in both bulk fluid temperature and pumping power. With the current trend, it is expected that the optimum performance of JIHS can surpass TMHS for cooling of larger areas.

It is important to note that the current comparison was performed between two cooling technologies that utilize enhanced surfaces, namely FFMHS and TMHS, and one cooling technology that does not utilize enhanced surface, which is JIHS. Although jet impingement on enhanced surfaces could be another cooling technology that can be used in this comparison study, this technology was not considered in this work, although it is recommended as a consideration for future work.

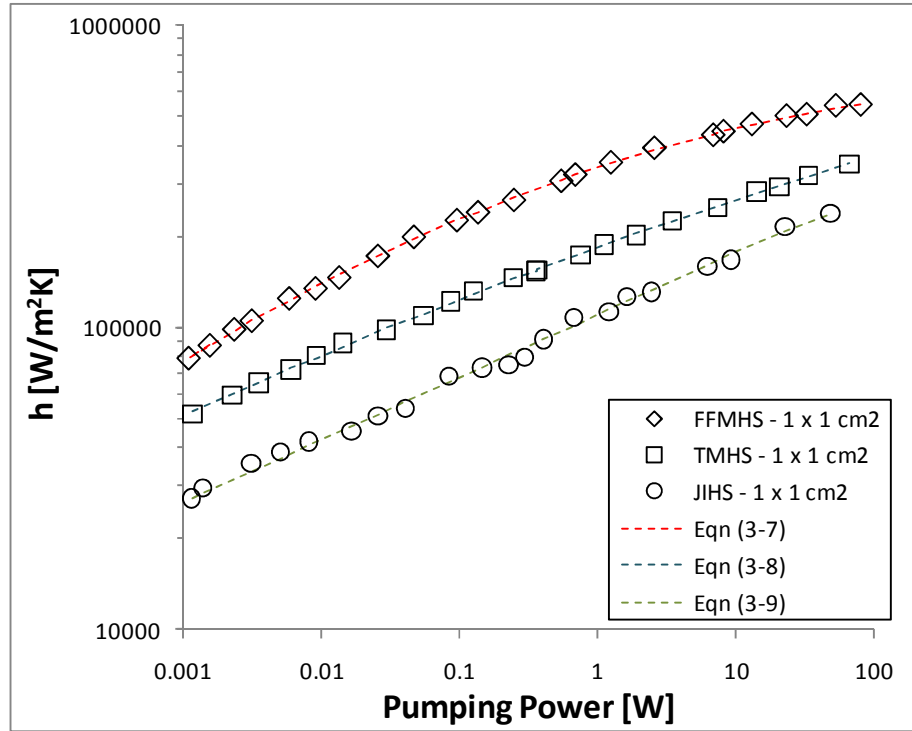


**Figure 4-19. Optimum Pareto solution for three cooling technologies for 1 x 1 cm<sup>2</sup> base area heat sink**

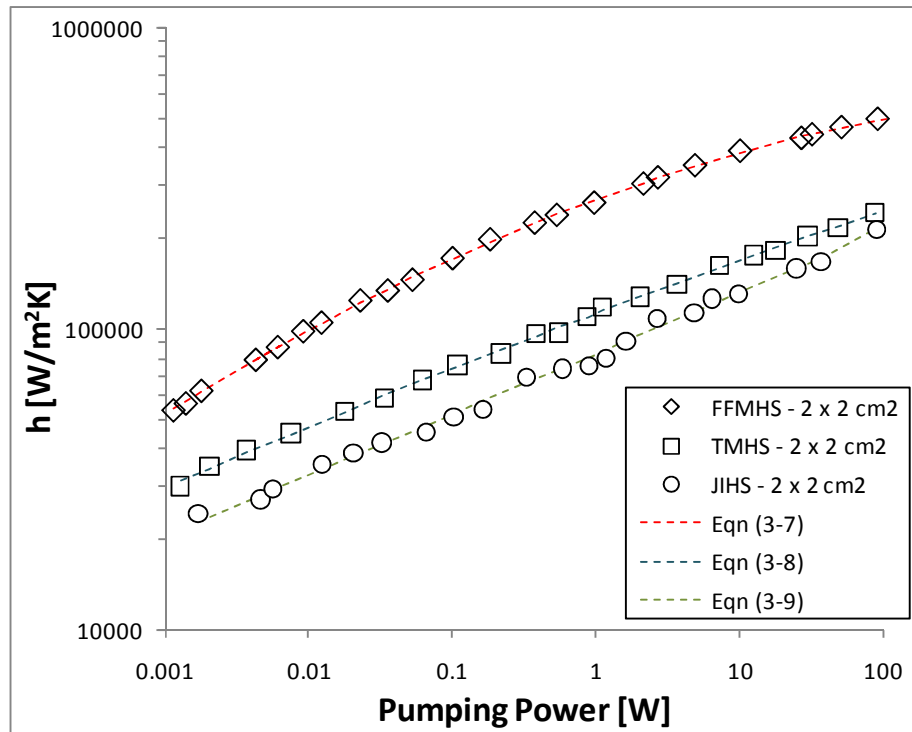


**Figure 4-20. Optimum Pareto solution for three cooling technologies for 2 x 2 cm<sup>2</sup> base area heat sink**

To calculate and compare the performance of three cooling technologies at given conditions of constant pumping power or constant heat transfer coefficients, a curve-fitting process was applied to the Pareto solutions. For finding the best equation to fit the given data TableCurve 2D software was utilized. The resulting three fitting equations for FFMHS (Equation (4-7)), TMHS (Equation (4-8)) and JIHS (Equation (4-9)) are shown below, and the list of the coefficients for each equation is given in Table 4-1. Based on these equations, four sets of comparison charts were created. The three cooling technologies were compared for heat transfer coefficients at constant pumping power of 0.01 W, 0.10 W and 1.00 W in Figure 4-21. Similarly, the second comparison shown in Figure 4-22 was performed for pumping power required at constant heat transfer coefficients of 100,000 W/m<sup>2</sup>K, 150,000 W/m<sup>2</sup>K and 200,000 W/m<sup>2</sup>K.

$$\ln h = \tilde{a} + \tilde{b} \left( \ln P_{\text{pump}} \right)^2 + \tilde{c} \ln P_{\text{pump}} \quad (4-7)$$

$$\ln h = \tilde{d} + \tilde{e} \left( \ln P_{\text{pump}} \right)^2 + \tilde{f} \ln P_{\text{pump}} \quad (4-8)$$

$$\ln h = \tilde{k} + \tilde{m} P_{\text{pump}}^{2.5} + \tilde{n} \ln P_{\text{pump}} \quad (4-9)$$

**Table 4-1. The curve fit coefficients for Equations (4-7),(4-8) and (4-9)**

	<b>1 x 1 cm<sup>2</sup> base area heat sink</b>	<b>2 x 2 cm<sup>2</sup> base area heat sink</b>
$\tilde{a}$	12.7301022	12.50469868
$\tilde{b}$	-0.00902189	-0.00902189
$\tilde{c}$	0.150087297	0.175101282
$\tilde{d}$	12.12144534	11.63300172
$\tilde{e}$	-0.00285679	-0.00192744
$\tilde{f}$	0.165114493	0.179407884
$\tilde{k}$	11.61038957	11.32459655
$\tilde{m}$	-0.0000019573	0.000000588428
$\tilde{n}$	0.20701319	0.201324384

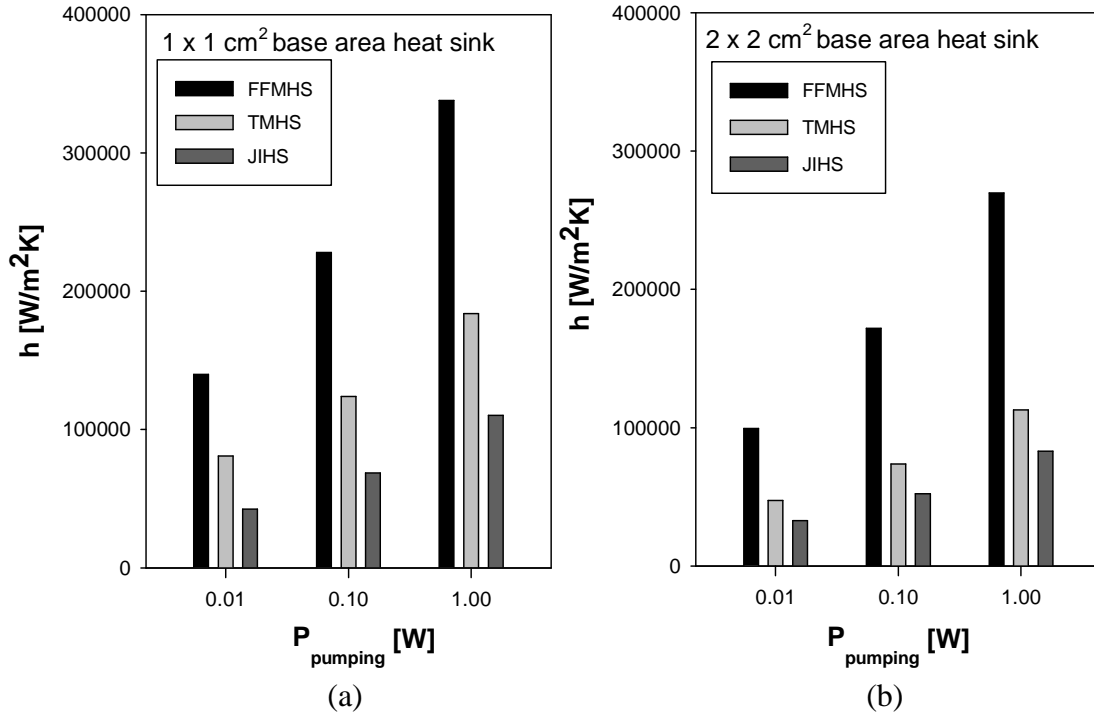


Figure 4-21. Optimum heat transfer coefficients for three cooling technologies at constant pumping power (a) 1 x 1 cm<sup>2</sup> heat sink, (b) 2 x 2 cm<sup>2</sup> heat sink

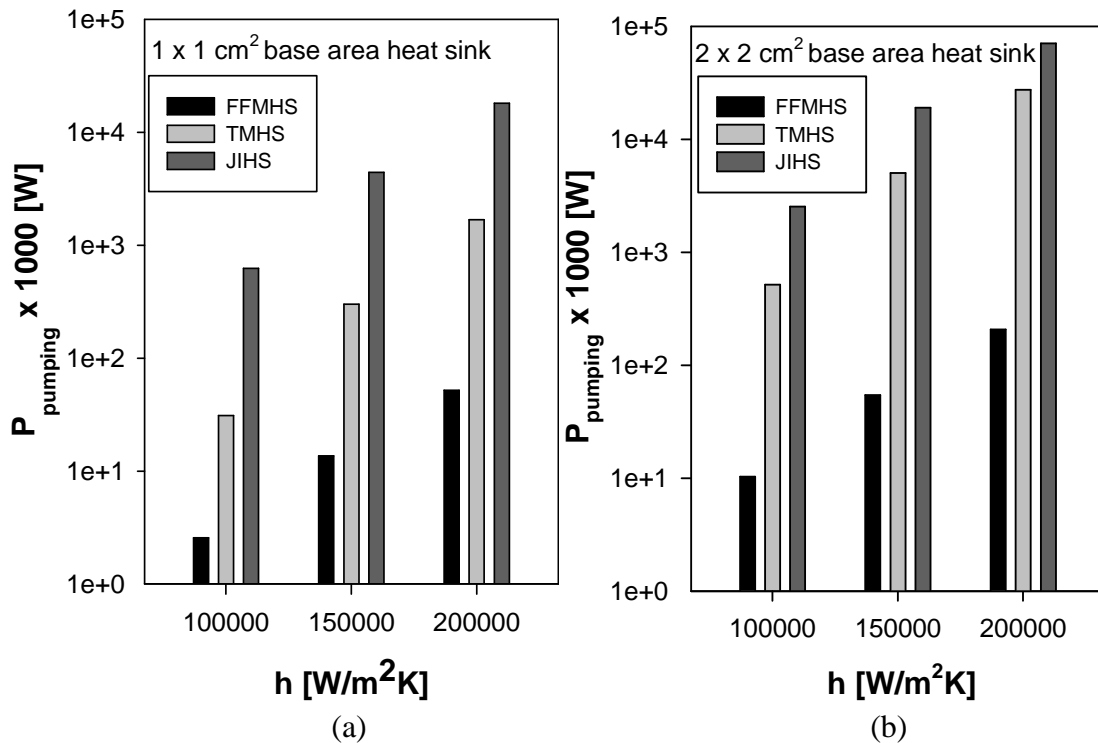


Figure 4-22. Optimum pumping power values for three cooling technologies at constant heat transfer coefficient (a) 1 x 1 cm<sup>2</sup> heat sink, (b) 2 x 2 cm<sup>2</sup> heat sink

The optimum heat transfer coefficients obtained for heat sink base area of  $1 \times 1 \text{ cm}^2$  are shown in Figure 4-21 (a). The FFMHS have higher performances at all given pumping power values. On average, heat transfer coefficients of FFMHS are more than 72% higher than TMHS, and 306% higher than JIHS. The performance difference is even more significant in Figure 4-21 (b), where the cooling technologies are compared for a heat sink base area of  $2 \times 2 \text{ cm}^2$ . For these conditions, the heat transfer coefficients of FFMHS are more than 208% higher than TMHS and more than 303% than JIHS. The difference in performance is even more pronounced when the three cooling technologies are compared for pumping power values at constant heat transfer coefficients. For the heat sink with  $1 \times 1 \text{ cm}^2$  base area case shown in Figure 4-22 (a), the FFMHS can achieve similar heat transfer coefficients with about 8.5% of pumping power required by TMHS and only 0.4% of power required by JIHS. For the heat sink with  $2 \times 2 \text{ cm}^2$  base area, the difference increased by having FFMHS with pumping power consumption within 2% of those of TMHS and 0.4% of JIHS. It is important to note that the pumping power values shown in Figure 4-22 (a) and (b) are multiplied by 1000 to avoid any negative value in the logarithmic scale.

## **4.7. Conclusions**

The Approximation Assisted Optimization (AAO) scheme coupled with a numerical simulation solver was first used to optimize and analyze the geometry of an FFMHS. The findings can be summarized as follows:

- At low Reynolds number flows, the optimum FFMHS designs favor microgrooved surfaces with high fin heights, high fin aspect ratios and with microchannels with large hydraulic diameters. Similarly, the feed channel

dimensions are large, with inlet feed channels slightly smaller than outlet feed channels. The secondary flows are negligible as dictated by low Dean numbers.

- Going to higher Reynolds number flows, both the heat transfer coefficients and the pumping powers values have a monotonic increasing trend. At the same time, the FFMHS designs tend to favor microgrooved surfaces and manifolds with smaller features increasing the local heat transfer coefficients and increasing the heat transfer area. The secondary flows have become to be important only at very high Reynolds numbers.
- Due to the small microchannel length and the conductive copper fin structure, the heat transfer in the longitudinal direction is significant and can reduce base surface temperature difference. The maximum surface temperature non-uniformity for all tested cases was less than  $2.5^{\circ}\text{C}$  and was further decreasing by increasing flow rate.
- The optimization code was able to capture the effect of the fabrication limitations of microgrooved surfaces. For high Reynolds number flows, the microchannel height of the optimum designs reaches the minimum values of 0.2 mm and remains constant when going to higher flow rates. This shows that the optimal performance values achieved in this work can be further increased if the capabilities of MDT are expanded to lower feature size microchannels.

The second part of this chapter focused on optimization of two other cooling technologies: Traditional Microchannel Heat Sinks (TMHS) and Jet Impingement Heat Sinks (JIHS). Then the optimum results for three investigated technologies were compared for cooling of two heat sinks with different base areas of  $1 \times 1 \text{ cm}^2$  and  $2 \times 2 \text{ cm}^2$ . The following results were obtained:

- FFMHS can operate much more efficiently in the parametrical range investigated in this study. For a constant pumping power and  $1 \times 1 \text{ cm}^2$  base cooling area, FFMHS can achieve 72% more heat transfer compared to TMHS and 306% compared to JIHS.
- For  $1 \times 1 \text{ cm}^2$  base cooling area and constant heat transfer performance, the pumping power required by FFMHS is only 8.5% of pumping power required by TMHS and 0.4% of pumping power required by a JIHS.
- When going to larger cooling areas, the performance difference of FFMHS compared with TMHS is even more significant. The manifolding system that forms the short parallel microchannel structure in FFMHS allows cooling of large areas without the penalty of heat transfer degradation due to rise in fluid temperature and increase in pressure drop and flow length.
- With the observed superior performance, FFMHS technology has the potential to replace TMHS, that are currently widely used for cooling of high heat flux surfaces.

## **CHAPTER 5: EXPERIMENTAL TEST SETUP**

This chapter gives a description of the test setup used for single-phase and two-phase experimental tests. In the first part of the chapter, the flow diagram and several pieces of equipment used in the tests are explained. The chapter continues with a description of the test section, the heater assembly and the microgrooved surfaces. The chapter ends with a discussion of selection of working fluids and description of heat balance method used to calculate the heat losses.

### **5.1. Experimental Test Setup**

A picture of the experimental test setup used for performance testing of FFMHT is shown in Figure 5-1, while a flow diagram is given in Figure 5-2. The test setup consisted of a primary closed loop and two external water-cooling loops. The primary loop was filled with refrigerant, which was circulated by a pump through a mass flow meter, pre-heater, filter, subcooler, test chamber and condenser. The secondary water loops were connected to the plate heat exchanger and subcooler, and each loop had its own chiller unit to reject the heat generated in the test chamber. The mass flow rate was measured using a Coriolis mass flowmeter, and a 20-micron filter was used to filtrate the fluid. The purpose of installing the pre-heater and the subcooler was to control the fluid conditions prior to the inlet of the test chamber. The test chamber was located at the highest elevation of the test setup and was where the heat was transferred from the test heat sink sample to the fluid, either by single-phase or two-phase heat transfer modes. A differential pressure transducer, an absolute

pressure transducer, thermocouples and a power supply were connected to the test chamber to measure pressure and temperatures and to supply the power to the heater inside the test chamber. The fluid at the outlet of the test chamber was directed to a plate heat exchanger, which worked as a condenser in two-phase mode and as a liquid-to-liquid heat exchanger in single-phase heat transfer mode. For the refrigerant loop, a bypass connection was installed to achieve flow rates below pump capacity. All thermocouple, power supply and pressure transducer outputs were connected to a data acquisition system, which was connected and controlled through a PC. Data were monitored in real time by a Labview program that has feedback options to control the test setup. A complete list of components used in the test setup are given in Table 5-1.

**Table 5-1. List of system components used in the experimental test setup**

<b>Component name</b>	<b>Manufacturer</b>	<b>Model</b>	<b>Range of Operation</b>	<b>Accuracy</b>
<b>Absolute Pressure Transducer</b>	Setra	280F	0-550kPa	0.20%FS
<b>Differential Pressure Transducer</b>	Validyne	DP15	0-86kPa-	0.25%FS
<b>Coriolis mass flow meter</b>	ABB K-Flow	K5	0-2kg/min	0.1%FS
<b>Power supply</b>	Sorensen	DCS300-4E	400V – 4A	0.1 %FS 0.1 %FS
<b>Data acquisition system</b>	Agilent	34970A	20 analog input channels	-
<b>Thermocouple</b>	Omega	T type	-200 – 350 °C	0.3 %
<b>Pump</b>	Micropump	Gear Pump	0.02-2 kg/min	-
<b>Chiller (for plate heat exchanger)</b>	Neslab	T type	5 – 35 °C	0.3 %
<b>Chiller (for subcooler)</b>	Neslab	LT-50	-20 – 35 °C	0.3 %

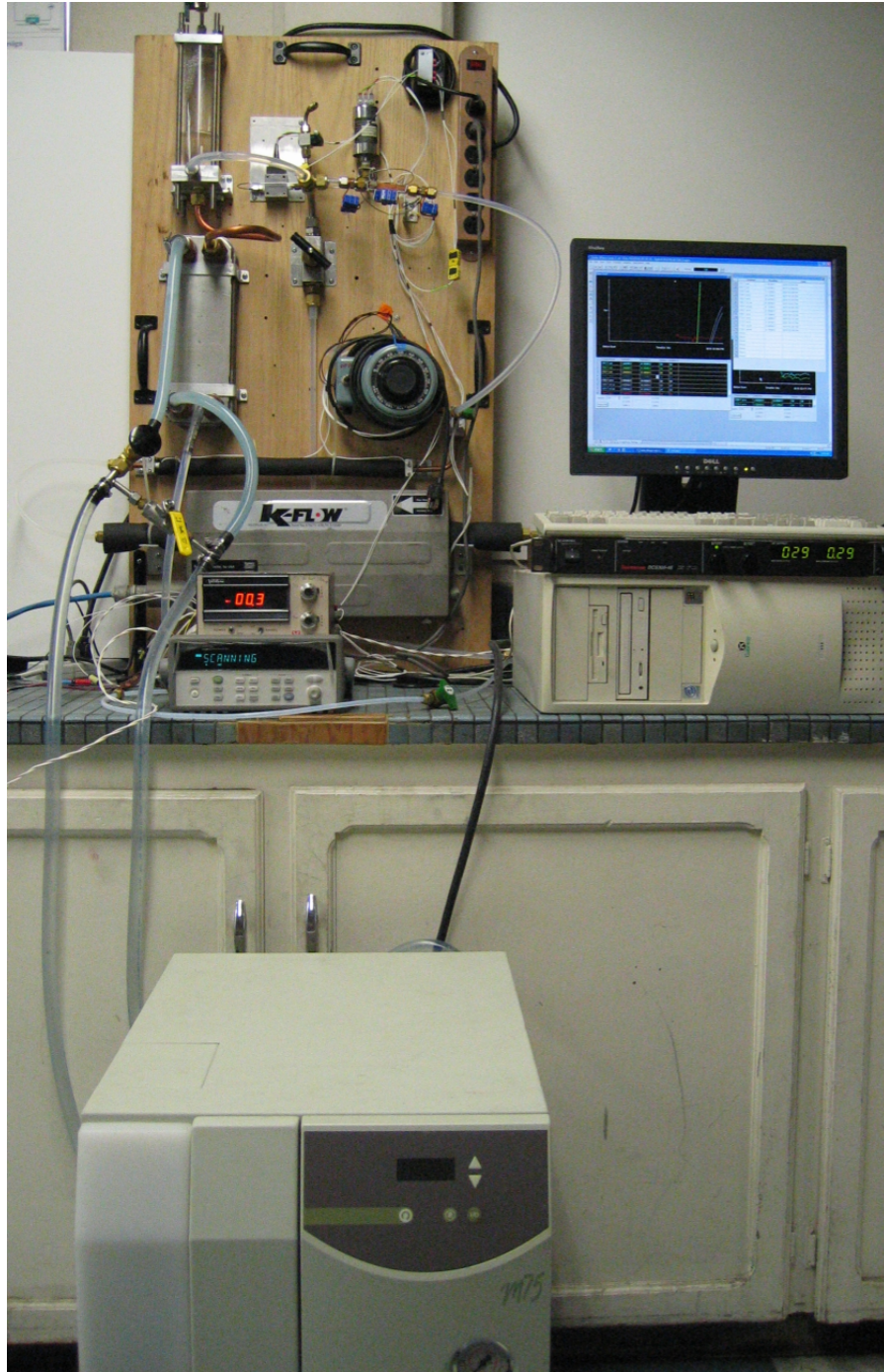


**Figure 5-1. Experimental test setup used for single-phase and two-phase thermal performance tests**

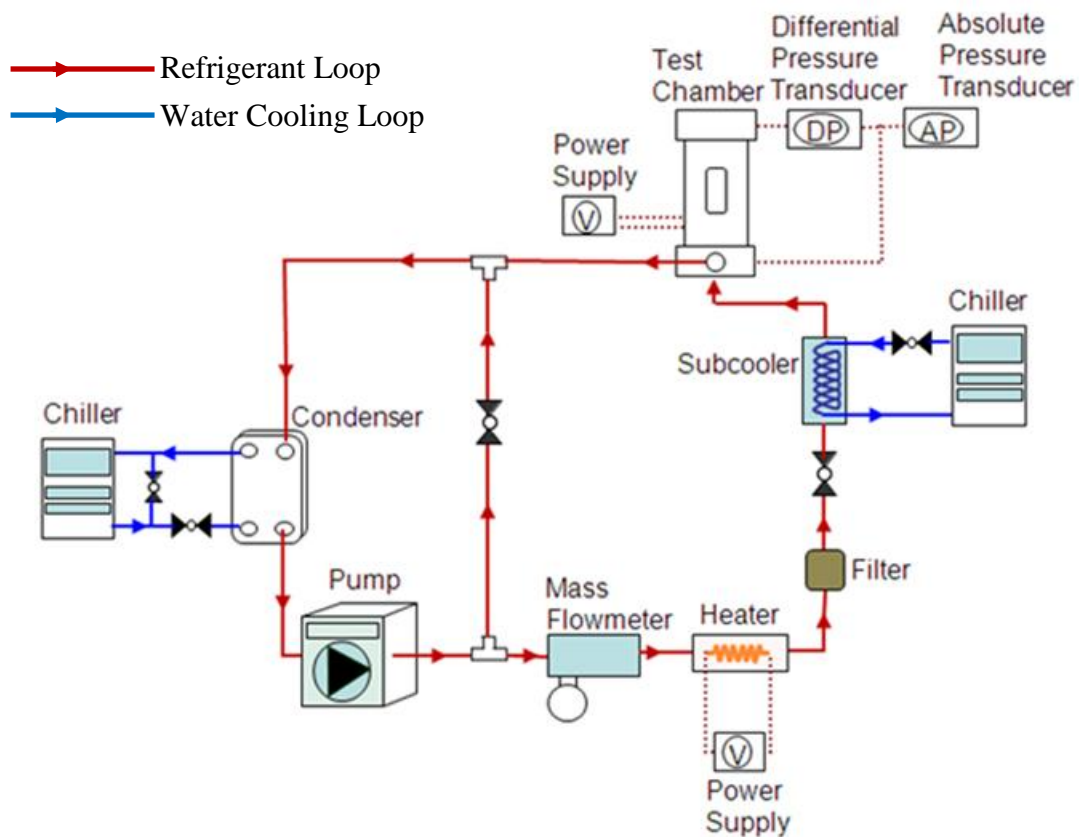


**Figure 5-2. Flow diagram of experimental test setup**

## 5.2. Test Chamber

A picture of the experimental test chamber used in this study is shown in Figure 5-3, and a schematic with a color representation of each component is shown in Figure 5-4. The chamber was a combination of several components located in a glass tube and sealed between two metal flanges. The transparent glass tube was 300 mm long, 76.2 mm (3") in inner diameter with a 3.2 mm (1/8") thick wall positioned vertically. Two rubber O-rings were used to seal the interface between the glass tops and metal frames and four threaded rods of 3/8-16 thread size were used to connect

the flanges and supply the required sealing pressure. The flow was sent to the test chamber through the flow distribution header which was connected to the top flange by a Swagelok fitting. The header consisted of a straight 3/8" tube, a mixing reservoir, a set of manifold and feed channels and two parallel 6-32 thread rods, all brazed together to form a single component. The heater assembly, which consisted of a base material supporting the resistive heater element and the microgrooved surfaces, was attached to the header. The base of the heater assembly had two holes that fits the two threaded rods on the header could slide freely along the rods. The heater assembly was installed by sliding it towards the header until the top of the microgrooved surface made contact with the top of the manifold channels. Two sets of springs and nuts were used to apply the force needed to keep the heater assembly in place. To apply an equal force and to maintain a uniform pressure distribution on the contact interface, the compression from each spring was kept similar by measuring and keeping the spring displacement equal. The sliding system and the nut-spring configuration also allowed easy connection and disconnection of the heater assembly to the header. All thermocouple wires, power connections and pressure tubes were transferred from the chamber to the outside of the chamber through leak-proof compression connections located on the top and bottom flanges. A refrigerant charging port was connected to the top flange of the chamber.

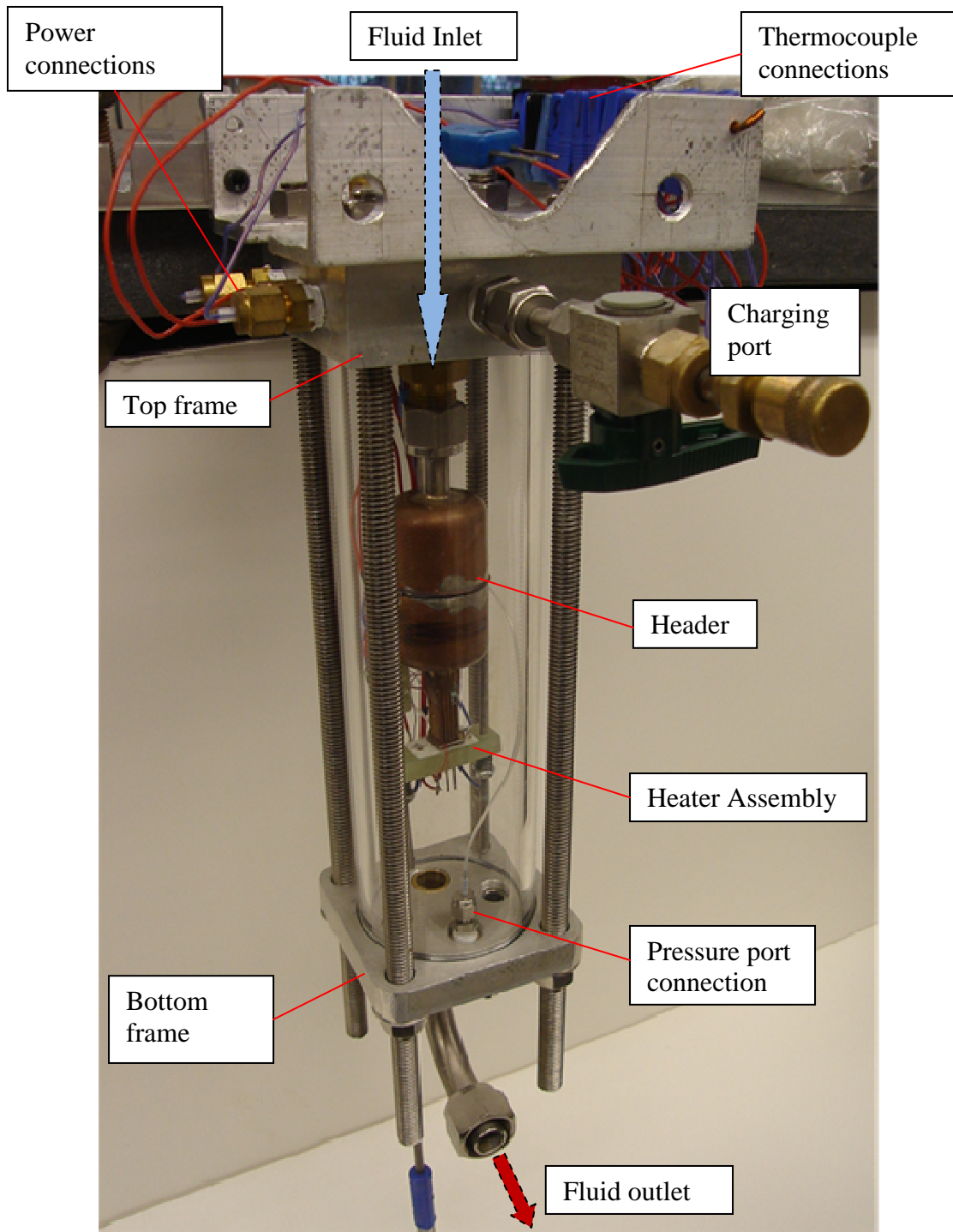


**Figure 5-3. Picture of the experimental test chamber**

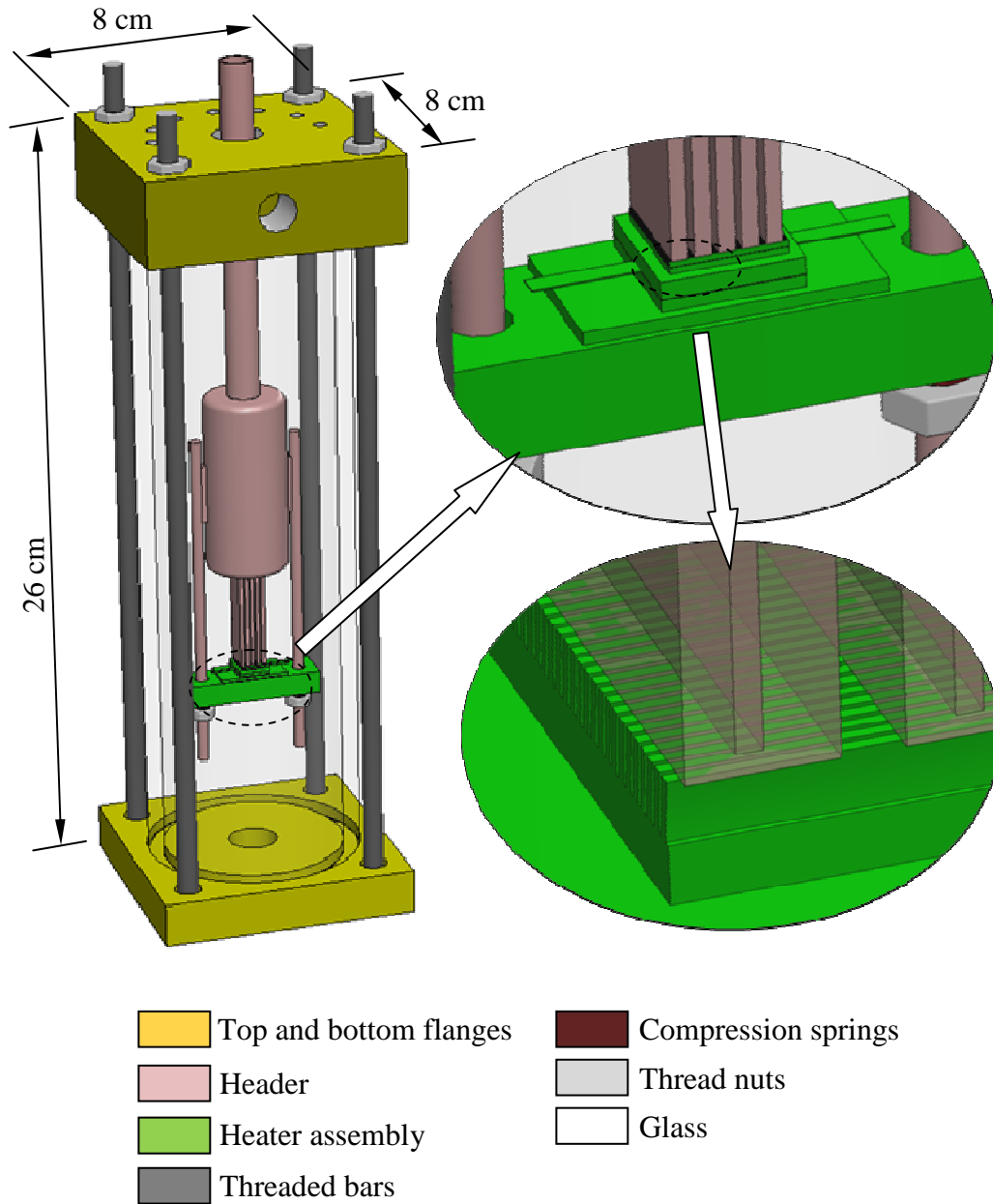


**Figure 5-4. Schematic of the experimental test chamber**

Drawings of the test chamber and its components with dimensions are given in detail in Appendix A. The geometric configuration of the header and packaging of the heater assembly will be discussed in detail in the next two sections.

### 5.2.1. Flow Distribution Header

The flow distribution header was a combination of several sub components such as a stainless steel inlet tube, mixing reservoir and the feed channels/manifolds running in parallel. All these sub-components were brazed together, and the resulting device is shown in Figure 5-5 (a) and (b). Complete dimensions of the flow distribution header are given in Appendix A. In this configuration, the fluid entered the header through the stainless steel tube and then flowed into the reservoir, which was a cylindrical volume made of copper and filled with porous mesh. The liquid then traveled to the other end of the reservoir and flowed into the feed channel/manifold system. The flow schematic in the designed header is shown in Figure 5-6.

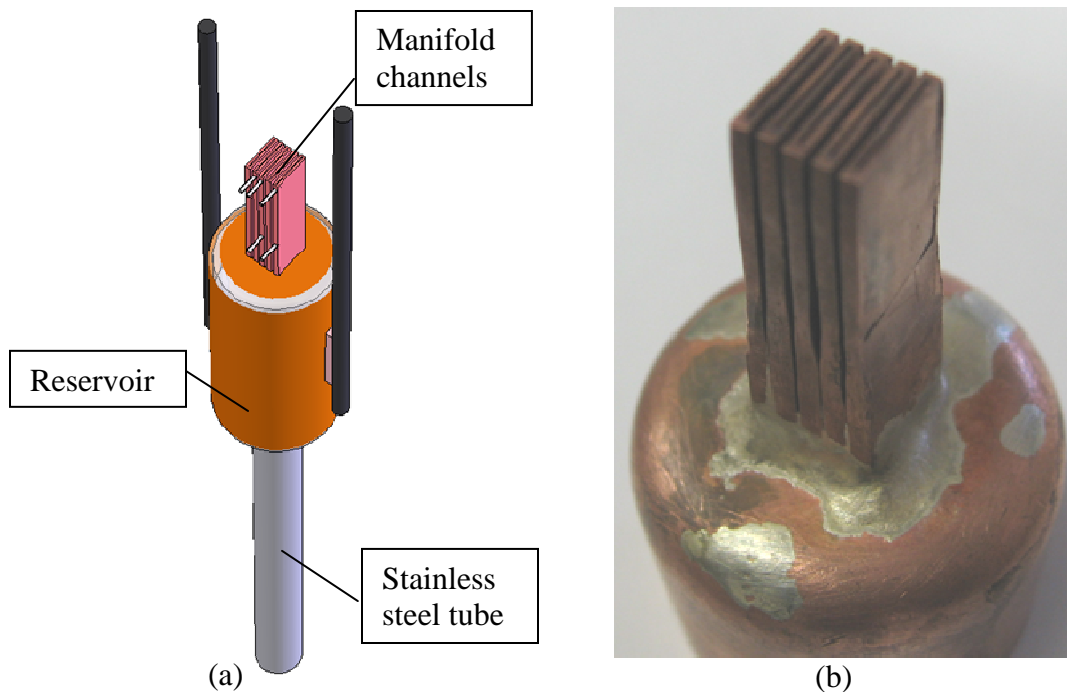


**Figure 5-5. (a) 3D view of flow distribution header, (b) picture of the actual flow distribution header**

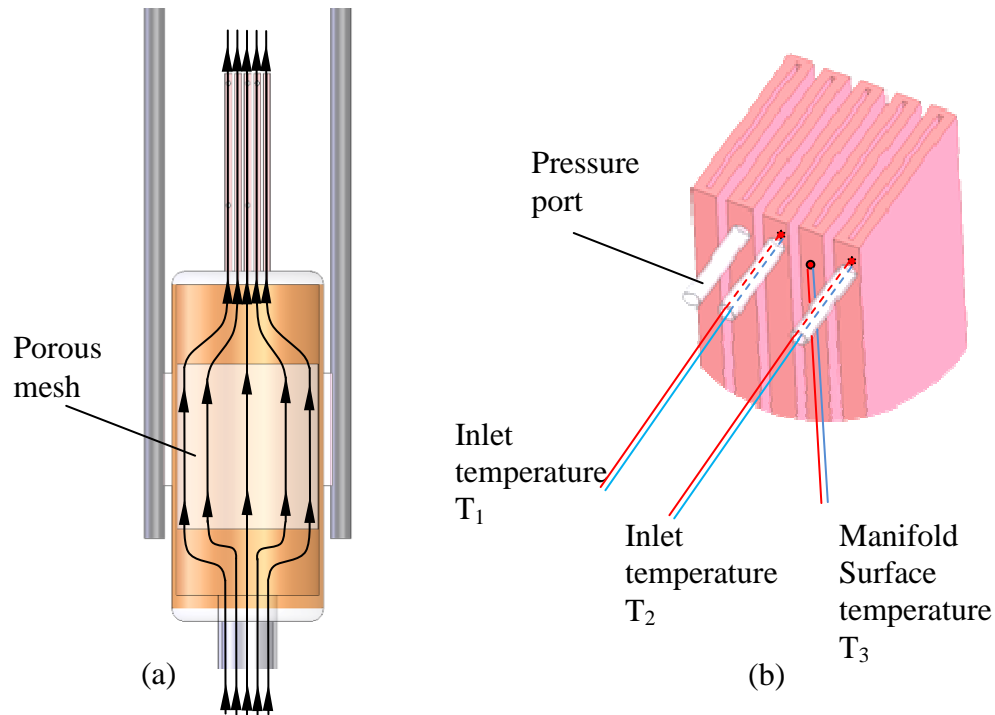


**Figure 5-6. (a) Flow distribution in the header, (b) Position of thermocouples**

The manifold channel system consists of five parallel copper channels, each with a wet cross-section area of 7.6 mm x 0.2 mm, wall thickness of 0.45 mm and channel spacing of 0.45 mm (distance between two neighboring channels). This channel configuration with small liquid feed channels and large outlet feed channels favors two-phase flow, while vapor channels require larger hydraulic diameters. The manifold channels were forged and brazed together. The top face of the manifold channels was machined using a 3/8" diameter end mill.

The purpose of including a reservoir was to ensure equal flow distribution for each of the five manifold channels. Incoming fluid entering the reservoir can create jet effects with a non-uniform, high velocity core and can affect the flow distribution in the manifold channels. To decrease this effect, a porous mesh was installed inside the reservoir. The mesh will create a high pressure drop region that will spread the jet

hitting the mesh and form a more uniform velocity distribution (Figure 5-5 (a)). Also for decelerating the incoming flow, the reservoir flow area was selected to be 14 times higher than inlet tube flow area. The ratio of manifold channels total flow area to the reservoir flow area was also about 40, which made the velocity distribution in the feed channels less sensitive to the low flow velocity in the reservoir and particularly in the inlet tube. The manifold channels can be represented as identical parallel channels connected to the same high-pressure source.

The fluid temperature at the exit of the manifold channels that was forced in the microgrooved surface was measured by two T-type thermocouples. The thermocouples were inserted into two of the manifold channels through 0.8 mm (1/32") outside diameter stainless steel tubes located 1 mm below channel top face. A pair of 0.025 mm (0.001") diameter insulated constantan wire and 0.1 mm (0.004") diameter of bare copper wire was used to form the thermocouples. The static pressure of incoming flow was measured using a similar 0.8 mm (1/32") diameter tube located 3 mm below the manifold channel's top face. A third T-type thermocouple was attached to the side of one of the manifold channels for measuring manifold surface temperature. This thermocouple was located 3 mm below manifold top face. The location and schematic view of thermocouples and pressure port are shown in Figure 5-6 (b).

### **5.2.2. The Heater Assembly**

The heater assembly and its components are shown in Figure 5-7 (a) and (b), and detailed drawings are given in Appendix A. Counting from bottom to top, the final assembly consisted of a composite material base, a 1 mm-thick PTFE Teflon

layer, a thin-film resistive heater, a thin solder layer, and the microgrooved surface. The base was machined from a G10 glass fiber composite slab having a thermal conductivity of 0.5 W/mK. The PTFE Teflon layer between the base and bottom of the heater was installed to provide thermal insulation. The bottom face of the microgrooved surface was soldered to the top face of the heater to reduce the uncertainties associated with thermal contact resistance. The microgrooved surface used in experimental tests had a 7.8x7.8 cm<sup>2</sup> base square area while the heater surface area was 9.5x9.5 cm<sup>2</sup>. The microgrooved surfaces were soldered to the center of the heater. The thin film heater consisted of four layers: a 0.55 mm thick alumina insulator, a thin resistive film heater, a 1.40 mm thick aluminum nitride heat spreader and 0.2 mm thick silver plated copper layer for soldering. The thin film was deposited on the heat spreader, while the insulation was glued with ceramic cement to the film to protect the heater. The electrical resistance of the heater was 101 ohms and remained almost constant during tests, with measured resistance variations of less than 0.5%. To measure the surface temperature, three T-type thermocouples 0.08 mm in diameter were located in 0.2 mm-deep grooves created on the back of the microgrooved surface. This configuration made it possible to measure heat transfer surface temperatures directly on the back of the microgrooved surface. The thermocouples were aligned equally spaced on the diagonal of the microgrooved surface from the center to the corner as shown in Figure 5-8.

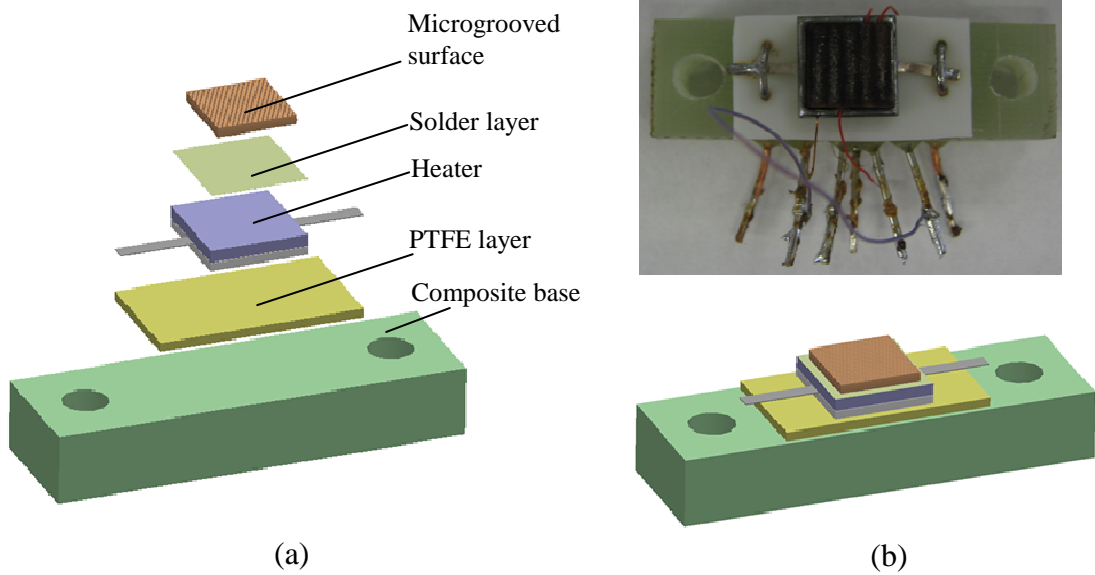


**Figure 5-7. The heater assembly (a) exploded schematic view, (b) actual picture and schematic of assembled view**

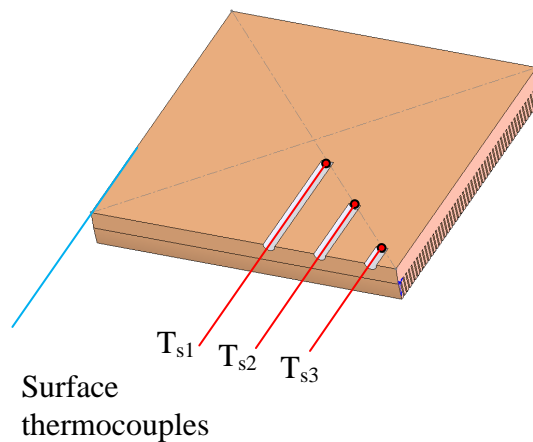


**Figure 5-8. Thermocouple locations on the back of the microgrooved surface**

### 5.3. Working Fluid Selection

The physical properties of working fluid determine to a large extent the thermal performances of cooling systems and limitations to the heat sink design. Important working fluid properties are viscosity, saturation pressure, heat of vaporization, freezing point, dielectric strength, flammability and toxicity. In this

section, these parameters were evaluated with the goal of selecting a suitable working fluid that could be used in a FFMHS application for electronics cooling.

Viscosity of a working fluid is a major contributor to the resulting pressure drop of the system. Most HFE and CFC refrigerants have lower viscosities than aqueous fluids such as water or ethylene glycol, which is one reason to select these types of refrigerants as a working fluid. Saturation pressure at electronics operation temperatures determines stress requirements to the heat sink enclosure as well as to the rest of the cooling loop. For most electronics, for reliable operation, the chip surface temperature needs to be kept below a certain value, usually 75°C for silicon-made micro-processing components and 105-135 °C for power electronics. The evaporation temperature in the heat sink needs to be several degrees lower to transfer heat through the electronics package and heat sink attachment thermal resistances. Another important issue related to saturation pressure is system storage temperatures. Military standards require system surviving storage temperature of 85°C. Well known high-pressure refrigerants (i.e. R134a, R410a) at this temperature often have system pressure too high to be practical for electronics. On the other hand, refrigerants with saturation pressure below atmospheric pressure are not desirable either. Low vapor pressure would require using large diameters for the vapor plumbing. The leakage of such system would result in air penetration into the system and significant degradation of the two-phase system performance.

The heat of evaporation significantly affects parameters of two-phase system. A high heat of evaporation reduces the mass flow of the working fluid in the system and required pumping power. Aqueous working fluids usually have significantly

higher heat of vaporization compared to non-aqueous fluids. However, their application is limited by high freezing points, which can be lowered by creating mixtures with non-aqueous soluble fluids (i.e. ethanol, methanol) and increasing the fraction of such fluid in the mixture. This in turn will cause a non-homogeneous saturation temperature or create a temperature glide and sometimes introduces flammability concerns. An ideal working fluid for electronics cooling should also have high dielectric strength. In case of a leakage, electrically conductive fluid can damage electronics. Engineering fluids have usually significantly higher dielectric strength compared with aqueous fluids, which often determines the fluid selection. Other important properties that affect working fluid selection are the toxicity and global warming potential of the fluid.

A list of the selected working fluid candidates is given in Table 5-2. The properties of the fluids are stated at 30 °C unless otherwise specified. HFE 7100 is an engineered fluid currently replacing FC-72 for many electronics cooling applications, particularly for single-phase convective cooling and partially for two-phase cooling. R134a is currently the most well known refrigerant used in many applications, including cooling of electronics operating below ambient temperature. R-245fa is a relatively new refrigerant that is being considered as a replacement for low-pressure refrigerants for HVAC applications. It has thermodynamic properties superior to FC and HFE series fluids and acceptable pressure at storage temperature (85°C). R-245fa also has higher latent heat of evaporation and reasonable viscosity and thermal conductivity, and it is nontoxic, nonflammable and has low global warming potential.

Therefore, R-245fa was selected as the main working fluid, and all tests were performed using this fluid.

**Table 5-2. Properties of common refrigerants at 30°C saturated liquid phase**

Fluid	HFE-7100	R-134a	R-245fa	Water
Chemical Formula	C <sub>4</sub> F <sub>9</sub> OCH <sub>3</sub>	C <sub>2</sub> H <sub>2</sub> F <sub>4</sub>	CHF <sub>2</sub> CH <sub>2</sub> CF <sub>3</sub>	H <sub>2</sub> O
Boiling Point (1 atm) [°C]	61	-26.09	14.91	100
Saturation pressure at 20°C [kPa]	22.3	571.59	124	2.34
Saturation pressure at 80°C [kPa]	173.2	2633.1	788	47.37
Density [kg/m <sup>3</sup> ]	1455	1188	1325	996
Surface Tension [mN/cm]	13.6	7.4	13.4	71.2
Kinematic Viscosity [cSt]	0.45	0.15	0.29	0.8
Latent Heat of Vaporization [kJ/kg]	120.9	173.1	188.8	2430
Specific Heat [kJ/kg-K]	1.134	1.443	1.369	4.183
Thermal Conductivity [W/m-K]	0.068	0.081	0.08	0.603
Dielectric Strength [kV/mm]	11	7	-	-
Dielectric Constant	7.4	9.3	-	78.5

#### 5.4. Calculation of Heat Losses

When working both in single-phase or two-phase mode, part of the fluid that leaves the heat sink will eventually come in contact with and flow over the components of the heater assembly. The temperature difference between the surface of the components and the fluid creates heat losses. These losses need to be evaluated in order to accurately calculate heat transferred by through the microgrooved surface channels. A 1D resistance analogy for the heat transfer in the heater assembly is shown in Figure 5-9.

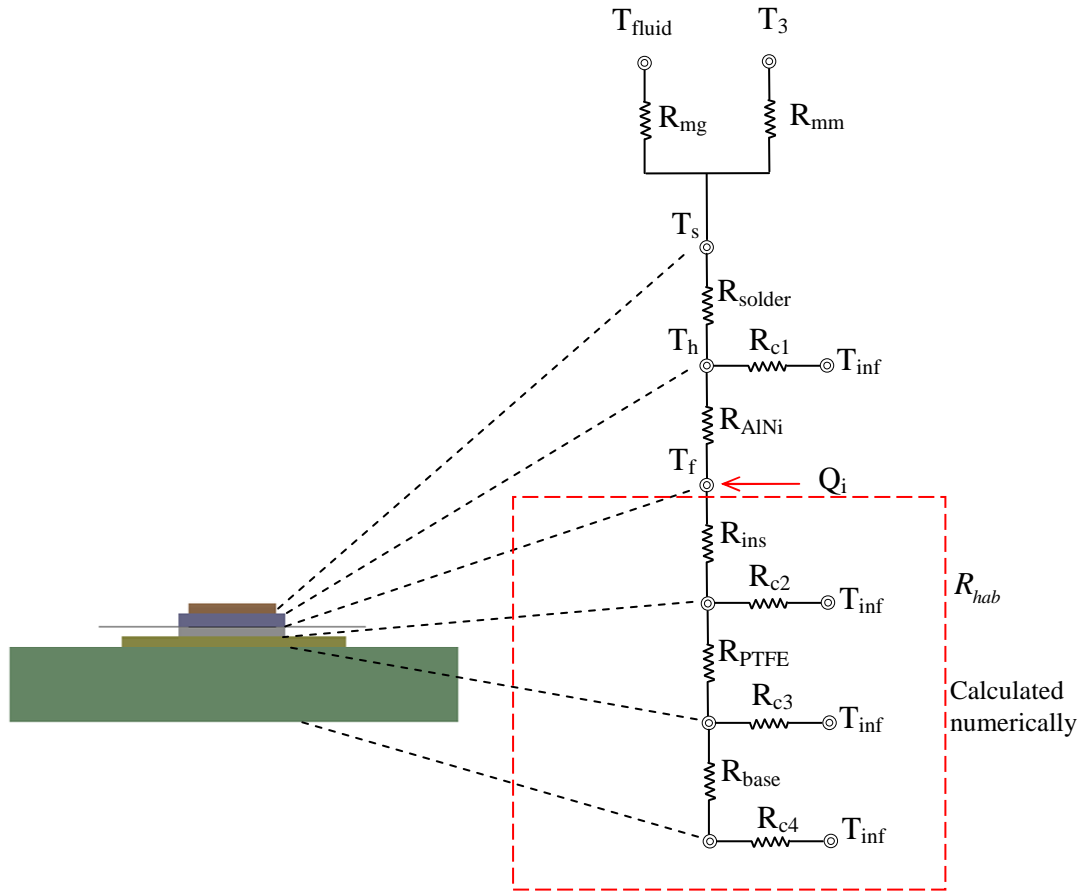


**Figure 5-9. Resistance analogy for heat transfer in heater assembly**

The heat was generated by the thin resistive film on the heater. The film thickness was between 12 microns to 25 microns and can be assumed to be an isothermal thin layer at temperature  $T_f$  for the present model. The heat generated by the thin film  $Q_i$  split in two directions, flowing from the bottom part to the base and from the top part to the microchannels and working fluid. The heat transferred to the bottom part was conducted through the heater ceramic cover, then through the PTFE layer and base material and was dissipated to the working fluid by convection through exposed surfaces to the fluid at  $T_{inf}$  temperature. The heat conducted to the upper part of the microgrooved surface base encountered the thermal resistances of the AlNi

substrate and solder layer  $R_{AlNi}$  and  $R_{solder}$ . The surface temperature  $T_s$  was measured by thermocouples located on the microgrooved surface, as shown in Figure 5-8. A small amount of heat was transferred from the side surfaces of the AlNi substrate to the working fluid based on the thermal resistance of  $R_{cl}$ . Finally, the heat input to the bottom of the microgrooved surface was transferred to the working fluid through the channel base and fin surfaces, and a small part was transferred to the header by conduction through the matching areas of fin tips and manifold channel face surfaces. The contact between fin tips and manifold face was a series of line contacts due to the non-flat fin tip geometry of microgrooved surfaces. Therefore, it was expected that heat conduction to the manifold would be small (thermal resistance  $R_{mm}$  is large) and the majority of the heat would be conducted to the fluid through thermal resistance from the microgrooved surface to the working fluid  $R_{mg}$ . An estimate of the parasitic losses will be provided in the following section.

The thermal resistance of the heat transferred to the bottom of the heater assembly was predicted using a simple numerical model that considers conduction through different layers. The numerical model consists of the composite base, the PTFE layer, the alumina cover of the heater and the resistive thin film. The thin film was modeled as a 2D layer due to its small thickness compared to the other components. The temperature distribution for a sample case for a boundary condition of 320 K resistor temperature is given in Figure 5-10, and a detailed description of the numerical model and applied boundary conditions is given in Appendix B. Here, most of the heat was lost by convection through the surfaces of the alumina cover, while the temperature gradients in composite base were almost negligible. The resulting

numerical model predicts the total thermal resistance  $R_{hab}$  as a function of mass flow rate.

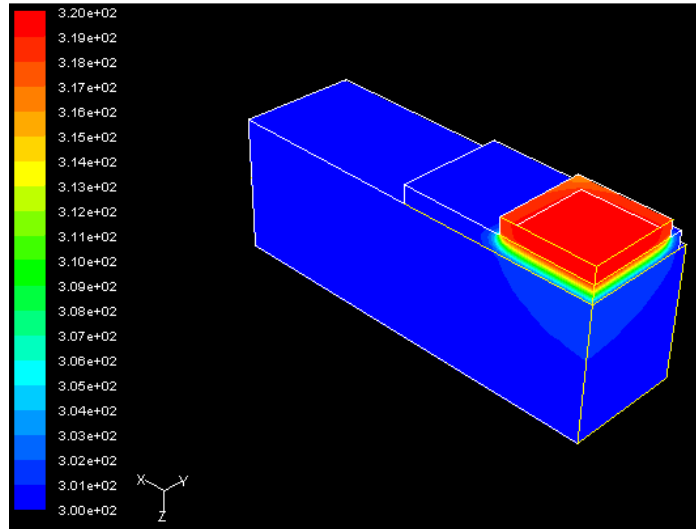


**Figure 5-10. Temperature distribution on the bottom part of the heater assembly for a thin-film resistor temperature of 320 K and 300K fluid temperature**

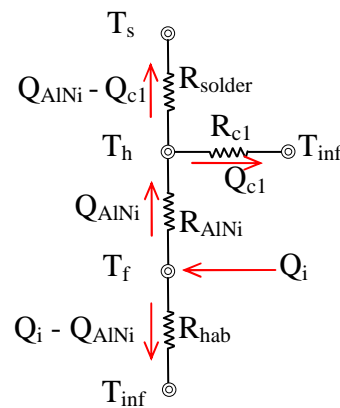


**Figure 5-11. Thermal resistance network between microgrooved surface base and ambient fluid**

The estimation of heat losses from the top part of the heater assembly was based on the simplified resistance network applied from the microgrooved surface to the fluid and is shown in Figure 5-11. Here the surface temperature  $T_s$ , fluid

temperature  $T_{inf}$ , total heat input  $Q_i$  and thermal resistance values are measured or calculated and are assumed to be known as *a priori*. The amount of heat transferred to each of the resistive branches needs to be determined to evaluate the heat losses. The remaining thermal resistance values can be defined as follows:

$$R_{AlNi} = \frac{t_{AlNi}}{A_{AlNi} k_{AlNi}} = \frac{t_{AlNi}}{L_{heater}^2 k_{AlNi}} \quad (5-1)$$

$$R_{c1} = \frac{1}{A_{c1} h_{film}} = \frac{1}{(4t_{AlNi} L_{heater} + L_{heater}^2 - L_{mg}^2) h_{film}} \quad (5-2)$$

$$R_{solder} = \frac{\delta_{solder}}{A_{solder} k_{solder}} = \frac{\delta_{solder}}{L_{mg}^2 k_{solder}} \quad (5-3)$$

where  $\delta_{solder}$  is the solder layer thickness,  $t_{AlNi}$  is the aluminum nitride substrate thickness,  $L_{heater}$  is the width of the square heater and  $L_{mg}$  is the width of the square microgrooved surface. Writing the energy balance between each temperature node reveals a set of four linear equations with four unknowns:

$$Q_i - Q_{AlNi} = \frac{T_f - T_{inf}}{R_{hab}} \quad (5-4)$$

$$Q_{AlNi} = \frac{T_f - T_h}{R_{AlNi}} \quad (5-5)$$

$$Q_{c1} = \frac{T_h - T_{inf}}{R_{c1}} \quad (5-6)$$

$$Q_{AlNi} - Q_{c1} = \frac{T_h - T_s}{R_{solder}} \quad (5-7)$$

The solution of the set of equations results the film resistor temperature as:

$$T_f = \frac{\varphi(R_{hab}R_{AlNi}Q_i + R_{AlNi}T_{inf}) + R_{hab}R_{c1}R_{AlNi}T_s + R_{hab}R_{solder}R_{AlNi}T_{inf}}{\varphi(R_{AlNi} + R_{hab}) - R_{hab}R_{solder}R_{c1}} \quad (5-8)$$

where

$$\varphi = R_{solder}R_{c1} + R_{c1}R_{AlNi} + R_{solder}R_{AlNi} \quad (5-9)$$

For a known  $T_f$  value, heater surface temperature  $T_h$  and heat transfer values of  $Q_{AlNi}$  and  $Q_{c1}$  can be evaluated using equations (5-4),(5-5),(5-6), and (5-7).

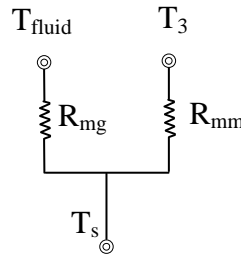


**Figure 5-12. Thermal resistance network between the microgrooved surface base and the fluid in the microchannel and manifold channel**

The thermal resistance network for heat that flows through the microgrooved surface base is shown in Figure 5-12. Two thermal resistance values can be assumed to be in parallel and working between temperatures differences of  $T_s - T_{fluid}$  and  $T_s - T_3$ . The first one ( $R_{mg}$ ) is the thermal resistance of the heat that is transferred to the fluid through the microchannel base and fin surfaces of the microgrooved surface. The second thermal resistance ( $R_{mm}$ ) is associated with the heat that is conducted through the contact surfaces of the fin tips and manifold channel top face. Due to the angled geometry of the finned surface this contact is theoretically a line contact with no area. However, due to the compression forces the fin tips and the manifold top surface may deform and create small contact areas. Due to high uncertainty

associated with this contact, the  $R_{mm}$  values were measured experimentally for each tested microgrooved surface.

To evaluate the  $R_{mm}$  resistance values and to eliminate the convective effect of  $R_{mg}$ , the working fluid in the test setup was discharged and the whole system was vacuumed using a vacuum pump. The vacuum level was below 1 kPa to minimize convection heat transfer. Then the heater was set up to a constant voltage, usually between 1W-4W, and the microgrooved base surface temperature ( $T_s$ ) and manifold surface temperature ( $T_3$ ) were recorded with respect to time. When the steady state condition was reached the thermal resistance value was calculated by:

$$R_{mm} = \frac{T_s - T_3}{Q_i} \quad (5-10)$$

The  $R_{mm}$  values calculated for the three surfaces experimentally tested in this study are shown in Figure 5-13. The graph plots the  $R_{mm}$  values versus temperature difference between the microgrooved surface and the manifold. For an ideal case, the thermal resistance is independent of temperature difference or heat flux, and therefore the almost constant variation shown in the figure was expected. On the other hand, it can also be concluded that the contact resistance decreases as the fin density of the microgrooved surface increases. On other words, the increase in contact lines per unit heat sink area decreases the contact thermal resistance. For calculation purposes the  $R_{mm}$  values for Surface 12, Surface 17 and Surface C were averaged as 4.56 K/W, 4.19 K/W and 2.92 K/W, respectively.

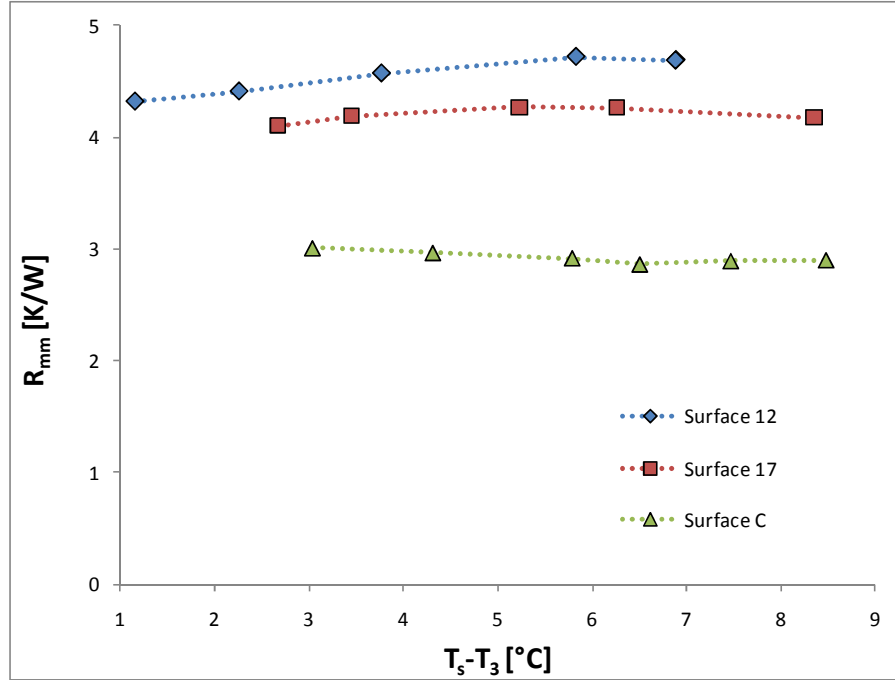


**Figure 5-13. Experimentally measured  $R_{mm}$  values**

#### 5.4.1. Heat Loss Evaluation and Calculation for a Sample Case

To be able to calculate the heat transferred to the working fluid in the microchannels, one needs to calculate the total amount of heat losses. For this calculation, the measured and known variables are: total heat input  $Q_i$ , mass flow rate  $\dot{m}$ , fluid temperature in the chamber  $T_{inf}$ , header temperature  $T_3$  and average surface temperature  $T_s = (T_{s1} + T_{s2} + T_{s3})/3$ . The calculation procedure has the following steps:

1. Calculate the thermal resistance values using Equations (5-1)-(5-3) , (5-10) and (9-2)
2. Evaluate resistive film temperature  $T_f$  based on Equations (5-8) and (5-9)

- Calculate the total heat loss to the ambient fluid  $Q_{af} = Q_i - Q_{AINi} + Q_{cl}$  by evaluating  $Q_{AINi}$  and  $Q_{cl}$  using Equations (5-4)-(5-7)
- Estimate the heat losses through the contact surfaces of microgrooved surface fin tips and manifold top face using  $Q_{mm} = \frac{T_s - T_3}{R_{mm}}$
- Calculate the total heat that was transferred to the working fluid through microgrooved surface microchannels by subtracting the total heat loss from the total heat input  $Q_{mg} = Q_i - Q_{af} - Q_{mm}$ .

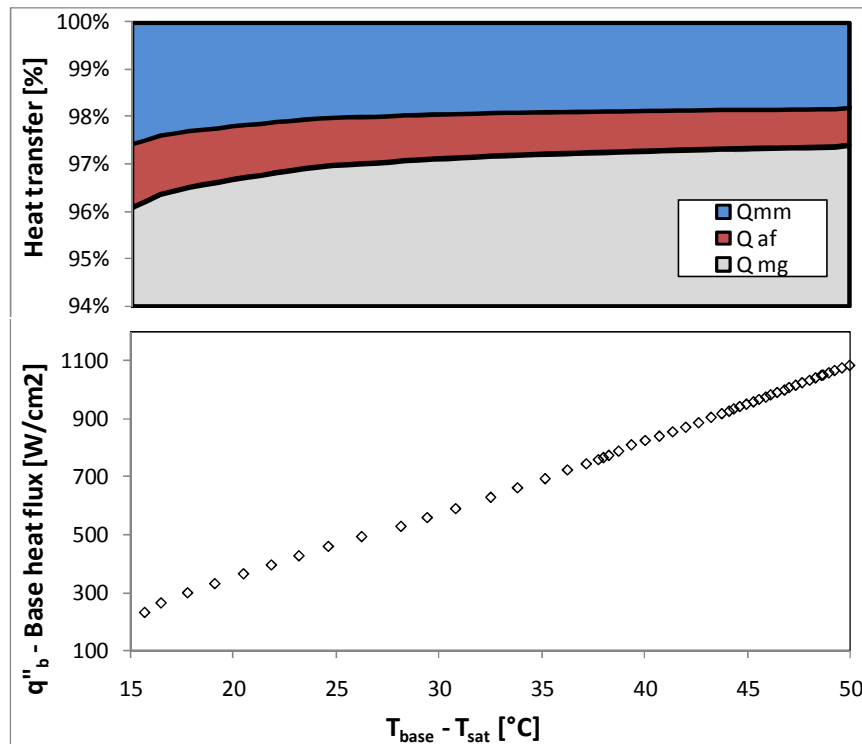


**Figure 5-14. Percentage of parasitic heat loss distribution and boiling curve for FFMHS using microgrooved Surface #17 at  $G=1000 \text{ kg/m}^2\text{s}$  constant mass flux**

The distribution of the incoming heat for one of the tested cases is shown in Figure 5-14. In the selected case the microgrooved Surface #17 was tested for saturated boiling with a microchannel mass flux of  $G=1000 \text{ kg/m}^2\text{s}$ . The base heat

flux in the boiling curve was calculated based on the heat transferred through microgrooved surfaces  $Q_{mg}$  and the base area of microgrooved surface. The percentage of heat losses is shown on the top of the boiling curve. The total heat losses were less than 4 % of the total input heat and they decreased with increased system heat flux.

## 5.5. Uncertainty Propagation Calculations

The calculated values, such as heat transfer coefficient or heat flux, are functions of measured values. For example, if the value of  $y$  is calculated based on several measured  $x_i$  values, it can be represented as  $y = f(x_1, x_2, x_3, \dots)$ . Each of the measured  $x_i$  values is associated with a random variability, which is referred to as its uncertainty. When the calculated value  $y$  is evaluated, the propagation of the measured variable uncertainties needs to be calculated. Here, the uncertainty of each of the  $x_i$  variables is assumed to be random and uncorrelated. The uncertainty of the measured value  $U_Y$  is then calculated based on:

$$U_Y = \sqrt{\sum_i \left( \frac{\partial Y}{\partial X_i} \right)^2 U_{X_i}^2} \quad (5-11)$$

All calculations were performed using Engineering Equation Solver (EES) software, which has specific subroutines that can numerically calculate and evaluate Equation (5-11). EES allows inputs of measurement uncertainty values as absolutes or as percentages of the full scale.

## **5.6. Summary**

An experimental test setup have been designed and fabricated. The test setup was equipped with thermocouples, pressure transducers and flow measuring flowmeters that can accurately measure the fluid and flow properties at various heat flux and mass flux inputs. R245fa was selected as the working fluid due to its favorable physical properties. The heat losses were evaluated based on a thermal resistance concept and for a typical set of two phase experimental data the total heat losses were predicted to be less than 4% of the total heat input. This test setup was used to collect the experimental results presented in next chapter.

## **CHAPTER 6: EXPERIMENTAL RESULTS ON FFMHS**

### **THERMAL PERFORMANCE**

This chapter explains the experimental procedure and experimental results obtained for FFMHS operating in single phase and two phase heat transfer modes. The first part of the chapter discusses experimental procedure that was employed to conduct the experiments, followed by the second part of the chapter which explains results for different microgrooved surfaces with different geometry and flow conditions and the findings obtained as a result of a comparative analysis. Finally, the chapter concludes with the critical heat flux observation and the explanation of possible mechanisms that can lead to CHF condition.

#### **6.1. Experimental Procedure**

The experimental procedure began by a system leakage test that consisted of three steps, which were repeated for each heater assembly. In the first step, the test setup was connected to a vacuum pump and evacuated until the system pressure dropped below 1 kPa. Then the system was closed and the vacuum pump was disconnected. The second step was to record the system pressure under vacuum conditions for no less than 10 hours. The system was considered leak-proof if the system pressure remained constant with respect to time. In case of leakage, leak detectors were used to find the leakages in the system. After leakages were fixed, steps one and two were repeated until the pressure in test setup remained constant for at least 10 hours. The third step was to charge the system with a working fluid. The

refrigerant R245fa, used in current experiments, has a saturation temperature of 14.9 °C at atmospheric pressure; therefore the system can be always kept under pressure, even at non operating conditions. There was no need to degas the system since there was no possibility of air leaking inside the system.

The experimental tests were performed by fixing the flow rate and increasing the heat flux gradually. The mass flow rate was controlled by adjusting the DC power of the gear pump. Saturation pressure of the system was kept constant by varying the chiller water temperature passing through the condenser. The tests were performed at inlet fluid pressures of  $220 \pm 20$  kPa. The heating power was regulated by the DC power supply that was controlled using a GPIB card connected to a PC. At each heat flux, data were recorded after the system reached steady-state conditions.

For single-phase tests, the heater temperature was kept below the saturation temperature of the incoming fluid to prevent boiling. Since single phase-heat transfer coefficients are not a function of heat flux, for each flow rate the heat flux was adjusted to create a temperature difference between the surface and fluid of more than 2°C to keep uncertainty of experiments at low values. The tests were performed by increasing the flow rate until these conditions could not be kept any longer.

Two-phase heat transfer experiments were performed for saturated boiling conditions. To maintain similar boiling conditions in all microchannels and at all heat fluxes, a two-phase test initiation procedure was performed. Before any data were taken, the system was set to desired flow rate. Heater power was gradually increased until boiling incipience occurred. This phenomenon could be visually observed through the glass of the test chamber or by real-time surface temperature

measurements. When boiling initiated, the vapor and liquid mixture was visible at the outlet of the heat sink, and a significant sudden temperature drop was observed in the surface temperatures. The heat input was then dropped to the desired value and the data collection process was initiated. It should also be noted that the current test setup was not designed for testing critical heat fluxes (CHF). Thermal mass of the heater assembly in the setup was extremely small; therefore, in the case of critical heat flux, the temperature jump in the heater assembly was high enough to destroy the assembly in a split-second. Therefore, data were first taken up to a fixed surface temperature that was sufficiently far from the critical heat flux for a given mass flux. The procedure was repeated by increasing the limiting surface temperature for each data set until the CHF condition occurred.

Control of fluid conditions before the inlet to the microgrooved surface was difficult to achieve. Although the inlet fluid temperature at the inlet to the test chamber could be controlled by the system pre-heater and subcooler, it was observed that the temperature in the inlet feed channel could be several degrees higher, closer to the saturation temperature of the fluid outside the heat sink in the test chamber. The energy gain was a result of the temperature difference between the fluid passing through the inlet tube, mixing chamber, feed channels and the saturation temperature in the test chamber. In most cases, the inlet to the test chamber was subcooled, and vapor in the test chamber condensed on the walls of the flow distribution header, supplying enough heat to increase the enthalpy of the refrigerant. The porous structure inside the mixing chamber also increased surface area and thus increased the heat transfer to the fluid. Since the tests were performed at constant inlet pressure, the

test chamber pressure varied depending on the pressure drop in the microgrooves, as did the saturation temperature. The final fluid temperature at the inlet to the microgrooved surface was also a function of fluid flow rate, which could change the energy carried in and out of the system, and the fluid velocity, which could change the convective heat transfer. Since controlling the inlet feed channel fluid temperature was not practical, tests were performed with varying subcooling values. Under these conditions, all tests were performed at subcooling values varying between 0.5 °C and 9.0 °C, and all recorded two-phase outlet qualities were greater than zero, suggesting that saturated boiling mode was present.

## 6.2. Data Reduction

The data reduction was performed based on the microgrooved surface and manifold schematic shown in Figure 6-1, which is the extended version of the computational domain shown previously in Figure 3-1. For a heat sink with a base area of  $L_s \times L_s$ , the number of microchannel systems running in parallel ( $N_{ch}$ ) is the number of channels under the footprint of manifold walls:

$$N_{ch} = 2N_{man} \frac{L_s - 2t_{man}}{W_{ch} + t_{fin}} \quad (6-1)$$

where  $N_{man}$  is the manifold number. The measured mass flux entering the heat sink is  $\dot{m}$ , therefore the mass flow rate in each microchannel is:

$$\dot{m}_{ck} = \frac{\dot{m}}{N_{ck}} \quad (6-2)$$

and the microchannel mass flux is calculated based on the cross section area of each microchannel:

$$G = \frac{\dot{m}_{ck}}{w_{ck} H_{ck}} \quad (6-3)$$

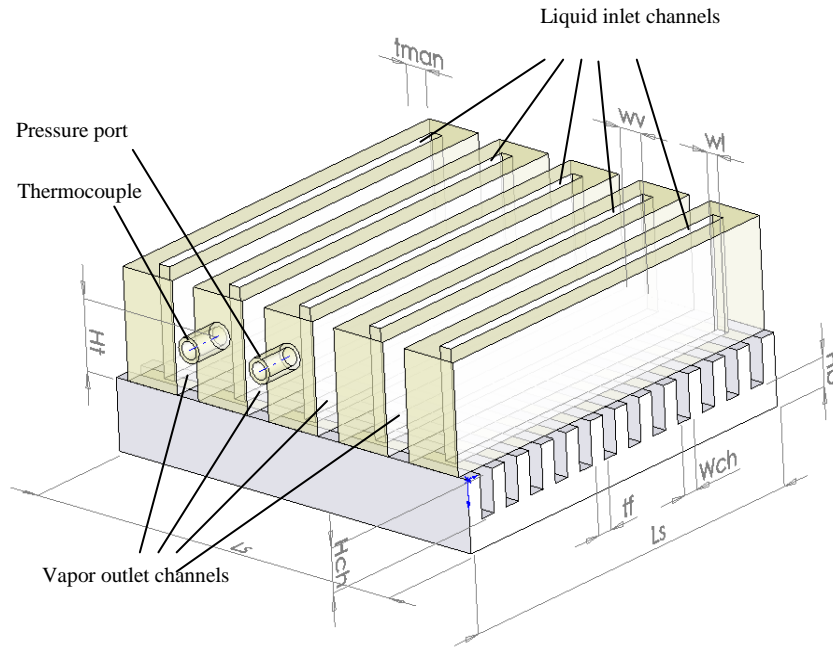


**Figure 6-1. Schematic of microgrooved surface and manifold configuration**

The total heat transferred to the working fluid is the difference between total heat input to the heater and the heat loss calculated based on the approach described in Section 5.4. The heat generated by the heater is the product of voltage and current passing through the heater; therefore:

$$q = VI - q_{loss} \quad (6-4)$$

The base heat flux is calculated based on base area as:

$$q_{base}'' = \frac{q}{A_h} = \frac{q}{L_s} \quad (6-5)$$

Similarly, the heat flux based on the heated microchannel walls can be defined as follows:

$$q_{wall}'' = \frac{q_{base}'' (w_{ch} + t_{fin})}{w_{ch} + 2H_{ch}} \quad (6-6)$$

In case of two-phase flow, the outlet quality can be calculated based on energy balance as:

$$x_{out} = \frac{\dot{m} (h_{in} - h_f) + q}{\dot{m} h_{fg}} \quad (6-7)$$

where  $h_{in}$ ,  $h_f$  and  $h_{fg}$  represent inlet, saturated liquid and evaporation enthalpies respectively.

In order to evaluate the heat transfer coefficients for both single-phase and two-phase flow tests, temperature information is needed. The surface temperature was averaged by the three surface thermocouples shown in Figure 5-8.

$$\bar{T}_s = \frac{1}{3} \sum_{i=1}^3 T_{s,i} \quad (6-8)$$

The thermocouples were located at the center plane between the bottom face and microchannel base and the half distance is defined as  $\delta_t = H_{base}/2$ . Then the base temperature can be evaluated as:

$$\bar{T}_{base} = \bar{T}_s + \frac{q_{base}'' \delta_t}{k_{cu}} \quad (6-9)$$

Then, the heat transfer coefficient defined for base heat sink area and for single-phase heat transfer is calculated as:

$$h_{base} = \frac{q_{base}''}{\bar{T}_{base} - T_{in}} \quad (6-10)$$

where  $T_{in}$  is the inlet fluid temperature measured in the inlet feed channel. A similar heat transfer coefficient can be defined for two-phase heat transfer as:

$$h_{base} = \frac{q_{base}''}{\bar{T}_{base} - \bar{T}_{sat}} \quad (6-11)$$

where  $\bar{T}_{sat}$  is the average saturation temperature. This value can be evaluated using the assumption that the saturation temperature changes linearly along the microchannel:

$$\bar{T}_{sat} = \frac{T_{sat}(P_{ch,i}) + T_{sat}(P_{ch,o})}{2} \quad (6-12)$$

To calculate saturation pressures at the inlet and outlet of the microchannel, defined as  $P_{ch,i}$  and  $P_{ch,o}$  respectively, the absolute pressure values at these locations need to be calculated. Pressure measurement in the test chamber was performed at two locations. The first pressure port was located at one of the inlet manifolds as shown in Figure 6-1, and it measures the static pressure  $P_1$  at this location. The second pressure port was located at the bottom of the test chamber and it measures the static pressure of the fluid  $P_2$  in the test chamber. Two factors contribute to pressure change between the measurement points and points where the pressure needs to be evaluated. First, pressure losses are created at the inlet and outlet due to area contraction and expansion. These kinds of losses are irreversible and are dissipated into heat. The second factors are the reversible pressure changes created due to flow area variation and can which be calculated using Bernoulli's equation. Based on this discussion,  $P_{ch,i}$  and  $P_{ch,o}$  can be defined as:

$$P_{ch,i} = P_1 + \rho \frac{V_{ch,i}^2}{2} (\sigma^2 - 1) - \Delta P_c \quad (6-13)$$

and

$$P_{ch,o} = P_2 - \rho \frac{V_{ch,o}^2}{2} + \Delta P_e \quad (6-14)$$

where the area contraction ratio is defined as  $\sigma = \frac{w_{ch}}{t_{fin} + w_{ch}}$ . The single-phase pressure loss due to contraction is:

$$\Delta P_c = K_c \rho \frac{V_{ch,i}^2}{2} \quad (6-15)$$

where  $V_{ch,i}$  is the fluid velocity at the inlet of the microchannel and  $K_c$  is the contraction coefficient defined as:

$$K_c = \left( \frac{1}{C_c} - 1 \right)^2 \quad (6-16)$$

Here,  $C_c$  is the jet contraction coefficient calculated as:

$$C_c = 0.6501 - 0.2093\sigma + 0.3863\sigma^2 \quad (6-17)$$

where area ratio  $\sigma$  is defined between  $0.2 \leq \sigma \leq 0.9$  (Webb, 2006).

The outlet pressure loss due to flow expansion needs to be calculated separately for single-phase and two-phase flow cases. For single-phase the loss is modeled as:

$$\Delta P_e = K_e \rho \frac{V_{ch,o}^2}{2} \quad (6-18)$$

where  $V_{ch,o}$  is the fluid velocity in the microchannel before the expansion, and the expansion loss coefficient is:

$$K_e = (1 - \sigma)^2 \quad (6-19)$$

For two phase flows, the expansion pressure drop can be calculated using following relation: (Ghiaasiaan, 2008)

$$P_{ch,o} = P_2 - \frac{G^2}{2\rho_l} (1 - \sigma^2) \left[ 1 + x \left( \frac{\rho_l}{\rho_g} - 1 \right) \right] \quad (6-20)$$

The heat transfer coefficient can be also calculated based on the wet microchannel area. For this purpose, the temperatures at the fin base are calculated based on thermal resistance of the copper base as:

$$\bar{T}_{base,fin} = \bar{T}_s - \frac{q_{base}'' \delta_t}{k_{cu}} \quad (6-21)$$

and the fin efficiency is defined as:

$$\eta_{fin} = \frac{q_{fin}}{hA_{fin}\theta_b} = \frac{\tanh mH_{ch}}{mH_{ch}} \quad (6-22)$$

where  $m$  is a constant evaluated as:

$$m^2 = \frac{h_{wall}P}{k_{cu}A_c} = \frac{h_{wall}2H_{ch}}{k_{cu}H_{ch}t_{fin}} = \frac{2h_{wall}}{k_{cu}t_{fin}} \quad (6-23)$$

The two-phase heat transfer coefficient based on microchannel wall area is then calculated as follows:

$$h_{wall} = \frac{q_{base}'' (w_{ch} + t_{fin})}{(2H_{ch}\eta_{fin} + w_{ch})(\bar{T}_{base,fin} - \bar{T}_{sat})} \quad (6-24)$$

### 6.3. Single Phase Heat Transfer and Pressure Drop

The heat transfer coefficients and pressure drops resulting from single-phase experimental tests are shown in Figure 6-2 and Figure 6-3. The experimental results were compared with numerical simulations performed for each microgrooved surface.

The numerical simulation procedure described in Section 3.3 was applied here except that refrigerant R-245fa was used instead of water as the working fluid. Also the fin tips selected were angled with a sharp edge, and the fin shape was slightly bent, similar to the profile pictures shown in Figure 2-2.

The heat transfer coefficient curves calculated for the base area and the pressure drop values for all three surface samples follow a monotonic and linear increase with mass flux on a log-log plot. This trend represents a power law dependence on flow rate. Similar observations were reported by (Copeland, 1995a) and (Ryu et al., 2003). The numerical and experimental values match reasonably well with most of the points lying in the uncertainty margin of experimental data, while better matching is achieved at high flow rates.

One important result that the figures imply is the relative dependence of mass flux on heat transfer coefficients and pumping power values. For example, the FFMHS utilizing microgrooved Surface #12 had a hydraulic diameter and flow area almost twice higher than Surface #C. When both samples were tested at a mass flux around  $1000 \text{ kg/m}^2\text{s}$  the pressure drop resulting from FFMHS with Surface #C was an order of magnitude higher than the values obtained for Surface #12. For the same given mass flux, when comparing for heat transfer coefficients, the difference was much smaller, with an increase of about only three times for Surface #C. This in turn also confirms the trend of Pareto fronts obtained from the single phase optimization study, where the pumping power changed over a much larger range compared with heat transfer coefficients.

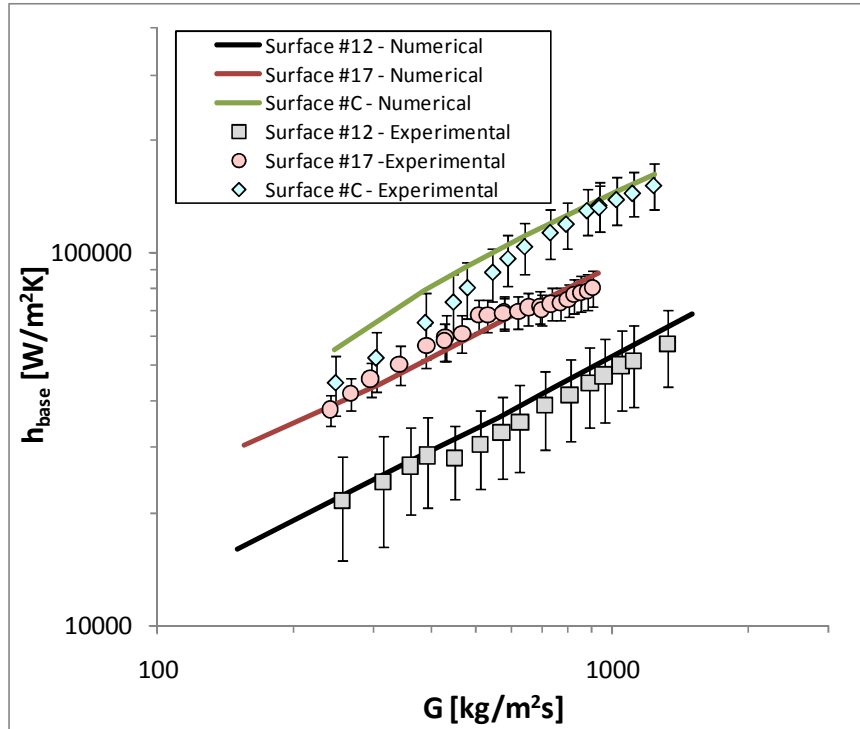


Figure 6-2. Single-phase results of experimental and numerical heat transfer coefficients

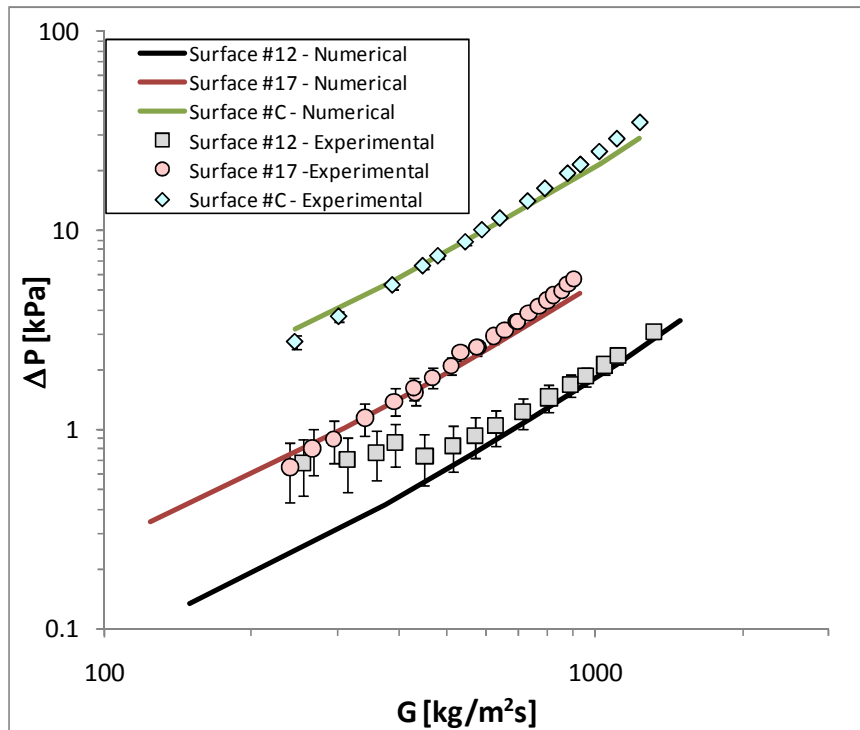
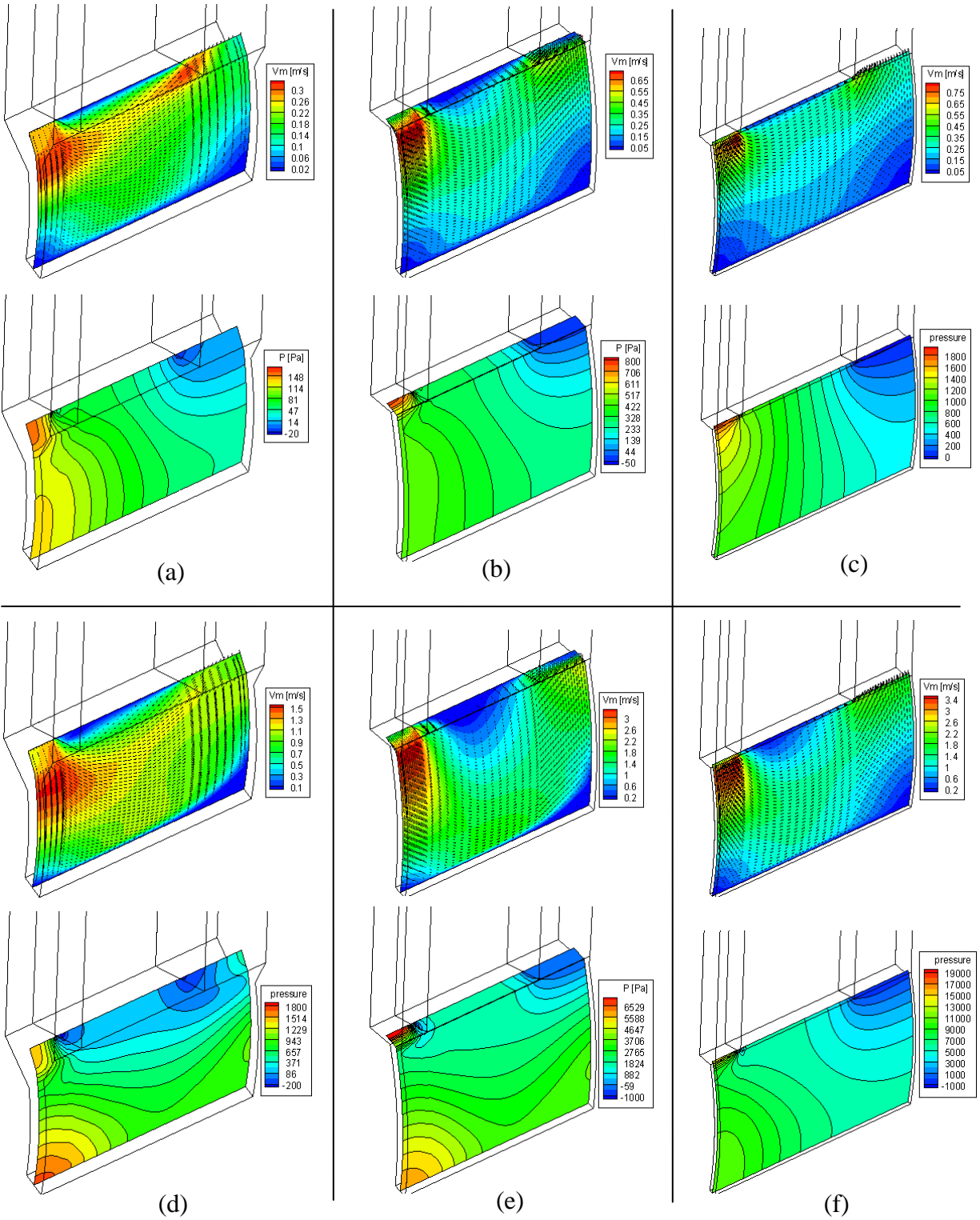


Figure 6-3. Single-phase results of experimental and numerical pressure drop values

Another interesting observation that was noticed for numerical simulations results was the different characteristic of flow at different mass fluxes and channel geometries. In order to explain this effect for the currently selected microgrooved surfaces, velocity and static pressure distribution along the channel center plane for each surface at low mass flux of  $G=200 \text{ kg/m}^2\text{s}$  and at high mass flux of  $G=1000 \text{ kg/m}^2\text{s}$  is presented in Figure 6-4 (a)-(f). This range of mass flux is the approximate range used for each microgrooved surface in two phase experimental tests. The inertia of fluid that flows in a channel is proportional to square of velocity while the pressure drop is proportional to channel length and mass flux and reversely proportional to channel hydraulic diameter. At low mass flux and low hydraulic diameter case (Figure 6-4 (c)) the inertia forces of the incoming fluid is smaller comparing to viscous forces. Therefore the fluid favors flowing through the path having the least flow resistance. In this case, this path is the minimum length between inlet and outlet feed channels, right under the manifold. This short bypass of the fluid creates a velocity stratification with higher velocities on the top of the channel and lower velocities close to the bottom region. The static pressure distribution for this case is more uniform with maximum pressure located at the inlet of the channel. When keeping the mass flux constant and increasing the hydraulic diameter (Figure 6-4 (a) and (b)), the inertia forces remain the same but viscous forces and flow resistance decrease significantly. Therefore the flow regime shifts to inertia dominated regime where the inertia forces can push the incoming liquid down to the bottom of the channel creating an impingement zone. The impingement zone is located at the bottom of the microchannel and under the inlet feed channel



**Figure 6-4. Velocity and static pressure distribution in the center plane for (a) Surface #12,  $G=200 \text{ kg/m}^2\text{s}$ , (b) Surface #17,  $G=200 \text{ kg/m}^2\text{s}$ , (c) Surface #C,  $G=200 \text{ kg/m}^2\text{s}$ , (d) Surface #12,  $G=1000 \text{ kg/m}^2\text{s}$ , (e) Surface #17,  $G=1000 \text{ kg/m}^2\text{s}$ , (f) Surface #C,  $G=1000 \text{ kg/m}^2\text{s}$ ,**

The effect of the impingement can be observed looking to the static pressure distribution map. When the incoming fluid flows towards the impingement zone, it starts to decelerate, it is forced to turn the 90° bend and it accelerates by moving toward the straight part of the microchannel. During the deceleration, the momentum of the fluid is conserved by rising up the static pressure which creates a secondary maximum pressure zone in the impingement zone. The same effect can be observed by keeping the hydraulic diameter constant and increasing the mass flux (Figure 6-4 (f)). With the increase in flow velocity, the inertia forces start to become dominant and overcome the viscous forces by pushing the fluid down to the bottom of the channel and creating the impingement zone. Overall, the flow conditions at mass flux of  $G=1000 \text{ kg/m}^2\text{s}$  looks to be inertia dominated for all microgrooved surface while at mass flux of  $G=200 \text{ kg/m}^2\text{s}$  the Surface #12 is inertia dominated while Surface #C is viscous dominated flow. Surface #17 looks to be in transition between two regimes.

#### **6.4. Two-Phase Heat Transfer and Pressure Drop**

The heat transfer coefficients and pressure drop data of two-phase heat transfer in FFMHS were collected for each of the selected three microgrooved surfaces. The experimental test conditions and uncertainty values for FFMHS utilizing microgrooved Surface #12, Surface #17 and Surface #C are given in Table 6-1, Table 6-2 and Table 6-3, respectively. For all tests the subcooling was kept below 10 °C and the outlet quality was maintained between zero and unity, indicating saturated boiling flow. The experimental tests were performed in the following order: Surface #17, Surface #12 and Surface #C. As noted before, the test section was mainly designed for collecting heat transfer coefficient and pressure drop data and

was not feasible for testing CHF conditions. Preliminary tests showed that the heater assembly has a high risk of burnout at CHF, due to low thermal mass of the system and low response frequency of the control loop. Successful CHF data was obtained only for Surface #17 for several flow rates and will be presented in later sections. For the rest of the chapter, the heat transfer coefficients ( $h$ ) are based on and calculated for the base heat sink area ( $h_{base}$ ) unless otherwise specified.

**Table 6-1. Experimental test conditions for FFMHS utilizing microgrooved Surface #12**

Test number	Nominal Mass Flux	Tested Mass Flux	Inlet Static Pressure	Sub cooling	$q''_{base}$ range	Outlet quality range	Uncertainty of $h_{base}$	Uncertainty of $h_{wall}$
	[kg/m <sup>2</sup> s]	[kg/m <sup>2</sup> s]	[kPa]	[°C]	[W/cm <sup>2</sup> ]	[-]	%	%
<b>Test #1-S12</b>	300	311-318	200.3-204.4	0.1-2.3	16.0-392.9	0.01-0.43	3.1-6.1	5.0-7.6
<b>Test #2-S12</b>	400	397-403	202.5-206.9	0.1-2.0	32.2-468.4	0.01-0.41	3.0-6.3	4.9-7.8
<b>Test #3-S12</b>	600	601-611	204.0-207.1	0.9-2.1	48.5-541.5	0.01-0.31	3.4-6.5	5.3-8.0
<b>Test #4-S12</b>	800	796-804	204.8-207.9	1.1-1.7	65.9-588.5	0.02-0.25	3.6-5.3	5.5-6.9
<b>Test #5-S12</b>	1000	990-1003	202.0-206.3	1.5-2.7	81.6-508.5	0.01-0.16	3.6-5.3	5.5-6.9
<b>Test #6-S12</b>	1200	1214-1228	202.5-204.4	2.5-4.2	81.4-666.8	0.01-0.16	3.9-6.0	5.8-7.7

**Table 6-2. Experimental test conditions for FFMHS utilizing microgrooved Surface #17**

Test number	Nominal Mass Flux	Tested Mass Flux	Inlet Static Pressure	Sub cooling	$q''_{base}$ range	Outlet quality range	Uncertainty of $h_{base}$	Uncertainty of $h_{wall}$
	[kg/m <sup>2</sup> s]	[kg/m <sup>2</sup> s]	[kPa]	[°C]	[W/cm <sup>2</sup> ]	[-]	%	%
<b>Test #1-S17</b>	200	199-202	199.0-205.4	2.4-3.4	25.2-462.2	0.01-0.67	2.6-17.1	4.7-21.0
<b>Test #2-S17</b>	300	296-302	200.2-205.3	1.2-1.8	24.0-572.0	0.01-0.57	3.3-16.0	5.3-18.8
<b>Test #3-S17</b>	400	393-402	199.1-203.6	1.2-2.1	32.2-728.2	0.01-0.54	3.9-11.1	5.8-13.3
<b>Test #4-S17</b>	500	495-503	200.0-2006.2	1.3-3.4	65.9-806.9	0.03-0.45	4.3-10.2	6.3-12.2
<b>Test #5-S17</b>	600	593-605	196.2-205.1	1.2-2.4	65.97-720.3	0.02-0.34	4.5-7.8	6.6-9.7
<b>Test #6-S17</b>	700	694-705	197.3-204.7	1.4-3.7	98.5-963.7	0.03-0.39	4.9-8.4	7.0-10.5
<b>Test #7-S17</b>	800	794-804	197.4-205.3	1.6-4.6	66.0-1021.8	0.01-0.35	5.0-8.6	7.2-10.6
<b>Test #8-S17</b>	1000	954-988	202.1-211.8	2.6-5.6	230.5-1099.8	0.05-0.31	5.1-5.2	7.1-7.4
<b>Test #9-S17</b>	1200	1190-1209	200.2-206.9	3.1-7.4	228.0-1154.3	0.03-0.24	5.3-5.4	7.7-8.1
<b>Test #10-S17</b>	1400	1396-1438	199.2-207.6	5.4-8.5	264.1-1229.9	0.02-0.20	5.5-6.9	7.9-9.1

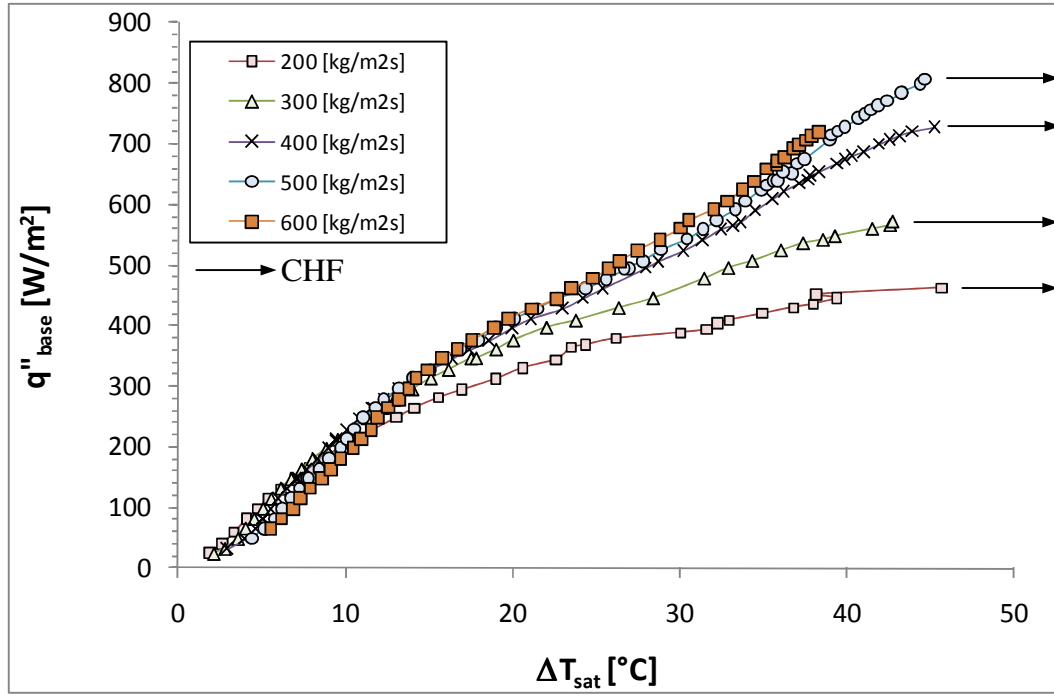
**Table 6-3. Experimental test conditions for FFMHS utilizing microgrooved Surface #C**

<b>Test number</b>	<b>Nominal Mass Flux</b>	<b>Tested Mass Flux</b>	<b>Inlet Static Pressure</b>	<b>Sub cooling</b>	<b>q''<sub>base</sub> range</b>	<b>Outlet quality range</b>	<b>Uncertainty of h<sub>base</sub></b>	<b>Uncertainty of h<sub>wall</sub></b>
	[kg/m <sup>2</sup> s]	[kg/m <sup>2</sup> s]	[kPa]	[°C]	[W/cm <sup>2</sup> ]	[-]	%	%
<b>Test #1-SC</b>	200	195-205	192.3-201.9	1.8-3.4	65.5-354.4	0.08-0.57	5.0-12.0	7.2-18.6
<b>Test #2-SC</b>	300	296-306	200.6-207.0	2.6-7.2	49.7-602.9	0.02-0.58	4.1-14.8	5.9-21.3
<b>Test #3-SC</b>	400	394-407	204.9-221.8	3.8-10.1	97.8-760.3	0.05-0.58	4.3-11.9	6.4-18.2
<b>Test #4-SC</b>	500	493-510	207.9-214.2	5.3-12.3	65.5-916.6	0.01-0.53	4.5-13.7	6.7-19.5
<b>Test #5-SC</b>	600	595-614	210.8-236.9	5.9-13.3	97.8-926.4	0.01-0.42	5.9-12.4	8.3-18.9
<b>Test #6-SC</b>	700	697-710	203.9-210.2	3.6-6.1	98.2-855.2	0.01-0.33	6.4-12.9	9.3-19.8
<b>Test #7-SC</b>	800	804-815	201.5-213.9	3.3-8.4	165.6-900.5	0.04-0.28	6.8-9.7	10.0-13.8
<b>Test #8-SC</b>	1000	1027-1082	201.2-217.9	5.6-9.9	196.8-831.9	0.01-0.17	7.6-10.6	11.4-15.6

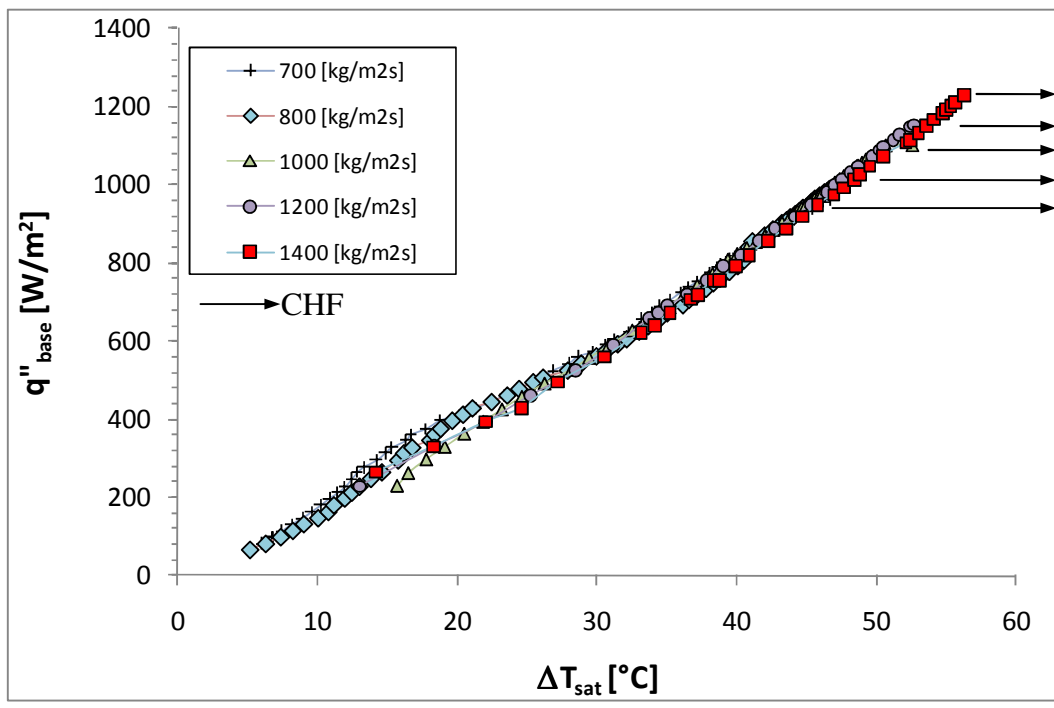
### 6.4.1. Surface #17

The two-phase experimental tests for FFMHS utilizing microgrooved Surface #17 were performed at ten different mass flux conditions ranging from 200 kg/m<sup>2</sup>s to 1400 kg/m<sup>2</sup>s, as shown in Figure 6-5 (a) and (b). The boiling curves are plotted for the base heat flux  $q_{base}''$  versus wall superheat  $\Delta T_{sat}$ , which is the temperature difference between average base surface temperature and average saturation temperature.

The trend of the curves can be summarized as follows. For low to medium heat fluxes of  $q_{base}'' < 300 \text{ W/cm}^2$ , the boiling curves show almost a linear increasing trend with slightly different slopes. In this region, the wall superheat increases when going to higher mass fluxes at a constant heat flux. This implies higher heat transfer efficiency at lower mass fluxes. On the other hand, when heat fluxes increase above  $q_{base}'' > 300 \text{ W/cm}^2$ , the trend is reversed, and departures from the main trend are observed, for low to medium mass fluxes of  $200 < G < 600 \text{ kg/m}^2\text{s}$ . The departing curves have a smaller slope on the chart, which indicates less heat transfer for a given wall superheat; therefore the heat transfer efficiency is expected to decrease compared with the main trend. The slope will continue to decrease until reaches CHF conditions. As shown in the figure, the heat flux values where the CHF was obtained are shown with the black arrow, denoting a large temperature jump for a small increase in heat flux.



(a)



(b)

**Figure 6-5 Boiling curves for FFMHS Surface #17 for (a)  $200 < G < 600 \text{ kg/m}^2\text{s}$  and (b)  $700 < G < 1400 \text{ kg/m}^2\text{s}$**

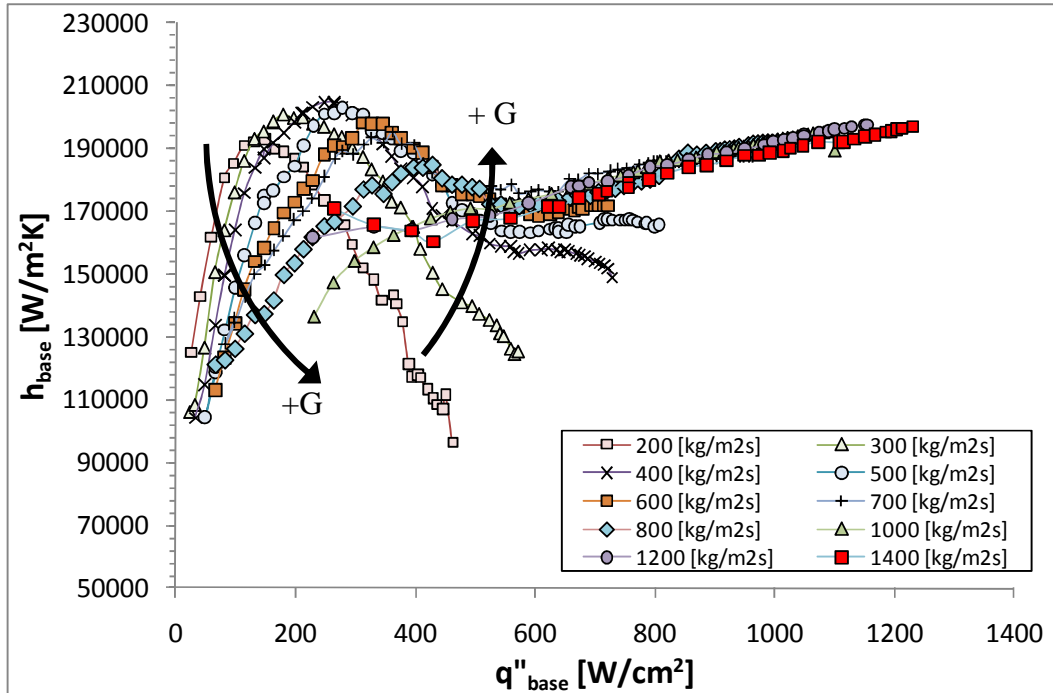
For medium to high mass fluxes and heat fluxes of  $G > 600 \text{ kg/m}^2\text{s}$  and  $q''_{base} > 600 \text{ W/cm}^2$ , the boiling curves are almost overlapped and increase in a linear fashion. In contrast to the low mass flux cases, the CHF condition here is achieved along the straight overlapping part of the boiling curve and does not show an early performance degradation. The maximum achievable heat flux was  $q''_{base} = 1.23 \text{ kW/cm}^2$  corresponding to a wall superheat of  $\Delta T_{sat} = 56.2 \text{ }^\circ\text{C}$ .

For the same set of data, the heat transfer coefficients based on heat sink base area versus base heat flux variation are given in Figure 6-6 (a). This classification is more convenient for heat sink designers since the definitions are based on the targeted cooling area and are not dependent on enhanced area parameters such as channel aspect ratio or fin efficiency. Figure 6-6 (b) shows the heat transfer coefficients based on wet channel area versus outlet quality. This definition is useful in comparing the hydraulic and thermal performance of different microchannel geometries of microgrooved surfaces. It is important to note that these two graphs are not independent because for a fixed heat flux and mass flux there exists only one outlet quality. In other words, for a constant mass flux case, to change the outlet equilibrium quality the heat flux needs to be changed and vice versa.

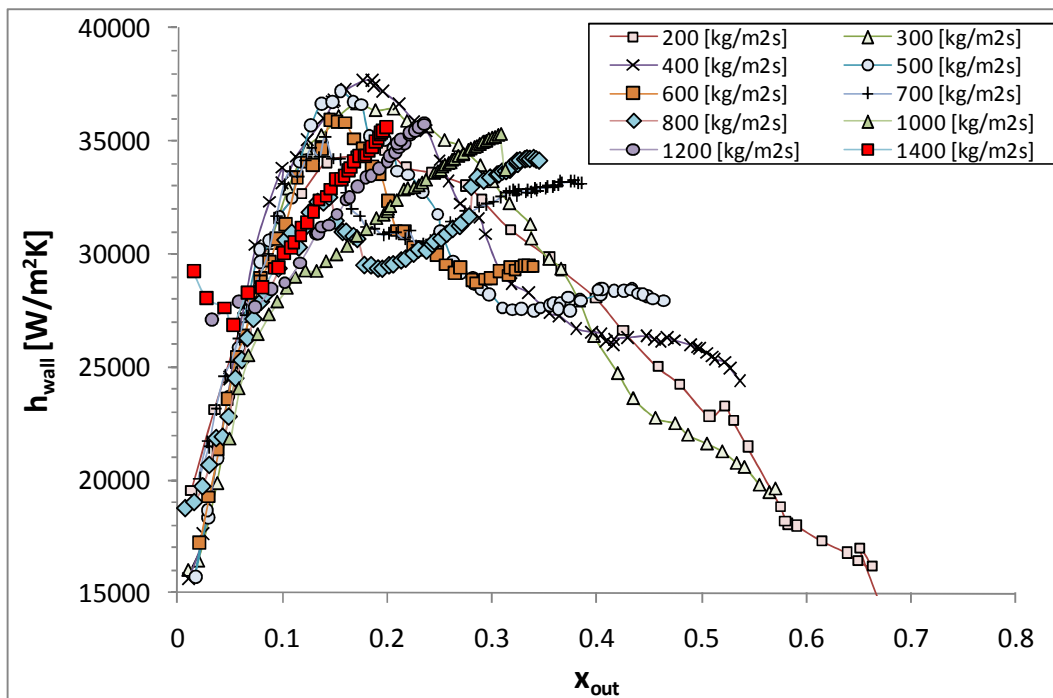
As shown in Figure 6-6 (a), at mass fluxes below  $G < 500 \text{ kg/m}^2\text{s}$  the heat transfer coefficient curves show a bell-like curve starting with initially increasing trend and then decreasing gradually until the CHF occurs. Here, the increase in heat transfer coefficients for all mass fluxes has a similar slope, while the decreasing trend is more dependent on mass flux. The increase in mass flux decreases the slope of the decreasing part of the curve, indicating an improvement in heat transfer and less

severe performance degradation. The maximum peak point remains between  $190,000 < h_{base} < 200,000$  W/m<sup>2</sup>K and shifts towards higher heat fluxes with increasing mass flux. It is interesting to note from Figure 6-6 (b) that the maximum heat transfer coefficients at these flow rates remain almost constant at  $x_{out} \approx 0.15$ . Here the steep increasing trend of heat transfer coefficients may suggest a flow regime mostly dominated by nucleate boiling which is a function of surface heat flux. The decreasing trend observed after the maximum may be the result of local dryouts which become less severe as the mass flux increases.

For heat transfer coefficients obtained for higher mass fluxes of  $G > 500$  kg/m<sup>2</sup>s, the trend is shifted as seen in Figure 6-6 (a). As the mass flux increases, the peak previously seen at lower mass fluxes further decreases and diminishes after  $G=1000$  kg/m<sup>2</sup>s. At the same time, the previously decreasing trend is also eliminated, and for high mass fluxes, both effects create a slow but monotonically increasing trend. More interestingly, all curves collapse altogether, forming a single line on the graph. This trend may suggest a convective boiling-dominated heat transfer regime since the heat transfer coefficients are slightly dependent on heat flux but are more dependent on outlet quality and mass flux (Figure 6-6 (b)). Another observation that results from these graphs is the trend of heat transfer coefficient before reaching CHF. For low mass fluxes and the bell curve-like trend the CHF always occurs when the heat transfer coefficients have a decreasing trend. On the other hand, at high mass fluxes, the boiling crisis phenomenon occurs on the curve shown in Figure 6-6 (a) where all the heat transfer coefficients are overlapped and have a slightly increasing trend.



(a)



(b)

**Figure 6-6. (a) Heat transfer coefficient based on base area versus base heat flux and (b) heat transfer coefficient based on wetted area versus outlet quality for FFMHS Surface #17**

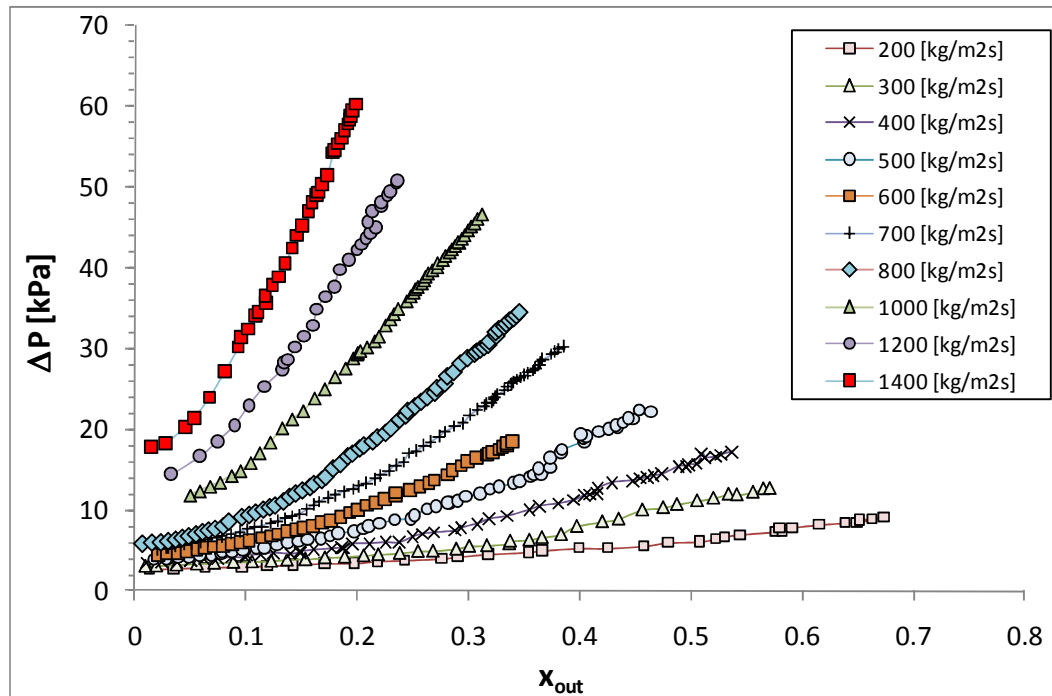


**Figure 6-7. Pressure drop values versus outlet quality for FFMHS Surface #17**

The pressure drop variation versus outlet equilibrium quality are shown in Figure 6-7. As expected, the pressure drop of the FFMHS is a function of both mass flux and outlet quality. For a constant mass flux, the pressure drop values show an exponential-like increase at low outlet quality values and a linear trend at higher outlet qualities. At the lowest tested mass flux of  $G=200 \text{ kg/m}^2\text{s}$  the system pressure drop reads less than 10 kPa, corresponding to a saturation temperature change of less than  $1.5^\circ\text{C}$ . On the other hand, when the system works at high mass fluxes the saturation temperature change can be significant and should be carefully considered in the design stages. A very large saturation temperature difference can increase the surface temperature non-uniformity of the heat sink base. For example, for  $G=1400 \text{ kg/m}^2\text{s}$  the maximum pressure drop was 60.4 kPa, which corresponds to a saturation temperature variation of  $7.8^\circ\text{C}$ .

### 6.4.2. Surface #12

The second set of experimental tests was performed on FFMHS microgrooved Surface #12. As shown in Table 2-1, all tested surfaces had similar microchannel heights and had the same fin-thickness-to-microchannel-width ratio of 2. The fin thickness and microchannel width of Surface #12 were about 1.5 times larger than those of Surface #17, which decreased the active enhanced surface area created by the microgrooved surface. To protect the heater assembly, no CHF tests were performed for this set of data. The wall superheat was kept below 45 °C for all tests.

For Surface #12, boiling curves for the tested mass fluxes are shown in Figure 6-8. For a given mass flux, the general trend is increased wall superheat with increase in heat flux. At heat fluxes below 300 W/cm<sup>2</sup> the boiling curves show little deviation, and for a constant heat flux, slightly higher wall superheats are achieved at higher mass fluxes. Above 300 W/cm<sup>2</sup> the curves come closer again, and starting with lower mass fluxes, separation from the trend occurs. Each curve departs from the main trend, making a smaller slope on the boiling curve, indicating performance degradation, which will eventually lead to CHF conditions. The maximum heat flux achievable for this data set was  $q_{base}'' = 666.7 \text{ W/m}^2$  corresponding to a wall superheat of 43.8 °C.

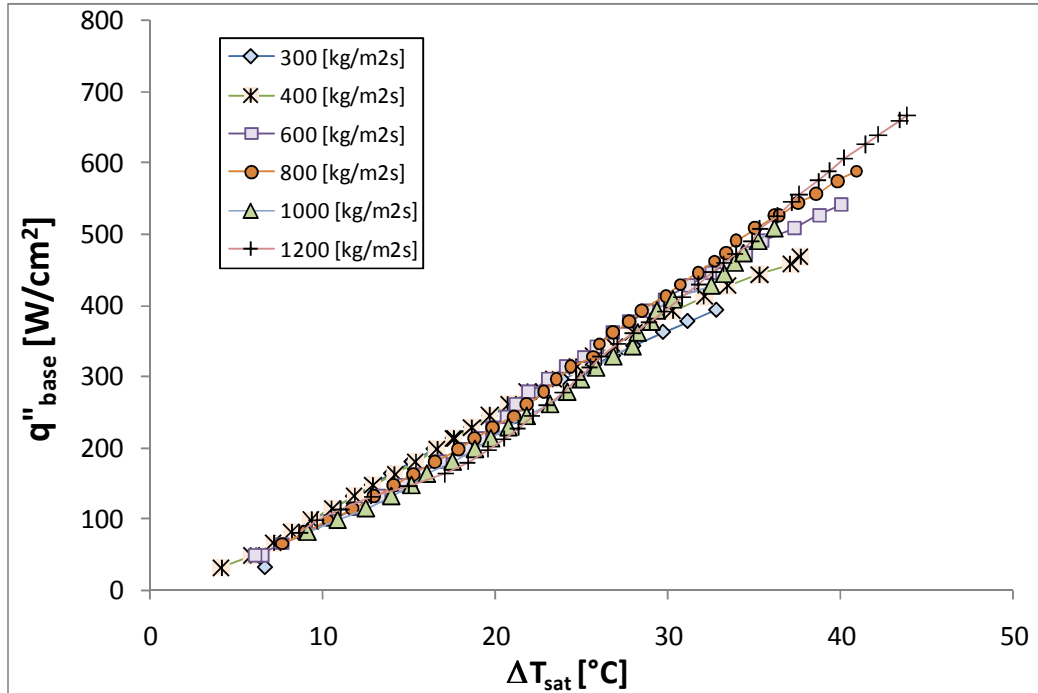
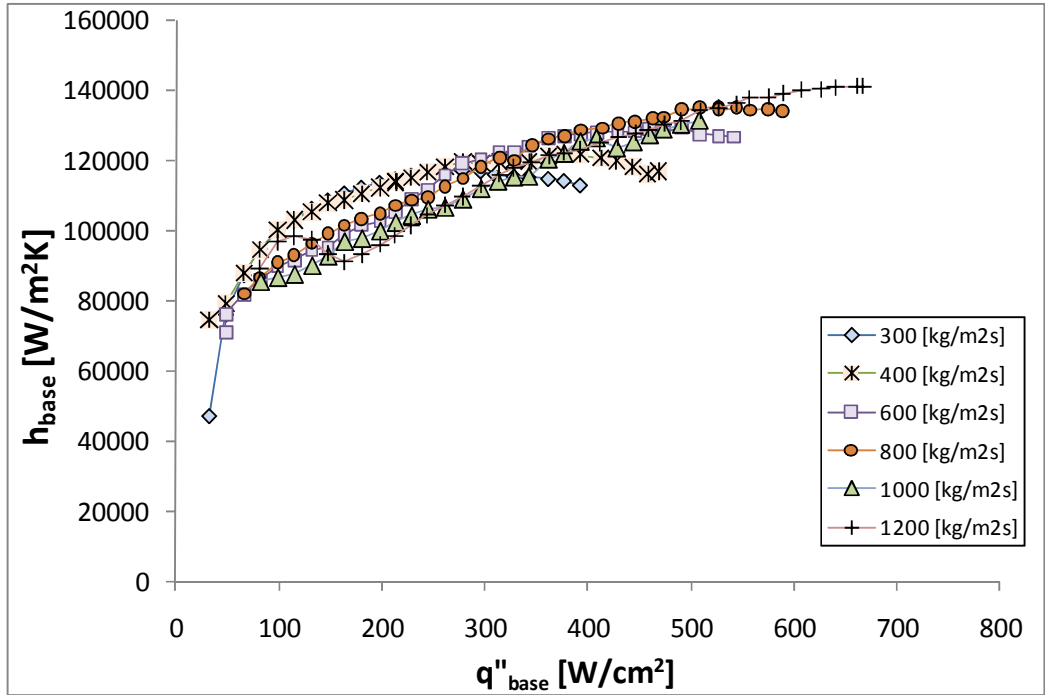
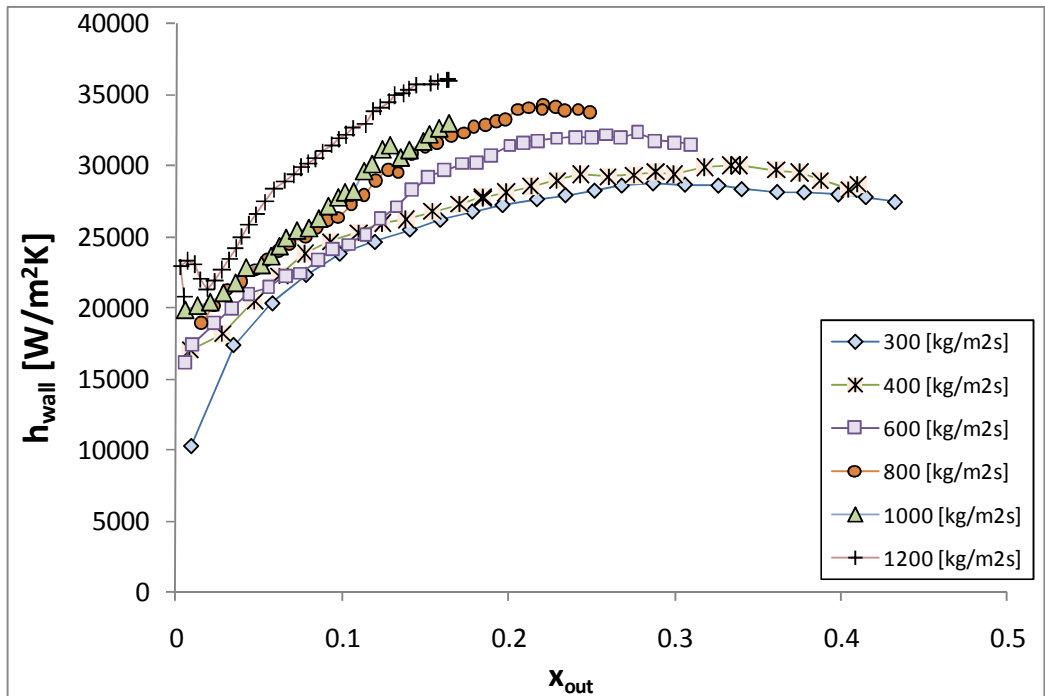


**Figure 6-8. Boiling curves for FFMHS Surface #12**

The heat transfer coefficients defined for the base area and for the wet microchannel area are given in Figure 6-9 (a) and (b). First, for the tested mass flux range, all heat transfer coefficient curves show a similar trend. As seen in Figure 6-9 (a), the general trend of heat transfer coefficients with increase in base heat flux is a gradual increase until a mild decrease begins. The curves have very similar slopes, and heat transfer coefficient values do not deviate much from each other. Also, the heat transfer maximum points observed for Surface #17 that occurred at low outlet qualities were not so distinguished here.



(a)



(b)

**Figure 6-9. Heat transfer coefficient based on base area versus base heat flux and (b) heat transfer coefficient based on wetted area versus outlet quality for FFMHS Surface #12**

The heat transfer coefficients versus outlet quality curves shown in Figure 6-9 (b) indicate that the heat transfer coefficient curves are almost similar in trend but start to shift to higher values when going to higher mass fluxes. For example, the corresponding heat transfer coefficient at quality of 10% for  $G=300 \text{ kg/m}^2\text{s}$  is  $23,000 \text{ W/m}^2\text{K}$ , while increasing the mass flux to  $G=1200 \text{ kg/m}^2\text{s}$  at the same outlet quality generates a heat transfer coefficient of  $h=30,000 \text{ W/m}^2\text{K}$ . This may be the result of an increase in convective boiling due to the increase in vapor velocity. The effect of velocity increase is more pronounced in pressure drop curves given in Figure 6-10. Interestingly, the curves tend to show an almost linear trend with increase in outlet quality. Also, as expected, the slope of the curve increases as the mass fluxes increase.

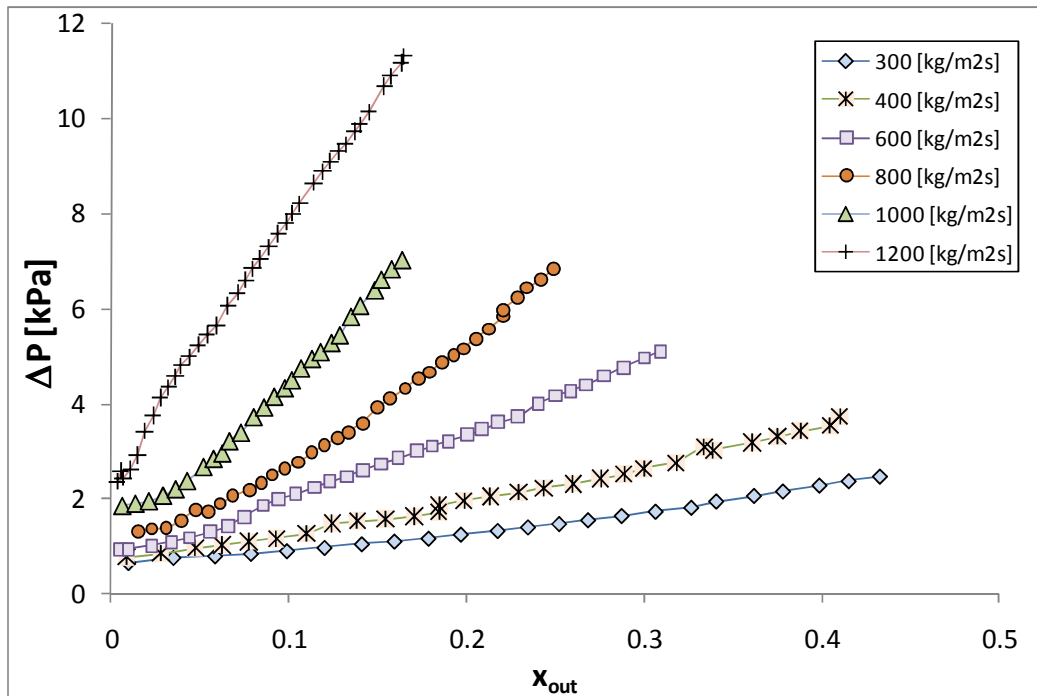


**Figure 6-10. Pressure drop values versus outlet quality for FFMHS Surface #12**

### 6.4.3. Surface #C

The last FFMHS that was tested experimentally utilizes microgrooved Surface #C, which is the surface with the highest channel aspect ratio and smallest channel width. As seen in Table 2-1, the channel width and fin thickness for Surface #C is about twice as small as that for Surface #17 and three times smaller than Surface #12. The corresponding boiling curve for the tested mass flux range is given in Figure 6-11. For low to medium base heat fluxes, less superheat is needed at low mass fluxes to achieve the same heat flux. In other words, the high mass flux values in this region are shifted to the right on boiling curve, which represents a decrease in heat transfer efficiency. By increasing the heat flux to higher values, two trends are visible. First, the boiling curves will start to come closer and eventually overlap at high mass fluxes. This trend is similar to the results obtained for FFMHS utilizing Surface #17 at high mass fluxes and Surface #12 at all major mass fluxes. The second trend departs from this trend starting from lower mass fluxes. The departing curves have a lower slope, indicating higher wall superheat for less base heat flux. Although no CHF tests were performed for the current case, the decrease in curve slope may indicate CHF conditions were approached. The maximum base heat flux achieved with this configuration was  $q_{base}'' = 926 \text{ W/cm}^2$ , which was obtained for a mass flux of  $G=600 \text{ kg/m}^2\text{s}$  at a wall superheat of  $41.4 \text{ }^\circ\text{C}$ . It should be noted, however, that higher heat fluxes are expected to be achieved with higher mass fluxes. All tests performed for mass fluxes exceeding  $G=600 \text{ kg/m}^2\text{s}$  were stopped before reaching a pressure drop value of about  $DP=60 \text{ kPa}$  to protect the pressure transducer.

The heat transfer coefficients are given in Figure 6-12 (a) and (b) versus base heat flux and outlet quality values, respectively. Again, two different trends are present. For most of the tested mass fluxes the heat transfer coefficients show a bell-like shape with a sharp increase at lower heat fluxes and then a decreasing trend after reaching a maximum. The maximum heat transfer increases with increasing mass flux until  $G=500 \text{ kg/m}^2\text{s}$  and then starts to decrease for higher mass fluxes. The monotonic decrease in heat transfer coefficient may represent a partial dryout condition in the microgrooves which deteriorates the heat transfer efficiency. The second trend is visible at the highest mass flux of  $G=1000 \text{ kg/m}^2\text{s}$ . With the increase in mass flux, the maximum point of the bell shaped curve decreases and at the highest tested mass fluxes it is not present anymore. Here, the heat transfer coefficients increase slowly with increase of heat flux, similar to heat transfer coefficients obtained for Surface #12.

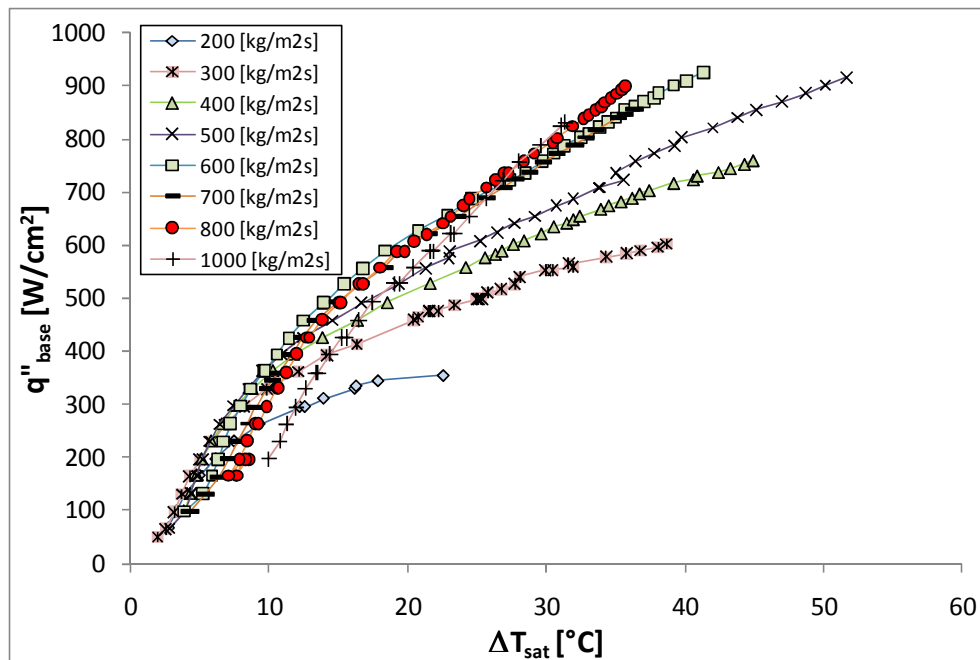
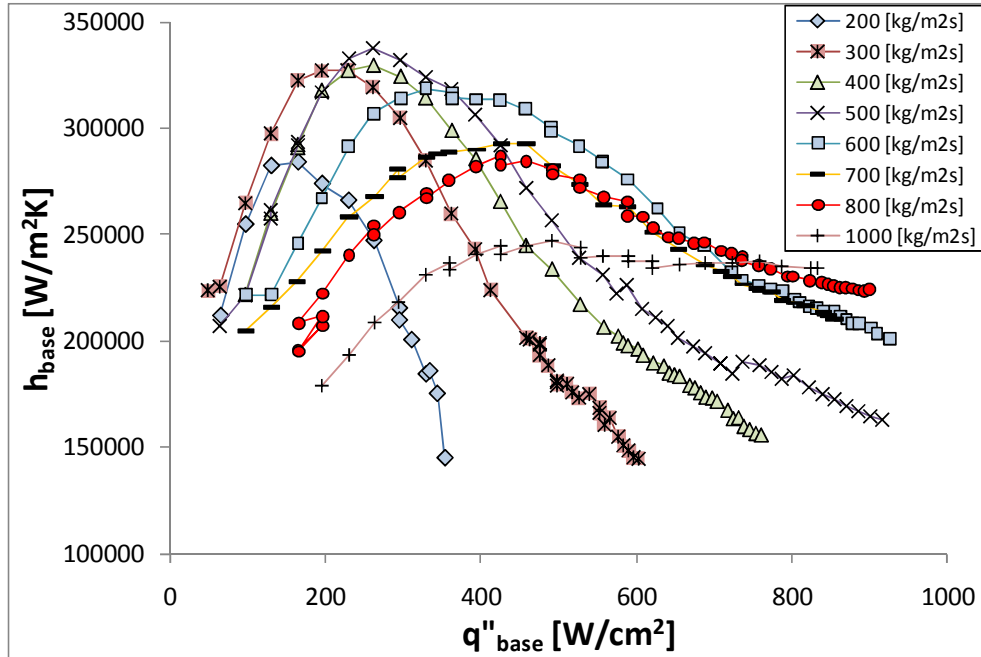
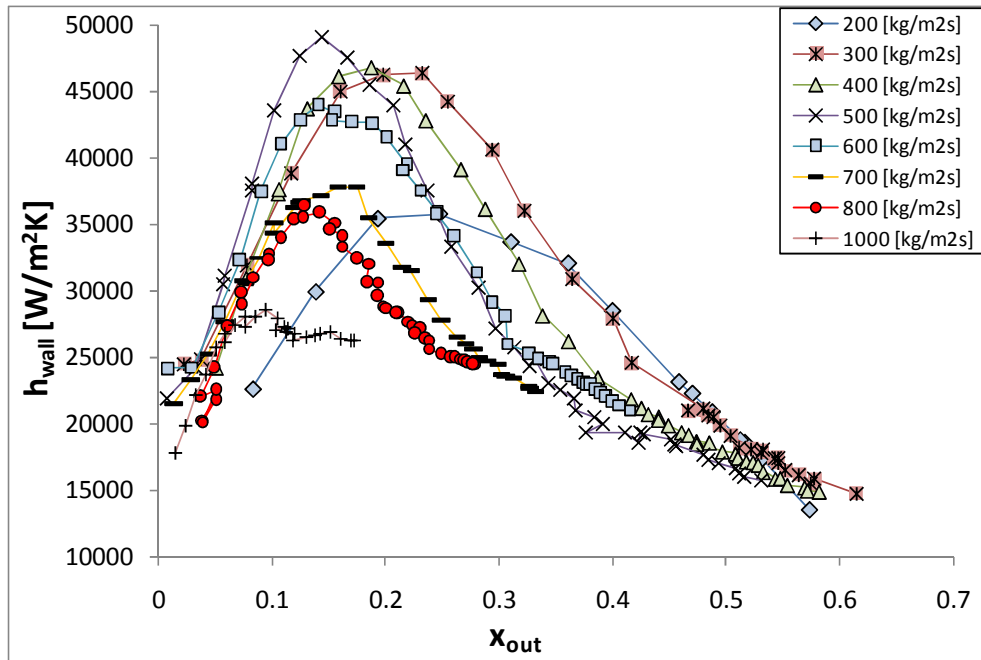


**Figure 6-11. Boiling curves for FFMHS Surface #C**



(a)



(b)

**Figure 6-12. Heat transfer coefficient based on base area versus base heat flux and (b) heat transfer coefficient based on wetted area versus outlet quality for FFMHS Surface #C**

The pressure drop values are shown in Figure 6-13. Similar to previous geometries, pressure drop curves exhibit a linear trend at high outlet qualities, and the pressure drop increases with an increase in mass flux and outlet quality. Due to smaller hydraulic diameter, pressure drops for Surface #C is significantly higher compared to other microgrooved surfaces at similar outlet qualities and mass fluxes. One important observation is that the highest heat transfer coefficients that technology currently provides, registered at low mass fluxes between  $G=300 \text{ kg/m}^2$  and  $G=500 \text{ kg/m}^2$  can be obtained with moderate pressure drops of less than 15 kPa.

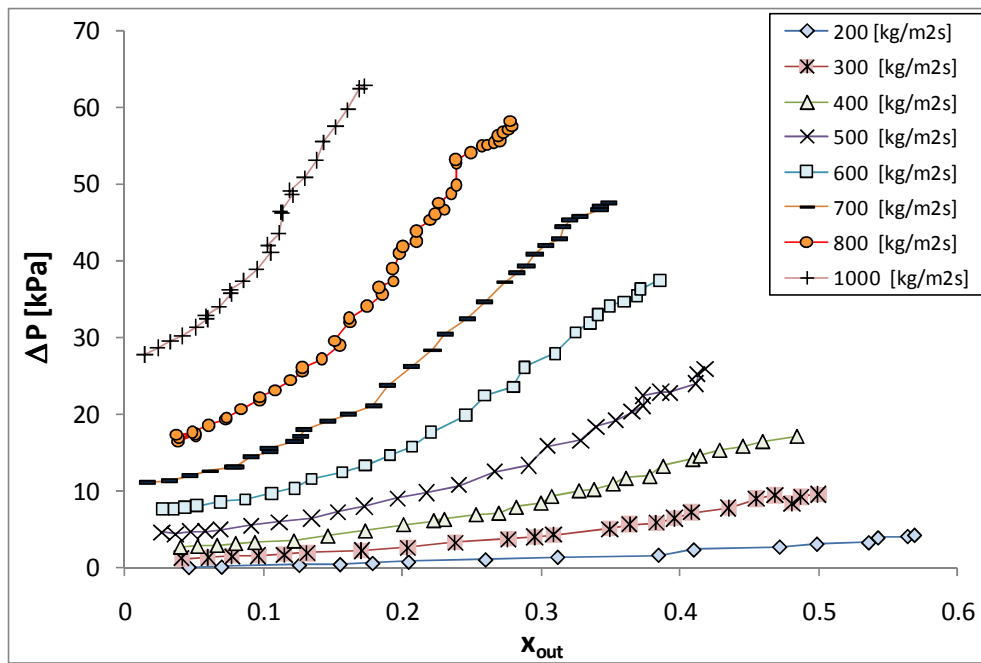


Figure 6-13. Pressure drop values versus outlet quality for FFMHS Surface #C

## 6.5. Comparison of Experimental Data with Convective Saturated Boiling Correlations

The experimental data presented in the previous section revealed different trends of heat transfer coefficient for different heat fluxes, mass fluxes and

microgrooved surface geometries. For small hydraulic diameter microchannels (Surface #C) at low to medium mass fluxes the heat transfer coefficients start to rise rapidly with increase in heat flux and outlet quality. Once the maximum heat transfer coefficients are reached, they start to drop sharply as the heat flux increases. The difference in heat transfer degradation is significant. The maximum wall heat transfer coefficients present at outlet qualities between  $15 < x_{out} < 20\%$  can drop from 50,000 W/m<sup>2</sup>K below to 15,000 W/m<sup>2</sup>K for outlet qualities higher than  $x_{out} > 50\%$ . At higher mass fluxes, the increase in mass flux decreases the dramatic variation in heat transfer coefficients by lowering down the maximum point and creating an increasing trend at high heat fluxes. If the hydraulic diameter of the microgrooved surface is increased about four times (Surface #12), a different heat transfer trend is present. For most of the experimentally tested data, the heat transfer characteristics are similar, with a slightly increasing trend with increase in heat flux and slightly dependent on mass flux. No maximum peaks and no sharp increase/decreases are present in this case. Heat transfer coefficients are generally lower compared with the maximum points observed for microgrooved Surface #C but higher than the minimum values at the end of the decreasing trend of Surface #C. For an intermediate microgrooved Surface #17, having microchannels with hydraulic diameters twice as large as Surface #C and twice as small as Surface #12, both heat transfer trends are visible. At low mass and heat fluxes the curves have a bell shape with visible maximums and sharp increase and decrease in heat transfer coefficient, while with increase in mass and heat fluxes the trend shifts to an almost monotonically slight increase in heat transfer coefficients. This trend suggests that the heat transfer characteristics for different

microgrooved surfaces, mass fluxes and heat fluxes may be controlled by different heat transfer mechanisms.

The first step in analyzing the possible heat transfer trend and heat transfer characteristic of FFMHS was to compare the current experimental data with heat transfer correlations. Since no appropriate correlations were available to predict the two-phase heat transfer in FFMHS, five different correlations developed for saturated flow boiling were tested for this purpose. The selected correlations were developed by (J. C. Chen, 1966), (Kandlikar, 1990), (Tran, Wambsganss, & France, 1996), (Lazarek & Black, 1982) and (Warrier, Dhir, & Momoda, 2002) and they will be discussed in next section. All of these correlations were proposed to predict saturated flow boiling heat transfer and they are developed to be used with refrigerants. The objective of this part of the study was to compare the heat transfer trend of current experimental data with correlations developed for straight channels and to analyze the resulting trends.

Since the convective flow in a FFMHS can be coupled with several complex phenomena such as flow turns, secondary flows and impingement effects, an exact prediction of two-phase heat transfer may not be possible. In order to be able to use the selected heat transfer correlations in this case, an assumption needs to be made. Here, the flow in the FFMHS shown in Figure 6-14 (a) was assumed to be as in a straight microchannel similar to the schematic shown in Figure 6-14 (b). With this assumption, the selected correlations can be easily applied without any complexity. However, the validity and error generation of this assumption need to be evaluated.

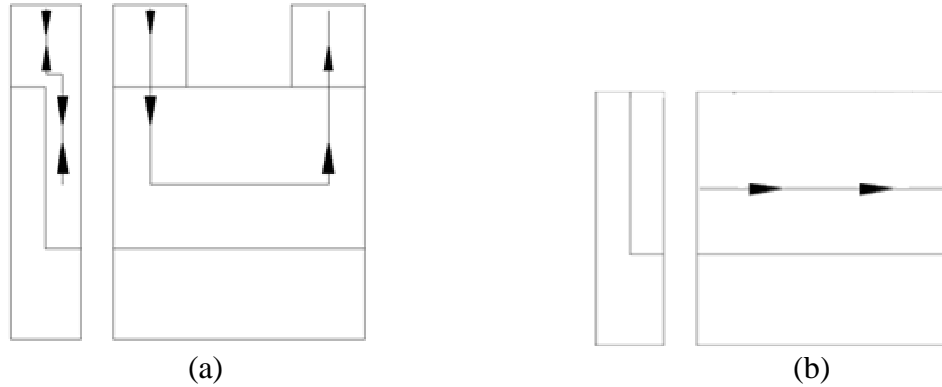


**Figure 6-14. Flow schematic in (a) an FFMHS (b) a straight microchannel**

The convective boiling heat transfer correlations were developed based on the heat transfer mechanisms that authors believed to be dominant in their experimental data. For example, Chen correlation uses the concept of addition of heat transfer coefficient of macroscopic convection and the microscopic nucleate boiling. The Kandlikar correlation predicts local heat transfer coefficients on the basis that the heat transfer is dominated by either nucleate boiling or convective boiling. The Tran, Lazatek and Black and Warriier correlations were developed for nucleate boiling-dominant heat transfer. In the nucleate boiling-dominant heat transfer regime, the convection effects are less pronounced, and most of the heat is removed by the bubble growth and ebullition process. On the other hand, in the convective boiling-dominant regime the bubble nucleation is suppressed and heat is removed mainly by liquid convection and thin film evaporation. Therefore, by assuming a well distributed flow in FFMHS, the convective effects of flow turning, secondary flows and impingement can be less effective in the nucleate boiling-dominant regime. The convective heat transfer regime is usually modeled by including the liquid single-phase heat transfer coefficient and multiplying it with a correction factor (J. C. Chen, 1966), (Kandlikar,

1990). For capturing the effects of single phase convective part, the heat transfer in both FFMHS and straight microchannel design were tested and compared. The effective heat transfer ratio between an FFMHS and a straight microchannel defined as  $\frac{h_{FFMHS}}{h_{MC}}$  was plotted against channel mass flux in Figure 6-15 for all three microgrooved surfaces. As seen in the figure, switching from an FFMHS to a straight microchannel flow with same dimensions can either enhance or reduce the heat transfer coefficient depending on microchannel geometry and flow condition. However, even at extreme conditions, the additional convective effects incorporated by the FFMHS did not exceed  $\pm 40\%$  difference. Or in other words, both flow configurations can give similar convective heat transfer performances at high mass fluxes for Surface #C, at medium mass fluxes for Surface #17, and at low mass fluxes for Surface #12. Therefore, it may be concluded that a similar difference in the same order can be expected from the heat transfer correlations that incorporate single-phase convective heat transfer coefficients.

For the correlations that predict local heat transfer coefficient  $h_z$ , vapor quality distribution needs to be known. For this purpose, the microchannel was divided into ten equal division channels, and by assuming equal heat flux on fins and microchannel bottom, the quality in each division channel was averaged between inlet and outlet. The average heat transfer coefficient then was calculated by integrating the local heat transfer coefficients based on local quality as:

$$h = \int_0^{x_{out}} h_z dx \quad (6-25)$$

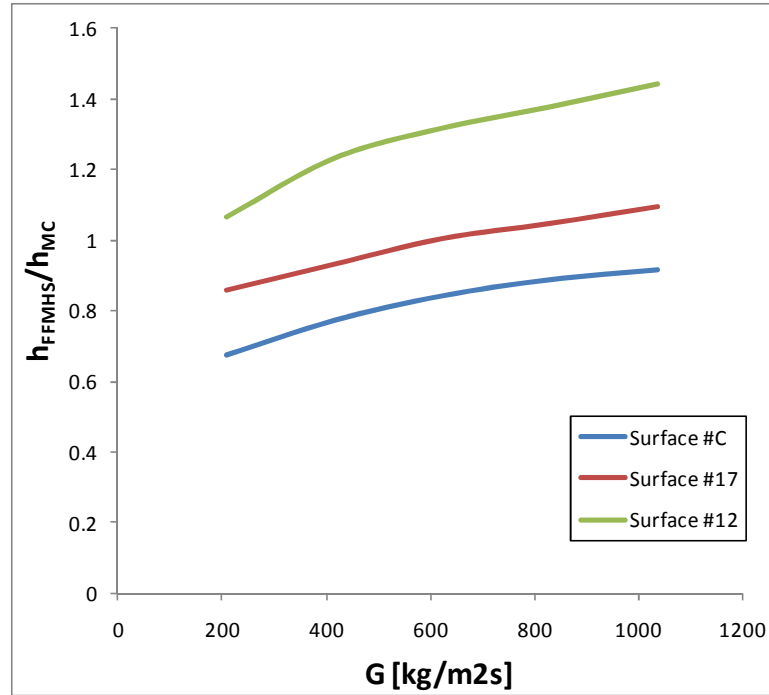


**Figure 6-15. Heat transfer coefficient comparison for single-phase convective heat transfer for selected microgrooved surfaces**

### 6.5.1. Chen correlation

The Chen correlation (J. C. Chen, 1966) is formulated based on additive heat transfer coefficients of macroscopic component resulting from convective heat transfer and the microscopic component, which takes place during the bubble nucleation and growth process. It was developed to predict saturated flow boiling in conventional channels with no liquid deficiency, and the applicable quality and heat flux ranges were defined as  $1\% < x < 71\%$  and  $6.2 < q'' < 2400 \text{ kW/m}^2$ . The two-phase heat transfer coefficient is calculated as:

$$h_x = Eh_{sp} + Sh_{nb} \quad (6-26)$$

The macroscopic component is defined as a modified Dittus–Boelter correlation as:

$$h_{sp} = 0.023(\text{Re}_l)^{0.8} (\text{Pr}_l)^{0.4} F \frac{k_l}{D_h} \quad (6-27)$$

The coefficient F represents the ratios of the two-phase Reynolds number to the liquid Reynolds number and is defined as:

$$F = \begin{cases} 1 & , \frac{1}{X_{tt}} < 0.1 \\ 2.35 \left( 0.213 + \frac{1}{X_{tt}} \right) & , \frac{1}{X_{tt}} > 0.1 \end{cases} \quad (6-28)$$

where Martinelli parameter is based on turbulent-turbulent flow:

$$X_{tt} = \left( \frac{1-x}{x} \right)^{0.9} \left( \frac{\rho_v}{\rho_l} \right)^{0.5} \left( \frac{\mu_l}{\mu_v} \right)^{0.1} \quad (6-29)$$

The microscopic heat transfer component is calculated as:

$$h_{nb} = 0.00122 \left[ \frac{k_l^{0.79} C_{pl}^{0.45} \rho_l^{0.49}}{\sigma^{0.5} \mu_l^{0.29} h_{lv}^{0.24} \rho_v^{0.24}} \right] \Delta T_{sat}^{0.24} \Delta P_{sat}^{0.75} S \quad (6-30)$$

where  $\Delta T_{sat} = T_w - T_{sat}$  and  $\Delta P_{sat} = P_{sat}(T_w) - P$ . The coefficient S is the nucleate boiling suppression factor and is correlated as:

$$S = \left[ 1 + (2.56 \cdot 10^{-6}) (\text{Re}_f F^{1.25})^{1.17} \right]^{-1} \quad (6-31)$$

### 6.5.2. Kandlikar correlation

Kandlikar correlation (Kandlikar, 1990) was originally developed for saturated convective boiling in conventional channels for water, refrigerants and cryogenic fluids. The correlation was validated successfully for a range of experimental data obtained from different publications. The correlation predicted the heat transfer coefficient well for a range of data for mass fluxes between

$50 < G < 4586 \text{ kg/m}^2\text{s}$ , channel hydraulic diameter between  $0.210 < D_h < 2.29 \text{ mm}$  and heat fluxes between  $2 < q'' < 600 \text{ kW/m}^2$  (Kandlikar & Steinke, 2003),(Peters & Kandlikar, 2007). However it should be noted that the correlation was not validated for microchannels with hydraulic diameter less than 100 microns with wall heat fluxes exceeding  $1000 \text{ kW/m}^2$ .

The Kandlikar correlation calculated the two-phase heat transfer coefficient differently for nucleate boiling dominant flow and convective boiling dominant flow and suggested taking the maximum value as the actual heat transfer coefficient:

$$h_x = \max(h_{nb}, h_{cb}) \quad (6-32)$$

$$h_{nb} = 0.6683Co^{-0.2}(1-x)^{0.8} h_{sp} + 1058Bo^{0.7}(1-x)^{0.8} F_{fl} h_{sp} \quad (6-33)$$

and

$$h_{cb} = 1.136Co^{-0.9}(1-x)^{0.8} h_{sp} + 667.2Bo^{0.7}(1-x)^{0.8} F_{fl} h_{sp} \quad (6-34)$$

where the convection number  $Co$  and boiling number  $Bo$  are defined as follows:

$$Co = (\rho_v / \rho_l)^{0.5} [(1-x)/x]^{0.8} \quad (6-35)$$

$$Bo = q'' / (Gh_v) \quad (6-36)$$

For calculation of single-phase heat transfer coefficient  $h_{sp}$ , the Dittus-Boelter equation is suggested. The coefficient  $F_{fl}$  is the fluid-surface parameter that includes the effect of surface tension and is defined for different surface materials and fluids. Kandlikar did not present the value for R245fa-copper in his list in (Kandlikar, 1990). Since most of the refrigerant-copper couples have a value ranging between  $1.0 < F_{fl} < 3.3$  the value of  $F_{fl}$  was selected as 1.0 for this study.

### 6.5.3. Tran correlation

Tran correlation (Tran et al., 1996) was developed for saturated flow boiling in microchannels and was validated with Refrigerants R12 and R113 for rectangular channels with hydraulic diameter of 2.4 mm. The correlation predicted the data for quality of  $x < 94\%$  and heat flux between  $3.6 < q'' < 129 \text{ kW/m}^2$ . The correlation was developed with the concept of convective boiling phenomena being dominated by nucleate boiling and is defined as:

$$h = 8.4 \cdot 10^5 \left( Bo^2 We_l \right)^{0.3} \left( \frac{\rho_l}{\rho_v} \right)^{-0.4} \quad (6-37)$$

where the Webber number for the liquid phase is

$$We_l = \frac{G^2 D}{\rho_l \sigma} \quad (6-38)$$

### 6.5.4. Lazarek and Black correlation

Lazarek and Black (Lazarek & Black, 1982) tested saturated convective boiling of R-113 in a single tube with  $D_h = 3.15 \text{ mm}$  for mass fluxes ranging between  $125 < G < 750 \text{ kg/m}^2\text{s}$  and heat flux between  $14 < q'' < 380 \text{ kW/m}^2$ . They concluded that the dominant heat transfer mechanism was nucleate boiling, and based on their data, they suggested the following correlation to predict the two-phase heat transfer coefficient:

$$h = 30 \left( Re_{lo} \right)^{0.857} Bo^{0.714} \frac{k_l}{D_h} \quad (6-39)$$

### 6.5.5. Warrier correlation

The Warrier correlation was proposed by (Warrier et al., 2002) to predict the experimental data they obtained for saturated flow boiling of FC-84 in rectangular channels with 0.75 mm hydraulic diameter. The experimental data were collected for a mass flux between  $557 < G < 1600$  kg/m<sup>2</sup>s and for a heat flux range of  $0 < q'' < 59.9$  kW/m<sup>2</sup>. The two-phase heat transfer correlation is based on the single-phase heat transfer coefficient multiplied by a correction factor that accounts for the effect of convective and nucleate boiling. :

$$h_z = E h_{sp} \quad (6-40)$$

$$E = 1.0 + 6Bo^{1/16} + f(Bo)x^{0.65} \quad (6-41)$$

$$f(Bo) = -5.3(1 - 855Bo) \quad (6-42)$$

### 6.5.6. Results

To test the selected heat transfer correlations, two experimental data sets at constant mass flux were selected for each microgrooved surface. Each data set was selected to represent the specific characteristic heat transfer trend previously reported in this chapter.

For microgrooved Surface #12, experimental data taken at  $G=300$  kg/m<sup>2</sup>s and at  $G=1200$  kg/m<sup>2</sup>s were compared with selected correlations in Figure 6-3 (a) and (b). As discussed earlier, for Surface #12 the heat transfer coefficient curves have a slight increasing trend with no visible sharp increase/decrease with increased mass and heat fluxes for all range of tested data. Therefore, the heat transfer coefficients have a similar trend for both low and high mass flux cases. At low to medium heat fluxes,

the correlations of Warrier and Lazarek and Black can predict the heat transfer coefficients better than other correlations. This may suggest that for the given data set, the heat transfer at low heat fluxes may be dependent on nucleate boiling. Since the nucleate boiling is dominant, the convective heat transfer in the microchannel, as well as the impingement and flow turning effects are less effective, and their contribution to overall heat transfer coefficient may be low. As the heat flux increases, heat transfer coefficients start to depart from the heat transfer trend given by the Warrier and Lazarek and Black correlations. This, in turn may suggest that the nucleate boiling heat transfer mechanism is no longer dominant or that the correlations are no longer valid. Indeed, both of these correlations are developed for nucleate boiling-dominant heat transfer regime and are validated for heat fluxes of  $q''_{wall} < 38 \text{ W/cm}^2$ . Extrapolating the correlations for higher heat fluxes may present questionable results. Another interesting observation is that Kandlikar correlation seems to predict the heat transfer coefficients only at very low heat fluxes. At higher heat fluxes, the correlation largely over-predicted the experimental results. Hydraulic diameters and heat fluxes of FFMHS tested in this study are much different from the conditions for which the correlations were validated. The Tran correlations show a different trend by always under-predicting the heat transfer coefficients. This may be because the coefficients of the correlation were developed for a database including only two refrigerants. It looks like the correlation could match the trend of other correlations if the correlation multiplier were modified. Chen correlation most successfully to predicted the trend of heat transfer coefficients at high heat fluxes. The difference between the experimental results and Chen correlation seems to

decrease as the heat flux increases. This in turn may suggest that at high heat fluxes, the two-phase heat transfer characteristic could be similar to the conventional channels.

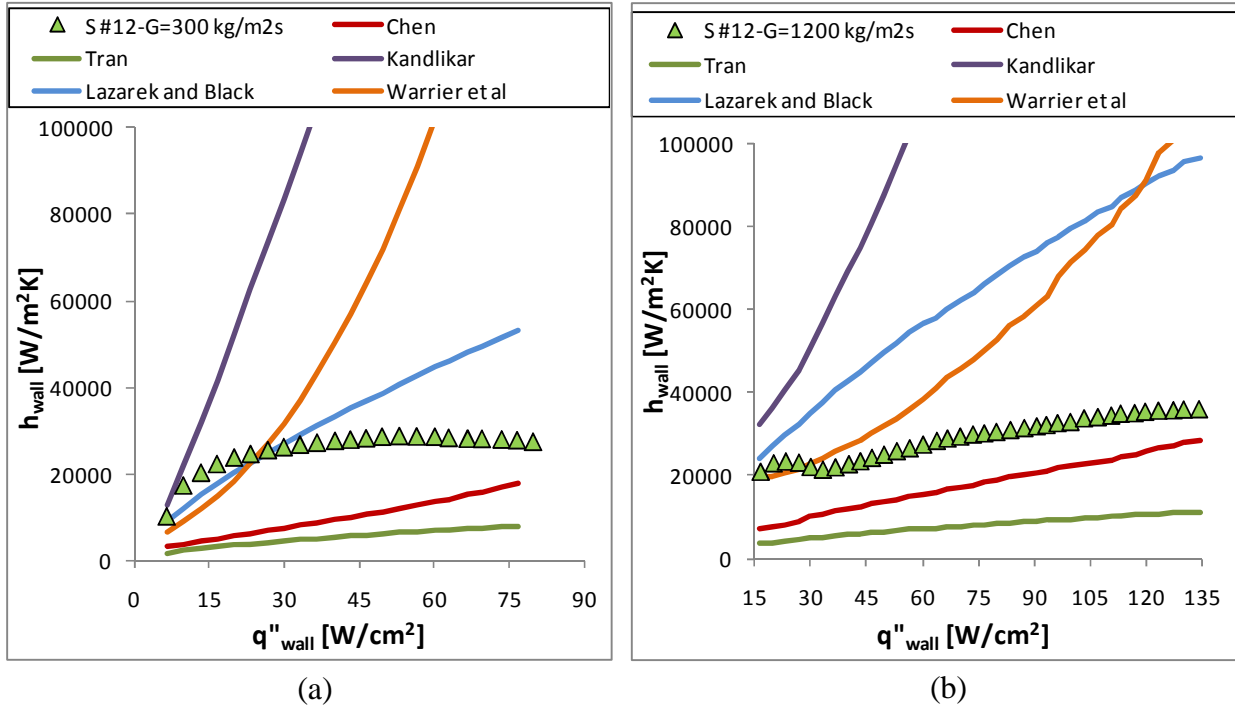


**Figure 6-16. Comparison of saturated convective boiling heat transfer correlations with experimental data of FFMHS Surface #12, (a)  $G=300$  kg/m<sup>2</sup>s and  $Re=100$ , (b)  $G=1200$  kg/m<sup>2</sup>s and  $Re=400$**

The heat transfer prediction curves of selected correlation in comparison with experimental data obtained at low and high mass fluxes for microgrooved Surface #C and Surface #17 are shown in Figure 6-17 (a)-(b) and Figure 6-18 (a)-(b), respectively. For both surfaces, at low mass fluxes a particularly interesting phenomenon is present. For the increasing trend, before the heat transfer coefficients reach the maximum point, the heat transfer coefficients can reach high values, surpassing almost all results predicted by heat transfer correlations. Only the Kandlikar correlation seems to predict the values at low heat fluxes, but later it largely over-predicts the rest of the data. After the maximum occurs, a sudden

decrease in the heat transfer occurs, which decreases the experimental heat transfer values to lower points, where all correlations except the Tran correlation over-predict the results. This trend is present for both microgrooved surfaces and cannot be explained by the selected heat transfer correlations. This can be the result of heat transfer being dominated by a heat transfer mechanism that the correlations did not account for. A possible heat transfer mechanism for the sharply increasing trend could be the thin-film evaporation process. In this heat transfer mode the fluid creates thin liquid films on the microgrooved surface fins, which in turn creates very low thermal resistance. The evaporation process of such thin films on large surfaces is very effective and can significantly enhance heat transfer. On the other hand, the decreasing trend can be partial dryout, in which the dry area can increase with increasing of heat flux. However, such mechanisms need to be clarified by other means.

For the high mass fluxes, all microgrooved surfaces present a similar trend. At low heat fluxes the heat transfer coefficients are close to Warrier and Lazarek and Black correlations, while increasing the heat flux shifts it to the Chen correlation. In this region, the heat transfer is expected to be dominated by nucleate boiling in microchannels at low vapor qualities and later switch to fully annular flow where the heat transfer is dictated by thin film evaporation.

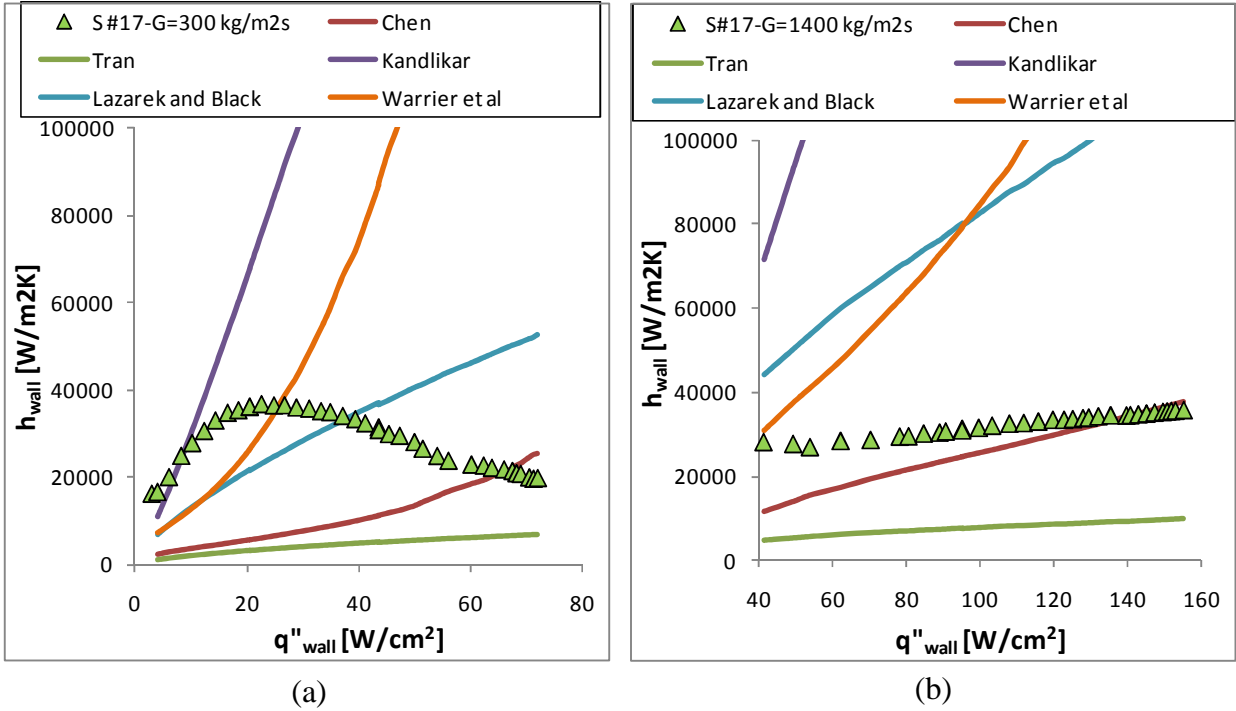


Figure 6-17. Comparison of saturated convective boiling heat transfer correlations with experimental data of FFMHS Surface #17, (a)  $G=300$  kg/m<sup>2</sup>s and  $Re=70$ , (b)  $G=1400$  kg/m<sup>2</sup>s and  $Re=320$

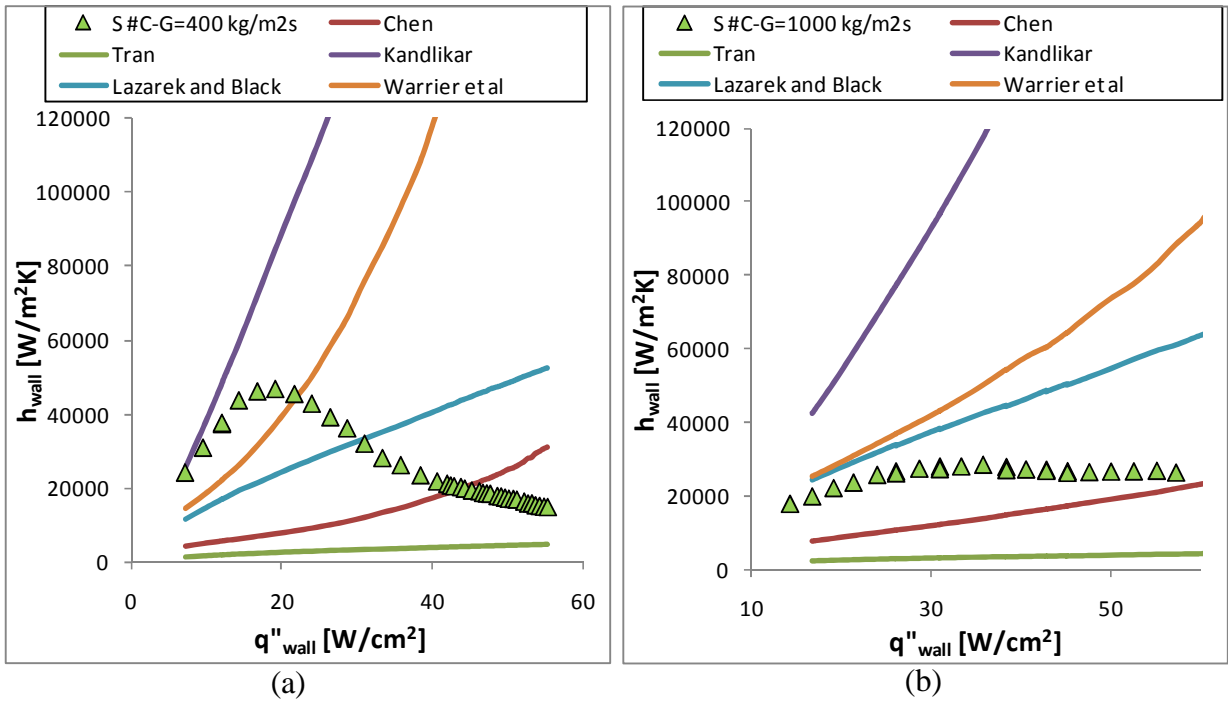


Figure 6-18. Comparison of saturated convective boiling heat transfer correlations with experimental data of FFMHS Surface #C, (a)  $G=400$  kg/m<sup>2</sup>s and  $Re=50$ , (b)  $G=1000$  kg/m<sup>2</sup>s and  $Re=130$

## 6.6. Critical Heat Flux Results

Critical heat flux is one of the limiting factors of a two-phase system that utilizes boiling heat transfer. For a system controlled by heat flux, the CHF occurs when a slight increase in heat flux creates a large jump in surface temperature. This effect is not desirable since it can damage both the cooling system and the electronics that have been cooled. Therefore, the design of a heat sink for high heat flux components is mostly dependent on the CHF, and its careful evaluation. For convective boiling in channels, the CHF mechanism is believed to result from two different mechanisms. The first mechanism is partial dryout, which can occur from the depletion of the liquid layer at flow regimes with high vapor qualities such as annular flow. The creation of a solid-vapor interface significantly increases the thermal resistance and forces the surface temperature to rise rapidly. The second mechanism is departure from nucleate boiling and is similar to the critical heat flux in pool boiling. At very high heat fluxes, the bubbles formed close to the heated wall can coalesce and rapidly form larger bubbles that can form a vapor blanket that will prevent the liquid from wetting the surface. In this case the thermal resistance is significantly high and heat transfer occurs again between the solid surface and the vapor in the vapor blanket.

For FFMHS, the flow in the microchannel is more complex, and the understanding of CHF with conventional straight channel mechanisms could be challenging. Nevertheless, the CHF needs attention, and the forces that can lead to these phenomena need to be addressed. As mentioned in Chapter 6, the current test setup was not designed to study CHF due to low thermal mass of heater assembly.

However, one effort has been made to collect reasonable data with one of the microgrooved surfaces, Surface #17. The CHF data was obtained after the heat transfer data with the selected microgrooved surface was successfully collected.

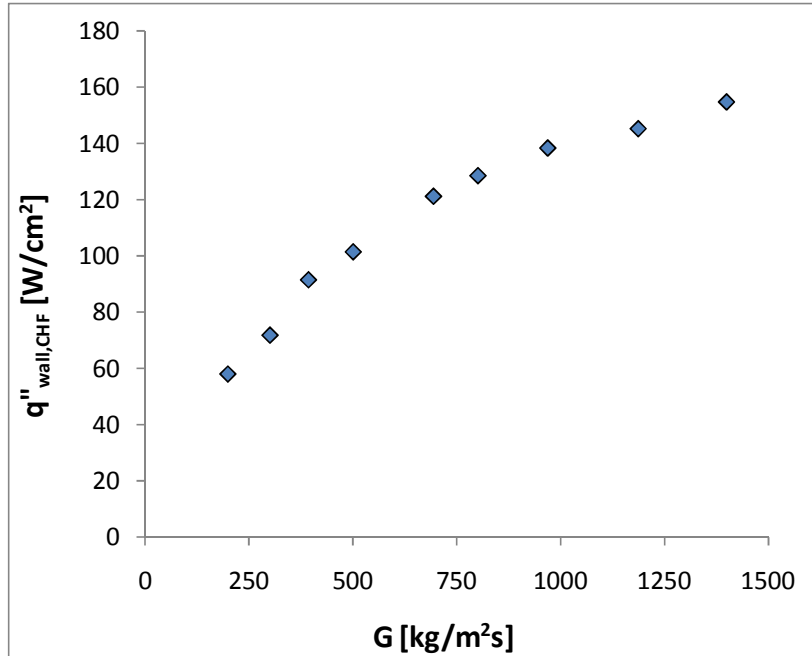


**Figure 6-19. Critical heat flux based on wet channel area versus channel mass flux data obtained for Surface #17**

A total of nine CHF values at different mass fluxes were experimentally obtained and the resulting graph is shown in Figure 6-19. The CHF values display an increasing trend with mass flux with the decreasing slope at higher mass fluxes. The decreasing slope with increase in mass flux also suggests that at higher mass fluxes the outlet quality is lower due to less vapor generation. For example, at the lowest mass flux of  $G=200 \text{ kg/m}^2\text{s}$  the outlet quality corresponding to CHF is  $x_{\text{out}}=64\%$ , while at the higher mass flux of  $G=1400 \text{ kg/m}^2\text{s}$  it drops to  $x_{\text{out}} = 20\%$ . The shift in the CHF curve slope may indicate the change in heat transfer mechanism which was observed at the middle mass fluxes ( $500\text{-}800 \text{ kg/m}^2\text{s}$ ). The shift in the dominant heat transfer mode may affect both the heat transfer performance and the critical heat flux.

However, additional studies need to be conducted to conform or reject this presumption.

An interesting observation was made during CHF data collection process and will be explained here. The test setup includes thermocouples to measure fluid inlet and microgrooved surface temperatures. Two inlet fluid thermocouples are located 1 mm below the contact interface of the manifold face and microgrooved surface fin tips (Figure 5-6 (b)). Three surface thermocouples measure microgrooved surface base temperature (Figure 5-8). All thermocouple and pressure transducers were connected to a data acquisition system, making continuous data collection possible. When achieving CHF condition, two major effects were present. First, the surface thermocouple read a sudden temperature jump, usually above 300 °C. After sensing the temperature jump the control system immediately shut down the heater to protect it from burnout. During this time, the pump was still running, sending liquid to the microgrooved surface and eventually cooling it down close to the inlet liquid temperature. The second effect was observed for inlet liquid thermocouple. As the surface experienced a jump in temperature, a similar jump in inlet fluid temperature was also present. After the maximum, since the heater was shut down, the inlet liquid temperature that flows in the manifold was not controlled by the saturation temperature at the outlet of the heat sink anymore, and the temperatures started to decrease gradually. The variations of surface and inlet liquid temperatures with time are given in Figure 6-20 at conditions of mass flux of 300 kg/m<sup>2</sup>, critical heat flux of  $q''_{\text{wall}} = 72.1 \text{ W/cm}^2$  and  $\Delta T_{\text{subcool}} = 2.6 \text{ °C}$ . Interestingly, the temperature jump in the inlet fluid temperature is close to the subcooling amount which indicates that some

amount of vapor in the microgrooved surface overcomes the inertia effects and was pushed back into the manifold. In this case, even for a short period of time, the inlet manifold might be blocked by the vapor and the heat transfer surface can be partially or totally dry. This in turn may create the large temperature jump that creates the CHF conditions. The same effect was also present for high mass fluxes, as shown in Figure 6-21 mass flux of  $1200 \text{ kg/m}^2$ , critical heat flux of  $q''_{\text{wall}} = 157.9 \text{ W/cm}^2$  and  $\Delta T_{\text{subcool}} = 8.5 \text{ }^\circ\text{C}$ . The temperature jump in inlet fluid temperature was less severe in this case, probably due to the mixing effect of vapor and subcooled liquid or due to the low data sampling frequency of  $0.8 \text{ Hz}$ , which might not capture the maximum peak. Nevertheless, the increase in inlet fluid temperature was present, which indicates vapor back flow into the inlet manifold that may be the main reason for CHF. While some of the effects mentioned above were detected by temperature measurement, a more fundamental explanation of the initiation and mechanism of CHF in FFMHS is needed.

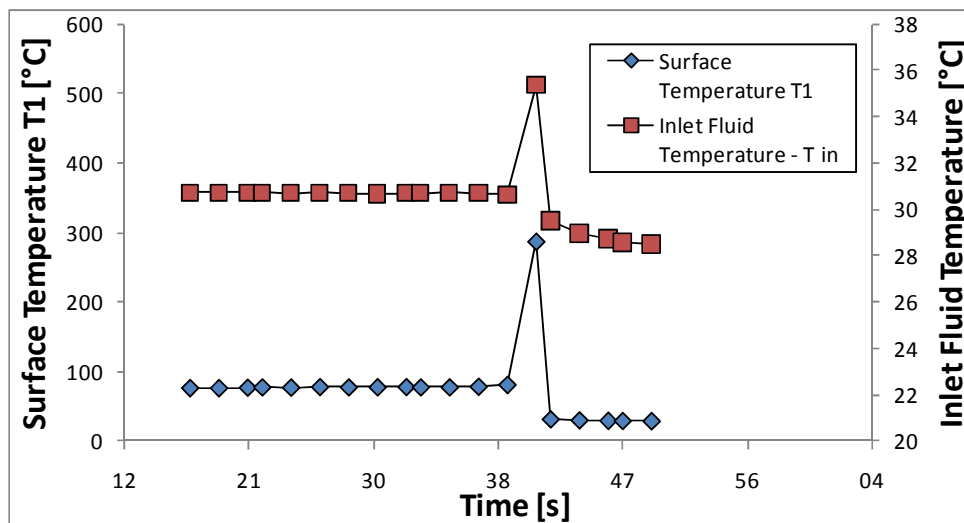


**Figure 6-20. Variation of surface temperature and inlet fluid temperature with time at critical heat flux condition for Surface #17,  $G=300 \text{ kg/m}^2\text{s}$  and  $q''_{\text{wall}} = 72.1 \text{ W/cm}^2$ ,  $\Delta T_{\text{subcool}} = 2.6 \text{ }^\circ\text{C}$**

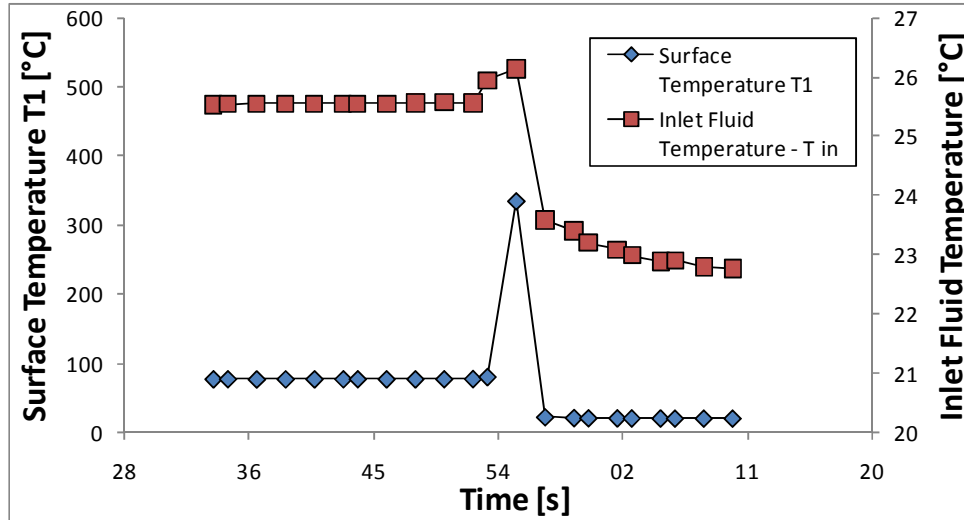


**Figure 6-21. Variation of surface temperature and inlet fluid temperature with time at critical heat flux condition for Surface #17,  $G=1400 \text{ kg/m}^2\text{s}$  and  $q''_{\text{wall}} = 154.9 \text{ W/cm}^2$ ,  $\Delta T_{\text{subcool}} = 8.5 \text{ }^\circ\text{C}$**

## 6.7. Performance Comparison of FFMHS with Other High Heat Flux Cooling Technologies

As shown in previous sections, the highest critical heat flux obtained for Surface #17 was  $q''=1230 \text{ W/cm}^2$  measured for average wall superheat of  $56.2 \text{ }^\circ\text{C}$  and subcooling of  $8.5 \text{ }^\circ\text{C}$ . The corresponding pressure drop was measured as  $60.3 \text{ kPa}$  and pumping power was calculated as  $1.13 \text{ W}$ . As a general design rule, a heat sink is desired to perform at high heat fluxes, with low wall superheat, low subcooling, low pressure drop and low pumping power. Therefore, differently than single phase study, comparing cooling technologies for two phase heat transfer mode is more challenging due to the heat sink performance being dependent on many more parameters. Nevertheless, a quantitative comparison can still be made by plotting the data over the two most important parameters. For this purpose, the two parameters were selected as maximum heat flux and pumping power over cooling capacity ratio. For these

parameters, when comparing FFMHS with cooling technologies previously reviewed in Table 2-4 , the resulting graph is shown in Figure 6-22. It should be noted however that the comparison parameters were selected based on their importance to the objective of the study. For example, for a comparison based on heat transfer efficiency, one of the axes should be replaced with heat transfer coefficient  $h$  .

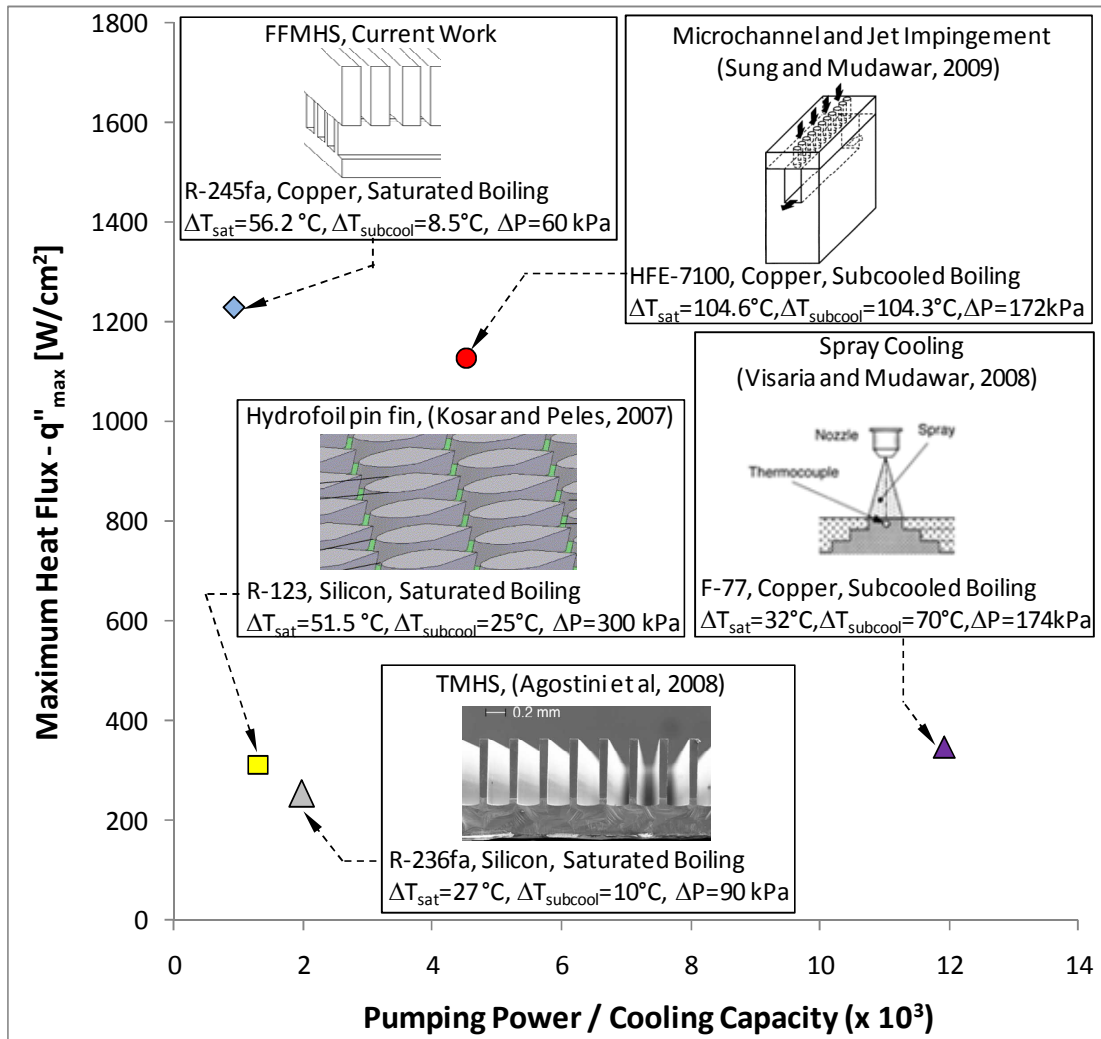


**Figure 6-22. Thermal performance comparison of different high heat flux cooling technologies**

The technology comparison shown in the figure clearly indicates that the FFMHS technology can remove much higher heat fluxes with less pumping power per cooling capacity ratio than any other investigated cooling system. More importantly, this feature is accomplished by a reasonable wall superheat, low subcooling and medium pressure drop. In fact, it is interesting to see that the current pressure drop value of FFMHS was significantly less than the values reported for other technologies, although it performed at much higher heat fluxes. Another important point for the comparison chart is that no two phase optimization was reported for any of the heat sink designs. For optimum conditions, the sequence and location of points on the graph may be significantly different. Therefore, for next studies of technology comparison, it is recommended to include and consider the effect of optimum designs on thermal performance.

## **6.8. Conclusions**

Three different microgrooved surfaces were experimentally tested to evaluate the thermal performance of FFMHS's in single-phase and two-phase heat transfer modes. For single-phase heat transfer, the heat transfer coefficients followed a linear trend when plotted versus mass flux on a log-log graph. Variation in mass flux and hydraulic diameter has more impact on pressure drop than heat transfer coefficients. For two-phase heat transfer, two different and distinct heat transfer trends were observed. At high hydraulic diameter, high mass flux and high heat flux, the heat transfer coefficients have a slowly increasing trend with increase in heat flux and outlet quality. The heat transfer coefficients in this regime more or less follow the Chen correlation, which was developed to predict saturated flow boiling in

conventional channels. At low hydraulic diameters, low mass flux and low qualities the heat transfer coefficients had a bell-like shape with a sharp increase at low vapor qualities until it reached the maximum peak point. After this point heat transfer coefficient started to decrease until the critical heat flux condition was achieved. The heat transfer coefficients at maximum point were the highest obtained along the experimental test range. None of the convective boiling heat transfer correlations could capture this bell like trend. The values at the intermediate hydraulic diameters and heat and mass fluxes showed a transition regime between two trends. In terms of system performance, FFMHSs have demonstrated that using a HFC fluid, the present heat sink configuration can cool a heat flux of  $q''_{base} = 1.23 \text{ kW/cm}^2$  with a superheat of  $\Delta T_{sat} = 56.2 \text{ }^\circ\text{C}$  and pressure drop of  $\Delta P = 60.3 \text{ kPa}$ . These values also indicate that FFMHS, with its current geometrical configuration, can cool higher heat fluxes and perform at lower pumping power levels comparing to several currently used and proposed high heat flux cooling systems.

Critical heat flux was tested for a single microgrooved surface, Surface #17. The results indicate that CHF values increase with mass flux while the outlet qualities have a decreasing trend. It was determined that vapor backflow in the inlet manifold is correlated with CHF and could be the reason the liquid supply line become clogged and create partial or complete dryout that led to CHF condition. However, a more detailed study would be necessary to support this finding.

Although the experimental results revealed some important aspects of heat transfer characteristics and CHF in FFMHS, the dominant mechanisms are still not

well understood. Therefore, a visualization study, which will be discussed in next chapter, was performed.

## **CHAPTER 7: VISUALIZATION STUDY**

The visualization study was conducted to improve understanding of the two-phase heat transfer mechanism in FFMHS. The visualization test section was designed as a cross-section of a single element of FFMHS with visual access and with the most realistic recreation of the heat transfer process. The visualization test section design and the test procedure are described in this chapter. The visualization results are explained with close reference as possible to two-phase experimental results presented in the previous chapter.

### **7.1. Introduction to Visualization Study**

The FFMHS two phase heat transfer results presented in Chapter 6 revealed several heat transfer trends that are different from the conventional micro-and mini-channels and which did not follow the trend of available saturated boiling heat transfer correlations. In particular CHF mechanism of two-phase flow in FFMHS is a challenge to understand and needs to be investigated more fundamentally. This visualization study was conducted to address these issues and to determine the flow regimes that are present in force-fed microchannel flow and dominate the heat transfer mechanism. However, such a visualization study possesses several challenges.

First of all, the flow pass in FFMHS is not as straight as in traditional microchannels and incorporates several turns and bends that require the flow to be distributed in a 3D space. In traditional microchannels, the flow often enters the

microchannel from one side, flows all the way to the end, and exits. In other words, the direction of velocity vectors at the inlet, in the channel and at the outlet is generally the same. In this configuration the bottom of the heat sink is flat and is attached to the heat source, and a transparent cover seals the top of the microchannel fins. Such design readily allows for visualization of two-phase flow in traditional microchannels and several publications explain in detail the test procedure. In FFMHS, this setup is not usually possible due to the presence of the inlet and outlet feed channels that feed the microchannels from the top and require additional vertical spacing. This generally interferes with the optical limitations associated with the lens of the high-speed camera, since the camera cannot be placed close to the microchannel. Another limitation with this configuration is that looking from the top, the flow under the feed channels is not easy to visualize, due to the large amount of liquid in the feed channels. This is a major drawback since the part of the microchannel between the inlet and outlet feed channels where the flow is straight occupies less than 60% of the total heat transfer area. The rest of the area is under the inlet and outlet feed channels. Also, the high aspect ratio of microgrooves would make flow visualization from the top of microgroove very difficult.

While the visualization of the actual heat sink was not feasible due to the complexities mentioned above, one potential solution was to select one or a few unit cells and visualize the two-phase phenomena for this particular configuration. This approach would be similar to the selection of the unit cell computational domain in the single-phase study (Figure 3-1). In this case the visualization could take place on the fin surface of the microchannel by eliminating one side of the heated

microchannel surface and replacing it with the transparent cover. This configuration would also allow the formation of inlet and outlet feed channels on the same plane with the microchannel fins. However, this configuration could generate results based on only one heated surface, provided the transparent cover were not heated by other means.

Finally, although selecting and testing a single unit cell appears to be an effective method, the main challenge arises from the flow control and energy balance of the short channel test section. For example, simulating a single unit cell of Surface #17 for a base heat flux of  $q_{base}'' = 1000 \text{ W/cm}^2$  at a mass flux of  $G = 1000 \text{ kg/m}^2\text{s}$  requires a heat input of 0.47 W and a mass flow rate of 0.02 gr/s. These values are very small, and control of heat input for such case could be very challenging because of uncertainty associated with heat losses and gains from various sources that cannot be controlled during experimental tests.

Based on the above discussion, the most practical solution for the current case was to select and scale up two of the unit channels connected to a common inlet. All geometrical dimensions were scaled up by a factor of five for the current study. The scaling of the heated area and flow area will result in heat fluxes and mass flow rates that can be practically controlled and monitored. The trade-off of this scaling process could be the decreasing effect of hydraulic diameter and variation of other forces dependent on geometry. Unfortunately, to the best of the author's knowledge, there is no publication that presents a similar technique successfully applied to a comparable two-phase flow visualization case. The approach in this study was to capture mainly the possible two-phase flow patterns and CHF mechanisms that can explain the

experimental data presented in previous chapter. Therefore, the visualization study should not be considered as a perfect solution representing alignment between a prototype and model, but rather as an effort to understand to the extent possible the heat transfer mechanisms in the special configuration at hand based on parametrical studies of significance in a real-scale FFMHS.

## **7.2. Visualization Test Section**

In order to perform the visualization tests a test section was designed and fabricated. The schematic of the test section assembly is shown in Figure 7-1 (a) and (b) for front and back isometric views, while the exploded view of test section components is given in Figure 7-2. The technical drawings and dimensions of all components are given in Appendix A. The test section was built around a base machined from brass and later nickel-plated. The base has a liquid inlet port and a vapor-liquid mixture outlet port, both with connections from the back side. The third opening on the base was a 2.42 mm x 7.75 mm rectangular hole, which was used to insert and install the heat conductor. The area around this opening was machined in order to decrease the base thickness and reduce the lateral heat losses. On the front side, the base has a 0.8 mm high and 2.2 mm-wide peripheral groove where an O-ring was placed. The test section was sealed with a transparent glass cover of 12.5 mm height compressed over the test section base. Two bolted aluminum frames sandwiched the test section and produced the force required for compression.

The heat to the system was provided through the heat conductor. The heat conductor was a copper element machined in a T-shape, with a larger area on the bottom and a smaller area faced to the top. The top face is the test surface and

simulated the microchannel fin and had same dimensions as the base opening (2.42 mm x 7.75 mm). It was inserted in the base opening with the face plane 0.40 mm above the test section face plane, and the two pieces were soldered altogether. The larger area of the conductor had a 10 mm x 10 mm area and was also soldered to a 9.5 mm x 9.5 mm thin film resistive heater that provided the heat used in the experiments.

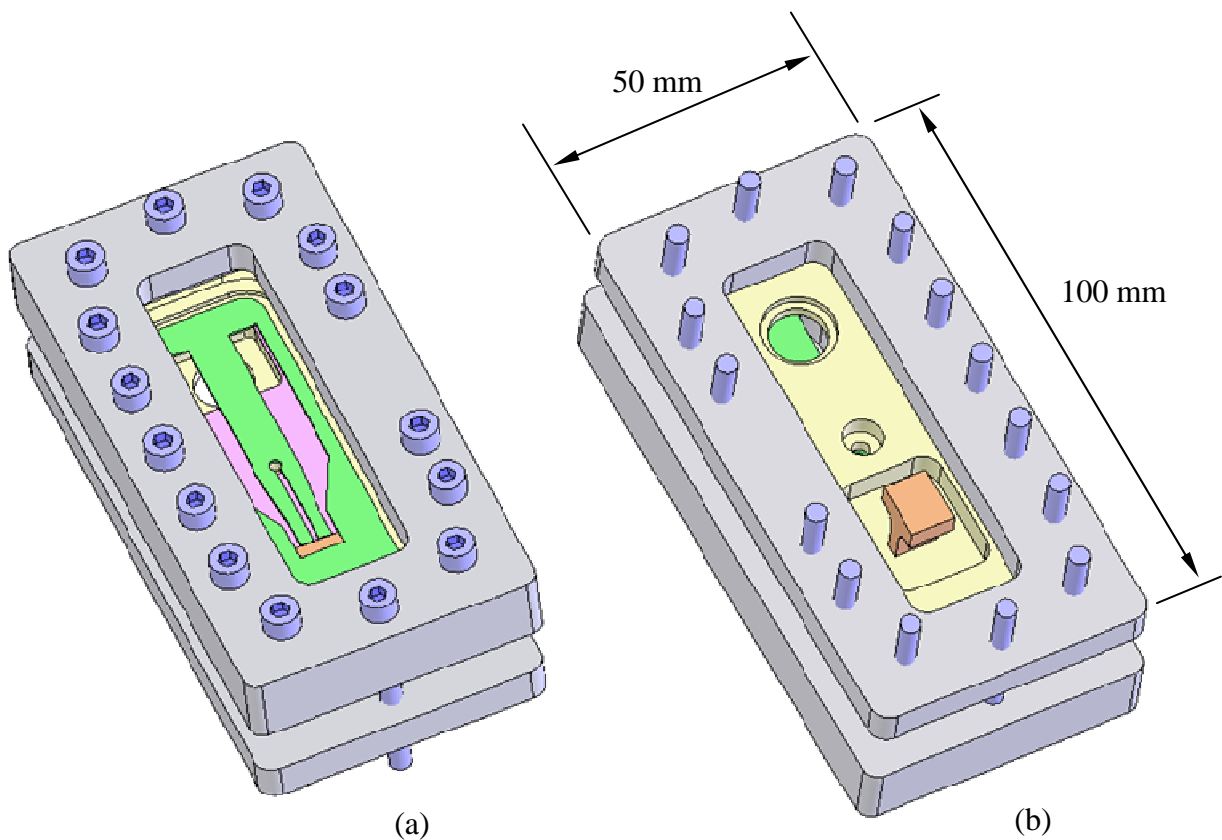


**Figure 7-1. Schematic of visualization test section (a) front isometric view (b) back isometric view**

Two layers of PTFE Teflon sheeting were used for flow distribution and the gap adjustment between the top of the heat conductor and the glass cover. For the first layer, Teflon Layer #1, parts were cut out of the layer to form the inlet and outlet feed channels. This layer conducted the inlet fluid coming from the inlet port located on

the test section base to the test surface of the heat conductor, which was the area of interest. The generated vapor-liquid mixture in this part was connected to the outlet port by two larger outlet feed channels formed on the same Teflon sheet. The thickness of this component was 40  $\mu\text{m}$  and was the same as the height of the test surface. The second Teflon sheet, Teflon Layer #2, was used to increase the gap between the test surface and the glass cover and also to provide thermal insulation. Two different layers with different thicknesses were used in this study: a thin layer with thickness of 70  $\mu\text{m}$  and a thicker layer with thickness of 225  $\mu\text{m}$ . Combining each of these layers with the rest of the test section resulted in test surfaces with gaps of 70  $\mu\text{m}$  and 225  $\mu\text{m}$ , respectively.

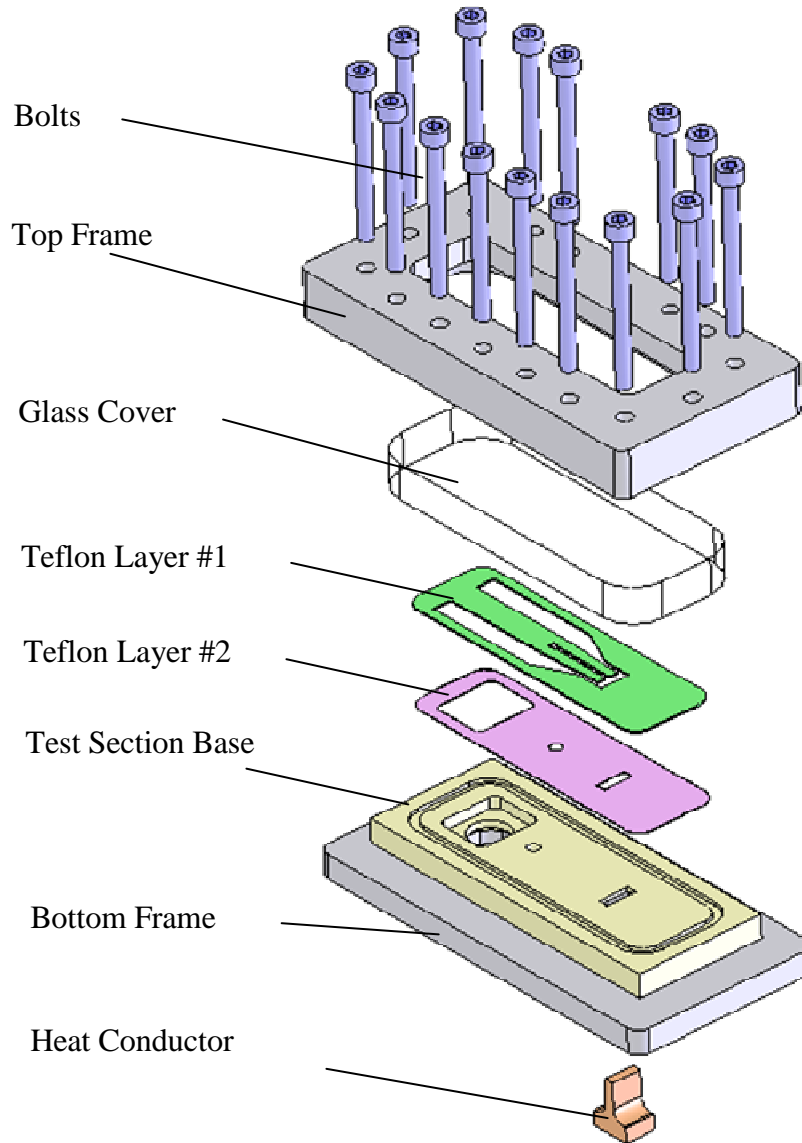


**Figure 7-2. Exploded view of visualization test section components**

The final configuration of the test surface is shown in Figure 7-4. The inlet feed channel provided the liquid, which was forced into the test surface where it experienced an area contraction at the inlet region. On the test surface, the fluid was heated by the surface, thus initiating convective boiling flow. The flow was separated into streams, each leading to an opposite outlet feed channel. The flow experienced an area expansion at the entrance to the outlet feed channels.

The visualization test section was integrated in the test loop used previously for system performance tests (Figure 5-2). Here the test chamber was replaced with the visualization test section. A high-speed camera captured the flow patterns and the two-phase phenomena along the test surface. A picture of the test setup showing the high-speed camera and test section is shown in Figure 7-3. The camera was able to capture 15,000 frames per second with a resolution of 256 x 128 pixels. This resolution captured one turn completely and half of the second turn, as shown in Figure 7-4. Since the flow was symmetric, only one turn was analyzed and, the second turn was assumed to have a similar flow pattern, unless otherwise specified.

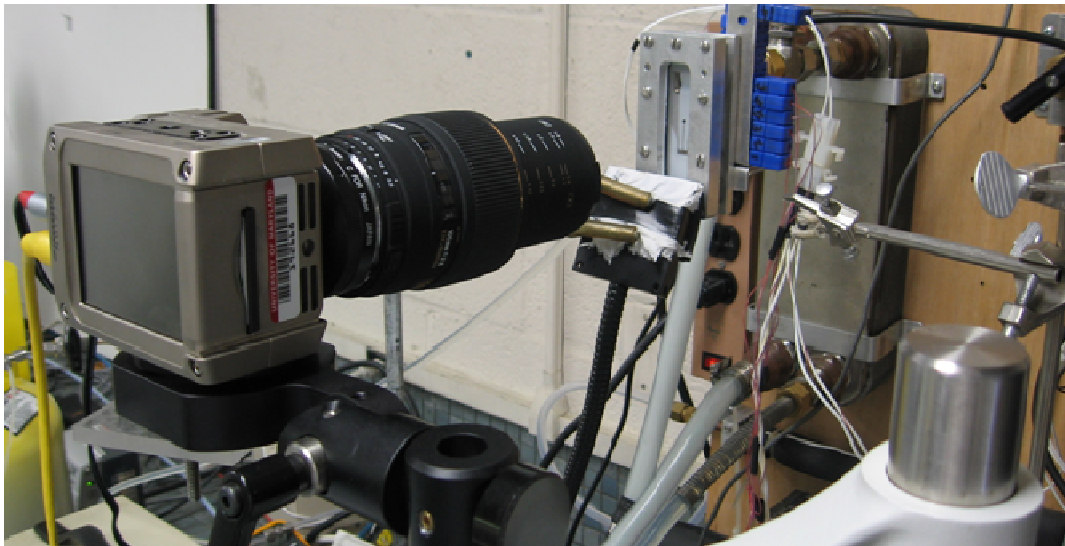


**Figure 7-3. Picture of the visualization test section**

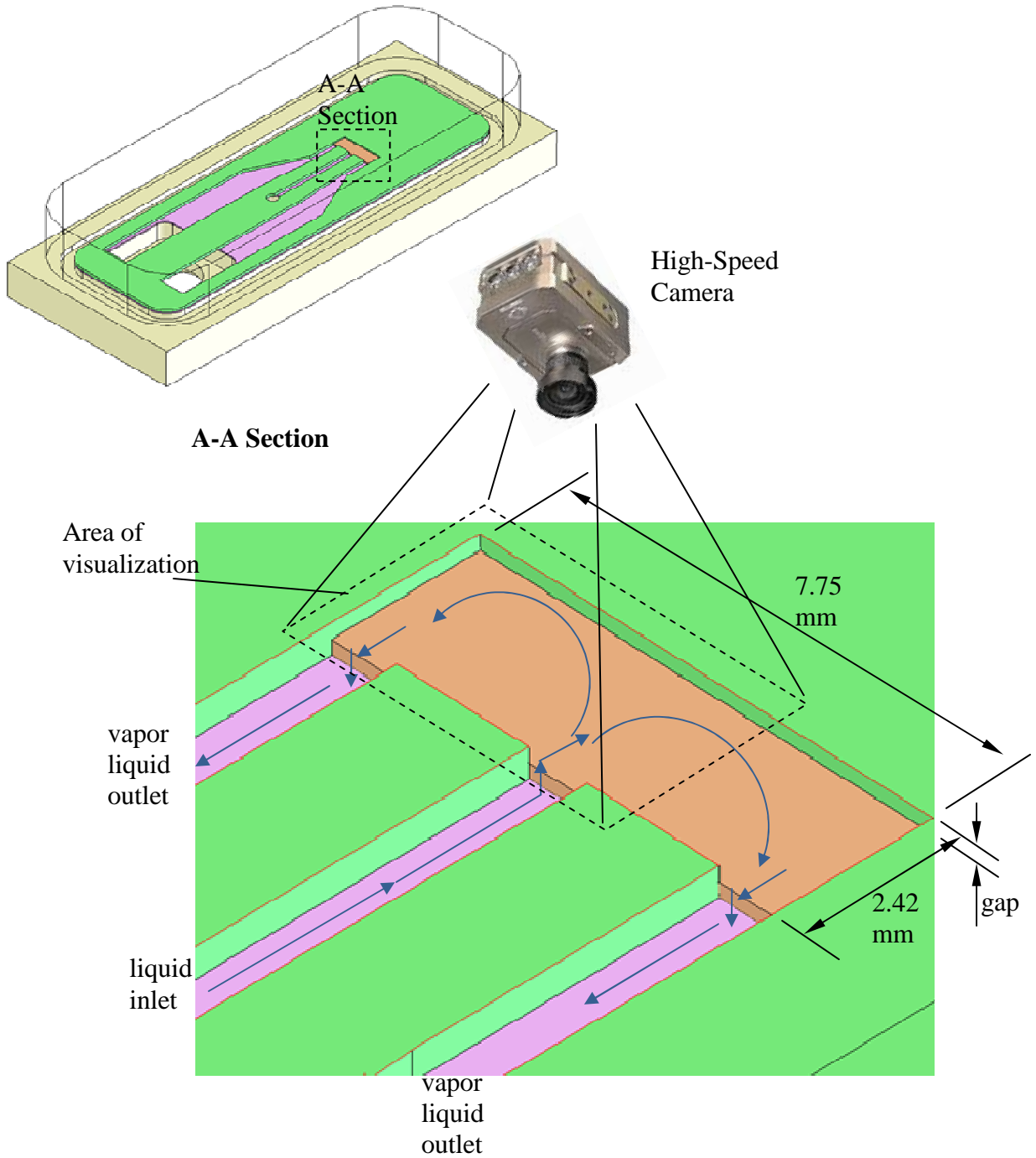


**Figure 7-4. Test surface and area of interest for the visualization study**

### 7.3. Heat Loss Calculations and Data Reduction

The heat supplied to the test section was generated through the resistive heater soldered to the heat conductor. While the primary objective of the heat conductor was to transfer this heat to the working fluid along the test surface, some part of it was transferred to the ambient through parasitic heat losses. Therefore, the heat losses needed to be evaluated to determine the amount of heat transferred directly to the fluid. The test section was equipped with thermocouples located at the inlet and outlet ports. Two thermocouples at the inlet port ( $T_i$ ) measured the inlet fluid temperature, while two thermocouples at the outlet port ( $T_o$ ) measured the two-phase vapor-liquid mixture saturation temperature. Another thermocouple ( $T_s$ ) was located in the heat conductor, 0.5 mm below the test surface (Figure 7-5 (b)).

To evaluate the heat transferred directly to the fluid  $q_f$ , the heat gains/losses had to be evaluated first. The heat generated by the heater was conducted to the heat conductor and flowed in the direction of the test surface (Figure 7-5 (a)). The surface of the heat conductor was not insulated, and therefore some part of the heat was transferred to ambient by convection and radiation ( $q_h$ ). The second source of heat loss was the heat conduction through the base material. The interface between the heat conductor and opening on the test section base was tightly fit and later filled with solder. Some part of heat was conducted through this interface to the test section base ( $q_b$ ). Besides heat losses, heat gains also needed to be considered. The major source of heat gain ( $q_a$ ) was the radiation from the lighting source that was necessary to capture successful images.

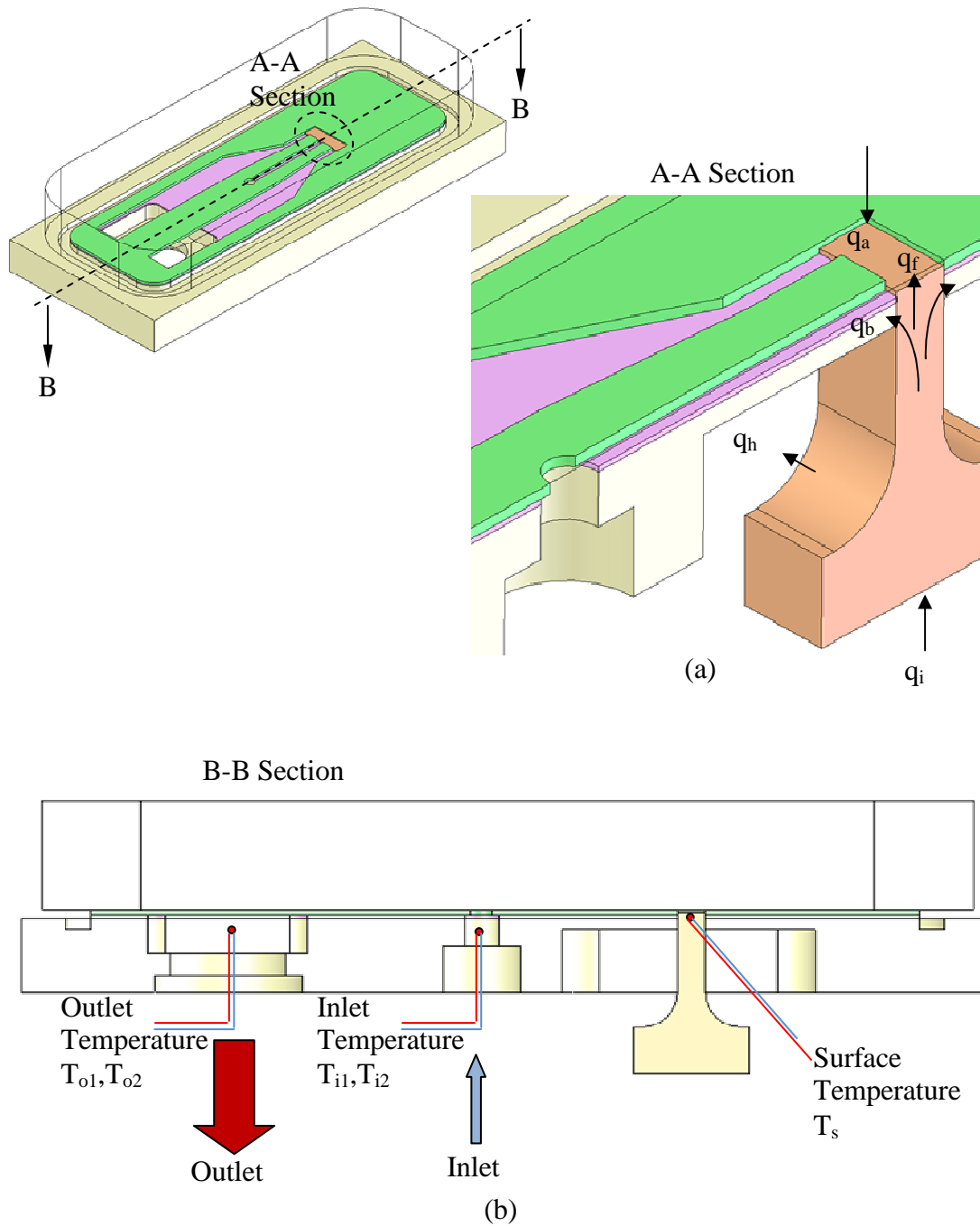


**Figure 7-5. (a) Heat conduction paths in the test set section, (b) Location of thermocouples**

Controlling the heat gains and losses was not practical; therefore, the net heat  $q_f$  transferred to the fluid was calculated based on heat balance performed for preliminary single-phase tests. The approach is based on single-phase data, calculating the total heat losses at various surface temperatures of  $T_s$ . Then the heat losses in the two-phase heat transfer mode can be estimated based on the same surface temperature. In the single-phase heat transfer mode, for any given  $T_s$  surface temperature, the total heat loss can be calculated as:

$$q_{loss} = q_i - \dot{m}c_p (\bar{T}_o - \bar{T}_i) \quad (7-1)$$

where  $\dot{m}$  is the measured mass flow rate,  $c_p$  is the specific heat,  $\bar{T}_i$  is the average inlet temperature and  $\bar{T}_o$  is the outlet fluid temperature. The resulting data at different surface temperatures for gaps of 70  $\mu\text{m}$  and 225  $\mu\text{m}$  are given in Figure 7-6 and Figure 7-7, respectively.

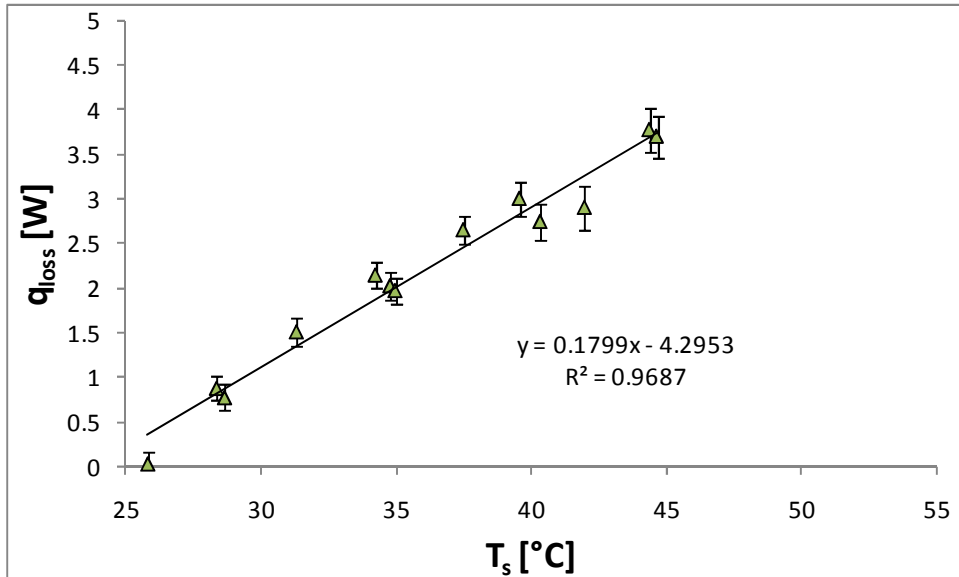
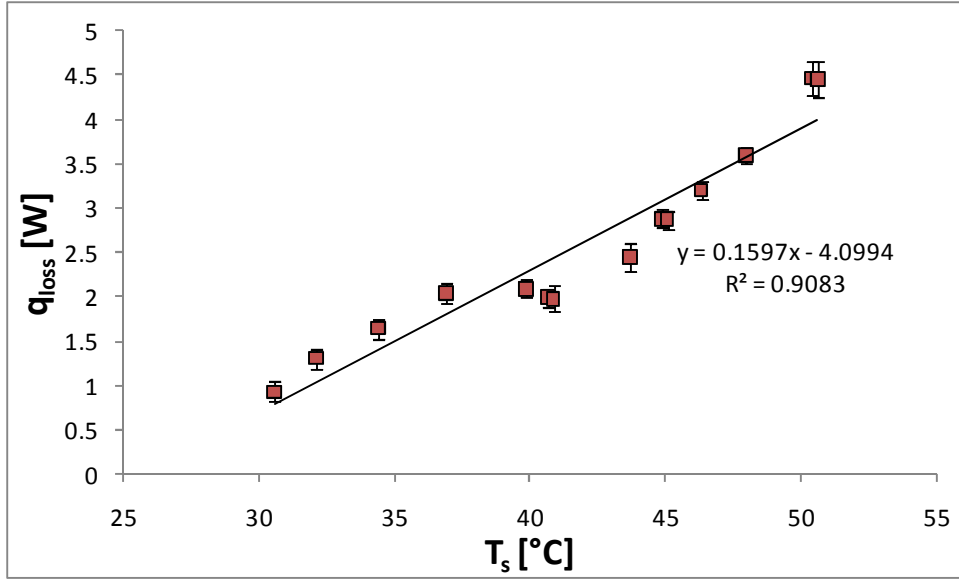


Figure 7-6. Calculated total heat losses for the test surface with a gap of 70  $\mu\text{m}$



**Figure 7-7. Calculated total heat losses for the test surface with a gap of 225  $\mu\text{m}$**

The dependence of heat loss on the surface temperature  $q_{loss} = f(T_s)$ , was correlated using a linear approximation as shown in the figures. For two phase tests, the heat transferred to the fluid was calculated as:

$$q_f = q_i - q_{loss} \quad (7-2)$$

The single-phase heat transfer was calculated based on the temperature difference between the inlet liquid temperature and saturated outlet temperatures. The tests were performed by setting the flow rate to a constant value and increasing the heat flux regularly. For each heat flux value, after the system reached steady state, the high-speed camera was used to collect the visualization videos. A summary of experimental tests performed in this study is listed in Table 7-1.

**Table 7-1. Summary of parameters used for visualization tests**

<b>Gap</b>	<b>Mass Flux</b>	<b>Nominal Mass Flux</b>	<b>Heat Flux</b>	<b>T<sub>i</sub></b>	<b>T<sub>o</sub></b>	<b>T<sub>s</sub></b>
<b>[<math>\mu\text{m}</math>]</b>	<b>[<math>\text{kg}/\text{m}^2\text{s}</math>]</b>	<b>[<math>\text{kg}/\text{m}^2\text{s}</math>]</b>	<b>[<math>\text{W}/\text{cm}^2</math>]</b>	<b>[<math>^{\circ}\text{C}</math>]</b>	<b>[<math>^{\circ}\text{C}</math>]</b>	<b>[<math>^{\circ}\text{C}</math>]</b>
225	199	200	3.1	29.3	32.6	37.7
225	196	200	4.6	29.3	33.5	39.1
225	196	200	9.3	31.6	36.0	42.9
225	198	200	15.5	32.1	36.5	45.1
225	198	200	23.9	32.6	36.7	47.8
225	188	200	32.8	33.0	36.9	49.8
225	193	200	46.2	33.3	37.1	52.9
225	193	200	88.9	29.6	31.7	59.2
225	195	200	103.0	30.1	31.9	67.7
70	242	240	9.8	26.8	34.0	37.9
70	239	240	13.4	26.5	34.1	39.7
70	246	240	15.1	26.7	34.2	40.9
70	245	240	18.2	26.9	34.4	42.6
70	241	240	40.9	26.0	35.1	52.9
70	784	780	17.7	26.5	29.7	39.7
70	794	780	24.1	27.1	34.1	43.6
70	793	780	31.8	27.4	34.6	46.1
70	791	780	46.7	27.8	35.1	50.4
70	786	780	61.9	28.1	35.1	54.1
70	794	780	81.4	28.2	35.1	57.7
70	789	780	92.0	28.4	35.0	60.5

#### 7.4. Visualization Results for Gap of 225 $\mu\text{m}$ and $G=200 \text{ kg}/\text{m}^2\text{s}$

Before presenting the two-phase visualization results, it is useful to determine the single-phase velocity field and static pressure distribution for the given conditions. As shown in Figure 7-8, in single-phase the flow is dominated by inertia forces, which push the liquid from the entrance down to the bottom of the channel. Close to the bottom, the flow impinges and creates a high pressure zone, makes a  $90^{\circ}$  turn, flows in the straight microchannel part, and leaves the test section after making the second turn at the exit. Due to the sharp manifold and test surface corners, a low-velocity recirculation zone is formed on the top part, leaving the high-velocity stream

close to the bottom of the channel. Another interesting observation is the high velocity concentration after the second turn, close to the exit to the feed channel. Due to centrifugal forces, the flow tends to move to the side of the feed channel, creating an area with higher velocities. This flow stratification implies that the centrifugal forces can be important for flow distribution at the outlet of the channel.

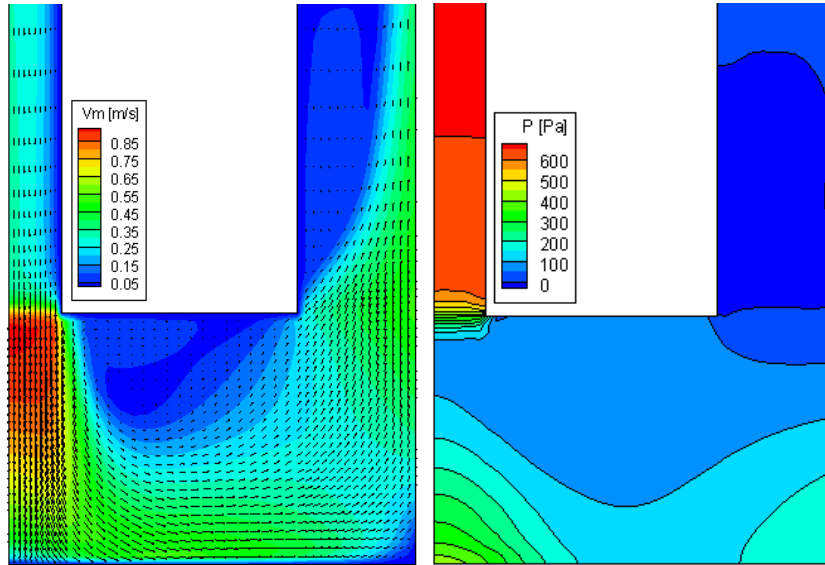


**Figure 7-8. Single-phase velocity vectors and static pressure distribution in test section for 225  $\mu\text{m}$  gap and  $G=200 \text{ kg/m}^2\text{s}$  mass flux**

The two-phase flow patterns and regimes observed at heat fluxes ranging from 3.1-9.3  $\text{W/cm}^2$  are shown in Figure 7-9 (a)-(c). At low heat fluxes, two different flow regimes are present: large vapor slug and bubbly flow. The large vapor slugs are present directly under the manifolds and closer to the inlet feed channel. These large slugs have a transient behavior, resulting from the recirculation zone in the flow field, which creates a low-velocity, high superheated region that favors early nucleation. The bubbles in this region rapidly grow and collapse to form larger bubbles and eventually one major vapor slug. The rotational flow field around the large slug also traps the small bubbles in the main flow, closer to the bottom of the channel. The

slugs grow continuously, and once they grow large enough they are swept away by the inertia of the main flow, and a new cycle of slug development starts in the same region. The second flow regime observed was the bubbly flow in the main flow with nucleation sites closer to the end of the test channel, before the outlet channel. This is because the highest wall superheat in the region is close the end of the channel, where the liquid received sufficient heat though the wall during the flow along the channel.

Increasing the heat flux to higher levels (Figure 7-9 (b)-(c)) has several impacts on flow regimes. First, superheat of wall and liquid increase due to increased heat transfer, which shifts nucleation towards the liquid inlet. The small bubbles are carried away by the main stream while they increase in size gradually. Once the density of relatively large bubbles is high enough, they will start to coalesce to form a slug flow with very large vapor slugs separated by thin liquid columns. In addition, the bubble growth and expansion due to the vapor generation process also affects the flow field in the channel. The large vapor slugs previously present at low heat fluxes become less evident and have a smaller hydraulic diameter and skewed shape. This in turn may suggest that the recirculation zones are less significant, their effect becoming negligible when the flow field is mostly dominated by expansion and coalescence of bubbly flow.

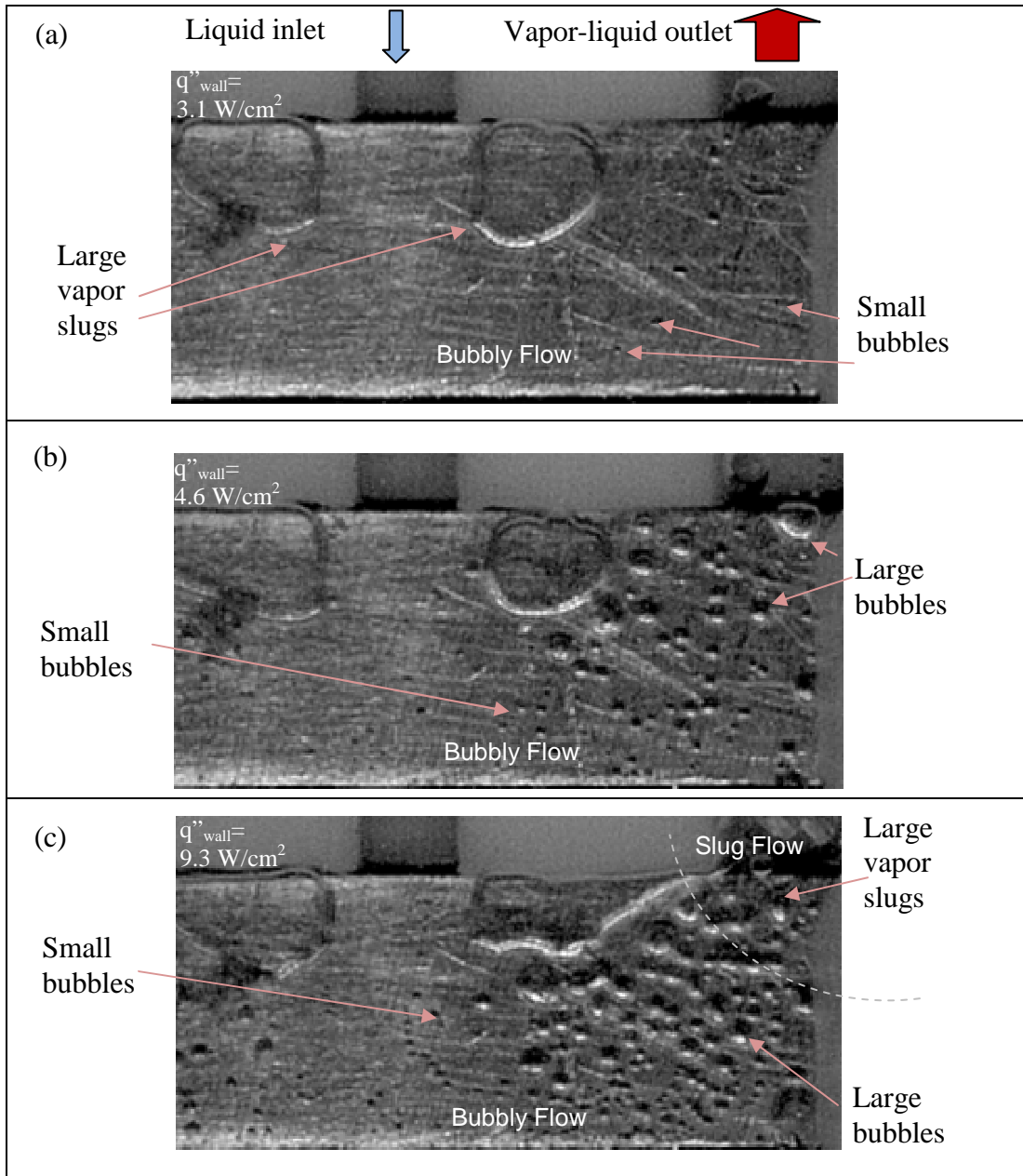


**Figure 7-9. Two-phase flow regimes for gap of 225  $\mu\text{m}$  and mass flux of  $G=200 \text{ kg/m}^2\text{s}$  at (a)  $q''_{\text{wall}}= 3.1 \text{ W/cm}^2$ , (b)  $q''_{\text{wall}}= 4.6 \text{ W/cm}^2$ , (c)  $q''_{\text{wall}}= 9.3 \text{ W/cm}^2$**

Two-phase flow patterns and regimes observed at heat fluxes ranging from 15.5-32.8  $\text{W/cm}^2$  are shown in Figure 7-10 (a)-(c). First of all, the increases in heat flux shifts the initial nucleation sites closer to the inlet region. In addition to the nucleation sites on the test surface, starting at the heat flux of 23.8  $\text{W/cm}^2$ , it was observed that a second nucleation region initiated at the interface between the inlet

feed channel and the test surface, where the inlet liquid is supplied into the test channel. This additional bubble generation region is caused by the liquid trapped under the small region in the forward-facing step flow where the velocity is low, allowing the superheat to build up. This effect is not expected in the actual FFMHS where there are no such “dead zones,” but nevertheless at these conditions the initial nucleation sites are closer to the inlet region where the flow regimes can be similar.

As the heat fluxes increase, the region dominated by the slug flow is shifted closer to the center of the channel. The liquid columns between the vapor slugs become thinner and eventually collapse to form a wavy annular flow shown in Figure 7-10 (c). Also the large vapor slugs under the manifolds seem to occupy less area and are almost compressed to the manifold wall. Again, the inertia created by vapor expansion overcomes the forces creating the recirculation zone, therefore creating a more uniform channel flow. At this point, the flow regimes starting with bubbly, then continuing with slug flow and ending with annular flow, look similar to well known flow regimes in conventional channels, although the transition between these flow regimes seems to be strongly influenced by the complex flow field in the channel. Another important observation is that although the flow is inertia-dominant and the fluid can reach to the bottom of the channel, the bubble coalescence and expansion process creates small flow disturbances, which can change slightly the flow regime transition lines. These transitions could be less clearly defined than two-phase flow in straight channels. The reason for such fluctuations is the strong coupling of inertia, bubble coalescence and expansion, and centrifugal forces that act on the fluid along the channel.

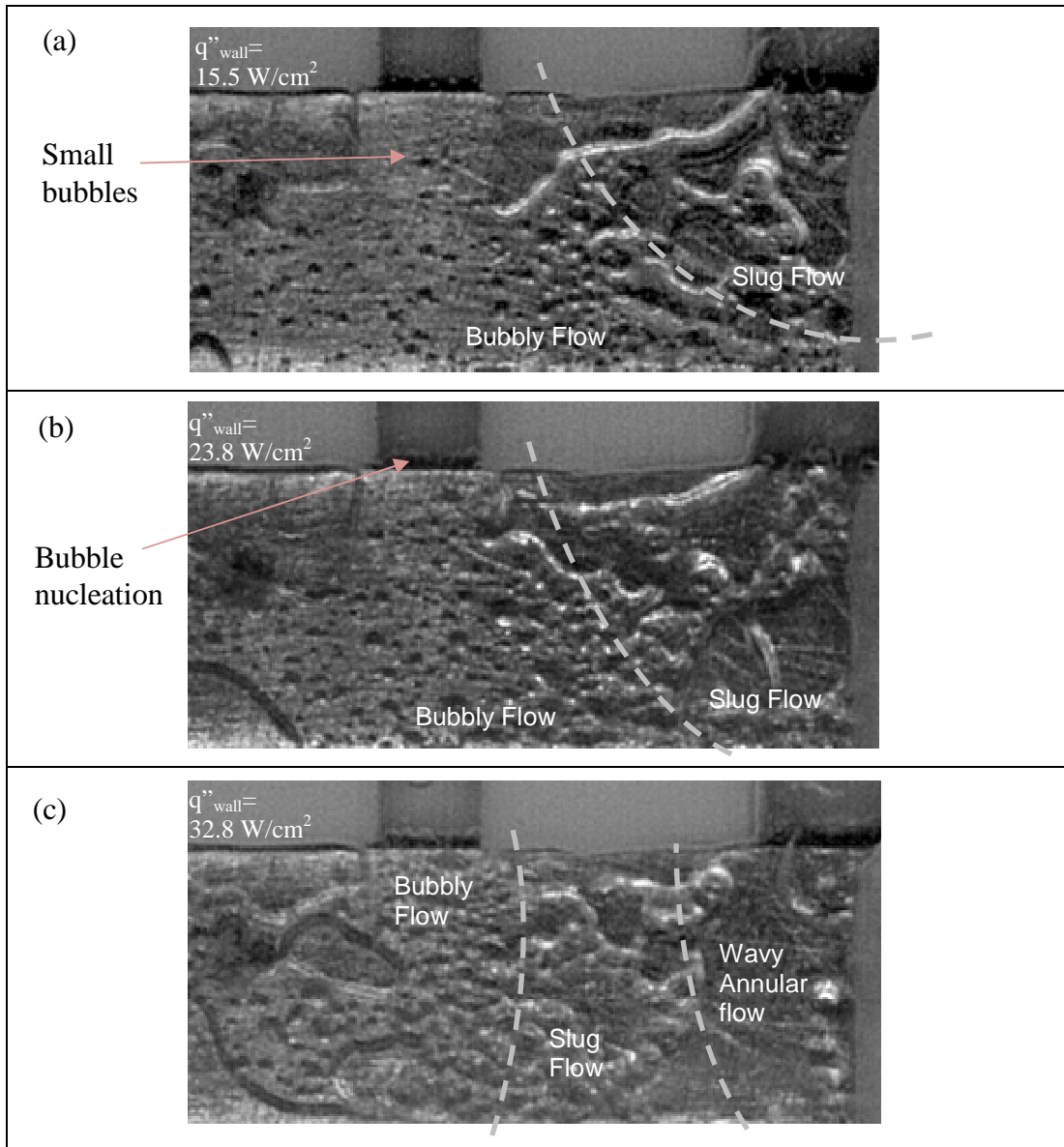


**Figure 7-10. Two-phase flow regimes for gap of 225 μm and mass flux of  $G=200 \text{ kg/m}^2\text{s}$  at (a)  $q''_{\text{wall}}= 15.5 \text{ W/cm}^2$ , (b)  $q''_{\text{wall}}= 23.8 \text{ W/cm}^2$  (c)  $q''_{\text{wall}}= 32.8 \text{ W/cm}^2$**

The two-phase flow patterns and regimes observed at heat fluxes of 46.2 W/cm<sup>2</sup> and 88.9 W/cm<sup>2</sup> are shown in Figure 7-11 (a)-(b). For high heat fluxes the bubbly flow regime is present only at the very narrow region close to the inlet and it rapidly transforms into slug flow. The slug flow regime is also present only for a short region, as the bubble coalescence is more severe under high heat fluxes. After this short slug flow dominant regime, most of the channel resembles a wavy annular

flow with liquid wetting most of the heat transfer area. However, it should be noted that this annular flow regime may include small liquid chunks which are carried to the bottom of the channel by inertia of the fluid and the vapor expansion at inlet region. As the heat flux reaches  $88.9 \text{ W/cm}^2$  it looks like most of the flow becomes wavy annular, with liquid waves present on the channel walls. The thickness of the liquid waves and the liquid film under the vapor was not measurable with the equipment used in the current experiments but it is believed to be changing along the channel and to be strongly dependent on geometry and flow conditions.

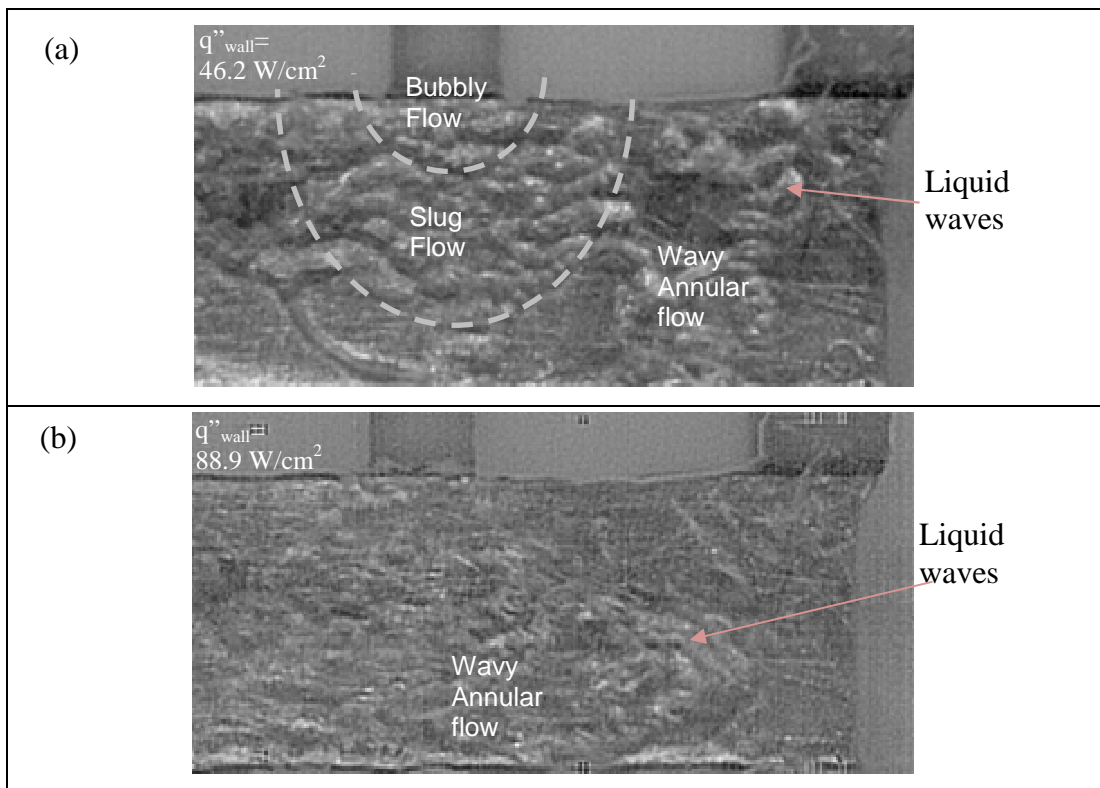


**Figure 7-11. Two-phase flow regimes for gap of  $225 \mu\text{m}$  and mass flux of  $G=200 \text{ kg/m}^2\text{s}$  at (a)  $q''_{\text{wall}} = 46.2 \text{ W/cm}^2$  (b)  $q''_{\text{wall}} = 88.9 \text{ W/cm}^2$**

As the heat transfer progressed to a value  $103.1 \text{ W/cm}^2$  an instability mode was observed in the test channel. For this condition, the pictures taken at several time steps are shown in Figure 7-12, and the sequence of events will be discussed here.

First, it was observed that the inertia forces were high and they could push a large amount of liquid to the bottom of the channel. As the liquid was slightly stratified, nucleation was initiated in this region and bubbles started to grow in the liquid layer. At this point, the bubbles were trapped in the liquid layer and could not be swept away from the bottom channel region. The reason for this effect could be the high-inertia liquid-vapor stream flowing from the top and covering the bubbly liquid layer, preventing it from escaping and flowing towards the outlet feed channel. Another impact on liquid layer trapping could be the centrifugal forces that act differently on the liquid and vapor phases. As the liquid-vapor mixture makes a sharp turn under the inlet feed channel and at the bottom of the test channel, the liquid in the mixture can be pushed on the already present liquid layer, creating additional flow resistance to bubbles to escape. As the bubbles are trapped in the liquid layer, they are fed by liquid evaporation and, after reaching a certain size create sufficient momentum to push incoming fluid and escape the trapping zone. This rapid vapor-expanding process happens very vigorously, such that it sweeps away all liquid present between bottom and outlet feed channel. Formation and expansion of this vapor blanket also affects the incoming liquid flow by creating an obstacle that increases the flow resistance and slows down the liquid inlet velocity. When the liquid input slows down, the vapor generation decreases, which leads to a decrease in pressure built and resistance to the liquid flow, after which liquid fills the channel again, starting the second cycle.

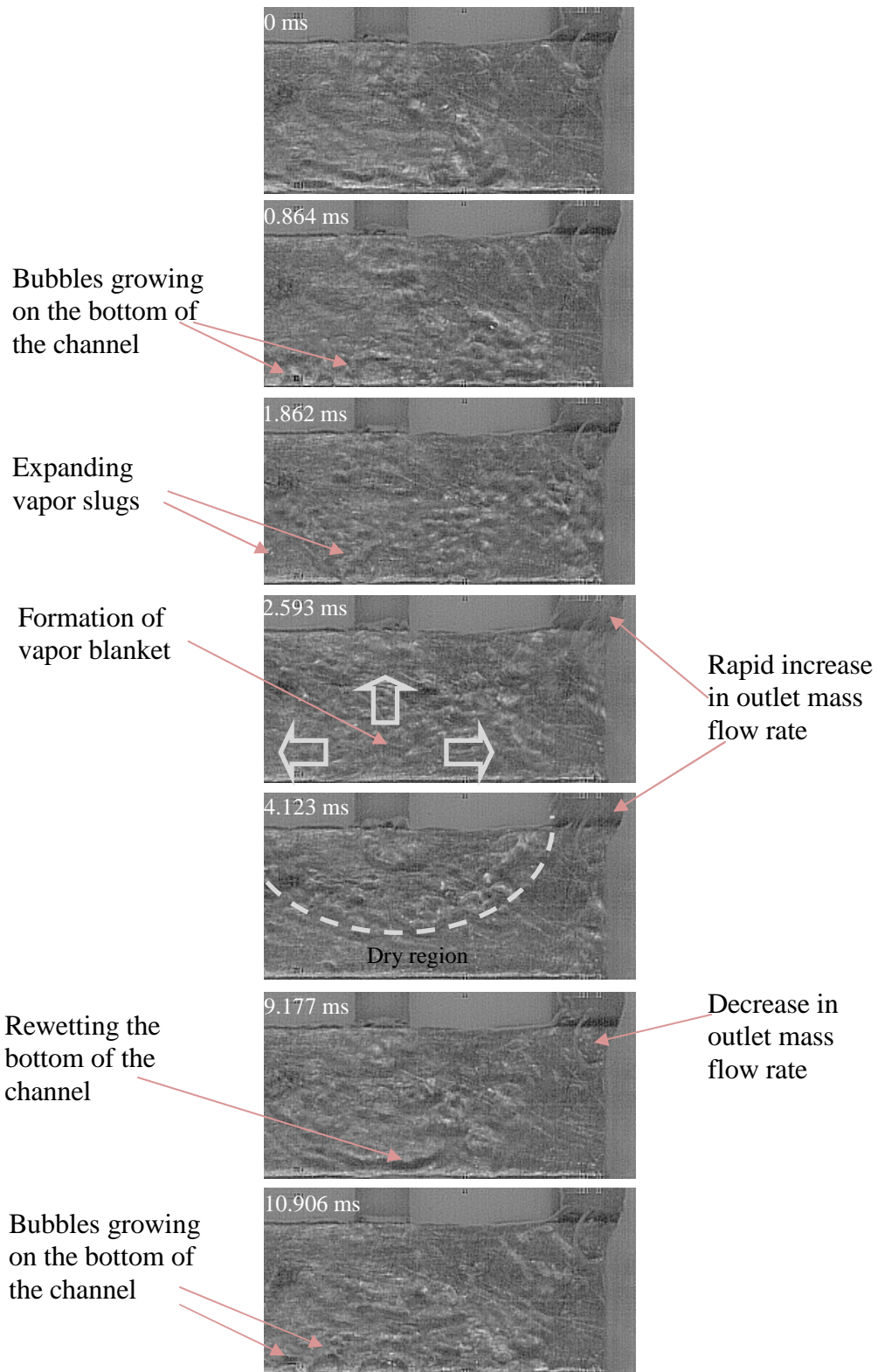


**Figure 7-12. Two-phase flow instability observed for gap of 225  $\mu\text{m}$ ,  $G=200$   $\text{kg/m}^2\text{s}$ ,  $q''_{\text{wall}}= 103.1$   $\text{W/cm}^2$**

The period between two cycles was measured at around 9 milliseconds and the phenomenon was consistent during the video recording time period of 0.3 seconds. Visualization at higher heat fluxes was not performed in order to protect the heater from the high temperatures that build on the heat conductor element. However, the dynamic flow instability observed at given conditions is believed to occur more drastically at higher heat fluxes where the momentum generated by the vapor blanket can grow significantly enough to push the vapor back into the inlet manifold and eventually disturb the flow supply, which will lead to CHF conditions in an FFMHS working in two-phase heat transfer mode.

### **7.5. Visualization Results for Gap of 70 $\mu\text{m}$ and $G=240 \text{ kg/m}^2\text{s}$**

For this configuration, the velocity vectors and static pressure distribution in single-phase are shown in Figure 7-13 (a)-(b), respectively. Here, the gap between the test surface and the glass is about three times smaller, and the mass flux ( $G=240 \text{ kg/m}^2\text{s}$ ) was kept close to the value of previous case ( $G=200 \text{ kg/m}^2\text{s}$ ). Although the mass flux values were close, the decrease in gap altered the flow characteristics in this case. The high flow resistance resulting from lower hydraulic diameter created a flow regime dominated by viscous forces. Therefore, the inertial forces in this case are less effective and do not push the liquid down to the bottom of the channel. Instead, the flow tends to bypass the channel by following the path of least resistance, which is the shortest length between the inlet and outlet feed channels. Therefore the static pressure curves aligned more uniformly along the longitudinal direction of the channel, and since the flow is not impinging there is no high-pressure zone under the inlet manifold and close to the bottom of the channel. As shown in the figure, the

velocities are higher at the top of the channel in the bypass zone, while at the channel bottom velocity magnitudes have minimum values. The flow recirculation zone at the top of the channel and close to the inlet feed channel is also very small and appears not to affect the uniformity of the flow significantly.

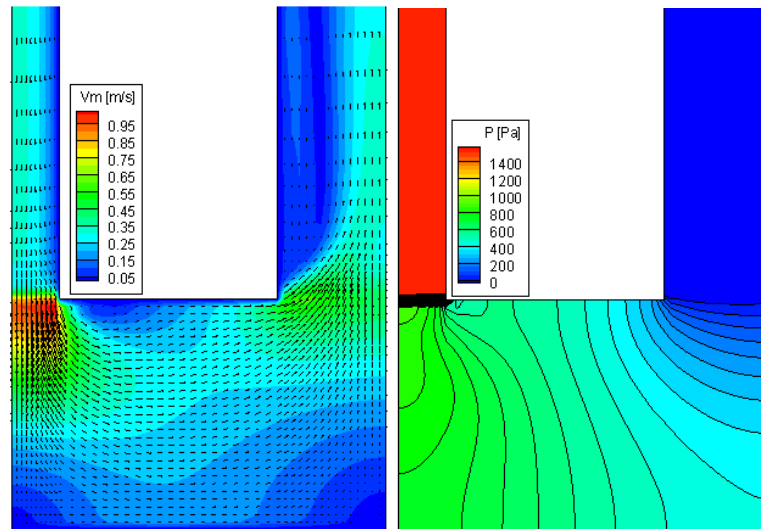


**Figure 7-13. Single-phase velocity vectors and static pressure distribution in test section for 70  $\mu\text{m}$  gap and  $G=240 \text{ kg/m}^2\text{s}$  mass flux**

The flow regimes observed at different heat fluxes ranging from  $9.8 \text{ W/cm}^2$  –  $18.2 \text{ W/cm}^2$  are shown in Figure 7-14 (a)-(d). At heat fluxes of  $9.8 \text{ W/cm}^2$  the two-phase flow regime was observed to consist of bubbly flow. The nucleation sites are closer to the bottom of the channel due to slower flow velocity and larger superheat. It was observed that the bubbles first depart from the heated surface and continue to flow with the fluid stream. When moving in the fluid, the bubbles grow due to the evaporation sustained by superheat of the liquid. After the bubbles grow to the size of the gap, they start to be confined by the channel walls. This bubble confinement effect forces the bubble to grow in lateral directions, parallel to the heated surface plane. Heat supplied from the liquid superheat and the heated wall generates a large amount of vapor that leads to a dynamic bubble expansion process. While the bubble

expands in the channel it creates a thin film of liquid underneath the vapor core. This thin liquid film zone results in low thermal resistance which can enhance significantly heat transfer. As the bubble grows, the liquid film is also depleting and the accumulating vapor in the bubble further accelerates the bubble velocity. After the bubble leaves the test area, the liquid in the upstream wets the surface, and a similar cycle is initiated again. It is important to note that the bubble dynamics observed in this case are different than those observed previously for 225  $\mu\text{m}$  gap in terms of flow regimes. For 225  $\mu\text{m}$  gap the individual small bubbles grew in the liquid before they coalesced and formed bigger bubbles. For 70  $\mu\text{m}$  gap, the bubble expansion is usually the results of individual bubbles, and not a combination of multiple bubble coalescence.

The visualization results obtained for heat fluxes of  $q''_{\text{wall}} = 13.4 \text{ W/cm}^2$  and  $q''_{\text{wall}} = 15.1 \text{ W/cm}^2$  are shown in Figure 7-14 (b) and (c), respectively. As the heat flux increases, liquid superheat and vapor generation during evaporation increase as well. Therefore the bubble expansion process becomes more and more vigorous, with single bubbles pushing the flow in all directions. The process is generally very chaotic due to the high inertia of vapor expansion, which affects the flow field and can alter the nucleation sites. When the heat flux is increased to  $q''_{\text{wall}} = 18.2 \text{ W/cm}^2$  the forces created by bubble expansion completely dominate the inertia of the incoming fluid and vapor back-flows into the inlet feed channel are observed. At this point, the bubble expansion at regions closer to the inlet usually block the liquid from rewetting the bottom area of the channel, and the heated surface remain mostly dry. Also, the increased heat flux hastens the evaporation of the thin liquid film,

increasing the time between initialization of dryout and rewetting. Therefore for the given conditions, a decrease in heat transfer performance is expected.

When the heat flux was increased to  $q''_{\text{wall}} = 40.9 \text{ W/cm}^2$  a dynamic instability mode was observed. The sequences of the two-phase flow regimes are shown in Figure 7-15. The cycle starts with liquid having high inertia coming from the inlet feed channel entering the almost completely dry channel. The incoming liquid wets the heated surface and the bubble expansion process initiates. First the nucleation of the small bubbles at the region close to the bottom of the channel is initiated. The bubbles grow until the diameter of bubbles reach the gap dimension and are geometrically confined. Then the heat transfer to the bubble rapidly expands it, pushing the fluid in all directions and slowing down the incoming liquid. When the fluid flow slows down, the nucleation of the liquid close to the inlet region is initiated and the same bubble expansion phenomena occurs, this time creating a large vapor slug that pushes the incoming liquid back into the inlet feed channel. While the inlet liquid is blocked, the remaining liquid in the channel is evacuated either by evaporation or nucleation of liquid bubbles. After most of the vapor is depleted in the test channel, the resistance previously created by vapor generation is eliminated and the incoming liquid wave starts the second cycle by feeding it into the channel. In this case, the incoming liquid has a higher velocity than in the case of lower heat fluxes with no observed flow instabilities. The reason is the pressure build-up in the inlet manifold when the mass flow rate decreases during the dynamic cycle. Here, the period of each cycle was around 12 milliseconds.

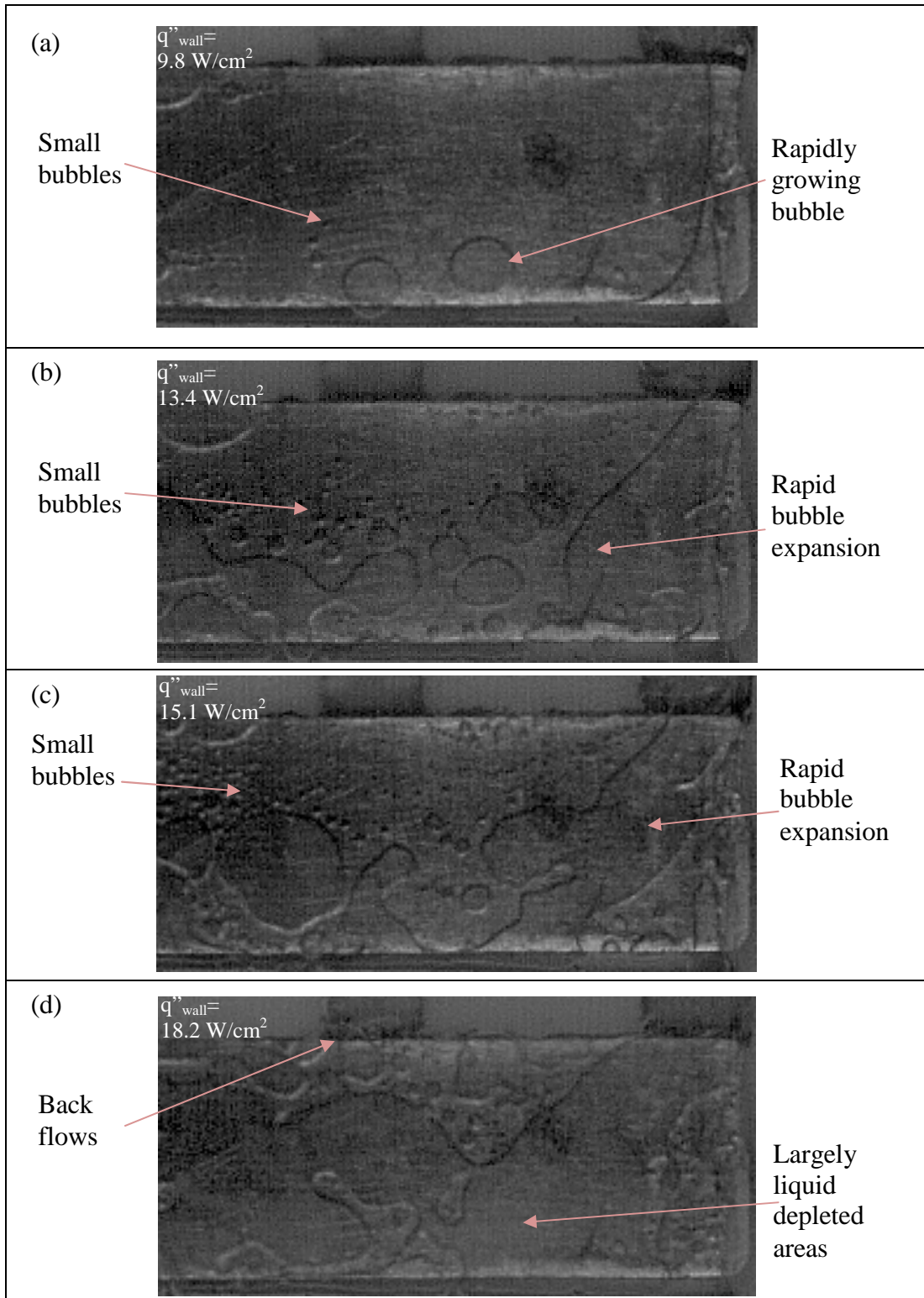


**Figure 7-14. Two-phase flow regimes for gap of  $70 \mu\text{m}$  and mass flux of  $G=240 \text{ kg/m}^2\text{s}$  at (a)  $q''_{\text{wall}}= 9.8 \text{ W/cm}^2$  (b)  $q''_{\text{wall}}= 13.4 \text{ W/cm}^2$  (c)  $q''_{\text{wall}}= 15.1 \text{ W/cm}^2$  (d)  $q''_{\text{wall}}= 18.2 \text{ W/cm}^2$**

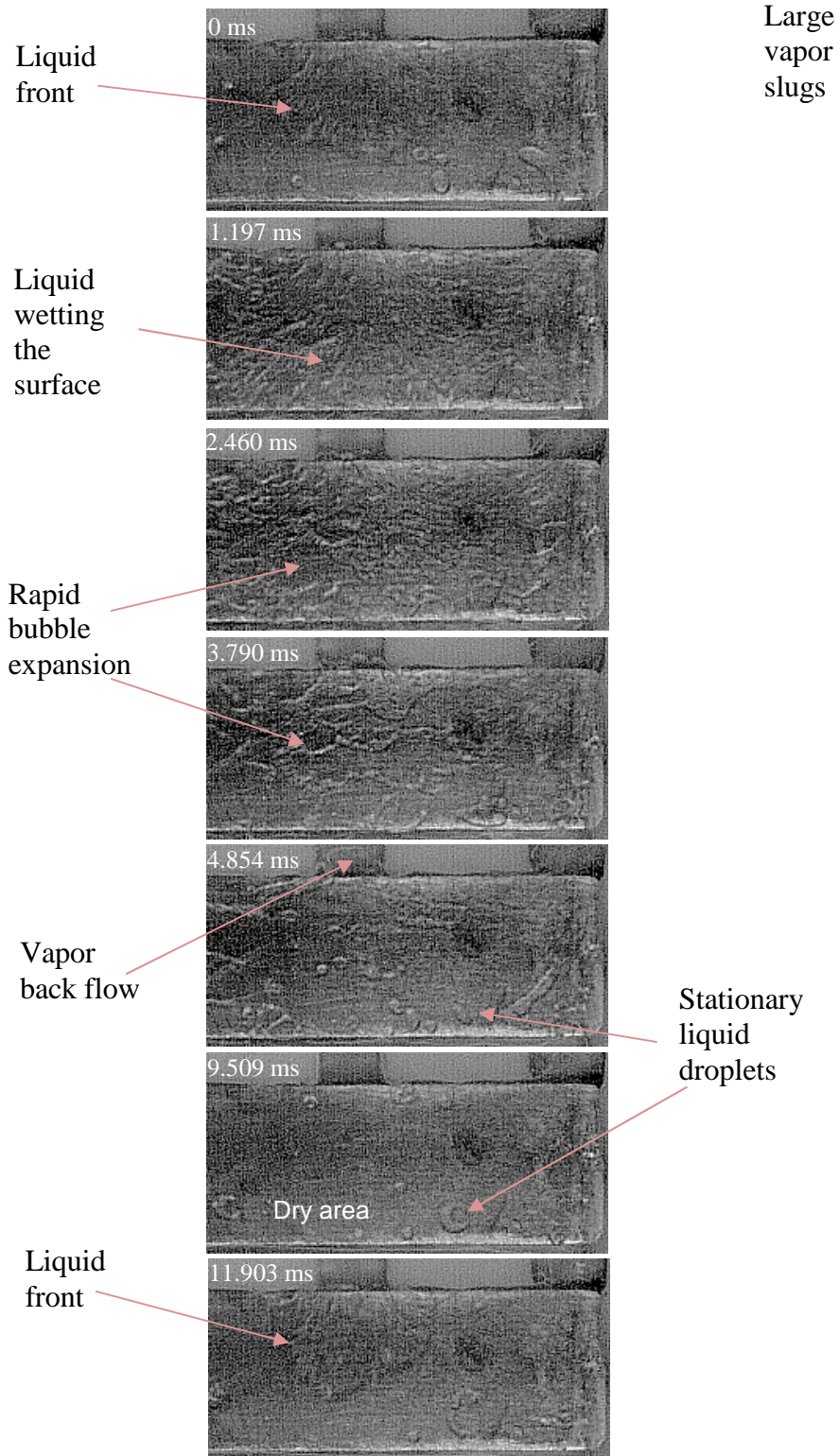


**Figure 7-15. Two-phase flow instability observed for gap of 70  $\mu\text{m}$ ,  $G=240$   $\text{kg/m}^2\text{s}$ ,  $q''_{\text{wall}}= 40.9$   $\text{W/cm}^2$**

## 7.6. Visualization Results for Gap of 70 $\mu\text{m}$ and $G=780 \text{ kg/m}^2\text{s}$

The third set of visualization tests was performed by keeping the gap at 70  $\mu\text{m}$  and increasing the mass flux to  $G=780 \text{ kg/m}^2\text{s}$ . The objective of these tests was to observe the effects of mass flux on the flow regimes for same channel gap. The single-phase velocity vectors and static pressure distribution in the test channel are shown in Figure 7-16 (a) and (b), respectively. As shown in the figure, the high mass flux has increased the inertia of the incoming liquid, and the flow impinges on the bottom of the test channel, creating a high static pressure zone. Therefore, the current low configuration is more inertia-dominated, and viscous forces have less effect.

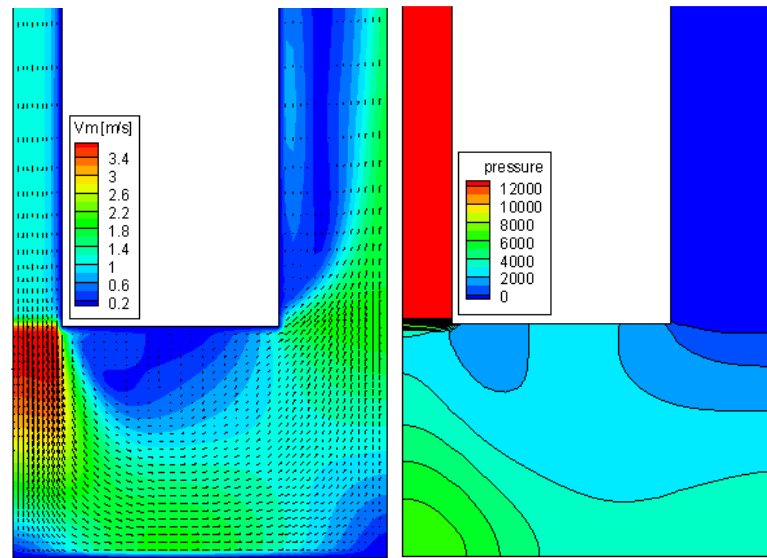


**Figure 7-16 Single-phase velocity vectors and static pressure distribution in test section for 70  $\mu\text{m}$  gap and  $G=780 \text{ kg/m}^2\text{s}$  mass flux**

The two-phase flow regimes observed for heat fluxes ranging from  $q''_{\text{wall}}=17.7 \text{ W/cm}^2$  to  $q''_{\text{wall}}=46.7 \text{ W/cm}^2$  are shown in Figure 7-17 (a)-(d). At the low heat flux of  $q''_{\text{wall}}=17.7 \text{ W/cm}^2$  the flow regime was observed to be bubbly flow. The bubbles were generated close to the channel outlet and grew as they moved along

with the flow. However the growth of the bubbles was not as dramatic as was observed in the previous case with low mass flux and similar heat flux, primarily due to the lower liquid superheat at higher mass flow rates and increased flow inertia. Another important observation is that the bubble diameters that nucleated from the surface are much smaller than the channel gap of 70 microns, indicating that bubble nucleation could occur also at smaller channel dimensions. As the heat flux increases (Figure 7-17 (b)), the transition to bubbly flow regime moves closer to the center of the channel. As the bubbles progress in the flow, they grow bigger than those of the previous heat flux due to increased liquid superheat created by higher heat flux and length of flow path. Close to the exit area the bubbles coalesce and form large vapor slugs surrounded by liquid columns.

An increase in heat flux to  $q''_{\text{wall}} = 31.8 \text{ W/cm}^2$  shifts the flow regime transition curves to the center of the channel. The amount of liquid separating big vapor slugs in the slug flow diminishes, and a wavy annular flow regime is observed at the end of the channel. Similarly, when the heat flux is set to  $q''_{\text{wall}} = 46.7 \text{ W/cm}^2$  the flow transitions occur much closer to the inlet region and the wavy annular flow regime occupies a larger area. At this heat flux, bubble nucleation was observed at the inlet region, similarly to the previous case at gap of 225  $\mu\text{m}$  and mass flux of 200  $\text{kg/m}^2\text{s}$ . Additionally, at this heat flux and mass flux of the coolant, the liquid trapped between the face side of the heat conductor and Teflon Layer #2 becomes sufficiently superheated, and nucleation starts in this gap. Bubbles created at this location are usually much larger and when entering the test channel can disturb the flow and the flow regime transition regions. These high-volume bubbles usually create disruption

in the bubble and slug flow regimes and can send liquid droplets and slugs into the annular flow regime.

When heat flux increases to higher values (Figure 7-18 (a)-(c)) the flow regime transitions occur mostly at the narrow region close to the inlet to the channel, while the frequencies and diameters of bubbles generated by secondary nucleation site increase too. At the highest heat flux tested of  $q''_{\text{wall}} = 92.0 \text{ W/cm}^2$  the secondary bubble nucleation becomes very dramatic, and the flow regime was observed to be mostly annular with large liquid slugs spread into the channel. In the actual FFMHS working mode the secondary nucleation sites are not expected to be present due to the fluid continuously wetting the entire fin surface exposed at inlet and eliminating the possibility of creating any dead zones. Another observation is that for given test conditions no dynamic instability mode was observed. This in turn may explain why the channel blocking phenomena discussed in previous sections is a function of mass flux as well as heat flux and channel hydraulic diameter.

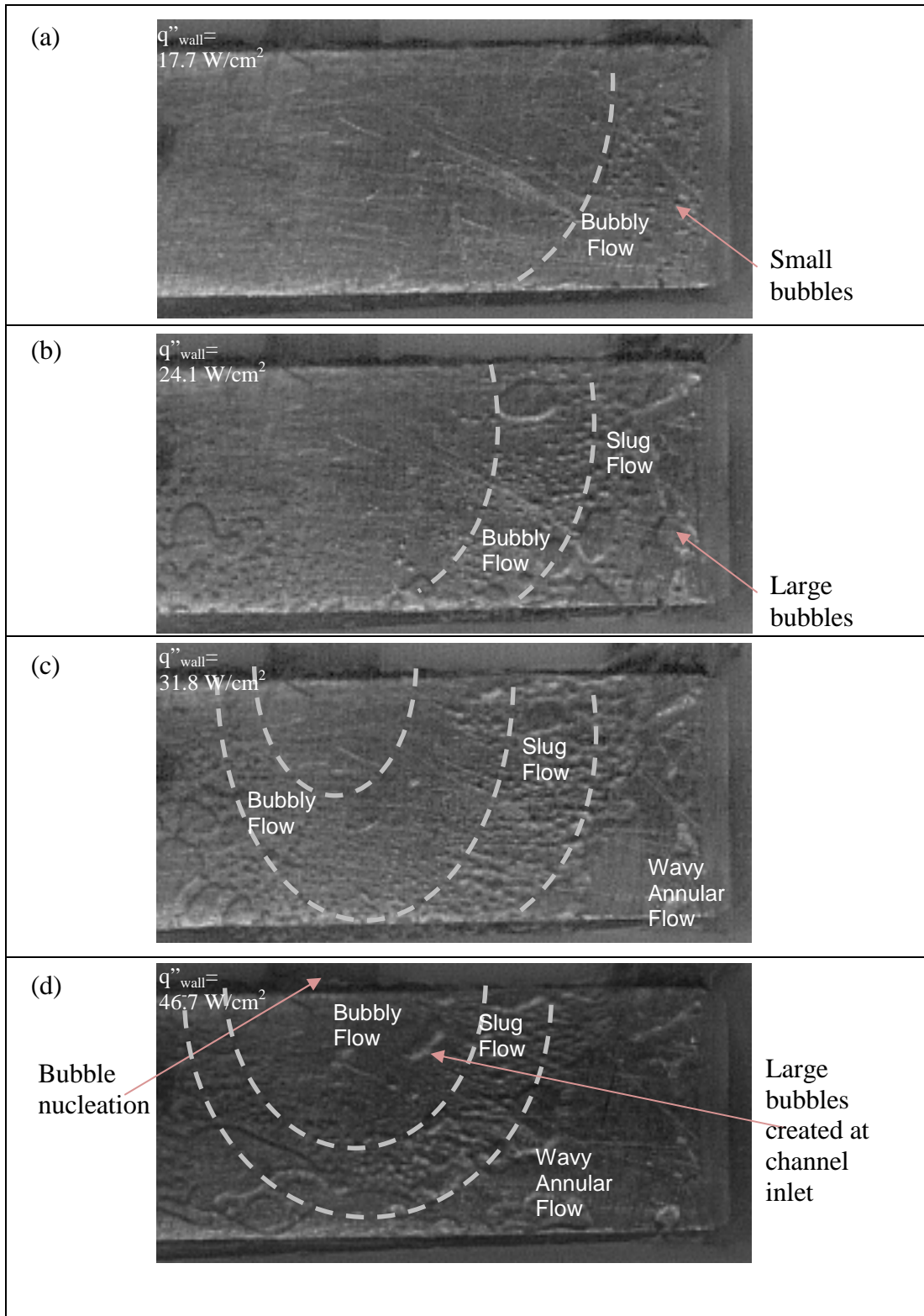


**Figure 7-17. Two-phase flow regimes for gap of  $70 \mu\text{m}$  and mass flux of  $G=780 \text{ kg/m}^2\text{s}$  at (a)  $q''_{\text{wall}} = 17.7 \text{ W/cm}^2$  (b)  $q''_{\text{wall}} = 24.1 \text{ W/cm}^2$  (c)  $q''_{\text{wall}} = 31.8 \text{ W/cm}^2$  (d)  $q''_{\text{wall}} = 46.7 \text{ W/cm}^2$**

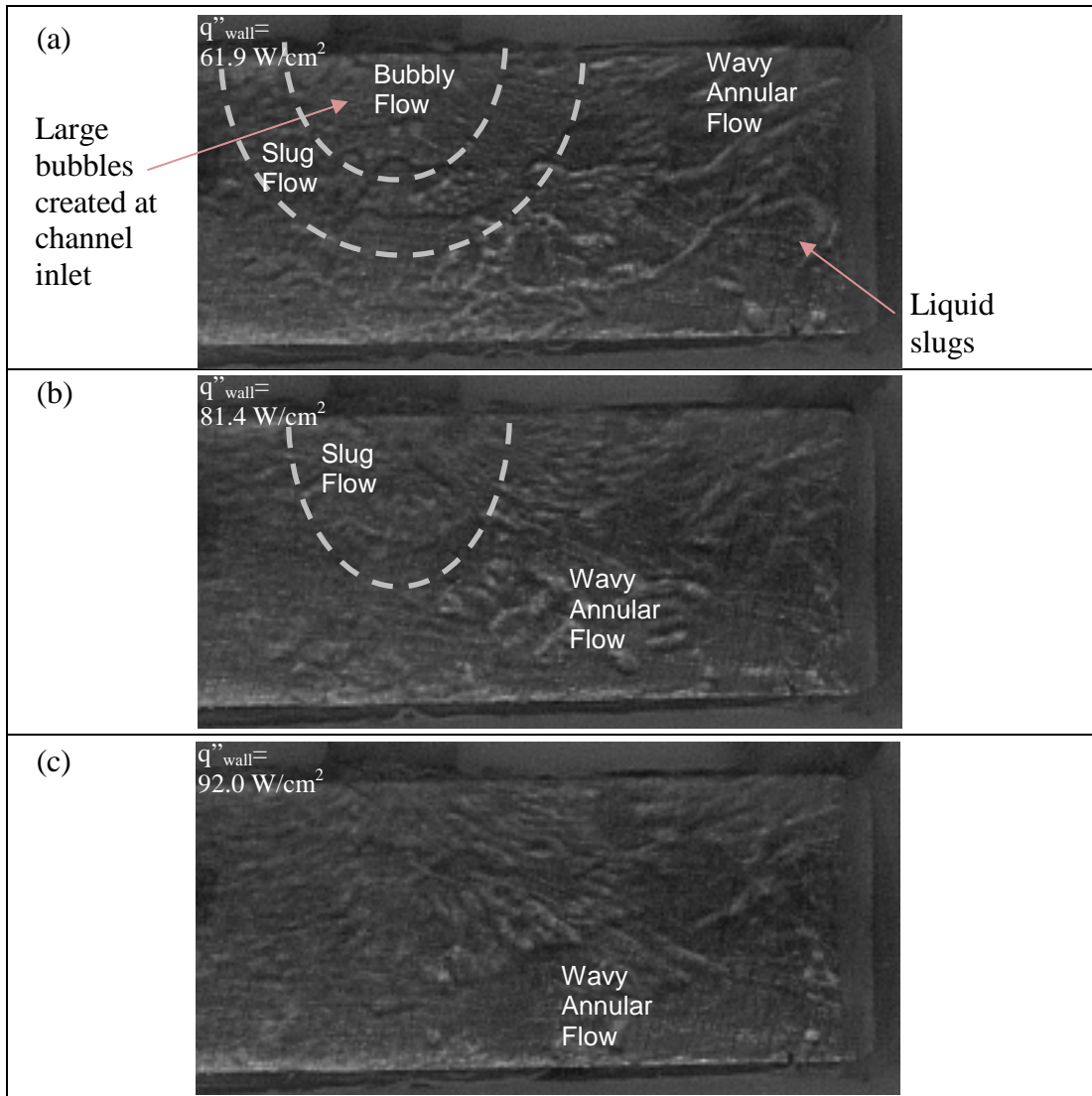


**Figure 7-18. Two-phase flow regimes for gap of  $70 \mu\text{m}$  and mass flux of  $G=780 \text{ kg/m}^2\text{s}$  at (a)  $q''_{\text{wall}}= 61.9 \text{ W/cm}^2$  (b)  $q''_{\text{wall}}= 81.4 \text{ W/cm}^2$  (c)  $q''_{\text{wall}}= 92.0 \text{ W/cm}^2$**

## 7.7. Conclusions

Three different cases with specified gap dimensions, mass fluxed and heat fluxed were investigated by visualization means with the goal of explaining the possible two phase flow regimes and CHF mechanisms in FFMHS.

First, it was found that the two-phase flow regimes are strongly dependent on flow characteristic. For the flow field where the viscous forces are dominant, fluid

follows the path with the least flow resistance, which is the minimum distance under the manifold and between inlet and outlet feed channels. In this case, the flow does not impinge on the bottom of the channel; therefore the velocities in this region are much smaller. This in turn leads to larger liquid superheats and the first nucleation sites appear close to the bottom of the channel. On the other hand, when the flow is inertia-dominant, the flow impinges on the channel bottom, and the first bubbles were observed in the recirculation zone under the manifold and along the flow stream, close to the exit to outlet feed channel.

Second, it was found that for the given set of flow and geometrical configurations, the dominant flow characteristic has also a significant impact on the heat transfer. For a viscous dominated flow, the velocities are generally small, and the bubble expansion mechanism is dominant over the whole channel. Bubbles that nucleate on the heated surface first detach and almost immediately grow to the size of the channel gap. At this point the bubble is confined and starts to grow rapidly in directions parallel to the plane of heated surface. The heat supplied to bubble vapor generation is believed to be transferred from both the highly superheated liquid and from the heated surface. This dynamic process results in two effects in the working characteristics of FFMHS. When the bubble expands, it forms an elongated bubble shape with a vapor core in the center and a thin liquid film on the wall. The thin liquid film heat transfer zones drastically increase the heat transfer coefficients at very low qualities. However, when the heat flux is further increased, the nucleation sites are increased, and the expansion process of multiple bubbles seems to affect and obstruct the flow path of the bubbles. This creates a more chaotic flow regime with

flow controlled by the inertia created by multiple bubble expansion. For a specific heat flux, the bubble expansion process become very rigorous, with bubbles expanding close to the inlet region where they begin sending vapor into the inlet feed channel. After this point, a dynamic instability flow is dominant. It was also observed that the heated walls for these conditions are less frequently wetted and stay dry for longer periods of time.

The phenomena described here can explain the rapidly increasing/decreasing trend observed for low to medium mass fluxes in FFMHS two-phase experimental tests obtained for Surface #C and Surface #17. As seen in Figure 6-4 (b) and (c), at low mass fluxes, both surfaces present a viscous-dominated flow regime with no significant impingement on the channel bottom. The single bubble expansion flow regime starts at very low qualities, and the heat transfer is enhanced mainly by the thin liquid film formed underneath the elongated bubble. Therefore, the heat transfer coefficients have a rapidly increasing trend in this region. The heat transfer coefficients increase until a point where further increase the heat flux creates multiple bubble expansion processes that obscure the bubbles and block the incoming liquid to wet the dry areas. The increase in dry areas followed by vapor back flows decrease the system overall performance, and heat transfer coefficients start to drop significantly.

For high mass fluxes, the inertia forces are dominant, and the incoming fluid can send the liquid down to the bottom of the channel, creating an impingement zone with a presence of secondary maxima in static pressure. The increase in mass flux also decreases the liquid superheat, therefore comparing to low mass flux case with

similar hydraulic diameter and heat flux, the forces created by bubble expansion are less severe and the inertia of incoming fluid is high enough to prevent large fluctuations and vapor backflows in the inlet feed channel. Therefore in these cases, the flow regime is observed to be similar to the flow regimes indicated for conventional channels. The first flow regime is bubbly flow, which shifts later to slug flow and finally to the wavy annular flow. In this case, the formation of large elongated bubbles is suppressed, therefore, the heat transfer at low mass fluxes is mainly controlled by bubble nucleation, which generally creates lower heat transfer coefficients than the thin film evaporation process earlier observed at lower mass fluxes. Therefore, the general trend of heat transfer coefficients follows a less steep monotonic increasing trend with no maximum peaks. This may explain the similar heat transfer trend shown generally at higher mass fluxes during FFMHS experimental tests (Figure 6-4 (d)-(f)). When compared to saturated boiling heat transfer correlations, the similarity of flow regimes with those in conventional channels seems to explain why heat transfer coefficients approach the values predicted by Chen correlations.

Third, two instability mechanisms were observed during visualization tests. The first mechanism is present when the inertia forces are dominant over viscous forces. As the flow regime become mostly wavy annular, nucleation in a small liquid layer in the impingement zone is blocked by high inertia of incoming fluid, most likely by the liquid that is accumulated by centrifugal forces during the flow turning. Therefore the bubbles are trapped and start to grow until the evaporative forces overcome the flow inertia forces. At this point, the created vapor blanket pushes the

liquid in all directions by expanding it towards the outlet of test channel and creating a disturbance in the flow. Although tests at higher heat fluxes were not performed due to the test section limitations, the phenomena are expected to behave vigorously and at some point to push the incoming liquid back into the inlet feed channel, creating back flows. This effect may explain the CHF observed for FFMHS at high heat and mass fluxes where the heat transfer coefficient has an increasing trend and the flow regime is expected to be wavy annular. At low mass fluxes, where the flow field is dominated mostly by viscous forces, the main mechanism of dynamic instabilities is observed to be a similar channel vapor blockage. However, in this case, the blockage of incoming liquid is created by the bubble expansion process occurring all around the test channel, which eventually becomes dominant and eventually sends vapor slugs back into the inlet feed channel, creating a pulsating flow. The chaotic rapid movement of the bubbles and the suppression of incoming liquid create large dry areas, and the heat transfer coefficients in this region decrease. This effect can in turn be related to the CHF condition created in FFMHS at low heat and mass fluxes where the heat transfer coefficients decrease.

The vapor backflows and the dynamic two phase flow instability observed here in form of pulsating flow, can explain the decreasing heat transfer trend resulting from large dryout periods and flow maldistribution. These effects are present when the evaporative forces created during boiling of the fluid in the microchannel overcome the inertia forces of the incoming liquid. To define the flow parameters at stable working conditions, a stability criterion has been developed. The parameter  $C$ , given in Equation (7-3), was derived based on evaporative and inertia force balance in

the FFMHS and the detailed derivation of this parameter is given in Appendix D. This parameter represents the ratio of liquid inertia to the vapor expansion in the microchannel. A large number of  $C$  represents a liquid inertia dominated flow, where the two phase flow regimes are expected to resemble those in conventional channels (i.e. bubbly flow, confined bubble flow, annular flow) and the heat transfer coefficients are expected to increase slightly with increase in heat flux.

$$C = \frac{\rho_v}{\rho_l} \frac{\dot{m}_{ck} h_{lv}}{q_{base}'' (w_{ck} + t_{fm}) \left( \frac{w_l}{2} + t_{max} + \frac{w_v}{2} \right)} \quad (7-3)$$

Variation of parameter  $C$  with respect to heat experimental heat transfer coefficient for Surface #12, Surface #17 and Surface #C are shown in Figure 7-19, Figure 7-20 and Figure 7-21 respectively. As shown in the figures, for values of  $C > 0.05$  the heat transfer coefficients have a monotonic decreasing trend. This region represents the increasing trend of heat transfer coefficients with increase in heat flux at low heat fluxes, which in turn results in high  $C$  values. At lower  $C$  values, the evaporative forces start to become comparable to inertia forces and the heat transfer coefficients follow a decreasing trend due to backflow and dryout mechanisms mentioned before. This transition criterion can be a useful parameter in design stages of FFMHS.

Fourth, for each visualization test where the flow instabilities were not present, it was observed that the inlet channel region was in liquid phase for low to medium heat fluxes, and the initiation of nucleate boiling was suppressed up to high heat fluxes. This is expected since the liquid that enters the microchannel is few degrees subcooled and the highest wall superheat is far away from this region. However a closer look to the nucleation incipience in this region can give additional

useful information regarding the liquid superheat that can be expected for microchannels with different hydraulic diameters.

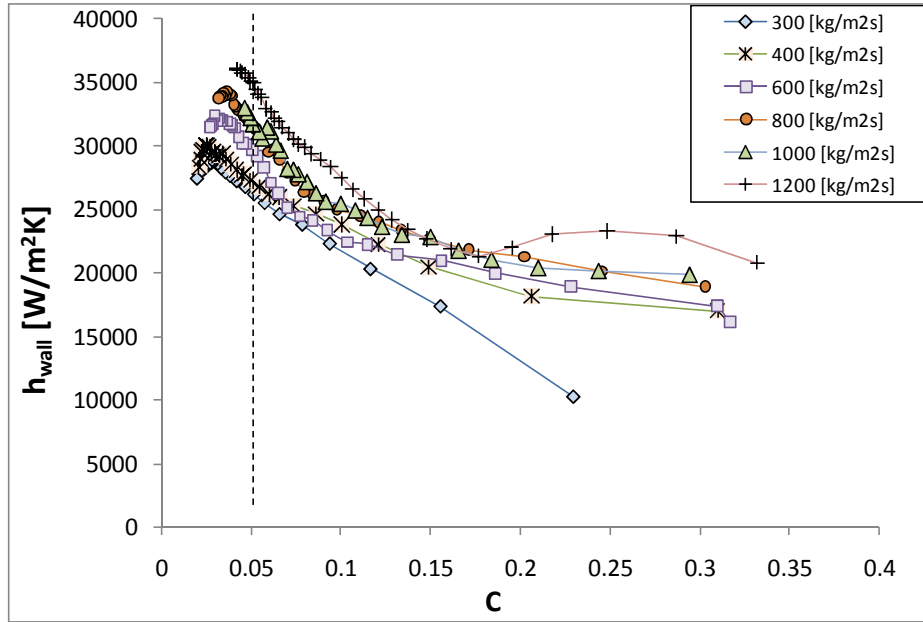


**Figure 7-19. Variation of experimental heat transfer coefficients with stability criteria for Surface #12**

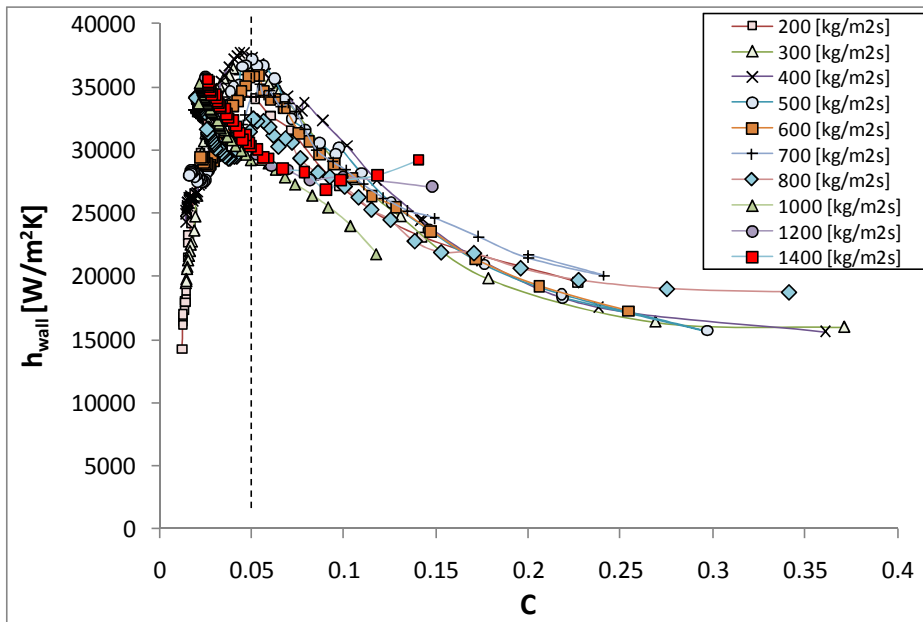


**Figure 7-20. Variation of experimental heat transfer coefficients with stability criteria for Surface #17**

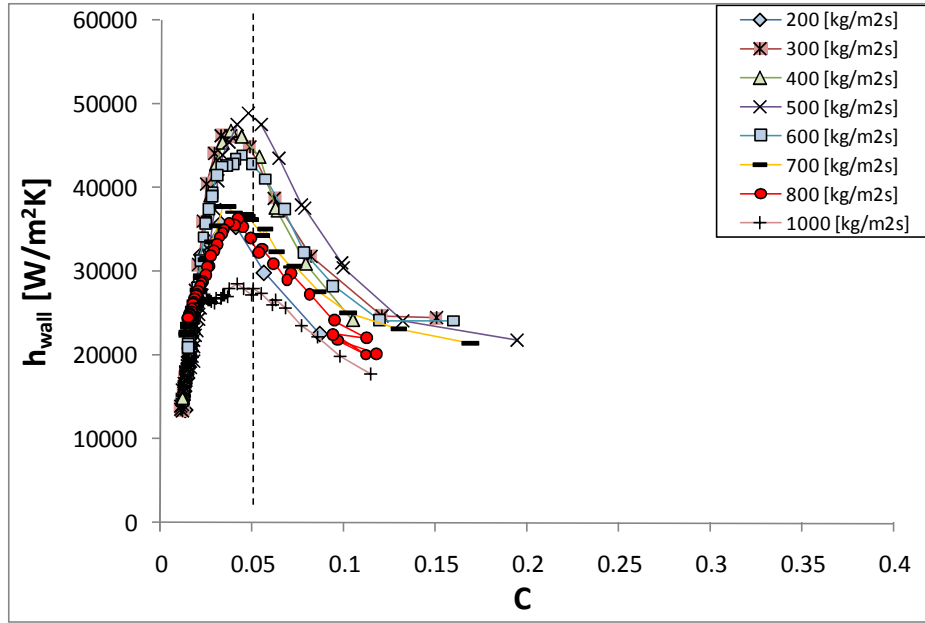


Figure 7-21. Variation of experimental heat transfer coefficients with stability criteria for Surface #C

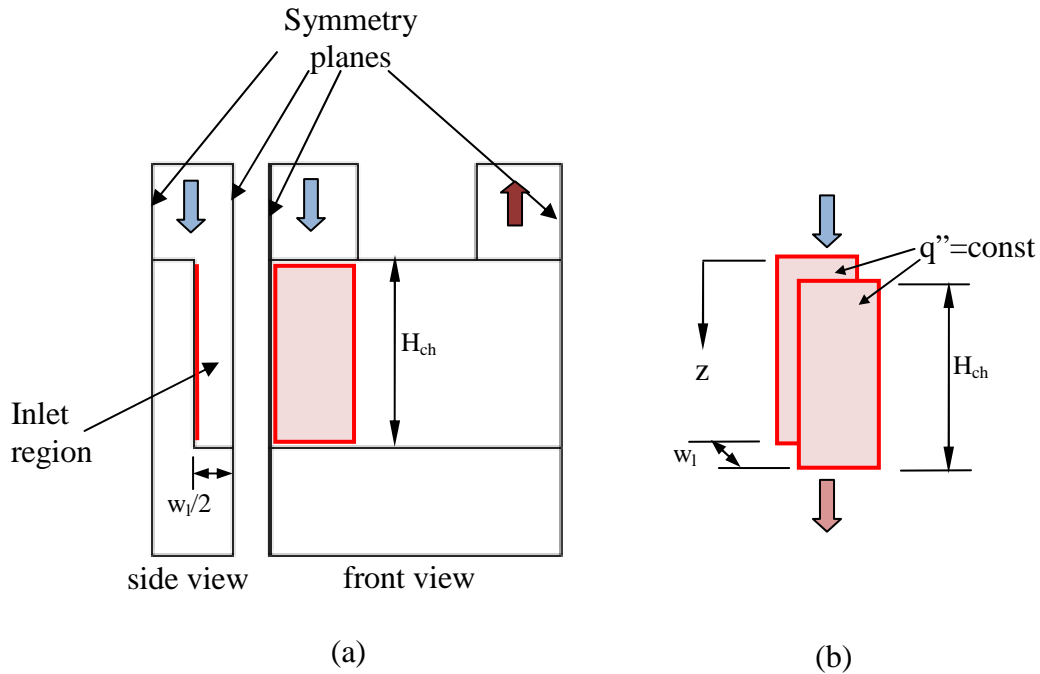
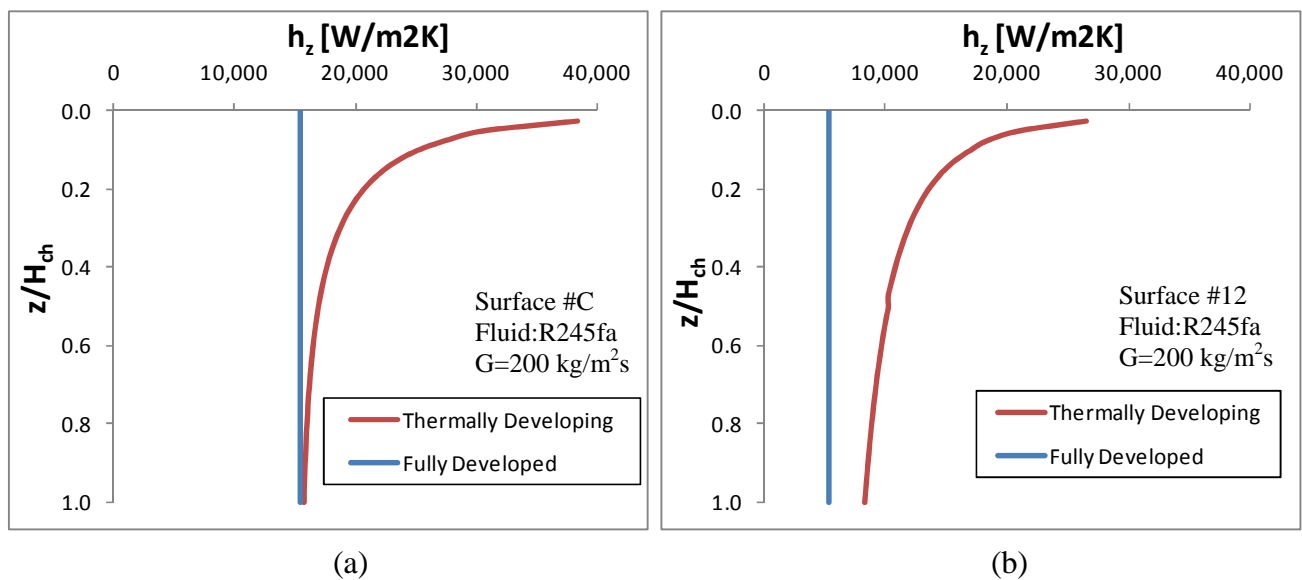


Figure 7-22. Schematic of flow model in the inlet region for (a) Half FFMHS unit cell (a) Flow between parallel plates with constant wall heat flux

For example, consider the inlet region shown in Figure 7-22 (a). Assuming that the fluid inertia is high, the liquid will enter from the top and it will flow towards the

bottom of the channel where it will create an impingement zone. To further simplify the case, this region was assumed as flow between two parallel plates as shown in Figure 7-22 (b), with same channel width ( $w_{ch}$ ) and channel length/height ( $H_{ch}$ ). In this case the flow will not create an impingement zone, instead it will be directed out from the bottom of the channel. Constant heat flux was applied to parallel plate walls. For this analysis, Surface #12 and Surface #C were selected since they represent the extreme geometries in terms of hydraulic diameter. For the flow configuration shown in Figure 7-22 (b), the local heat transfer coefficient along the inlet region for Surface #C and Surface #12 are calculated and shown in Figure 7-23 (a) and (b) respectively. For both cases, the flow is thermally developing, and due to lower hydraulic diameter, the local heat transfer coefficients of Surface #C are higher than those calculated for Surface #12. In fact, for fully developed flow, the local heat transfer coefficients are reversely proportional to hydraulic diameter; therefore they are almost three times higher for Surface #C comparing to Surface #12.



**Figure 7-23. Local heat transfer coefficients versus non dimensional entrance length for (a) Surface #C, (b) Surface #12**

The wall superheat required for onset of nucleate boiling can be calculated based on principles given in Section 2.4.3, using Equation (2-23) and local heat transfer coefficients given above. For a constant heat flux, the bulk temperature can be calculated as a function of distance from the inlet  $z$ .

$$\Delta T_{bulk,z} = T_i + \frac{2q''z}{\rho w_{ch} V_i c_p} \quad (7-4)$$

Using Equation (7-4), the wall superheat and liquid superheat are evaluated as:

$$\Delta T_{sat,wall,z} = \left( T_{bulk,z} + \frac{q''}{h_z} \right) - T_{sat} \quad (7-5)$$

$$\Delta T_{sat,liq,z} = \Delta T_{bulk,z} - T_{sat} \quad (7-6)$$

The variation of Equations (2-23), (7-5) and (7-6) with non dimensional distance from the entrance are shown in Figure 7-24 (a) and (b) for Surface #C and Surface #12 respectively. The blue curve represents the minimum wall superheat required to initiate nucleation, by assuming saturated liquid inlet and that all size of crevices are available on the heated surface. The red curve represents the actual wall superheat and the green line denotes the liquid superheat. The Onset of Nucleate Boiling (ONB) will occur when the wall superheat (red curve) exceeds the theoretical minimum required wall superheat of ONB (blue curve). Defining the ONB location will also determine the amount of liquid superheat at the same location. For example, for Surface #C, the ONB will occur at  $z/H_{ch} = 0.28$  down the inlet which also corresponds for a wall superheat of 4.5 °C. At this point, the liquid is also superheated to a value of 2.0 °C, due to suppression of nucleation upstream the ONB point. For larger hydraulic diameter microgrooved surfaces with same heat flux, mass

flux and saturation temperature, the initiation of boiling is much earlier. For example, for Surface #12 the ONB was calculated to occur at  $z/H_{ch} = 0.15$  and the corresponding wall and liquid superheats were 3.6 °C and 0.3 °C respectively. With this, it was demonstrated that for similar flow and heat input conditions, the hydraulic diameter has a significant impact on liquid and wall superheat values present in the system prior to nucleation. For smaller channels, the local heat transfer coefficient is much higher and the amount of thermal mass carried by the fluid is much less at constant heat flux, mass flux and saturation temperatures. Therefore the ONB will occur further downstream of the channel, which in turn will lead to building large amounts of liquid and wall superheat. As the hydraulic diameter is increased, this effect becomes less pronounced. This effect, combined with smaller bubble confinement at higher hydraulic diameters, explains the decreasing effect of rapid bubble expansion phenomena when going from small hydraulic diameter of Surface #C to higher hydraulic diameters of Surface #12.

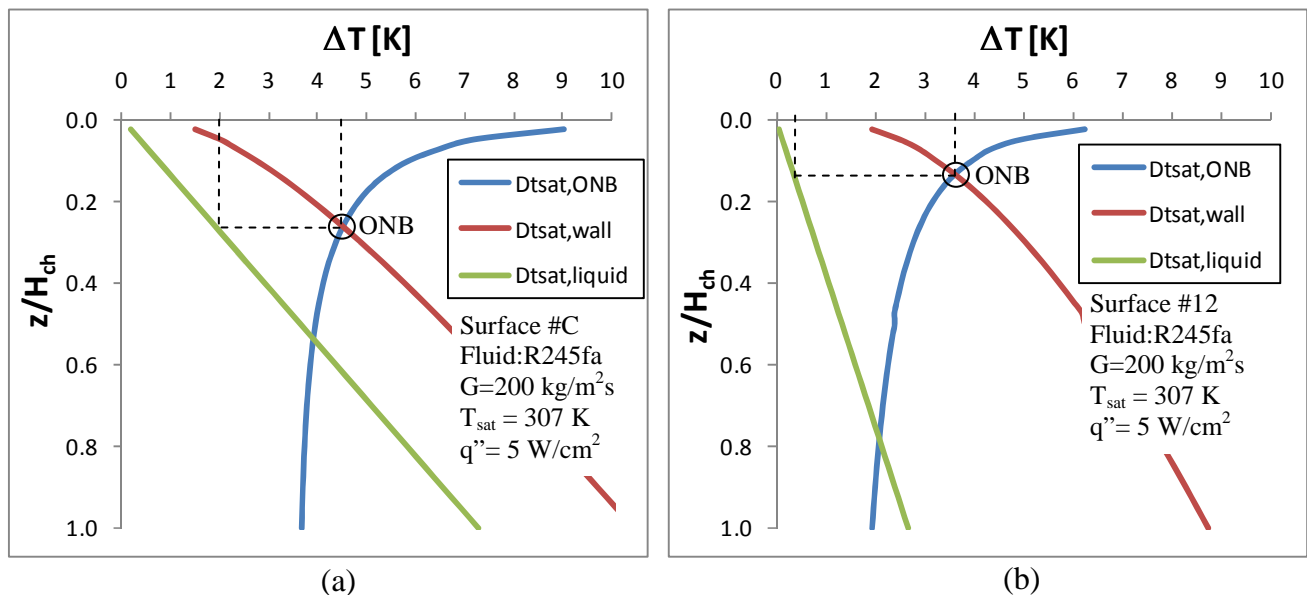


**Figure 7-24. Onset of Nucleate Boiling (ONB) and wall and liquid superheats calculated for (a) Surface #C, (b) Surface #12**

# CHAPTER 8: CONCLUSIONS AND FUTURE WORK

## RECOMMENDATIONS

### 8.1. Conclusions Summary

The present research is the first of its kind to develop a better understanding of single-phase and phase-change heat transfer in FFMHS through flow visualization, numerical and experimental modeling of the phenomena, and multi-objective optimization of the heat sink and its comparison with two widely known cooling technologies, namely jet impingement and traditional micro channels.

From an overview of the work conducted in the present study, a number of conclusions can be drawn which can be summarized based on the single-phase and phase-change studies in the present work. For single-phase heat transfer, a numerical study was performed to investigate the thermal performance and to optimize the geometry and flow of FFMHS. The main findings of this part of the study are as follows:

- The geometry and Reynolds number have a significant effect on both flow regimes and heat transfer characteristics. At low Reynolds numbers, the flow is viscous-dominated, which results in velocity stratification by creating a bypass zone between the inlet and outlet feed channels at the top of the microchannel. This effect in turn creates inefficient dead zones with low fluid circulation and low heat transfer.
- When the Reynolds number is increased, usually by increasing the hydraulic diameter or mass flux, the flow becomes inertia-dominated and the velocity

stratification reverses with a higher fluid core close to the bottom of the microchannel and with fluid recirculation zones close to the top part. The increase in fluid velocity also initiates secondary flows manifested in the form of vortex pairs in the microchannel cross-section. The vortices and flow impingement in turn reduce the convective thermal resistance and create local heat transfer maximums.

- The geometrical parameters that most strongly affect the heat transfer and pressure drop were microchannel height, microchannel width and inlet/outlet feed channel dimensions.
- An optimized FFMHS can operate much more efficiently in the parametrical range investigated in this study compared to TMHS and JIHS. For constant pumping power and a  $1 \times 1 \text{ cm}^2$  base cooling area, FFMHS can achieve 72% more heat transfer compared to TMHS and 306% compared to JIHS. For a  $1 \times 1 \text{ cm}^2$  base cooling area and constant heat transfer performance, the pumping power required by FFMHS is only 8.5% of the pumping power required by TMHS and 0.4% of the pumping power required by a JIHS.
- When going to larger cooling areas, the performance difference of FFMHS compared with TMHS is even more significant. The manifolding system that forms the short parallel microchannel structure in FFMHS allows cooling of large areas without the penalty of heat transfer degradation due to a rise in fluid temperature and increase in pressure drop and flow length.

- With the observed superior performance, FFMHS technology has the potential to replace TMHS technology that is currently widely used for cooling of high heat fluxes.

To investigate the thermal performance of FFMHS in two-phase heat transfer mode a two-step experimental approach was considered. In the first step, a parametric study was performed to study the effects of microgrooved surface geometry, heat flux and mass flux. The heat transfer characteristics resulting from this study were later explained by a visualization study performed in the second step. The main findings of this part can be summarized as follows:

- FFMHS have demonstrated that with an HFC fluid, the present heat sink configuration can cool a heat flux of  $q_{base}'' = 1.23 \text{ kW/cm}^2$  with a superheat of  $\Delta T_{sat} = 56.2 \text{ }^\circ\text{C}$  and pressure drop of  $\Delta P = 60.3 \text{ kPa}$ .
- At high hydraulic diameter, high mass flux and high heat flux, the heat transfer coefficients have a slowly increasing trend with an increase in heat flux and outlet quality. The flow is dominated by inertial forces, and the flow regimes and transitions are expected to be similar to conventional microchannels. The heat transfer coefficients in this regime follow the Chen correlation, which was developed to predict saturated flow boiling in conventional channels.
- At low hydraulic diameters, low mass flux and low qualities the heat transfer coefficient curves have a bell-like shape with a sharp increase at low vapor qualities until they reach the maximum peak point. Here the flow is dominated by the viscous forces, and a single bubble expansion phenomenon is observed.

The thin liquid film under the elongated bubble can create an annular-like high heat transfer regime at low qualities. However, at high heat fluxes the bubble expansion becomes more chaotic, having a negative impact on heat transfer by blocking liquid inlet and creating vapor backflows.

- The CHF of FFMHS increases with mass flux, while the outlet qualities have a decreasing trend. The vapor backflow in the inlet manifold correlates with CHF, and this mechanism results from the vapor blankets that block the inlet liquid that wets the heated surface. At high mass fluxes the vapor is generated at the bottom of the channel, while at low mass fluxes the vapor is generated along the channel with bubbles close to the inlet, sending vapor into the inlet feed channel and creating vapor backflows.

## **8.2. Future Work Recommendations**

This is the first comprehensive study of the innovative force-fed micro channel heat sinks for high heat flux cooling. As documented in this study, the technique has demonstrated significant advantages over other technologies conventionally used for high heat flux cooling. Very high heat transfer coefficients, yet low pressure drops, make the technique attractive to other areas of heat transfer applications such as thermal energy conversion and waste heat utilization.

Energy conversion and management are at the core of modern technology research; however, the applications of force-fed heat transfer in these areas will have many specific applications beyond the high heat flux cooling. For example, HVAC or ocean thermal energy conversion (OTEC) systems operate at very low temperature difference intervals. Heat has to be transferred at a minimum temperature difference

to make those processes efficient. In this case, future work should focus on low heat fluxes and minimum temperature differences that were not explored in this study.

The future work recommendations are divided into two sections based on heat transfer mode: single-phase and two-phase. For single-phase heat transfer the following future work research is recommended:

- The current optimization was performed based on five parameters. Four of these parameters were geometrical and one was the flow parameter. The geometrical parameters were selected based on a parametric study that indicated the most important four out of eight possible parameters. Future research should extend the number of parameters, based on the computational limitations and capabilities. The next important parameters, which were not included in this study but are suggested for the future work, are fin aspect ratio and manifold thickness. Using these recommendations, the optimal performance of FFMHS could be further increased.
- The current optimization was based on copper microgrooved surfaces and water as the working fluid. The study could be extended to other material-working fluid couples, such as refrigerants and silicon-based microgrooved surfaces, which are commonly used in current power electronics cooling systems. The resulting database would provide a technical tool that will allow selection of optimum working FFMHS geometries at different inputs and materials.
- Another possible benefit of this work is the potential to perform an economical feasibility analysis and to optimize FFMHS based on cost evaluations. Cost

could be included as the third function in the multi-objective optimization procedure. The optimization results then could identify the most economically feasible heat sink design based on thermal performance characteristics and/or other criteria.

- The technology performance comparison study investigated in this work was performed on FFMHS and two well-established high heat flux cooling technologies, TMHS and JIHS. The comparison study could be further extended by including several other cooling technologies such as spray cooling, inline and staggered pin fins and offset strip pin fins.

The future research recommendations for two phase heat transfer of FFMHS are summarized as follows:

- The parametrical study needs to be extended for a larger selection of microgrooved surface geometries and working fluids. This will lead to formation of a larger database of heat transfer coefficients and pressure drop data. The heat transfer performance trends observed in this study should be compared to the trends observed at difference geometrical FFMHS configurations, and the consistency or deviation of this trend needs to be addressed. The large database will also form the base to allow building correlations that can predict heat transfer coefficients and pressure drops.
- The current test section was not designed to test CHF due to the low thermal mass of the heater assembly. A secondary test chamber with heaters attached to a larger copper heat distributor would solve this problem. This test section

would increase the fabrication complexities but would allow testing CHF. The test setup control could be enhanced by addition of a fast response control circuit that could cut the power of the heater in a very short time after the temperature jump is sensed.

- The test section used in visualization tests in this study was a scaled-up model of the actual microgrooved surfaces. It was mainly designed to generate pictures and video images that can capture the effect of hydraulic diameter, mass flux and heat flux on two-phase flow regimes. The results obtained for parametric FFMHS experimental tests were explained by the assumption that similar phenomena occur at small scale too. Although these results were satisfactory, it is recommended that they be validated with a test section that can capture the flow regimes at the micro-scale. This test section needs to be carefully designed to be able to control and monitor significantly lower heat and mass fluxes. The heat gains and heat losses through lighting equipment, conduction heat losses, and radiation heat losses through the surface of the test section also need special attention.
- The two phase test section designed and fabricated in this study was developed to accurately simulate two phase phenomena in FFMHS and to understand the flow regimes and heat transfer mechanisms in these heat sinks in laboratory conditions. However, this flow configuration with long straight feed channels is not very practical for heat sink designs. A more practical and compact design that utilizes the same force fed concept can be developed using a zigzag manifold design, as shown in Figure 8-1. This low profile heat sink design is

more compact and easier to manufacture. The fluid enters the heat sink from one side, flows into the feed channels, it is distributed into the microchannels and is directed out of the heat sink from the opposite side. The manifold is compressed between the microgrooved surface and the flat plate located on the top of the heat sink. The feed channels and the dimensions of the zigzag header are designed based on the flow configuration. For two phase flow, the inlet feed channels are smaller comparing to the outlet feed channels to accommodate the large vapor flow. Fabrication and demonstration of such a heat sink will lead to a more compact and yet efficient low profile heat sink.

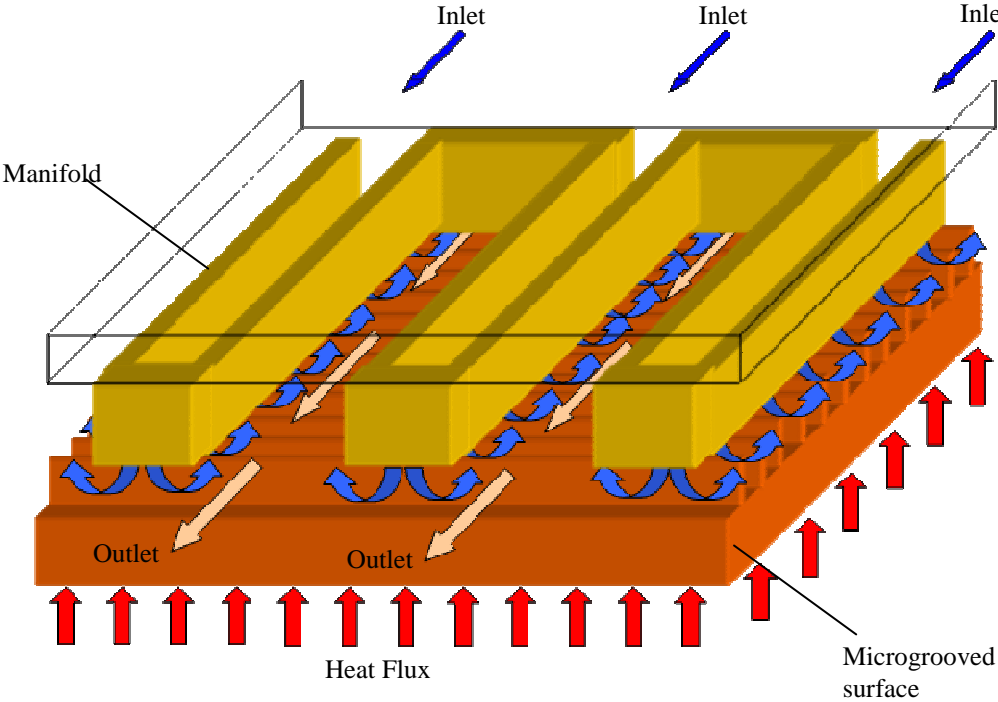


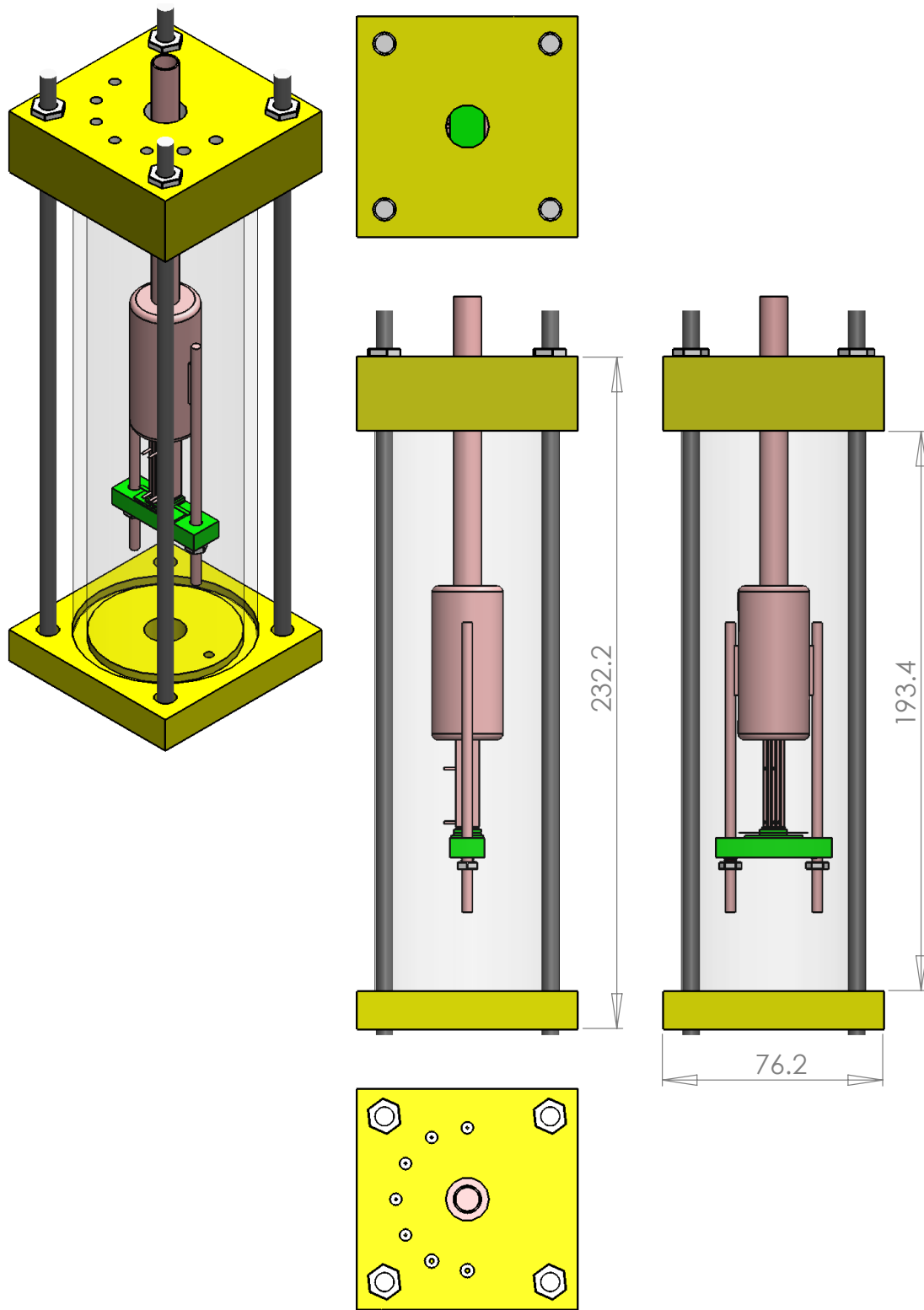
**Figure 8-1. Low profile FFMHS with zigzag manifold design**

## **CHAPTER 9: APPENDICES**

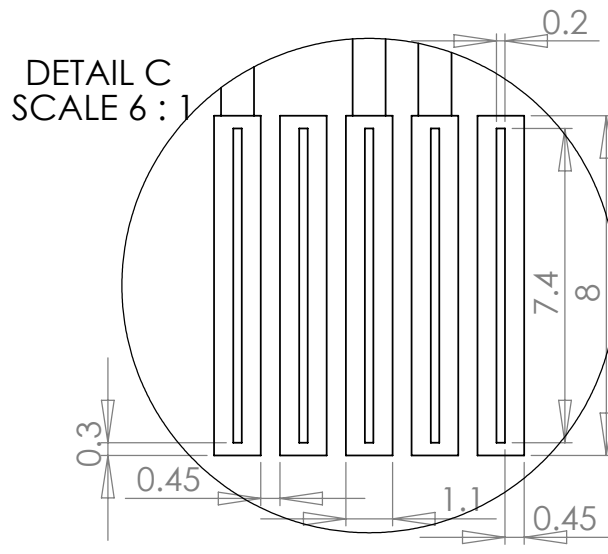
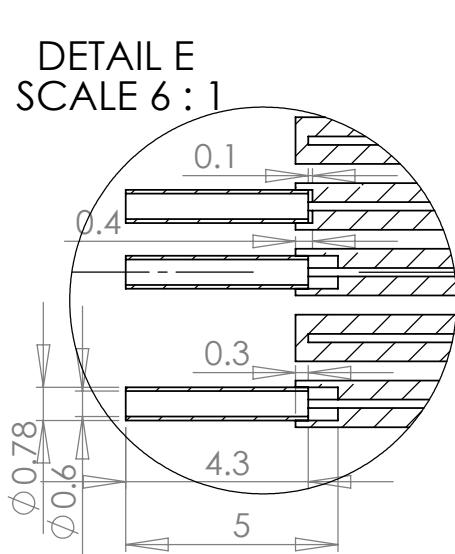
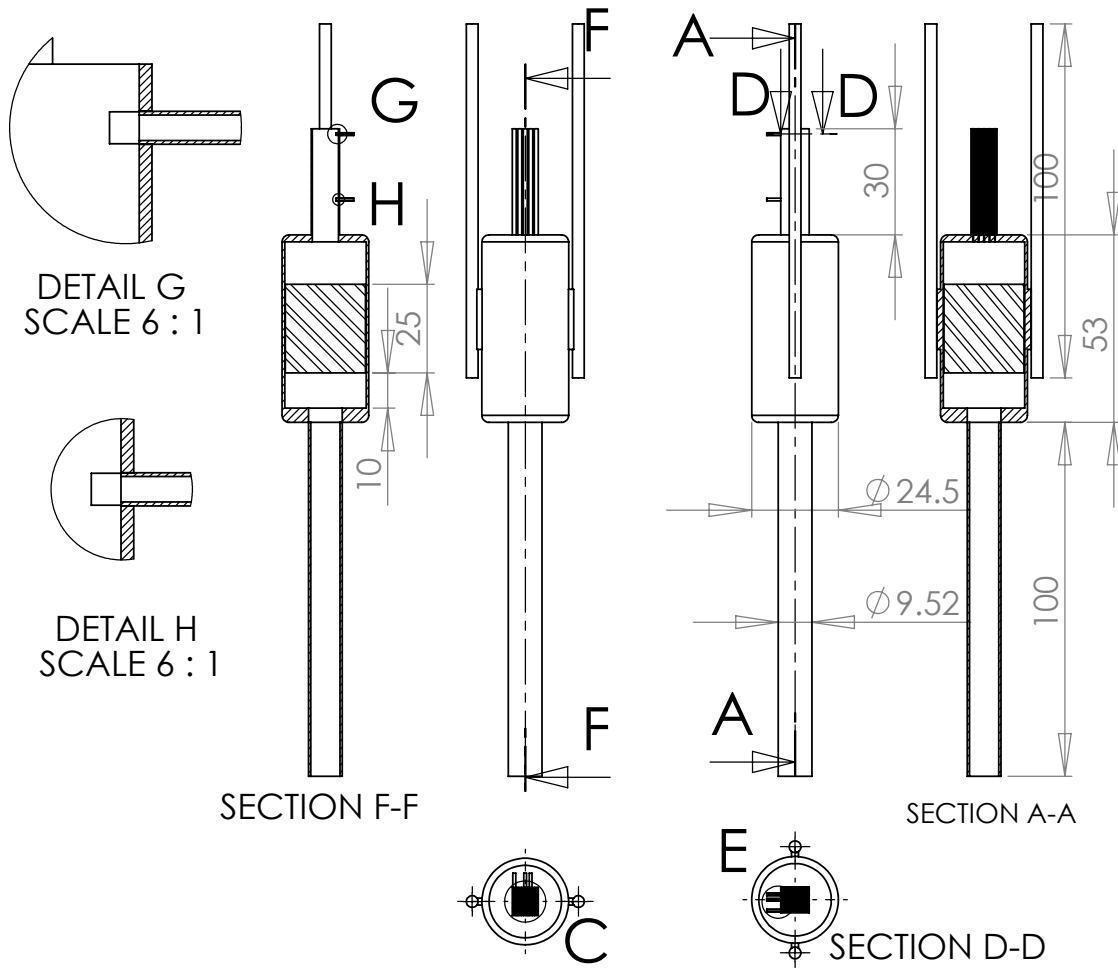
### **9.1. Appendix A**

The technical drawings and dimensions of the parts used in the experimental test chamber and visualization test section are given in this appendix. All dimensions are in mm unless otherwise specified.

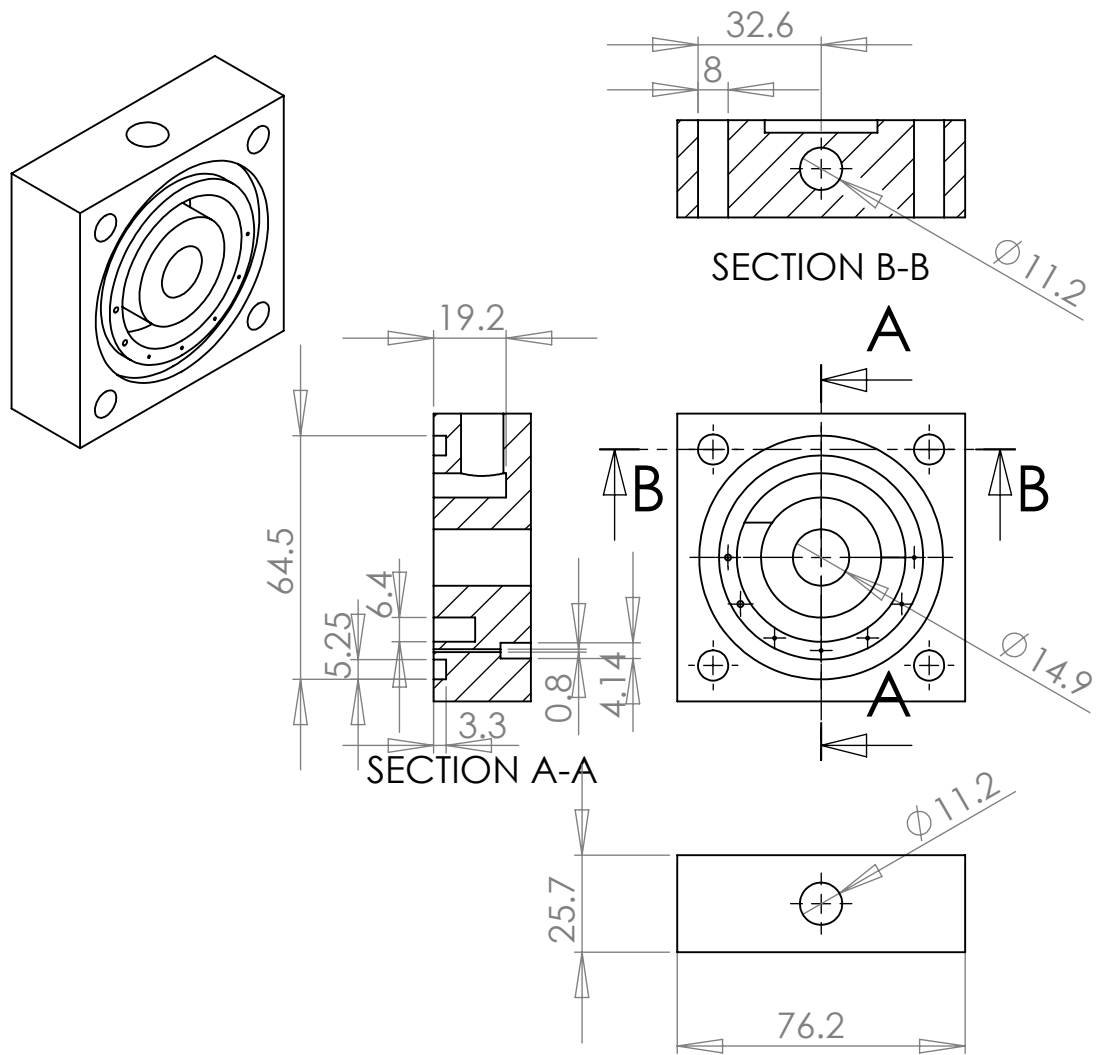
### 9.1.1. Test chamber assembly



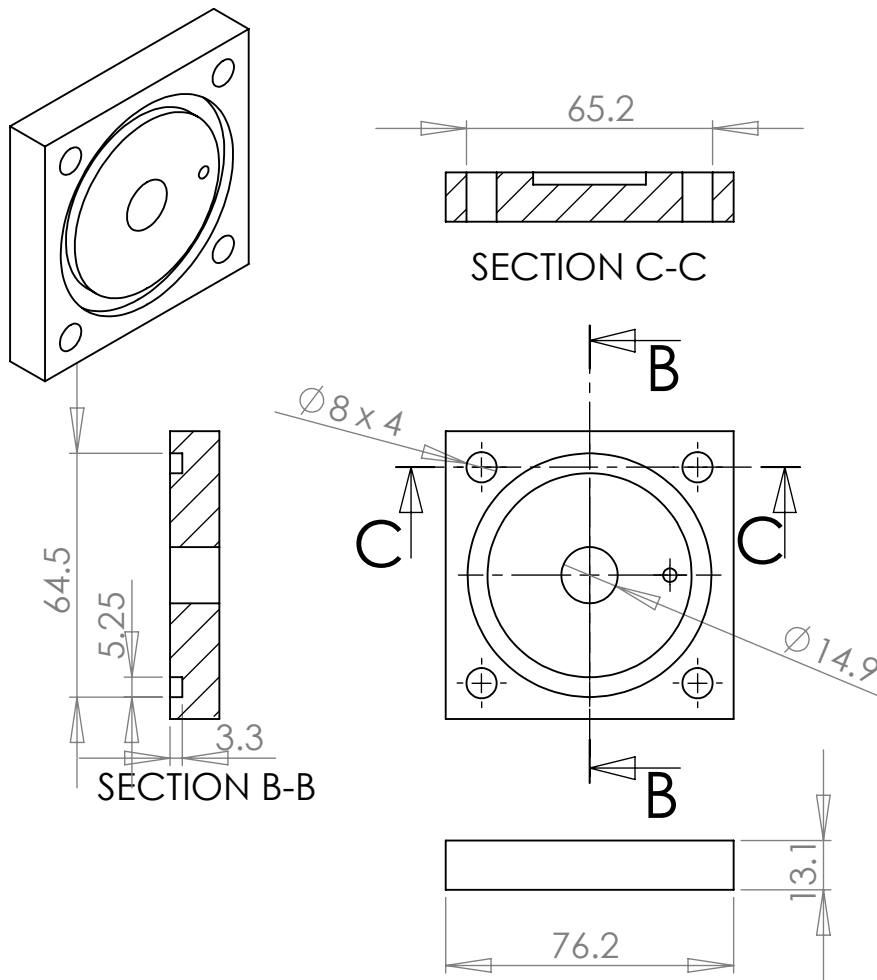
### 9.1.2. Test Chamber Flow Distribution Header



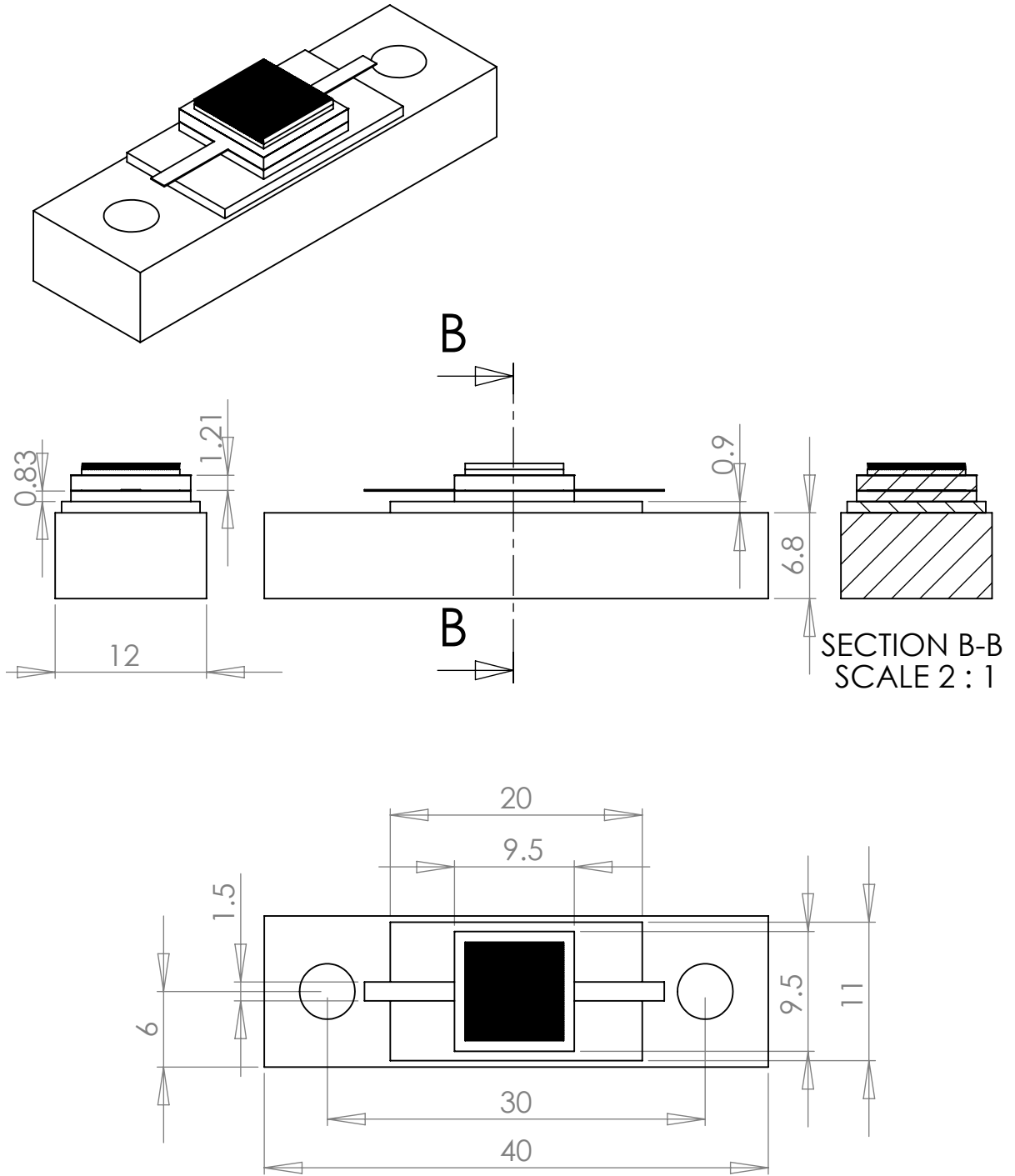
### 9.1.3. Test Chamber Top Flange



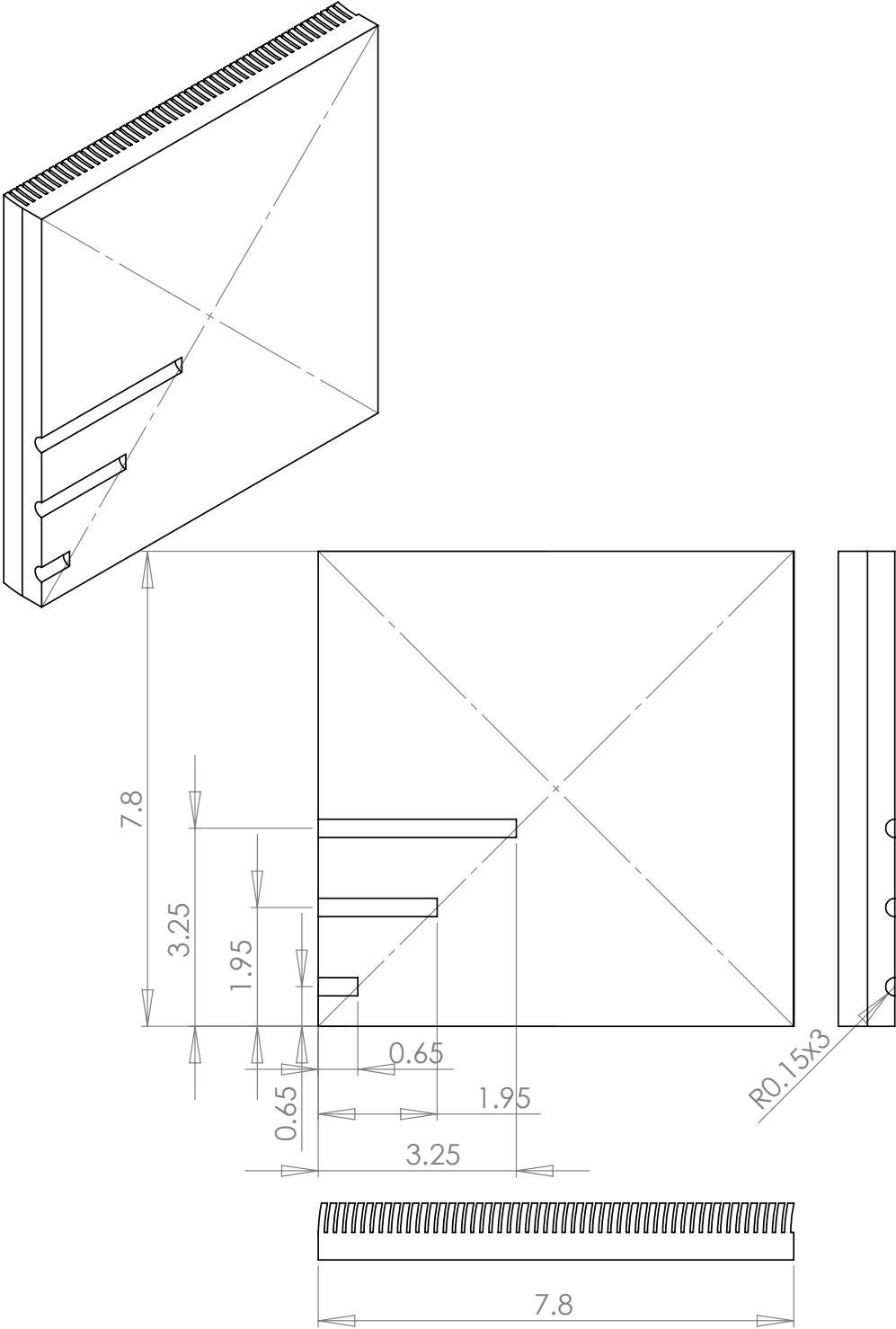
### 9.1.4. Test Chamber Bottom Flange



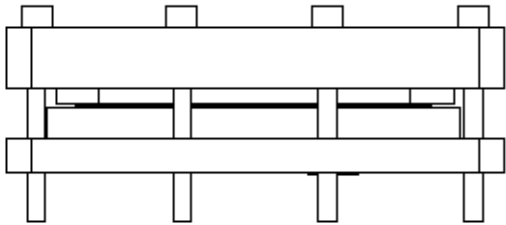
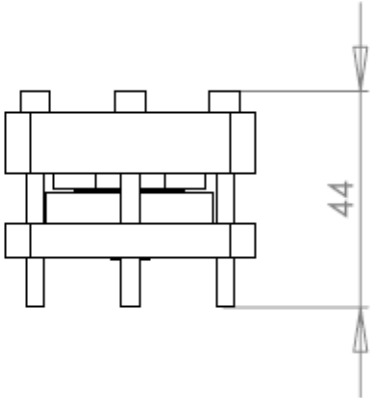
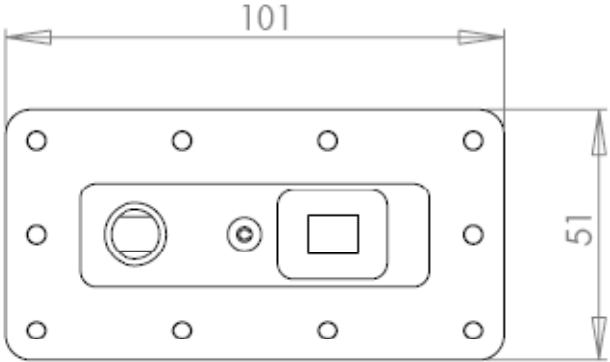
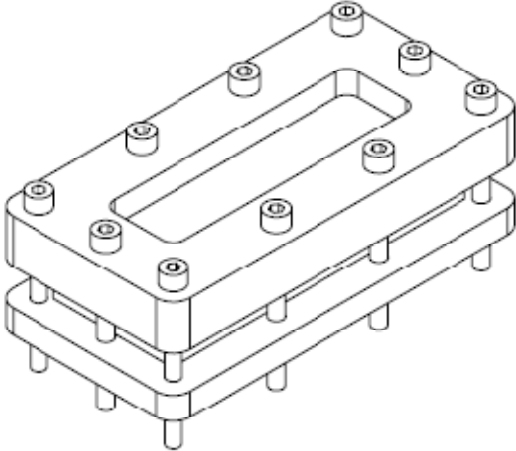
### 9.1.5. Test Chamber Heater Assembly



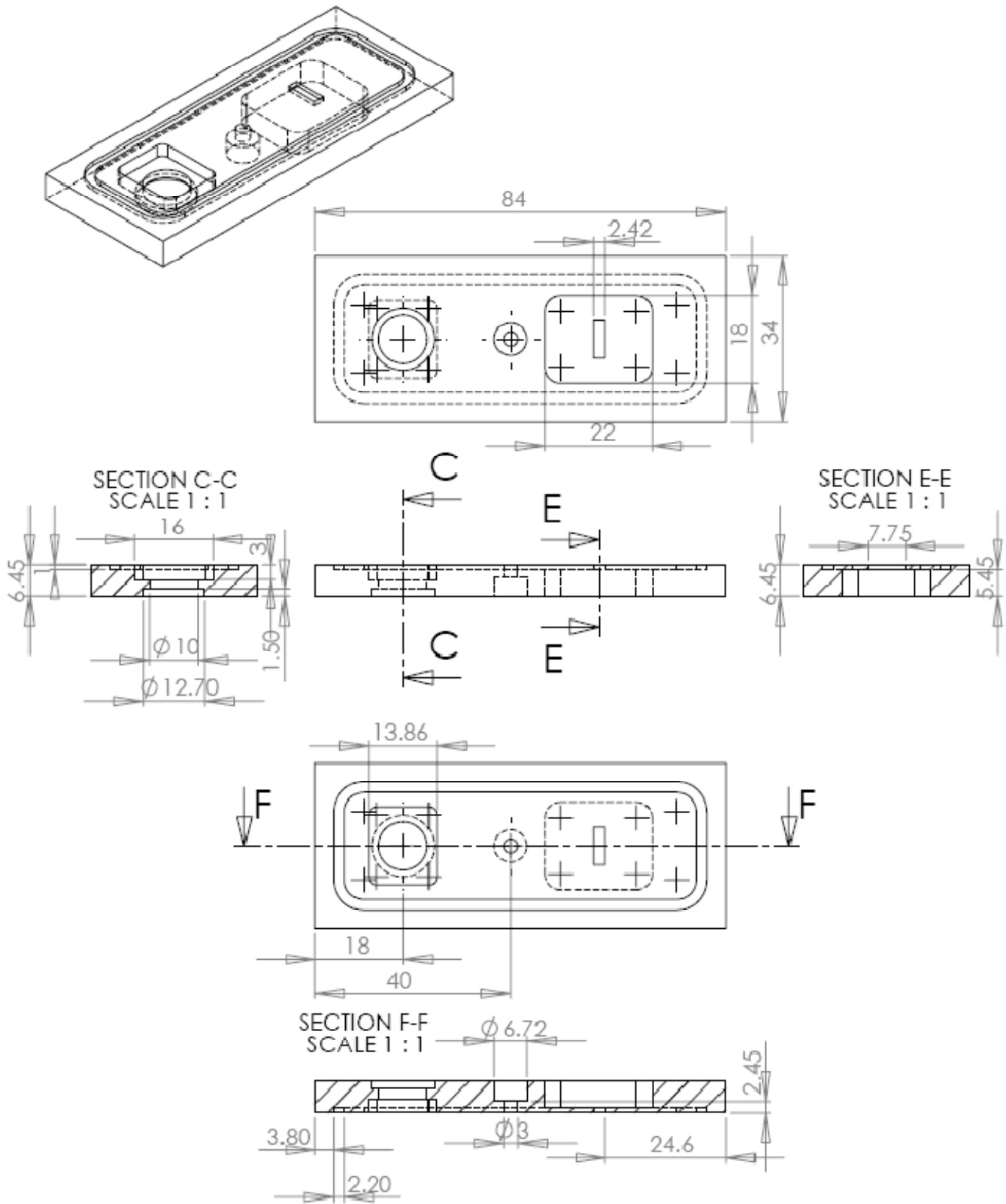
9.1.6. Test Chamber Microgrooved Surface



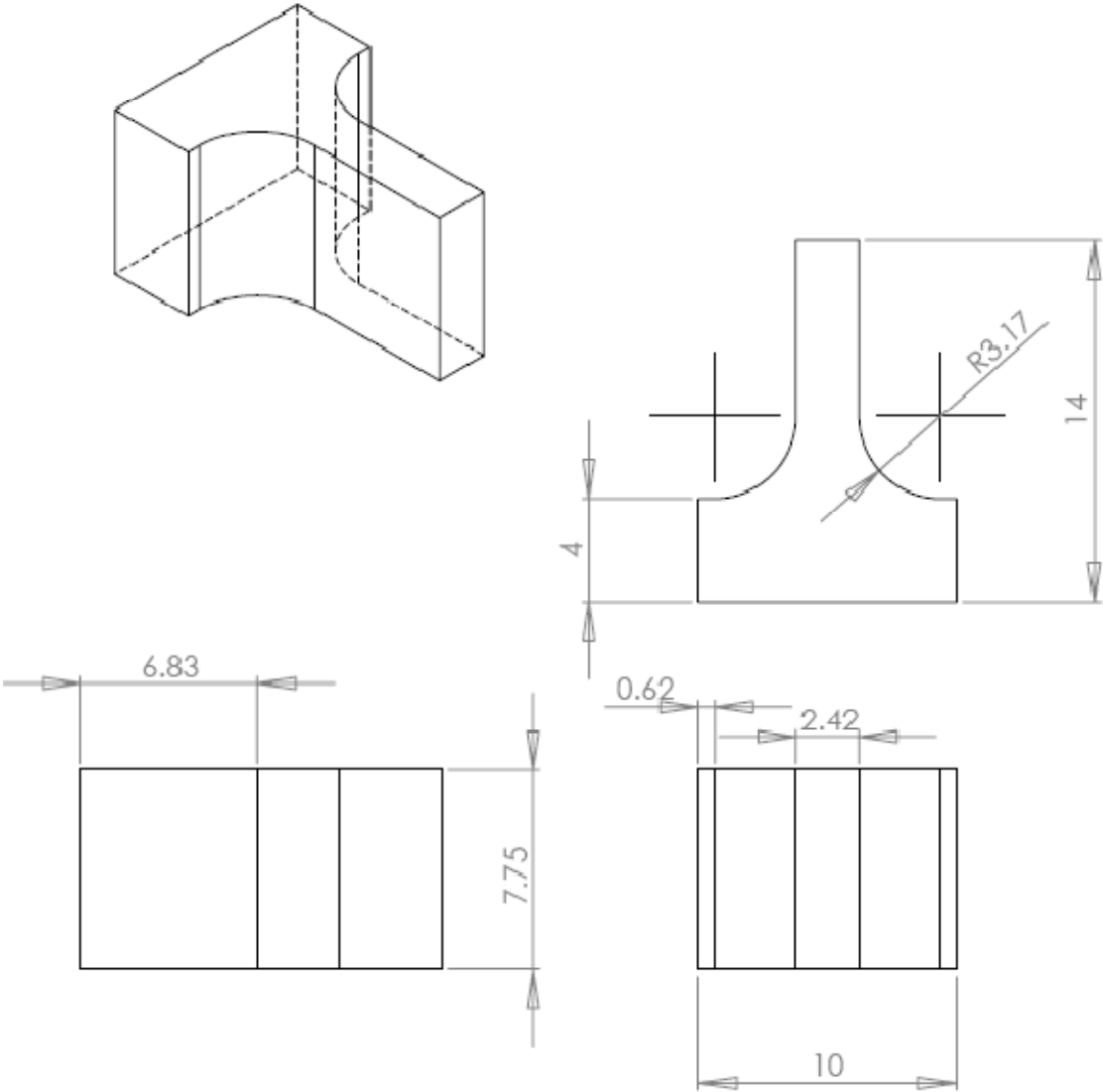
9.1.7. Visualization Test Section Assembly



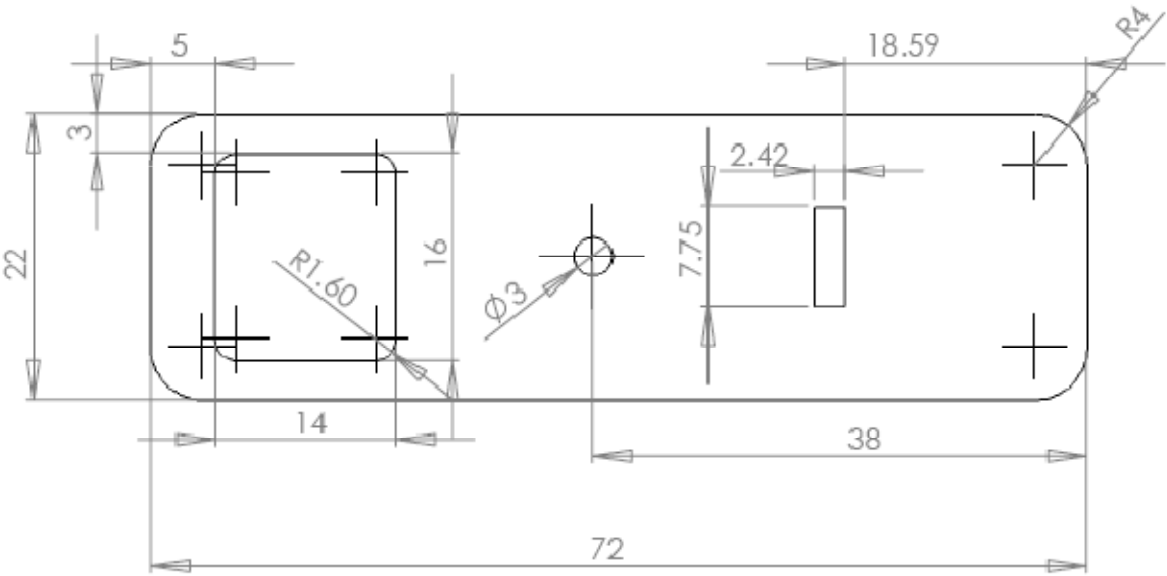
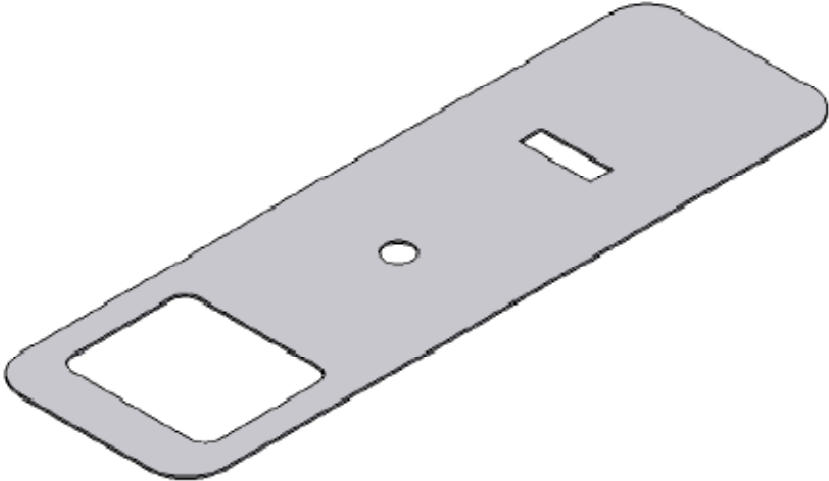
### 9.1.8. Visualization Test Section Base



9.1.9. Visualization Test Section Heat Conductor



9.1.10. Visualization Test Section Teflon Layer 2





## 9.2. Appendix B

The computational domain shown in Figure 9-1 is one quarter of the actual heater assembly. Therefore symmetry boundary condition was applied at specified faces. Three different components considered in this study are the composite base, PTFE layer and the alumina substrate. The thermal conductivity values for each of these substrates were selected as 1 W/mK, 0.5 W/mK and 18 W/mK respectively. The thin film resistor was modeled as a 2D layer on the top surface of alumina substrate. The contact resistance between each layer was neglected by assuming perfect contact condition. The final meshed geometry consists of 43919 tetrahedral cells and is shown in Figure 9-2.

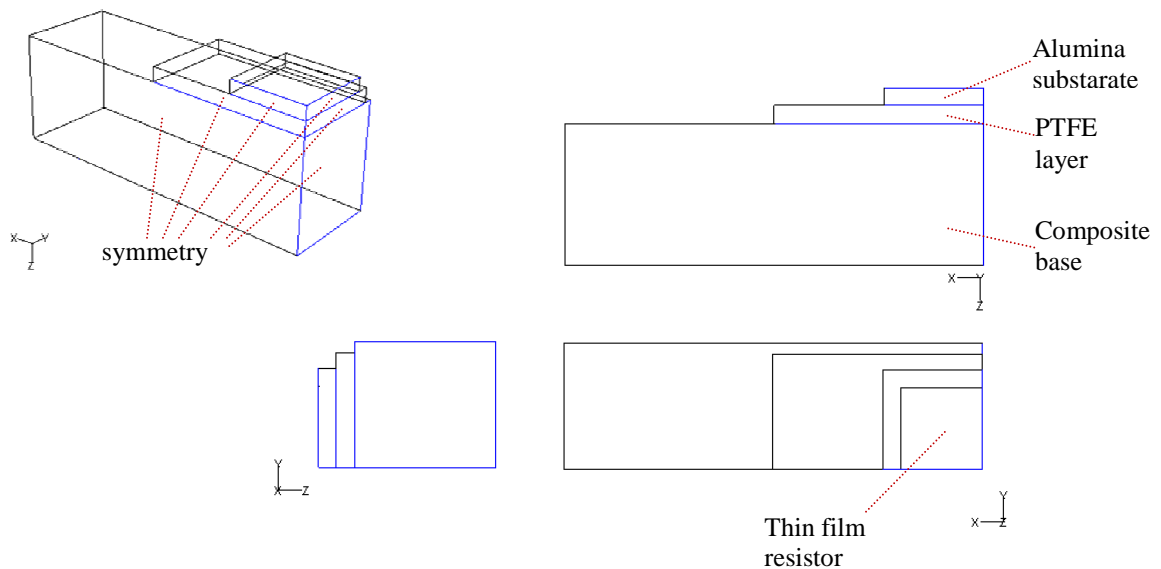


**Figure 9-1. Boundary conditions and computational domain**

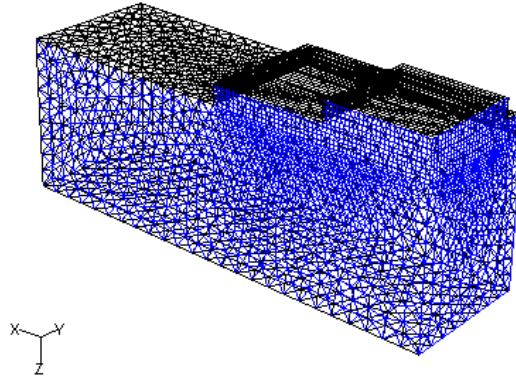


**Figure 9-2. The meshed geometry used in numerical model**

The thermal resistance from the surface to the fluid is a function of convective heat transfer coefficient. After exiting the manifold, the gravitation forces pull the fluid down and fluid flows downward wetting the side surfaces of the heater and the heater assembly. The convective heat transfer coefficient was evaluated based on evaporative falling film heat transfer mode. For evaporation over a uniformly distributed falling liquid film in a vertical tube, the average heat transfer coefficient was estimated using the correlation given by (Seban, 1978):

$$h_{\text{film}} = 0.821 \left( \frac{\mu^2}{k^3 \rho^2 g} \right)^{-1/3} \left( \frac{4\Gamma}{\mu} \right)^{-0.22} \quad (9-1)$$

where  $\Gamma = \dot{m} / L_f$  represents the mass flow rate per unit depth, perpendicular to flow direction. Applying convective boundary condition with specified heat transfer coefficient for surfaces in contact with fluid, the numerical model was solved for a range of mass flow rates. The values of total thermal resistance  $R_{hab}$ , defined between film temperature and ambient fluid temperature, versus heat sink mass flow rate is given in Figure 9-3. Thermal resistance values are slightly lower at low mass flow rates due to the thinning of the film thickness and enhancing convective heat transfer.

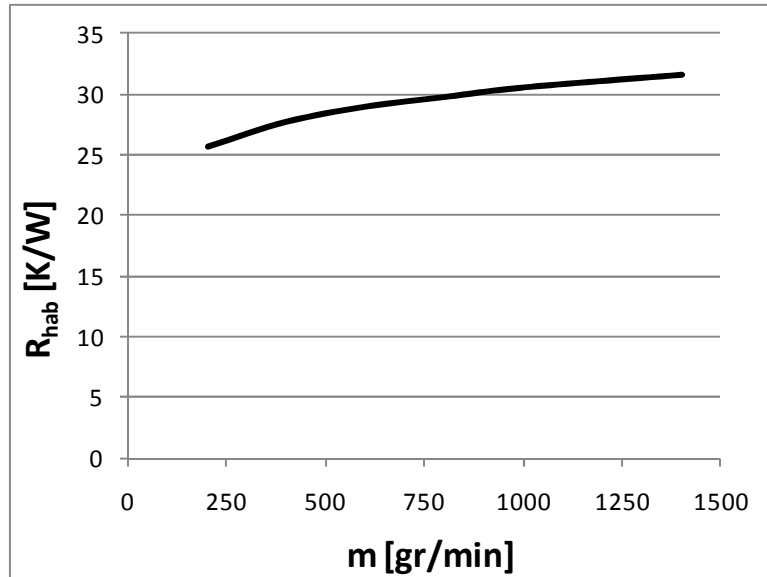


**Figure 9-3. Total thermal resistance versus mass flow rate for the bottom part of the heater assembly**

The thermal resistance values given in Figure 9-3 can be fit into a power law equation as a function of mass flow rate:

$$R_{hab} = 14.6357 \dot{m}^{0.1064} \quad (9-2)$$

where  $\dot{m}$  is the total mass flow rate of the heat sink with the units of grams per minute. The regression equation can predict the numerical results with a mean absolute error less than 0.20%.

## 9.3. Appendix C

### 9.3.1. TMHS Model Used in Optimization

The microchannel geometry used in the mathematical model is shown in Figure 9-4. It consists of a base material on the bottom, the single microchannel, two side fins with half thickness and the adiabatic cover on the top.

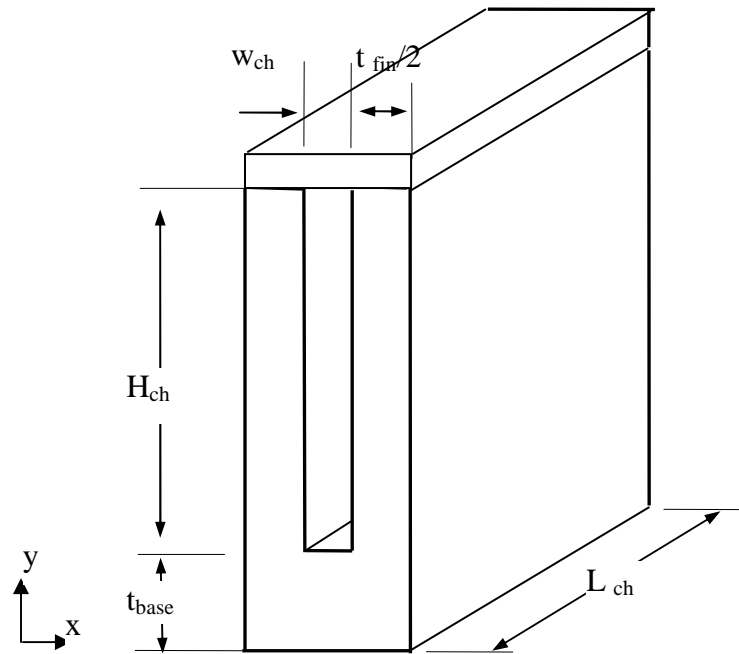


**Figure 9-4. Mathematical model of TMHS**

Due to high the axial conduction of the copper, the base surface was assumed to be at constant temperature. For a given inlet and base temperature the outlet temperature can be calculated as:

$$\frac{T_{base} - T_{out}}{T_{base} - T_{in}} = \exp\left(-\frac{1}{\dot{m}_{ch} c_p R_t}\right) \quad (9-3)$$

Where  $\dot{m}_{ck}$  is the mass flow rate in the microchannel,  $c_p$  is the specific heat of water and  $R_t$  is the total thermal resistance from base surface to the water.  $R_t$  includes the conduction through the base wall and the force convection resistance from the microchannel wet surface:

$$R_t = \frac{t_{base}}{k_{Cu}(t_{fin} + w_{ch})L_{ch}} + \frac{1}{\eta_0 \bar{h} A_t} \quad (9-4)$$

where  $A_t = 2H_{ch}L_{ch} + w_{ch}L_{ch}$  is the total wet area and  $\bar{h}$  is the average convection coefficient.  $\eta_0$  is the overall surface efficiency defined as:

$$\eta_0 = 1 - \frac{A_f}{A_t}(1 - \eta_f) = 1 - \frac{2H_{ch}}{2H_{ch} + w_{ch}}(1 - \eta_f) \quad (9-5)$$

Here, the fin efficiency  $\eta_f$  for straight rectangular fins needs to be calculated.

For a given mass flow rate the fluid velocity  $V_{ch}$  and Reynolds number are calculated as:

$$V_{ck} = \frac{\dot{m}_{ck}}{\rho H_{ck} w_{ck}} \quad (9-6)$$

$$Re = \frac{\rho V_{ch} D_h}{\mu} \quad (9-7)$$

where  $D_h$  is the hydraulic diameter defined as:

$$D_h = \frac{4H_{ch}w_{ch}}{2(H_{ch} + w_{ch})} \quad (9-8)$$

For thermally developing flow, the overall heat transfer coefficient can be calculated as a function of dimensionless thermal entry length:

$$x^* = \frac{L_{ch}}{\text{Re Pr } D_h} \quad (9-9)$$

The average Nusselt number for laminar thermally developing flow at constant temperature boundary condition can be calculated from (Lian-Tuu & Chu, 2002):

$$(Nu_m)_T = \begin{cases} g_1 (x^*)^{-1/3} & , 0.005 < x^* < 0.01 \\ g_2 + g_3 / x^* & , x^* > 0.01 \end{cases} \quad (9-10)$$

where

$$g_1 = 2.038 - 2.206\gamma + 2.738\gamma^2 - 1.181\gamma^3 \quad (9-11)$$

$$g_2 = 7.554 - 17.287\gamma + 23.533\gamma^2 - 10.79\gamma^3 \quad (9-12)$$

and

$$g_3 = 0.0229 + 0.0546\gamma - 0.0417\gamma^2 - 0.0141\gamma^3 \quad (9-13)$$

Here  $\gamma$  is the aspect ratio which takes a value between zero and one and is defined as:

$$\gamma = \frac{w_{ch}}{H_{ch}} \quad (9-14)$$

From here the average heat transfer coefficient is calculated from definition of Nusselt number:

$$\bar{h} = \frac{(Nu_m)_T k}{D_h} \quad (9-15)$$

where  $k$  represents the thermal conductivity of water. Using the heat transfer coefficient, the average fin efficiency can be calculated as:

$$m = \left( \frac{\bar{h} P_f}{k_{Cu} A_{fc}} \right)^{1/2} = \left[ \frac{\bar{h} (2t_{fin} + 2L_{ch})}{k_{Cu} t_{fin} L_{ch}} \right]^{1/2} \quad (9-16)$$

and

$$\eta_f = \frac{\tanh(mH_{ch})}{mH_{ch}} \quad (9-17)$$

where  $k_{Cu}$  is the thermal conductivity of the copper. With known inlet and outlet fluid temperatures the total heat transfer is then evaluated as:

$$q = \dot{m}_{ck} c_p (T_o - T_i) \quad (9-18)$$

and the heat transfer coefficient based on footprint area and defined between base surface temperature and inlet fluid temperature is:

$$\begin{aligned} h &= \frac{q}{A_{base} (T_{base} - T_i)} = \frac{\dot{m}_{ck} c_p \frac{T_o - T_i}{T_{base} - T_i}}{A_{base}} = \frac{\dot{m}_{ck} c_p}{A_{base}} \left( 1 - \frac{T_{base} - T_o}{T_{base} - T_i} \right) = \\ &= \frac{\dot{m}_{ck} c_p}{A_{base}} \left[ 1 - \exp \left( - \frac{1}{\dot{m}_{ck} c_p R_t} \right) \right] \end{aligned} \quad (9-19)$$

For a square TMHS with heat sink dimensions of ( $L_{ch} \times L_{ch}$ ) the total pumping power can be calculated as:

$$P_{pump} = \frac{W_p L_{ch}}{W_{ch} + t_{fin}} \quad (9-20)$$

where  $W_p$  is the pumping power for a single microchannel and is defined as the product of volumetric flow rate  $\dot{V}$  and total pressure difference  $\Delta P_t$  between inlet and outlet manifolds.

$$W_p = \dot{V} \cdot \Delta P_t \quad (9-21)$$

Volumetric flow rate is calculated as:

$$\dot{V} = \frac{\dot{m}_{ck}}{\rho} \quad (9-22)$$

and the total pressure drop is the sum of channel frictional pressure drop, inlet and outlet local entrance pressure losses caused by sudden contraction and expansion.

$$\Delta P_t = \Delta P_f + \Delta P_c + \Delta P_e \quad (9-23)$$

The friction pressure drop is calculated using the average friction coefficient for laminar hydrodynamically developing flow:

$$\Delta P_f = 4 f_{app} \frac{L_{ch}}{D_h} \rho \frac{V_{ch}^2}{2} \quad (9-24)$$

where the friction coefficient is defined as (Copeland, 1995a):

$$f_{app} \text{Re} = \left[ \left( 3.2 x^{+ -0.57} \right)^2 + \left( f \text{Re} \right)_{fd}^2 \right]^{1/2} \quad (9-25)$$

Here  $x^+$  is nondimensional hydrodynamic entrance length and is calculated as:

$$x^+ = \frac{L_{ch}}{\text{Re} D_h} \quad (9-26)$$

For fully developed flow the  $(f \text{Re})_{fd}$  term is a function of aspect ratio only and is calculated as:

$$(f \text{Re})_{fd} = 23.922 - 30.201\gamma + 32.897\gamma^2 - 12.439\gamma^3 \quad (9-27)$$

The inlet local pressure loss is calculated as sudden contraction between two channels with different dimensions:

$$\Delta P_c = K_c \rho \frac{V_{ch}^2}{2} \quad (9-28)$$

and the contraction coefficient is:

$$K_c = \left( \frac{1}{C_c} - 1 \right)^2 \quad (9-29)$$

where  $C_c$  is the jet contraction coefficient calculated as (Webb, 2006):

$$C_c = 0.6501 - 0.2093\sigma + 0.3863\sigma^2 \quad (9-30)$$

where area ratio  $\sigma$  is defined between  $0.2 \leq \sigma \leq 0.9$ .

The outlet pressure loss due to flow expansion is modeled as sudden flow expansion and is calculated as:

$$\Delta P_e = K_e \rho \frac{V_{ch}^2}{2} \quad (9-31)$$

and the expansion coefficient is:

$$K_e = (1 - \sigma)^2 \quad (9-32)$$

### 9.3.2. TMHS Optimization Results

The numerical values obtained from the optimization study of TMHS and JIHS are listed below.

**Table 9-1. Optimum results obtained for the 1 x 1 cm<sup>2</sup> TMHS**

Normalized variables				Optimized geometry and flow variables				Objective Functions	
x1	x2	x3	x4	H <sub>ch</sub>	t <sub>fin</sub>	w <sub>ch</sub>	Re	h	P <sub>pump</sub>
-	-	-	-	[mm]	[mm]	[mm]	-	[W/m <sup>2</sup> K]	[W]
0.8236	0.4450	0.8939	0.0148	4.153	0.439	0.341	44	32059	1.02E-04
0.8355	0.4147	0.9961	0.0171	4.211	0.422	0.312	49	37000	1.77E-04
0.7581	0.3699	0.8896	0.0209	3.839	0.406	0.277	58	41601	3.44E-04
0.7385	0.2894	0.8958	0.0201	3.745	0.395	0.228	56	47085	5.93E-04
0.7054	0.3430	0.8369	0.0358	3.586	0.390	0.252	92	51544	1.17E-03
0.5214	0.3150	0.8276	0.0298	2.703	0.296	0.180	78	59591	2.25E-03
0.5343	0.3224	0.8862	0.0379	2.765	0.293	0.181	97	65472	3.50E-03
0.4900	0.2889	0.8486	0.0411	2.552	0.276	0.159	104	72506	5.99E-03
0.4641	0.2598	0.9718	0.0374	2.428	0.246	0.132	96	81045	9.23E-03
0.5002	0.2125	0.9865	0.0424	2.601	0.262	0.125	107	88884	1.43E-02
0.4246	0.2313	0.8740	0.0597	2.238	0.239	0.120	147	98461	2.93E-02
0.2578	0.2940	0.9561	0.0491	1.437	0.147	0.086	122	109597	5.43E-02
0.3043	0.2098	0.9359	0.0569	1.661	0.172	0.081	140	121693	8.70E-02
0.3529	0.1436	0.9938	0.0574	1.894	0.190	0.073	141	131690	1.26E-01

0.2709	0.1623	0.9027	0.0684	1.500	0.158	0.065	167	145324	2.43E-01
0.3580	0.1208	0.8896	0.0978	1.918	0.203	0.072	234	153746	3.58E-01
0.2614	0.2059	0.8897	0.0997	1.455	0.154	0.072	238	154380	3.61E-01
0.2432	0.2193	0.9378	0.1324	1.367	0.141	0.068	313	173033	7.47E-01
0.2260	0.1621	0.9002	0.1185	1.285	0.135	0.056	281	187932	1.12E+00
0.1346	0.2210	0.8302	0.1168	0.846	0.092	0.045	278	201680	1.89E+00
0.1486	0.1856	0.8930	0.1418	0.913	0.096	0.043	335	225302	3.44E+00
0.0856	0.2154	0.9137	0.1271	0.611	0.064	0.031	301	249949	7.28E+00
0.1075	0.1645	0.9591	0.1694	0.716	0.073	0.030	398	282025	1.40E+01
0.1318	0.1244	0.9052	0.2177	0.833	0.087	0.032	509	292797	2.04E+01
0.0762	0.2003	0.9807	0.2141	0.566	0.057	0.026	500	319225	3.35E+01
0.0554	0.1752	0.9345	0.2105	0.466	0.048	0.021	492	347748	6.61E+01
0.0777	0.1690	0.9304	0.3905	0.573	0.059	0.025	904	370843	1.33E+02
0.0595	0.1247	0.9071	0.3743	0.485	0.051	0.018	867	416197	2.99E+02
0.0366	0.1218	0.9388	0.3341	0.376	0.039	0.014	775	452389	5.57E+02
0.0161	0.1883	0.8667	0.3920	0.277	0.030	0.013	908	468249	8.28E+02
0.0257	0.1039	0.8867	0.3993	0.323	0.034	0.011	924	495415	1.38E+03
0.0147	0.1547	0.8813	0.5061	0.270	0.029	0.012	1169	516888	2.13E+03
0.0203	0.0758	0.9113	0.4608	0.297	0.031	0.009	1065	543168	3.55E+03
0.0088	0.1028	0.9946	0.6006	0.242	0.024	0.008	1385	595246	9.31E+03

**Table 9-2. Optimum results obtained for the 2 x 2 cm<sup>2</sup> TMHS**

Normalized variables				Optimized geometry and flow variables				Objective Functions	
x1	x2	x3	x4	H <sub>ch</sub>	t <sub>fin</sub>	w <sub>ch</sub>	Re	h	P <sub>pump</sub>
-	-	-	-	[mm]	[mm]	[mm]	-	[W/m <sup>2</sup> K]	[W]
0.7812	0.7915	0.7208	0.0185	3.950	0.459	0.564	52	15605	1.08E-04
0.9648	0.6377	0.8057	0.0215	4.831	0.535	0.551	59	18577	1.61E-04
0.8573	0.5796	0.7100	0.0240	4.315	0.505	0.481	65	20549	2.83E-04
0.9565	0.4272	0.9638	0.0196	4.791	0.488	0.369	55	25507	5.15E-04
0.8328	0.4654	0.8417	0.0340	4.198	0.456	0.367	88	30106	1.28E-03
0.9476	0.3035	0.9317	0.0286	4.749	0.492	0.292	75	34915	2.04E-03
0.9468	0.3224	0.9401	0.0420	4.744	0.489	0.303	106	39586	3.69E-03
0.8735	0.2287	0.8364	0.0419	4.393	0.478	0.238	106	45124	7.47E-03
0.8251	0.2766	0.9050	0.0687	4.160	0.437	0.244	167	53174	1.79E-02
0.6799	0.3420	0.9490	0.0866	3.464	0.355	0.229	208	59032	3.36E-02
0.8025	0.2132	0.9602	0.0910	4.052	0.413	0.197	218	67894	6.15E-02
0.5389	0.2191	0.8890	0.0763	2.787	0.295	0.143	185	76023	1.08E-01

0.3623	0.2913	0.7609	0.0963	1.939	0.220	0.127	230	82827	2.17E-01
0.4746	0.1952	0.9237	0.1060	2.478	0.258	0.117	253	96888	3.83E-01
0.5492	0.2333	0.9340	0.1781	2.836	0.293	0.148	418	97073	5.45E-01
0.2733	0.2967	0.8989	0.1184	1.512	0.159	0.093	281	109712	8.70E-01
0.3860	0.1595	0.9362	0.1143	2.053	0.212	0.086	272	117935	1.11E+00
0.2963	0.2883	0.9608	0.1827	1.622	0.165	0.095	428	127966	2.02E+00
0.1843	0.2635	0.9176	0.1295	1.085	0.113	0.061	307	140228	3.67E+00
0.2617	0.1714	0.9330	0.1864	1.456	0.151	0.064	437	162922	7.18E+00
0.2180	0.1263	0.9132	0.1582	1.246	0.130	0.047	372	176476	1.26E+01
0.2224	0.2542	0.9736	0.3236	1.268	0.128	0.068	751	182351	1.77E+01
0.1726	0.1947	0.8732	0.2677	1.029	0.110	0.050	623	203183	2.96E+01
0.1347	0.2054	0.8083	0.2875	0.846	0.094	0.044	668	217291	4.83E+01
0.1660	0.1165	0.9203	0.2814	0.997	0.104	0.036	654	243659	8.75E+01
0.1607	0.1213	0.9329	0.3723	0.971	0.100	0.036	863	265802	1.62E+02
0.1056	0.1419	0.9127	0.3744	0.707	0.074	0.028	867	295116	3.19E+02
0.1075	0.1108	0.8910	0.4980	0.716	0.076	0.026	1150	328739	7.44E+02
0.1038	0.1109	0.9151	0.5931	0.698	0.073	0.025	1368	348674	1.20E+03
0.0696	0.1595	0.9454	0.6331	0.534	0.055	0.022	1460	373638	1.89E+03
0.0712	0.0843	0.9525	0.5433	0.542	0.055	0.017	1254	400412	3.18E+03
0.0640	0.0937	0.9607	0.6079	0.507	0.052	0.017	1402	416367	4.36E+03
0.0595	0.1298	0.9930	0.9592	0.486	0.049	0.018	2206	443964	8.82E+03

### 9.3.3. JIHS Optimum Results

Table 9-3. Optimum results obtained for JIHS

Normalized variables					Optimized geometry and flow variables					Objective Functions	
x1	x2	x3	x4	x5	H <sub>ch</sub>	w <sub>l</sub>	t <sub>man</sub>	w <sub>v</sub>	Re <sub>pp</sub>	h	P'' <sub>pump</sub>
-	-	-	-	-	[mm]	[mm]	[mm]	[mm]	-	[W/m <sup>2</sup> K]	[W/m <sup>2</sup> ]
0.8772	0.9699	0.3264	0.9488	0.0004	0.182	0.364	0.231	0.357	1	3386	2.52E-03
0.8145	0.8597	0.1785	0.9508	0.0007	0.172	0.326	0.171	0.358	2	4412	4.23E-03
0.6366	0.8445	0.0765	0.7554	0.0013	0.145	0.321	0.131	0.289	2	5681	1.14E-02
0.2701	0.9264	0.0614	0.7245	0.0013	0.091	0.349	0.125	0.279	2	6523	2.12E-02
0.5047	0.8788	0.1999	0.7647	0.0025	0.126	0.333	0.180	0.293	4	7684	2.95E-02
0.4734	0.9198	0.0636	0.7518	0.0035	0.121	0.347	0.125	0.288	4	8700	4.67E-02
0.4520	0.8314	0.0963	0.7441	0.0041	0.118	0.316	0.139	0.285	5	9745	7.20E-02
0.4730	0.8405	0.1099	0.7437	0.0047	0.121	0.319	0.144	0.285	6	10208	8.93E-02
0.2723	0.8149	0.0964	0.7291	0.0056	0.091	0.310	0.139	0.280	7	12311	1.99E-01
0.0959	0.6183	0.1270	0.6805	0.0103	0.064	0.241	0.151	0.263	11	18175	1.31E+00
0.0546	0.6478	0.0176	0.6905	0.0125	0.058	0.252	0.107	0.267	14	20822	2.06E+00
0.0380	0.5204	0.0129	0.6630	0.0172	0.056	0.207	0.105	0.257	18	24356	4.25E+00
0.0491	0.6160	0.0331	0.7245	0.0290	0.057	0.241	0.113	0.279	30	27169	1.16E+01
0.0516	0.4188	0.0107	0.6746	0.0297	0.058	0.172	0.104	0.261	31	29536	1.39E+01
0.0403	0.4877	0.0071	0.6331	0.0433	0.056	0.196	0.103	0.247	44	35609	3.10E+01
0.0371	0.4136	0.0139	0.6428	0.0521	0.056	0.170	0.106	0.250	53	38924	5.08E+01
0.0513	0.4019	0.0060	0.6302	0.0653	0.058	0.166	0.102	0.246	66	42022	8.02E+01
0.0378	0.3059	0.0572	0.6143	0.0749	0.056	0.132	0.123	0.240	76	45523	1.65E+02
0.0297	0.3454	0.0014	0.6536	0.0966	0.054	0.146	0.101	0.254	97	51213	2.56E+02
0.0379	0.3036	0.0155	0.5970	0.1080	0.056	0.131	0.106	0.234	109	54017	4.04E+02
0.0496	0.4515	0.0070	0.6425	0.1766	0.057	0.183	0.103	0.250	177	68992	8.28E+02

0.0467	0.5471	0.0235	0.5764	0.2373	0.057	0.217	0.109	0.227	238	73745	1.45E+03
0.0900	0.3413	0.0657	0.5738	0.2634	0.063	0.144	0.126	0.226	264	75288	2.25E+03
0.0413	0.3212	0.0766	0.5734	0.2666	0.056	0.137	0.131	0.226	267	79857	2.94E+03
0.1002	0.3990	0.0788	0.4990	0.3536	0.065	0.165	0.132	0.200	354	91418	4.03E+03
0.0636	0.2365	0.1535	0.4864	0.3537	0.060	0.108	0.161	0.195	354	108291	6.71E+03
0.1149	0.2810	0.1263	0.5531	0.4898	0.067	0.123	0.151	0.219	490	112765	1.20E+04
0.1753	0.2300	0.1042	0.4213	0.5044	0.076	0.105	0.142	0.172	505	126117	1.61E+04
0.0655	0.1489	0.1202	0.5009	0.4896	0.060	0.077	0.148	0.200	490	130817	2.45E+04
0.1510	0.1124	0.1283	0.4294	0.6468	0.073	0.064	0.151	0.175	647	159376	6.20E+04
0.0564	0.1393	0.1372	0.5117	0.8206	0.058	0.074	0.155	0.204	821	167361	9.14E+04
0.1428	0.0791	0.1677	0.4060	0.9137	0.071	0.053	0.167	0.167	914	214502	2.24E+05
0.1518	0.0203	0.1185	0.3494	0.9146	0.073	0.032	0.147	0.147	915	237451	4.80E+05

## 9.4. Appendix D

As observed in visualization study discussed in Chapter 7, the pulsating flow and the two-phase flow instabilities in FFMHS result in subsequent decrease in heat transfer coefficients. Therefore, a simple flow stability criterion has been developed for two phase flow in FFMHS. The criterion is based on the balance between the inertia forces of the incoming liquid and the evaporative forces of vapor generated in the microchannel. The flow is assumed to be non-pulsating when the liquid inertia forces can suppress the evaporative forces. When the evaporative forces are dominant, the incoming flow will be pushed back creating flow pulsation and very large dryouts, therefore decreasing the heat transfer coefficients and heat transfer efficiency of the heat sink.

For two phase flow in the single unit cell shown in Figure 3-1 one can define the liquid velocity in straight section of the microchannel as:

$$v_l = \frac{\dot{m}_{ck}}{\rho_l H_{ck} w_{ck}} \quad (9-33)$$

where  $\dot{m}_{ck}$  is the mass flow rate in the unit cell,  $\rho_l$  is the liquid density and  $H_{ck}$  and  $w_{ck}$  are the microchannel height and width, respectively. The vapor velocity for the same microchannel cross-section area can be defined as:

$$v_v = \frac{q''_{base} (w_{ch} + t_{fin}) \left( \frac{w_l}{2} + t_{man} + \frac{w_v}{2} \right)}{\rho_v h_{lv} H_{ch} w_{ch}} C \quad (9-34)$$

where  $q''_{base}$  is the heat flux applied at the base of the microgrooved surface,  $t_{fin}$  is the fin thickness,  $w_l$  is the inlet feed channel width,  $w_v$  is the outlet feed channel width,

$t_{man}$  is the manifold thickness,  $\rho_v$  is the vapor density,  $h_{lv}$  is the latent heat and  $C$  is a parameter that accounts for the vapor escaping from the outlet feed channel. By considering a balance between these two forces, the equilibrium is assumed to be satisfied when:

$$\frac{v_v}{v_l} = 1 \quad (9-35)$$

By substituting Equations (9-33) and (9-34) into Equation (9-35) the stability criteria can be defined as:

$$C = \frac{\rho_v}{\rho_l} \frac{\dot{m}_{ck} h_{lv}}{q_{base}'' (w_{ck} + t_{fm}) \left( \frac{w_l}{2} + t_{man} + \frac{w_v}{2} \right)} \quad (9-36)$$

## REFERENCES

- Abdelaziz, O., Aute, V., & Radermacher, R. (2009). Multi-Scale Simulation for Novel Heat Exchanger Designs. *Applied Thermal Engineering*, In Review.
- Abdelaziz, O. A. A. (2009). *Development of Multi-Scale, Multi-Physics, Analysis Capability and its Application To Novel Heat Exchanger Design and Optimization* (PhD Thesis): University of Marylando. Document Number
- Agostini, B., Fabbri, M., Park, J. E., Wojtan, L., Thome, J. R., & Michel, B. (2007). State of the art of high heat flux cooling technologies. *Heat Transfer Engineering*, 28(4), 258-281.
- Agostini, B., Thome, J. R., Fabbri, M., & Michel, B. (2008). High heat flux two-phase cooling in silicon multimicrochannels. *Ieee Transactions on Components and Packaging Technologies*, 31(3), 691-701.
- Agostini, B., Thome, J. R., Fabbri, M., Michel, B., Calmi, D., & Kloter, U. (2007a). High heat flux flow boiling in silicon multi-microchannels - Part I: Heat transfer characteristics of refrigerant R236fa. *International Journal of Heat and Mass Transfer*.
- Agostini, B., Thome, J. R., Fabbri, M., Michel, B., Calmi, D., & Kloter, U. (2007b). High heat flux flow boiling in silicon multi-microchannels - Part II: Heat transfer characteristics of refrigerant R245fa. *International Journal of Heat and Mass Transfer*.
- Aute, V., Abdelaziz, O., Azarm, S., & Radermacher, R. (2008). *Cross-validation Based Single Response Adaptive Design of Experiments*. Paper presented at the Proc. 12th AIAA/ISSMO Multidisciplinary Analysis and Optimization Conference, Victoria, British Columbia, Canada.
- Bar-Cohen, A., Arik, M., & Ohadi, M. (2006). Direct liquid cooling of high flux micro and nano electronic components. *Proceedings of the Ieee*, 94(8), 1549-1570.
- Bergles, A. E., Lienhard, J. H., Kendall, G. E., & Griffith, P. (2003). Boiling and evaporation in small diameter channels. *Heat Transfer Engineering*, 24(1), 18-40.
- Bertsch, S. S., Groll, E. A., & Garimella, S. V. (2008). Refrigerant flow boiling heat transfer in parallel microchannels as a function of local vapora quality. *International Journal of Heat and Mass Transfer*, 51, 4775-4787.
- Bowers, M. B., & Mudawar, I. (1994). High flux boiling in low flow rate, Low pressure drop mini-channel and micro-channel heat sinks. *Int. J. Heat Mass Transfer*, 37(2), 321-334.
- Chen, J. C. (1966). Correlation for boiling heat transfer to saturated fluids in convective flow. *Process Design and Development*, 5(3), 322-329.
- Chen, T. L., & Garimella, S. V. (2006). Measurements and high-speed visualizations of flow boiling of a dielectric fluid in a silicon microchannel heat sink. *International Journal of Multiphase Flow*, 32(8), 957-971.
- Copeland, D. (1995a). Manifold Microchannel Heat Sinks: Analysis and Optimization. *Thermal Science and Engineering*, 3(1), 7-12.

- Copeland, D. (1995b). Manifold Microchannel Heat Sinks: Numerical Analysis. *ASME Cooling and Thermal Design of Electronic Systems*, 15, 111-116.
- Copeland, D., Behnia, M., & Nakayama, W. (1997). Manifold microchannel heat sinks: Isothermal analysis. *Ieee Transactions on Components Packaging and Manufacturing Technology Part A*, 20(2), 96-102.
- Cornwell, K., & Kew, P. (1992). *Boiling in small parallel channels*. Paper presented at the Proceedings of the International Conference on Energy Efficiency in Process Technology.
- Dean, W. R. (1927). Note on the motion of fluid in a curved pipe. *Phil. Mag*, 20, 208-223.
- F-Chart-Inc. (2009). Engineering Equation Solver: <http://www.fchart.com/ees/ees.shtml>.
- Fabbri, M., Wetter, A., Mayer, B., Brunschwiler, T., Michel, B., Rothuizen, H., et al. (2006). *Microchip Cooling Module Based on Fc72 Slot Jet Arrays without Cross-Flow*. Paper presented at the SEMI-THERM 2006, Dallas, TX.
- Fluent-Inc. (2008). Fluent 6.2 Documentation Manual, User's Manual. Retrieved December, 2009
- Ghiaasiaan, M. (2008). *Two-Phase Flow, Boiling and Condensation in Conventional and Miniature Systems*. Cambridge: CAMBRIDGE UNIVERSITY PRESS.
- Goldberg, D. (1989). *Genetic Algorithms in Search, Optimization, and Machine Learning*: Addison-Wesley Professional.
- Haller, D., Woias, P., & Kockmann, N. (2009). Simulation and Experimental Investigation of Pressure Loss and Heat Transfer in Microchannel Networks Containing Bends and T Junction. *International Journal of Heat and Mass Transfer*((In review)).
- Harirchian, T., & Garimella, S. V. (2008). Microchannel size effects on local flow boiling heat transfer to a dielectric fluid. *International Journal of Heat and Mass Transfer*, 51(15-16), 3724-3735.
- Harpole, G. M., & Eninger, J. E. (1991). *Micro-Channel Heat Exchanger Optimization*. Paper presented at the Proceedings of Seventh IEEE Semi-Therm Symposium.
- Hilbert, R., Janiga, G., Baron, R., & Thévenin, D. (2006). Multi-objective shape optimization of a heat exchanger using parallel genetic algorithm. *International Journal of Heat and Mass Transfer*, Volume 49, Issues 15-16, July 2006, Pages 2567-2577.
- Hsu, Y. Y., & Graham, R. W. (1961). An analytical and Experimental Study of the Thermal Boundary Layer and Ebullition Cycle in Nucleate Boiling. *NASA TN-D-594*.
- Incropera, F. P., & DeWitt, D. P. (2002). *Fundamentals of Heat and Mass Transfer*: John Wiley and Sons.
- Jankowski, N. R., Everhart, L., Morgan, B., Geil, B., & McCluskey, P. (2007). Comparing Microchannel Technologies to Minimize the Thermal Stack and Improve Thermal Performance in Hybrid Electric Vehicles. *IEEE*, 124-131.
- Johnson, R. T., Jones, B., & Fowler, J. W. (2008). *COMPARING DESIGNS FOR COMPUTER SIMULATION EXPERIMENTS*. Paper presented at the 2008 Winter Simulation Conference.

- Joye, D. D. (1994). Optimum Aspect Ratio for Heat Transfer Enhancement in Curved Rectangular Channels *Heat Transfer Engineering*, 15(2), 32-38.
- Ju, H., Huang, Z., Xu, Y., Duan, B., & Yu, Y. (2001). Hydraulic performance of small bending radius helical coil-pipe. *J Nucl Sci Technol*, 18, 826-831.
- Kandlikar, S. G. (1990). A General Correlation for Saturated Two-Phase Flow Boiling Heat Transfer in Horizontal and Vertical Tubes. *Journal of Heat Transfer*(112), 219-228.
- Kandlikar, S. G. (2002). Fundamental issues related to flow boiling in minichannels and microchannels. *Experimental Thermal and Fluid Science*, 26, 389-407.
- Kandlikar, S. G. (2003). *Flow Boiling in Microchannels - Non dimensional Groups and Heat Transfer Mechanisms*. Paper presented at the Congrès de la Société Française de Thermique 2003, Grenoble.
- Kandlikar, S. G. (2004). Heat Transfer Mechanisms During Flow Boiling in Microchannels. *Transactions of the ASME*, 126(8), 8-16.
- Kandlikar, S. G. (2005). High flux heat removal with microchannels - A roadmap of challenges and opportunities. *Heat Transfer Engineering*, 26(8), 5-14.
- Kandlikar, S. G., & Balasubramanian, P. (2003). *Single-Phase Flow Characteristics and Effect of Dissolved Gases on Heat Transfer Near Saturation Conditions in Microchannels*. Paper presented at the International Mechanical Engineering Conference and Exposition 2002, New York.
- Kandlikar, S. G., & Bapat, A. V. (2007). Evaluation of jet impingement, spray and microchannel chip cooling options for high heat flux removal. *Heat Transfer Engineering*, 28(11), 911-923.
- Kandlikar, S. G., Garimella, S. V., Colin, S., Li, D., & King, M. R. (2004). *Heat Transfer and Fluid Flow in Minichannels and Microchannels*. Oxford: Elsevier.
- Kandlikar, S. G., & Steinke, M. (2003). *Predicting Heat Transfer During Flow Boiling in Minichannels and Microchannels*. Paper presented at the ASHRAE TRANSACTIONS.
- Kandlikar, S. G., & Upadhye, H. R. (2005). *Extending the Heat Flux Limit with Enhanced Microchannels in Direct Single-Phase Cooling of Computer Chipp*. Paper presented at the Invited Paper presented at IEEE Semi-Therm 21, San Jose.
- Kays, W. M., & Crawford, M. E. (1980). *Convective Heat and Mass Transfer*. New York: McGraw-Hill.
- Kendall, G. E., Griffith, P., Bergles, A. E., & Lienhard, J. V. (2001). *Small diameter effects on internal flow boiling*. Paper presented at the Proc. IMECE-2001, New York.
- Khan, W. A., Culham, J. R., & Yovanovich, M. M. (2009). Optimization of Microchannel Heat Sinks Using Entropy Generation Minimization Method. *IEEE TRANSACTIONS ON COMPONENTS AND PACKAGING TECHNOLOGIES*, 243-251.
- Kim, D.-K. (2007). Closed-form correlations for thermal optimization of microchannels. *International Journal of Heat and Mass Transfer*, 5318-5322.
- Kim, J. H. (2007). Spray cooling heat transfer: The state of the art. *International Journal of Heat and Fluid Flow*, 28(4), 753-767.

- Kim, S. J. (2004). Methods for Thermal Optimization of Microchannel Heat Sinks. *Heat Transfer Engineering*, 37-49.
- Kim, Y. I., Chun, W. C., Kim, J. T., Pak, B. C., & Baek, B. J. (1998). Forced Air Cooling by Using Manifold Microchannel Heat Sinks. *KSME International Journal*, 12(4), 709-718.
- Kockmann, R., Engler, M., & Haller, D. (2005). Fluid Dynamics and Transfer Processes in Bended Microchannels. *Heat Transfer Engineering*, 26(3), 71-78.
- Kosar, A., & Peles, Y. (2007). Boiling heat transfer in a hydrofoil-based micro pin fin heat sink. *International Journal of Heat and Mass Transfer*, 50(5-6), 1018-1034.
- Kuo, C. J., & Peles, Y. (2007). Local measurement of flow boiling in structured surface microchannels. *International Journal of Heat and Mass Transfer*, 50(23-24), 4513-4526.
- Langhaar, H. L. (1942). Steady flow in the transition length of a straight tube. *J. Appl. Mech*, 9, A55-A58.
- Lazarek, G. M., & Black, S. H. (1982). Evaporative heat transfer pressure drop and critical heat flux in a small vertical tube with R-113. *Int. J. Heat Mass Transfer*, 25, 945-960.
- Lee, H. J., & Lee, S. Y. (2001). Heat transfer correlation for boiling flows in small rectangular horizontal channels with low aspect ratios. *International Journal of Multiphase Flow*, 27(12), 2043-2062.
- Lee, J., & Mudawar, I. (2005a). Two-phase flow in high-heat-flux micro-channel heat sink for refrigeration cooling applications: Part I - pressure drop characteristics. *International Journal of Heat and Mass Transfer*, 48(5), 928-940.
- Lee, J., & Mudawar, I. (2005b). Two-phase flow in high-heat-flux micro-channel heat sink for refrigeration cooling applications: Part II - heat transfer characteristics. *International Journal of Heat and Mass Transfer*, 48(5), 941-955.
- Lee, P. S., & Garimella, S. V. (2008). Saturated flow boiling heat transfer and pressure drop in silicon microchannel arrays. *International Journal of Heat and Mass Transfer*, 51(3-4), 789-806.
- Lee, P. S., Garimella, S. V., & Liu, D. (2005). Investigation of heat transfer in rectangular microchannels. *International Journal of Heat and Mass Transfer*, 48(9), 1688-1704.
- LeVegue, R. J. (2002). *Finite Volume Methods for Hyperbolic Problems*: Cambridge University Press.
- Lian-Tuu, Y., & Chu, R. C. (2002). *Thermal Management of Microelectronic Equipment: Heat Transfer Theory, Analysis Methods and Design Practices*: American Society of Mechanical Engineers.
- Lie, Y. M., & Lin, T. F. (2005). Saturated flow boiling heat transfer and associated bubble characteristics of R-134a in a narrow annular duct. *International Journal of Heat and Mass Transfer*, 48(25-26), 5602-5615.
- Lie, Y. M., & Lin, T. F. (2006). Subcooled flow boiling heat transfer and associated bubble characteristics of R-134a in a narrow annular duct. *International Journal of Heat and Mass Transfer*, 49(13-14), 2077-2089.

- Ligrani, P. M., Choi, S., Schallert, A. R., & Skogerboe, P. (1996). Effects of Dean vortex pairs on surface heat transfer in curved channel flow. *International Journal of Heat and Mass Transfer*, 39(1), 27-37.
- Lin, S., Kew, P. A., & Cornwell, K. (2001). Two-phase heat transfer to a refrigerant in a 1 mm diameter tube. *International Journal of Refrigeration-Revue Internationale Du Froid*, 24(1), 51-56.
- Liu, D., & Garimella, S. V. (2005). Analysis and optimization of the thermal performance of microchannel heat sinks. *International Journal for Numerical Methods in Heat & Fluid Flow*, 7-26.
- Liu, D., & Garimella, S. V. (2007). Flow boiling heat transfer in microchannels. *Journal of Heat Transfer-Transactions of the Asme*, 129(10), 1321-1332.
- Lophaven, S. N., Nielsen, H. B., & Søndergaard, J. (2002). *DACE - A MATLAB Kriging Toolbox* (Technical Report IMM-TR-2002-12). Lyngby – Denmark: Technical University of Denmark. Document Number)
- Meyer, T. M., Mudawar, I., Boyack, C. E., & Hale, C. A. (2005). Single-phase and two-phase cooling with an array of rectangular jets. *International Journal of Heat and Mass Transfer*, 49(1-2), 17-29.
- Mitchell, M. (1998). *An Introduction to Genetic Algorithms*: The MIT Press.
- Mudawar, I. (2001). Assessment of high-heat-flux thermal management schemes. *Ieee Transactions on Components and Packaging Technologies*, 24(2), 122-141.
- Ng, E. Y. K., & Poh, S. T. (1999). Investigative Study of Manifold Microchannel Heat Sinks For Electronic Cooling Design. *Journal of Electronics Manufacturing*, 9(2).
- Park, K., Oh, P., & Lim, H. (2006). The application of the CFD and Kriging method to an optimization of heat sink. *International Journal of Heat and Mass Transfer*, 3439-3447.
- Peles, Y. P., Yarin, L. P., & Hestroni, G. (2001). ‘Steady and Unsteady Flow in a Heated Capillary. *Int. J. Multiphase Flow*, 4(27), 577–598.
- Peng, H., & Ling, X. (2007). Optimal design approach for the plate-fin heat exchangers using neural networks cooperated with genetic algorithms. *Applied Thermal Engineering*, Volume 28, Issues 25-26, April 2008, Pages 2642-2650.
- Peters, J. V. S., & Kandlikar, S. (2007). *Further Evaluation of a Flow Boiling Correlation for Mmicrochannels and Minichannels*. Paper presented at the Proceedings of the Fifth International Conference on Nanochannels, Microchannels and Minichannels, Puebla, Mexico.
- Phillips, R. J. (1987). *Forced Convection, Liquid Cooled, Microchannel* (M.S. Thesis,). Cambridge, MA: Dept. of Mechanical Engineering, Massachusetts Institute of Technology. Document Number)
- Qu, W., & Mudawar, I. (2004). Measurement and correlation of critical heat flux in two-phase micro-channel heat sinks. *Int. J. Heat Mass Transfer*, 47, 5749-5763.
- Rosaguti, N. R., Fletcher, D. F., & Haynes, B. S. (2007). Low-Reynolds number heat transfer enhancement in sinusoidal channels. *62(3)*, 694-702.

- Ryu, J. H., Choi, D. H., & Kim, S. J. (2003). Three Dimensional Numerical Optimization of a Manifold Microchannel Heat Sink. *International Journal of Heat and Mass Transfer*, 46, 1553-1562.
- Sacks, J., Welch, W. J., Mitchell, T. J., & Wynn, H. P. (1989). Design and Analysis of Computer Experiments. *Statistical Science*, 409-435.
- Saitoh, S., Daiguji, H., & Hihara, E. (2005). Effect of tube diameter on boiling heat transfer of R-134a in horizontal small-diameter tubes. *International Journal of Heat and Mass Transfer*, 48(23-24), 4973-4984.
- Schneider, B., Kosar, A., & Peles, Y. (2007). Hydrodynamic cavitation and boiling in refrigerant (R-123) flow inside microchannels. *International Journal of Heat and Mass Transfer*, 50(13-14), 2838-2854.
- Seban, R. A. (1978). *Transport to falling films*. Paper presented at the 6th International Heat Transfer Conference, Washington.
- Shah, R. K., & London, A. L. (1978). *Laminar Flow Forced Convection in Ducts* (Vol. Supplement 1). New York: Academic Press.
- Shao, B., Sun, Z., & Wang, L. (2007). Optimization design of microchannel cooling heat sink. *International Journal of Numerical Methods for Heat & Fluid Flow*, 628-637.
- Shewry, M. C., & Wynn, H. P. (1987). Maximum Entropy Sampling. *Journal of Applied Statistics*, 14:898-914.
- Sieder, E. N., & Tate, G. E. (1936). *Ind. Eng. Chem.*, 28(1429).
- Steinke, M. E., & Kandlikar, S. G. (2003). *Flow Boiling and Pressure Drop in Parallel Microchannels*. Paper presented at the First International Conference on Microchannels and Minichannels, New York.
- Steinke, M. E., & Kandlikar, S. G. (2004). An experimental investigation of flow boiling characteristics of water in parallel microchannels. *Journal of Heat Transfer-Transactions of the Asme*, 126(4), 518-526.
- Sung, M. K., & Mudawar, I. (2009). CHF determination for high-heat flux phase change cooling system incorporating both micro-channel flow and jet impingement. *International Journal of Heat and Mass Transfer*, 52(3-4), 610-619.
- Thome, J. R., Dupont, V., & Jacobi, A. M. (2004). Heat transfer model for evaporation in microchannels Part I: presentation of the model. *International Journal of Heat and Mass Transfer*, 47(14-16), 3375-3385.
- Thors, P., & Zoubkov, N. (2009). USA Patent No. US 7,509,828 B2.
- Tran, T. N., Wambsganss, D. M., & France, D. M. (1996). Small circular and rectangular rectangular channel. *International Journal of Multiphase Flow*, 22(3), 485-498.
- Tuckerman, D. B., & Pease, R. F. W. (1981). High-Performance Heat Sinking for VLSI. *IEEE Electron Device Letters*, Vol. EDL2, No. 5, 126-129.
- Ujhidy, A., Nemeth, J., & Szepvolgyi, J. (2003). Fluid flow in tubes with helical elements. *Chemical Engineering and Processing*, 42, 1-7.
- Van Beers, W. C. M. (2005). *Kriging Metamodeling in Discrete Event Simulation: An Overview*. Paper presented at the Proceedings of the 2005 Winter Simulation Conference.

- Versteeg, H. K., & Malalasekera, W. (2007). *An introduction to Computational Fluid Dynamics: The finite Volume Method*: Prentice Hall.
- Visaria, M., & Mudawar, I. (2008). Theoretical and experimental study of the effects of spray inclination on two-phases spray cooling and critical heat flux. *International Journal of Heat and Mass Transfer*, 51(9-10), 2398-2410.
- Warrier, G. R., Dhir, V. K., & Momoda, L. A. (2002). Heat transfer and pressure drop in narrow rectangular channel *Exp. Therm. Fluid Sci*, 26, 53-64.
- Webb, R. L. (2006). Entrance and Exit Losses for Developing Flow in Parallel Plate Channels. *Heat Transfer Engineering*, 27(10), 30-35.
- Wikipedia®. (2009). Wikipedia, the free encyclopedia.
- Xia, G., Liu, Q., Qi, J., & Xu, J. (2008). Influence of Surfactant on Friction Pressure Drop in Manifold Microchannels. *International Journal of Thermal Sciences*, 47, 1658-1664.
- Xie, G. N., Sunden, B., & Wang, Q. W. (2008). Optimization of compact heat exchangers by a genetic algorithm. *Applied Thermal Engineering*, Volume 28, Issues 28-29, June 2008, Pages 2895-2906.
- Xin, R. C., & Ebdian, M. A. (1997). The effects of Prandtl numbers on local and average convective heat transfer characteristics in helical pipes. *J Heat Transfer*(119), 463-467.
- Yan, Y. Y., & Lin, T. F. (1998). Evaporation heat transfer and pressure drop of refrigerant R-134a in a small pipe. *International Journal of Heat and Mass Transfer*, 41(24), 4183-4194.
- Yanase, S., Mondal, R. N., & Kaga, Y. (2005). Numerical study of non-isothermal flow with convective heat transfer in a curved rectangular duct. 44(11), 1047-1060.
- Yen, T. H., Shoji, M., Takemura, F., Suzuki, Y., & Kasagi, N. (2006). Visualization of convective boiling heat transfer in single microchannels with different shaped cross-sections. *International Journal of Heat and Mass Transfer*, 49(21-22), 3884-3894.
- Yun, R., Heo, J. H., & Kim, Y. C. (2006). Evaporative heat transfer and pressure drop of R410A in microchannels. *International Journal of Refrigeration-Revue Internationale Du Froid*, 29(1), 92-100.
- Zhang, L., Wang, E. N., Goodson, K. E., & Kenny, T. W. (2005). Phase change phenomena in silicon microchannels. *Int. J. Heat Mass Transfer*, 48, 1572-1582.